APPLIED
COMPUTATIONAL
ELECTROMAGNETICS
SOCIETY
JOURNAL

The illustrations on the front cover have been obtained from the research groups at the Department of Electrical
Engineering, The University of Mississippi.

THE APPLIED COMPUTATIONAL ELECTROMAGNETICS SOCIETY

JOURNAL

TABLE OF CONTENTS

Broadband Dual-Use Array with Planar Log Periodic Dipole Elements

Seth A. McCormick and William O. Coburn

Army Research Laboratory
Adelphi, Maryland 20783, United States of America
seth.a.mccormick.civ@mail.mil, william.o.coburn.civ@mail.mil

Abstract ─ This paper presents a phased array consisting of 8 horizontally positioned planar log periodic dipole array antennas for use over the frequency range of 800 to 1,300 MHz. The array is dual use in that it can either scan in azimuth with a narrow beam or be forward looking with a null-filled broad beam. To achieve the broad beam, the 8-element array is divided into two 4-element subarrays. The main beam of each subarray is then pointed near the first null of the 8-element uniform array radiation pattern to "fill" the nulls. The results for the narrow beam configuration produce an azimuthal beamwidth of 15° with 15 dBi of gain, and the null-filled configuration produces an increase in azimuthal beamwidth to 55° (40° increase) with a peak gain of 10 dBi (loss of 5 dB). Note that this paper only presents the antenna development and array testing but not any system hardware.

Index Terms ─ Antipodal antennas, null filling, phased arrays, planar log periodic dipole array, sub arrays.

I. INTRODUCTION

Achieving high gain with a relatively broad beamwidth can be a challenge for antenna engineers. Given the inverse relationship between gain and beamwidth, where a large gain implies a small beamwidth and vice versa, the antenna engineer must prioritize one or accept a middle ground for both (or change the beamwidth criterion from 3 dB). Still, designing a single antenna element that meets both gain and broad beam requirements can be a challenge as the radiation pattern cannot be easily manipulated.

For phased arrays, however, the radiation pattern can be easily manipulated and thus generate a high gain, broad beam radiating aperture. In phased arrays, the radiated phase front can be electronically controlled, thereby steering the beam to any forward location in azimuth and elevation given a sufficient number of elements. With the ability to manipulate the shape of the beam, it is possible to maximize both beamwidth and gain with a phased array system by sub-dividing the array into scanned subarrays. The subarrays can then point to near the first null of the uniform array pattern,

filling the nulls, thereby broadening the beam. Similar methods are seen in pattern synthesis and is typically called null filling [1], but for the presented array, null filling will refer to the first nulls of the combined array pattern instead of just locations of lost coverage [2].

This paper describes the design of planar log periodic dipole array (LPDA) antenna elements for use in a dual function array. The antennas and array are designed and evaluated using FEKO [3], a commercial computational electromagnetics (CEM) code using the Method of Moments (MoM). The frequency band to be covered is 800 to 1,300 MHz. The 8-element array must be able to scan in azimuth for one configuration, and must maximize both forward gain and azimuthal beamwidth in the other configuration.

Several design variations of the antenna and array were examined with the final design being an 8-element horizontal array. The development of the antenna elements and testing of the scanning and null filling are presented in the next two sections.

II. PLANAR LOG PERIODIC DIPOLE ARRAY ELEMENT

An LPDA element is chosen to obtain the required gain-bandwidth product. The conventional LPDA is a linear array of parallel dipoles with unequal lengths, L_n, widths, w_n and spacing, d_n, fed by a twisted transmission line [4]. A planar version is designed that exceeds the bandwidth requirement having scale factor $\tau = l_{n+1}/l_n = w_{n+1}/w_n = d_{n+1}/d_n = 0.9$ with 14 dipole elements [5]. It has total length, L = 335.5 mm, and total width, W = 322.3 mm not including the substrate where L is the full array length and W would correspond to the longest dipole length including the center trace width.

A compact version is designed to minimize length by linearly scaling the entire structure by 2/3 which increases the gain at the highest frequencies. The surface current distribution at 900 MHz is compared in Fig. 1, indicating that the original design radiates from the smaller dipoles so is approaching the end of its frequency bandwidth. This planar LPDA has 14 antipodal dipole elements with total length L = 223.6 mm and W = 210.7 mm without substrate. Including the substrate, the total length and

width are 239.3 mm and 232.7 mm respectively. Both use 1.57 mm substrate thickness where the center trace is 4.15 mm in width. This trace width is not included in the antipodal dipole arm lengths. The first dipole, which sets the low frequency as $l_1 \approx \frac{\lambda_L}{2} = 686$ MHz, has dimensions $l_1 = 210.85$ mm and $w_1 = 7.16$ mm for the compact design with a center spacing to the next dipole of $d_1 = 28.32$ mm. Following a linear scale, the next element length would be $l_2 = \tau l_1 = 189.77$ mm and width would be $w_2 = \tau w_1 = 6.44$ mm with next dipole spacing $d_2 = \tau d_1 = 25.49$ mm.
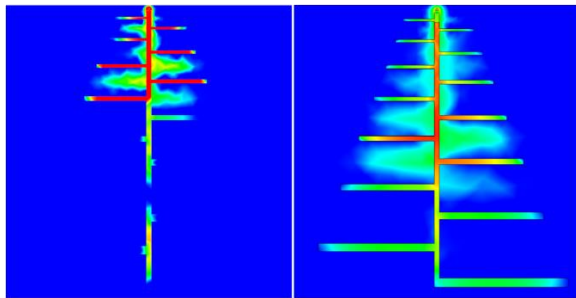
Fig. 1. Planar LPDA antenna elements top view (left) original and (right) compact design, not to scale.

Additional design approaches investigated included variations in the trace and pin-feed connection at the tip of the planar LPDA. Various configurations of the feed cable were considered but not included in the model, with one example shown in Fig. 2. This investigation determined that contrary to what is typically found in the literature, electrical connections of the cable shield to the trace degraded performance, so an insulated cable was subsequently used. This was found for either spot or continuous solder joints.

The cable shield is connected only at the tip of the trace and insulated with a Kapton thin film over its length. This final feed point design was modeled with a short section of coaxial cable with a waveguide port. A finer mesh is used on the feed where the center conductor is modeled as a cylinder connected to the bottom trace. A cylinder was used instead of a wire because of the thin wire limitation in MoM where the segment to radius ratio was too large to mesh the actual center conductor. The dielectric extending from the cable shield (see Fig. 2) was included with negligible difference. This model was sufficient to represent the feed point to obtain an accurate input impedance.

The simulation required 1.7 GB and 0.1 hours per frequency on 4 CPUs. The result for this initial LPDA on Duroid is shown in Fig. 3 for the measured reflection coefficient compared to the simulated result. The agreement between simulation and measurement is fair, justifying the chosen feed model.
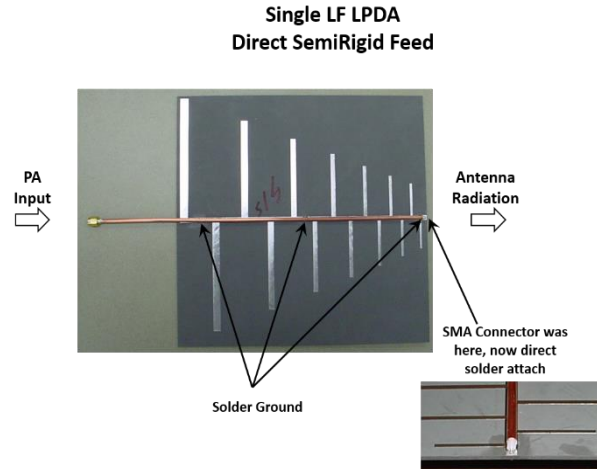
Fig. 2. Planar LPDA initial fabrication.
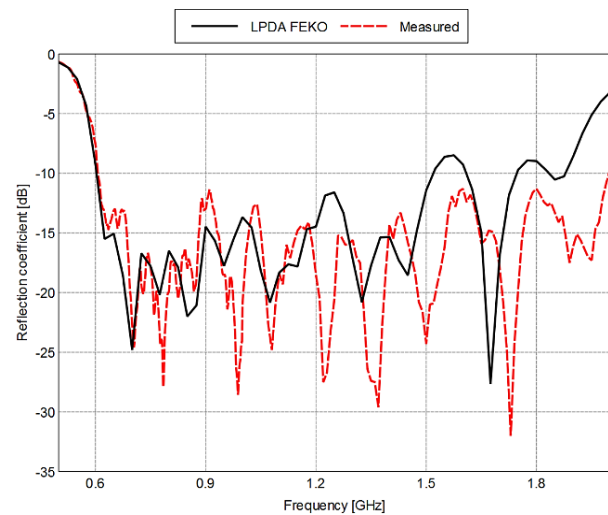
Fig. 3. Planar compact LPDA on Duroid reflection coefficient comparison.

The final planar LPDA design was slightly longer to accommodate a longer trace for the pin-feed connection at the tip of the antenna. The dipole arms were also rounded at the tips. The feed cable was routed along but insulated from the center trace. The final result for the planar LPDA on Duroid is shown in Fig. 4 and Fig. 5 for the measured reflection coefficient and gain compared to the simulation results respectively. A commercial time-domain finite-difference (TDFD) solver, GEMS [6], was used for code-to-code validation. The time-domain solver is more efficient to capture the measured oscillations in the reflection coefficient compared to the large number of frequencies that would be required in the frequency domain. The E-plane pattern comparison is shown in Fig. 6 at 900 and 1300 MHz where the simulation and measurement are in agreement except in the backlobe.
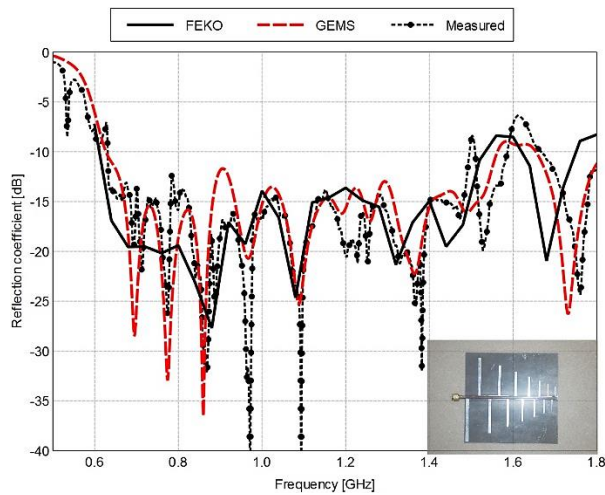
Fig. 4. Planar LPDA reflection coefficient comparison.
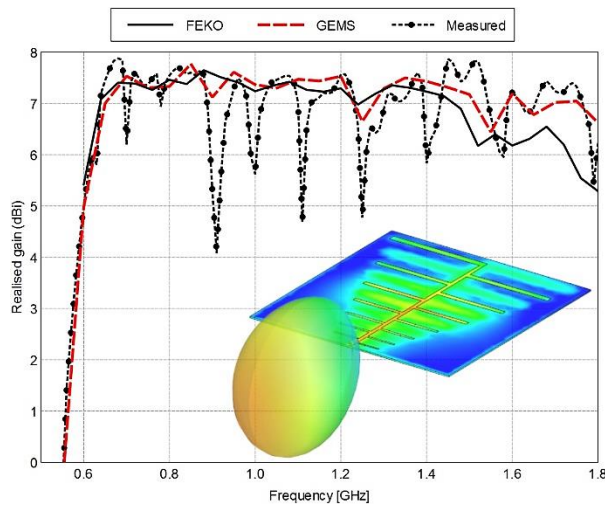
Fig. 5. Planar compact LPDA gain comparison.
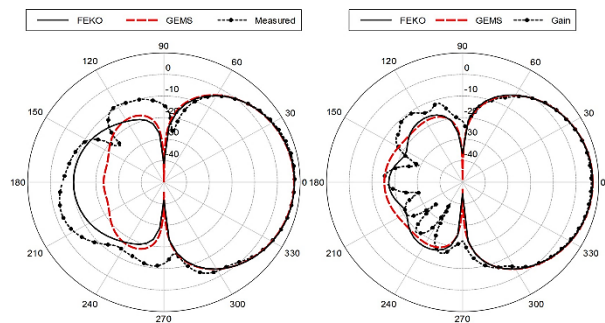
Fig. 6. Planar LPDA E-plane radiation pattern at (left) 900 MHz and (right) 1300 MHz.

The cost of fabricating the planar LPDA elements on Duroid was a concern, so FR4, a flame resistance glass reinforced epoxy laminate, was chosen as the final substrate to reduce cost. The higher loss substrate (tanδ = 0.02) produced a ~1.7 dB gain penalty compared to using the much lower loss (tanδ = 0.001) RT/Duroid® 5880 laminates. The planar design on FR4 vs. Duroid substrates will have roughly an order of magnitude lower fabrication cost but with a significant gain penalty.

With Duroid, the compact LPDA has similar gain as the original antenna but with a 10 dB larger back lobe. The FR4 version has at least 1.6 dB less gain but a 10 dB lower back lobe. The boresight gain versus frequency is shown in Fig. 7 where the original LPDA has reduced gain above 1200 MHz. The compact design meets the bandwidth requirement although the FR4 version has reduced gain. The measured gain for the prototypes has some artifacts associated with noise limitations in the anechoic chamber measurements.
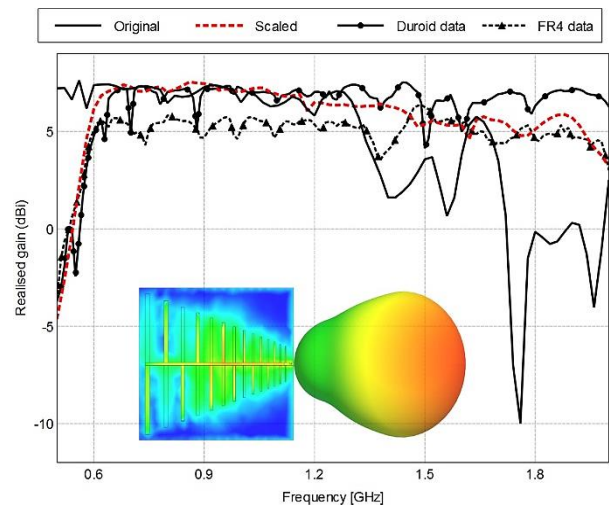
Fig. 7. Simulated boresight gain versus frequency compared to the measured gain for the compact LPDA on Duroid and FR4 substrates.

The different configurations of the planar LPDA were evaluated through measurement, where it was determined that any variations found were negligible. The difference in configurations involved how the feed point at the top of the planar LPDA was fabricated as well as rounding the corners of the dipole elements to remove unwanted electric current discontinuities. The best design was found to be an insulated cable running along the center trace with a through-hole for the center conductor and the cable shield connected only at the end of the center trace. The simulated and measured reflection coefficient are shown in Fig. 8 for the planar LPDA with the feed model shown in the inset figure. Only 8 mm of the coaxial cable with waveguide port is included in the simulation where the solid center conductor extends 1.7 mm beyond the cable shield with right angle bend.
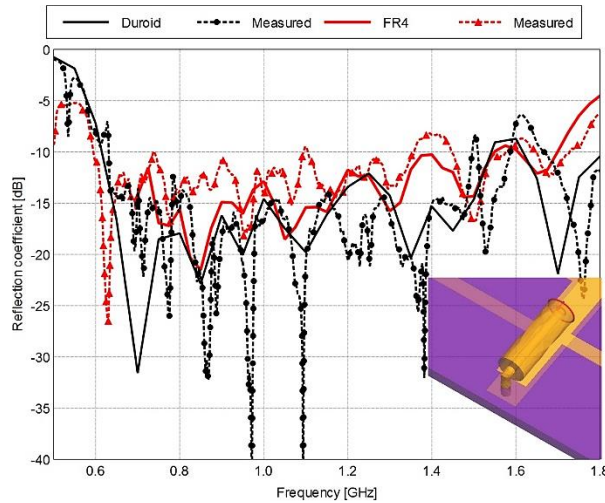
Fig. 8. Planar LPDA reflection coefficient comparison for Duroid and FR4.

The comparison shows relatively good agreement between simulation and measurement. The measurement also shows that the FR4 is not as well matched as the Duroid. The E-plane patterns at 900 MHz are shown in Fig. 9 where, with Duroid substrate, the gain is 7.7 dBi compared to 6 dBi using FR4, confirming that the dielectric losses reduce the antenna efficiency.
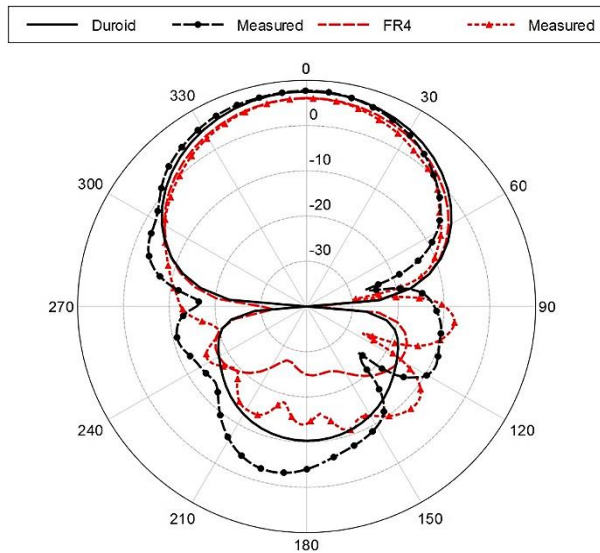
Fig. 9. Planar compact LPDA E-plane comparison for Duroid and FR4 substrates.

III. ARRAY MEASUREMENTS

The planar LPDA elements are matched over the frequency band 800 to 1,300 MHz. The array spacing was chosen to be a half-wavelength centered in that band, i.e., 1,075 MHz 139.5 mm (5.49 in.). The planar LPDA elements are oriented at 45° (slant-polarization)

in order to transmit both horizontal and vertical field components with respect to the ground.

The 8-element horizontal array provides high gain (15.5 dBi), electronic scanning, and a narrow beam in azimuth (14.6°) with broad beamwidth in elevation. With this design, the maximum array width is 1.25 m with a maximum height of 0.68 m. The planar LPDAs are mounted inside a plastic enclosure with a polycarbonate radome (1/8 in. thick) on the enclosure front which is then mounted to a metal enclosure housing the amplifiers and phase shifters.

The model used for in-situ simulations is shown in Fig. 10. The presence of the metal electronics enclosure has only a small influence on the forward gain. Note that the plastic enclosures were not meshed for simulation and are only kept to maintain proper antenna placement when adjusting element positions. Measurements with and without the polycarbonate radome indicate negligible difference. The elements use simple edge ports instead of the coaxial wave port feed for efficient computation.

The simulation for 8-elements without substrates at 3 m above a lossy half space ($\varepsilon_r = 10$, $\sigma = 5$ mS/m) required only 450 MB and 90 s/frequency on 4 CPUs. Including the substrates was a severe computational penalty requiring 132 GB and 17.5 hours per frequency on 16 CPUs. The lossy half space was modeled using the infinite half space dielectric in FEKO. The fields in the half space are computed by solving the exact Somerfield integral equations in the media. While slower to compute than the reflection coefficient approximation, the results are more akin to the real world. Simulations showed that pattern perturbations in the azimuthal plane are negligible, and that there is interference in the elevation plane due to ground bounce.
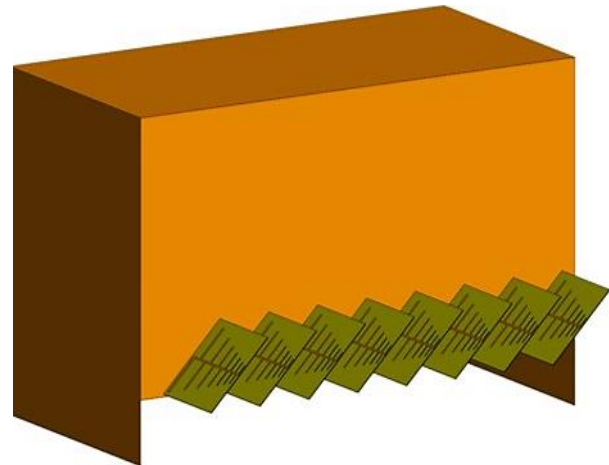
Fig. 10. In-situ model for 8-element horizontal array on metal enclosure located at 3 m above soil.

The comparison between simulation and measurement for in-phase antenna elements is shown

in Fig. 11. Scanning was implemented and tested using 8 voltage controlled phase shifters. The data was taken over a ±90° span in azimuth to prevent damage to the input cable during rotation. Figure 11 shows that the peak gain and beamwidth are as expected with the first null occurring at ±18° from boresight. The simulation is in good agreement with some minor asymmetries in the measured sidelobes. These asymmetries are associated with differences in the polarization dependencies of the chamber since slant polarization is used in the chamber measurements. In particular, asymmetries due to wall side vs. door side.
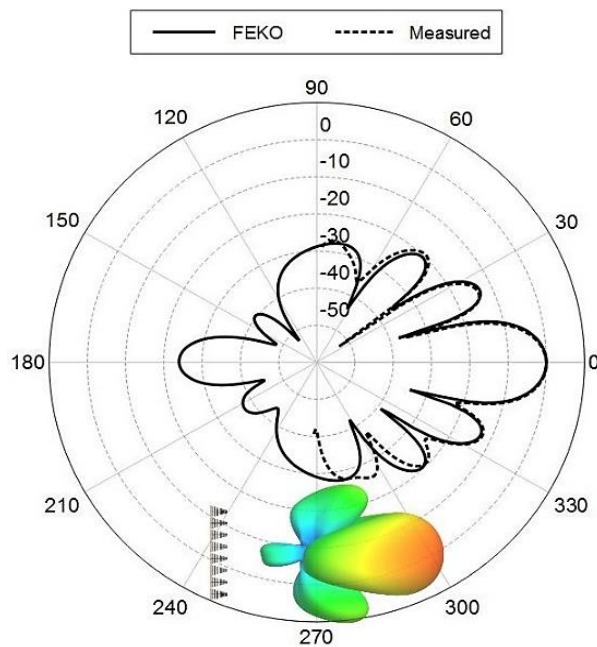
Fig. 11. 8-element horizontal array normalized azimuthal pattern comparison at 900 MHz.

Figures 12 and 13 show the raw measured azimuthal pattern when scanning at 900 and 1,300 MHz respectively. The legend gives the phase progression used to scan to the associated azimuth positions. The asymmetric decrease in beam peak from scanning the array to one side and then to the other is most likely due to the measurement environment where there can be asymmetries due to absorber placement (door side versus wall side) with differences between horizontal and vertical polarization.

The inconsistency in beam location between 900 and 1,300 MHz is expected from array theory, where the phase progression is frequency dependent and would need compensation at 1,300 MHz to scan to the same position as the 900 MHz case. The measured results conclude that the scanning configuration is a success, but care would need to be taken when setting the phase progression to make sure that the array scans to the correct location.

Accomplishing the secondary function, where both a wide beam and high gain are required, necessitated splitting the 8-element array into two 4-element horizontal arrays. Initial hypothesis supposed pointing the main beam of each subarray towards the 3 dB beamwidth location (7°) of the uniform 8-element array azimuthal pattern would achieve a broad beam. But further study showed that it is preferred to phase the two 4-element subarrays so as to point just past the first nulls instead (at 20° from boresight).
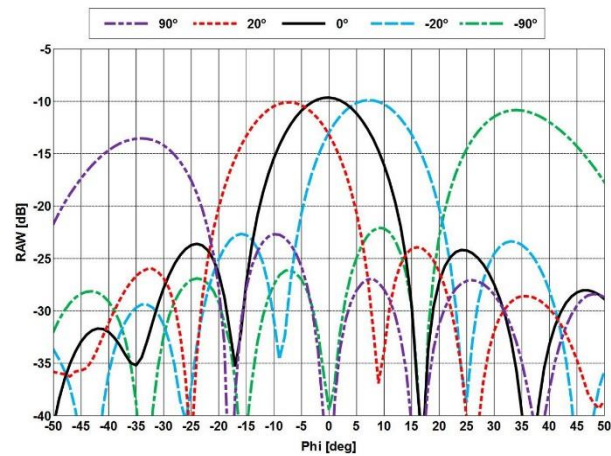
Fig. 12. Electronically scanned 8-element array raw patterns at 900 MHz.
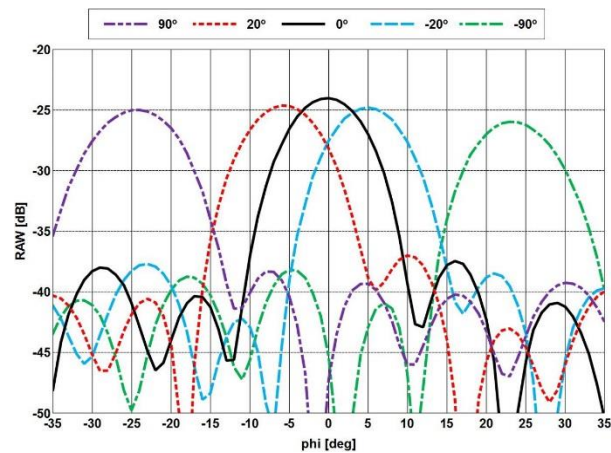
Fig. 13. Electronically scanned 8-element array raw patterns at 1,300 MHz.

The 4-element E-plane patterns are shown in Fig. 14 (left) when pointed at 17° resulting in a peak gain of 11.8 dBi. Figure 14 (right) shows the combined subarray pattern for 7°, 20°, and 24° beam peak location. It was found that pointing these subarrays at 20° off boresight provided a larger beamwidth with ~1.5 dB less gain compared to pointing at the 17° null locations. Scanning the subarrays to 7° produced little change in the

beamwidth and gain, and scanning the beam to the actual null location does not give the desired beamwidth. The best results occurred when the subarrays were pointed slightly past the nulls at 20°. Pointing the subarrays past 20° results in a significant decrease in broadside gain.
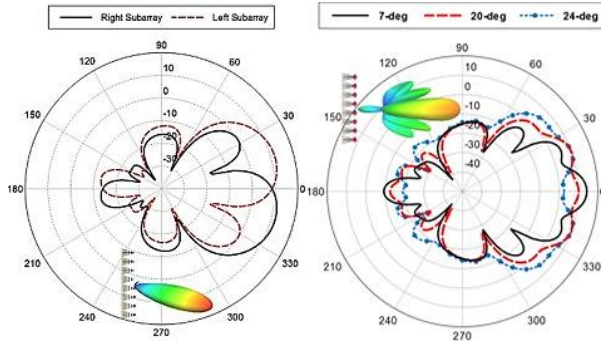
Fig. 14. 4-element subarrays simulated azimuthal patterns pointed at 17° (left) and combined subarrays with scan angles of 7°, 20°, and 24° (right) at 900 MHz.

The simulated and measured azimuthal pattern for subarrays pointed at 17° and 20° is shown in Fig. 15, indicating a 10.1 dBi boresight gain with the second peak at 9.8 dBi and the larger beamwidth for 20°. The simulated results show that pointing the subarrays slightly past the null location gives the best results. This approach provides the desired 55° beamwidth with gain ~1 dB less than a single 4-element subarray. This pattern could be continually scanned over ±12° to provide somewhat higher gain over the forward sector as shown in Fig. 16. Then having high gain covering the forward sector would depend on the scan rate which would be application specific.
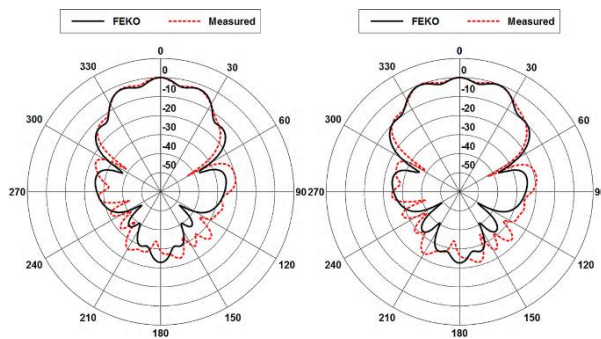
Fig. 15. Combined 4-element subarray azimuthal pattern comparison with scan angle of 17° (left) and 20° (right) at 900 MHz.

Validation of the subarrays was performed as shown in Fig. 17. Both the left and right subarrays show good agreement with simulation, with the difference in forward gain being the exclusion of the FR4 substrate from

simulation. The removal of the substrate was done to minimize the required system memory and computational time. Again, there are some slight asymmetries between the left and right subarrays which is due to the measurement environment.
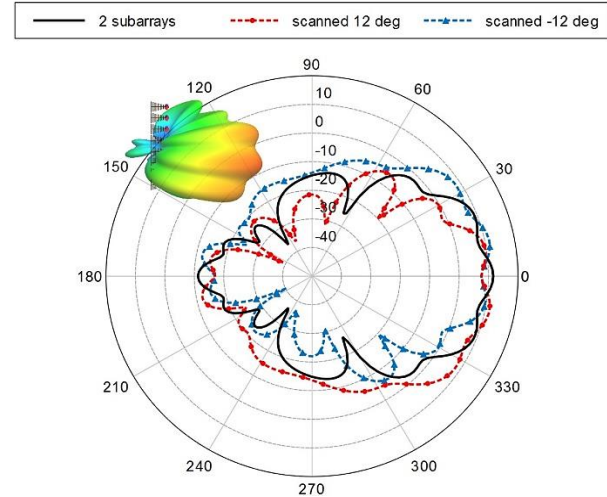
Fig. 16. Scanned null-filled azimuthal patterns at 900 MHz.
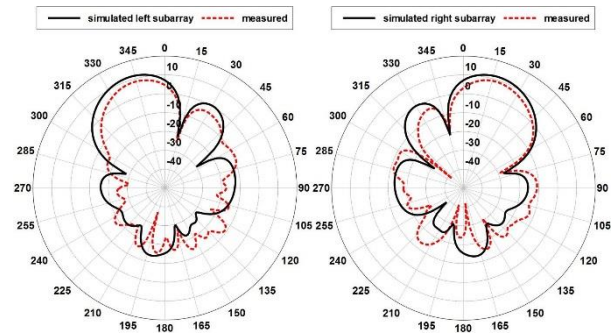
Fig. 17. Simulated and measured left and right subarray azimuthal pattern comparison at 900 MHz.

Measurements at 850 MHz and 950 MHz for the combined null filled pattern showed that the beamwidth will decrease with increasing frequency. This is to be expected as the element spacing and phase progression are frequency dependent, meaning that some loss of beamwidth will inevitably occur. The element pattern is not a cause of the decreasing beamwidth, as the gain has already been shown to be relatively flat with increasing frequency.

IV. CONCLUSION
This paper has presented the design, simulation, and measurement of a dual use 8-element horizontal array and its individual planar LPDA elements for the frequency band of 800 to 1300 MHz. A typical LPDA was scaled to be more compact than a traditional design

with little impact on performance. Modifications to the compact LPDA allow the antenna to be fed from the rear rather than the front, but care had to be taken to make sure that the coaxial cable was well insulated from the center trace. If the cable was attached to this trace then performance degradation would occur.

The dual use 8-element horizontal array was designed to transmit (receive) slant-polarization. In one configuration, the array needed to be able to scan in azimuth with a narrow beam, and in the other configuration, needed to maximize azimuthal beamwidth and forward gain. The second configuration was accomplished through null filling in which the 8-element array was divided into two 4-element subarrays. The beam of each subarray was scanned just past the associated first null of the broadside 8-element azimuthal pattern. The combined subarray pattern produced an azimuthal beamwidth of 55° (versus 15° for 8-elements) with 10 dBi of gain (versus 15 dBi for 8-elements). The measurements in a tapered anechoic chamber for the array in both configurations and for a single antenna element are in good agreement with simulation, thereby confirming proper function of this array designed by simulation.

REFERENCES

[1] J. A. Rodriguez and F. Ares, "Synthesis of shaped beam antenna patterns with null filling in the sidelobe region," *IEEE Electronic Letters*, vol. 33, no. 24, pp. 2004-2005, November 1997.

[2] D. Shin, et al., "Design of null filling antenna for automotive radar using the genetic algorithm," *IEEE Antennas and Wireless Propagation Letters*, vol. 13, pp. 738-741, 2014.

[3] FEKO, ver. 14.0.401, Altair, Troy, MI, 2016.

[4] C. Peixeiro, "Design of log-periodic dipole antennas," *IEE Proceedings*, vol. 135, no. 2, pp. 98-102, April 1988.

[5] W. L. Stutzman and G. A. Thiele, *Antenna Theory and Design*. John Wiley & Sons, New Jersey, 2013.

[6] GEMS, ver. 7.90.21, 2COMU, Inc., Fairfax, VA, 2014.

Seth A. McCormick received his BS. in Electrical Engineering in 2014 and is currently pursuing a MEE from Virginia Polytechnic Institute. He currently works as an Electronics Engineer for the Army Research Laboratory (ARL). Prior to that, he was a Contractor with General Technical Services LLC at ARL. As a member of the antenna team under the Sensors and Electron Devices Directorate, he uses several CEM codes for the design and modeling of antennas and for general EM analysis. His primary research interests are in antenna design and analysis, CEM, electromagnetic materials, and electromagnetic theory. He is a Member of ACES and a Student Member of Sigma Xi. He has authored or coauthored 11 publications.

William O. Coburn received his BS in Physics from Virginia Polytechnic Institute in 1984. He received an MSEE in Electro Physics in 1991 and Doctor of Science in Electromagnetic Engineering from George Washington University (GWU) in 2005. His dissertation research was in traveling wave antenna design. He has 36 year's experience as an Electronics Engineer at the Army Research Laboratory (formerly the Harry Diamond Laboratories) primarily in the area of CEM for EMP coupling/hardening, HPM, target signatures and antennas. He currently is in the RF Electronics Division of the Sensors and Electron Devices Directorate applying CEM tools for antenna design and EM analysis. He is a Senior Member of the IEEE, APS Society and Fellow of the Applied Computational EM Society (ACES) serving on the ACES Board of Directors. He is a Member of the USNC-URSI, Commission A and B (2010), *Sigma Xi* and an Adjunct Professor at the Catholic University of America. Coburn has authored or coauthored about 45 publications and 4 patents.

Study, Design and Fabrication of a CPW Fed Compact Monopole Antenna with Circular Polarization for Ultra Wide Band Systems Application

Majid Shokri, Somayeh Asiaban, and Zhaleh Amiri

Young Researchers and Elite Club, Urmia Branch, Islamic Azad University, Urmia, Iran
ma.shokri@yahoo.com

Abstract ─ A compact circularly polarized square slot antenna (CPSSA) is presented in this paper, which is appropriate for UWB applications requiring high data rate transmission. This antenna operates across 2.8 GHz to 10.8 GHz with an impedance bandwidth (IBW) of 117.6% for VSWR $\leq$ 2. The antenna consists of a trapezoidal shaped radiation patch which is fed through a coplanar waveguide (CPW) and includes two inverted L-shaped ground arms at the two opposite corners of the slot to excite two orthogonal resonant modes for circular-polarization (CP) radiation. Furthermore, two square slits at the two other opposite corners of the slot are applied to enhance its IBW. The antenna exhibits CP bandwidth of 50.5% across 3.7 GHz-6.2 GHz, which is suitable for WLAN, WiMAX and C-bands. In addition, the antenna has a considerably compact volume of $25 \times 25 \times 0.8$ mm^3. The measured and simulated results confirm the usefulness of the antenna for practical applications.

Index Terms ─ CPW-fed, circularly polarized, UWB application.

I. INTRODUCTION

Circularly polarized signals are used in modern systems such as wireless communications, radar and satellite to provide better mobility and weather penetration than linearly polarized ones. This is because CP prevents severe polarization mismatch between transmitter and receiver, which is otherwise encountered in such systems. In particular, fast growing communication systems require compact, low cost, CP antennas with a high data rate capability to be used in wireless applications. Despite low profile CP microstrip based antennas with high-Q are the best option for aforementioned requirement [1]. Circular-polarization can be implemented using various types of techniques such as: loading a cross patch at the center of the square slot [2], using asymmetric CPW-fed square slot antenna [3], applying a crane-shaped strip in the ground plane [4], and opening the radiation slot at the lower left side of the slot [5].

Attributes of such CPSSA include: (a) broadband performance, (b) construction on a single layer for low cost production, (c) low profile, and (d) compatibility for integration with monolithic microwave integrated circuit (MMIC) technologies. These characteristics afforded by such antennas have made them increasingly popular for applications such as imaging, vehicular radar, and communications [6–7].

The CPSSA structures reported in recent literature have a simple slot structure, which can be implemented in various ways, namely, by: (a) embedding two inverted L grounded strips around two opposite corners of the slot [7], (b) inserting a lightning-shaped feed-line and inverted L grounded strips [8], (c) embedding a T-shaped grounded metallic strip that is perpendicular to the axial direction of the coplanar waveguide feed-line [9], (d) utilizing a spiral slot in the ground-plane [10], and (e) utilizing embedded arc-shaped grounded metallic strip for circular and linear polarization [11].

In order to distribute the magnetic currents in the slots so that the two orthogonal resonant modes with an equal magnitude and 90° phase difference can be excited. The CPSSA structure needs to be constructed in one of the following ways: (a) by loading in the square slot a crisscross patch [12], (b) in order to realize the proposed antenna, miniature circular polarized square slot antenna is used with L-shape and crooked T-shape grounded strips located at the slots opposite corners to reduce cross-polarization [13], (c) by protruding into the square slot a meandering [14] or inverted L-shaped [15] conducting strip connected to the signal strip of the CPW, or (d) by loading the CPW-fed antenna with an inductive slot [16]. On the other hand, in order to achieve wide impedance bandwidth, we need UWB antennas which includes planar monopole antennas (PMAs). Ease of fabrication and appropriate radiation properties are some of these antennas advantages [17–20].

In this paper, we present a significantly compact and structurally simple CPSSA exhibiting an impedance bandwidth of 117.6% that extends from 2.8 GHz-10.8 GHz and CP bandwidth of 50.5% across 3.7 GHz-6.2 GHz.

II. ANTENNA DESIGN

The geometry of the proposed single-layer CPW-fed CPSS antenna is shown in Fig. 1. The antenna consists of a square ground plane, two identical inverted L-shaped

ground strips at the two opposite corners of the slot, two square slits at the two other opposite corners of the slot, and a trapezoidal shaped radiation patch connected to the feed-line. Furthermore, a rectangular-shaped tuning stub attached to the feed-line.
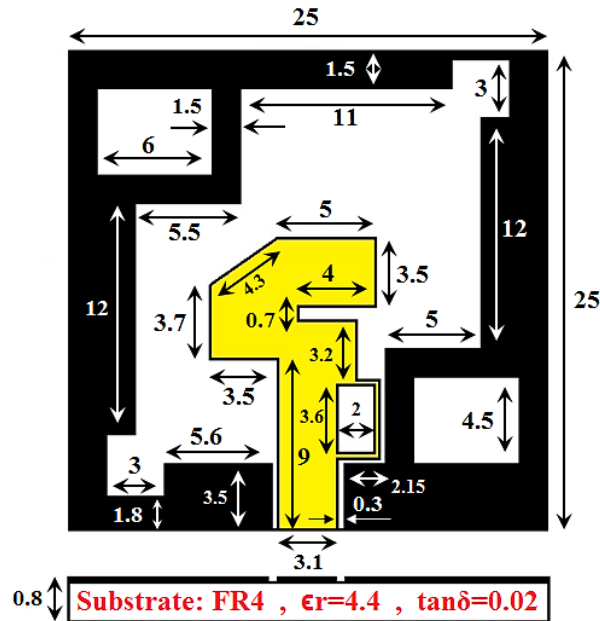
Fig. 1. Geometry of the proposed CPW-fed CPSSA. (All dimensions in millimeters).

The proposed CPSSA has been constructed on a commercially available FR4 dielectric substrate with a loss tangent of 0.02, permittivity of 4.4 and dimension of $25\times25\times0.8$ mm^3. To achieve 50Ω characteristic impedance, the width and length of the coplanar waveguide feed-line is 3.1 mm and 9 mm, respectively.

The gap between the feed-line and the ground-plane is 0.3 mm. The length of the feed-line structure affects the field distributions in the antenna aperture. The feed-line is extended from the CPW section to control the antenna's impedance match. The sizes of the inverted L-shaped strip arms are 6 mm and 4.5 mm. Other dimensions are given in Fig. 1. Additionally, to understand how this antenna design is achieved, Fig. 2 displays the four designing steps to realize the proposed antenna. The antenna in step-1 consists of a rectangular strip as the feed-line and the ground plane with a rectangular slot.

In step-2, a trapezoidal-shaped radiation patch and a rectangular-shaped tuning stub are attached to the feed line. In step-3 and step-4, two identical inverted L-shaped ground strips at the two opposite corners of the slot and the two square slits at the two other opposite corners of the slot are applied to the ground plane.

These modifications result in the improvement of the antenna's IBW and ARBW, as shown in Fig. 3 and Fig. 4.
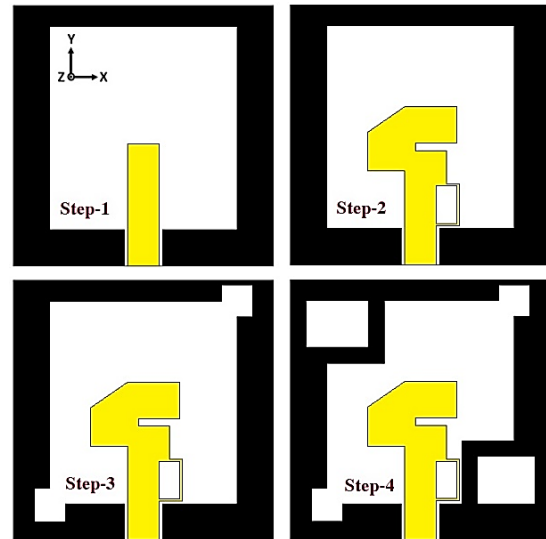
Fig. 2. Four designing steps to accomplish the proposed CP antenna.
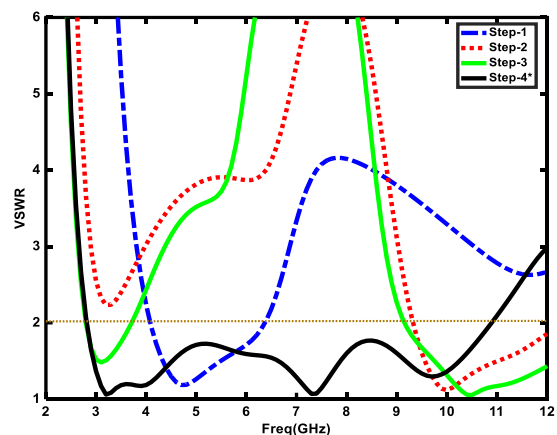
Fig. 3. VSWR responses for the designing steps of the proposed antenna.
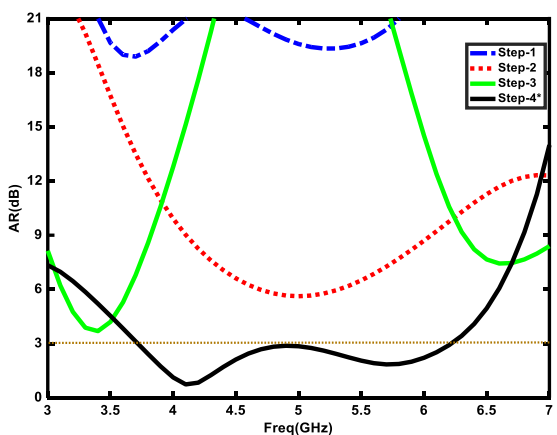
Fig. 4. AR curves for the designing steps of the proposed antenna.

III. RESULTS AND DISCUSSION

The main objectives of developing the antenna design have been to enhance its impedance bandwidth, generate CP, and expand the polarization bandwidth. Fig. 5 and Fig. 6 show the measured and simulated IBW and ARBW of the proposed antenna. It's demonstrated in these figures that by adjusting the sensitive parameters of the antenna and applying the optimal values the wide IBW and ARBW of 117% and 50.5%, respectively, can be achieved.
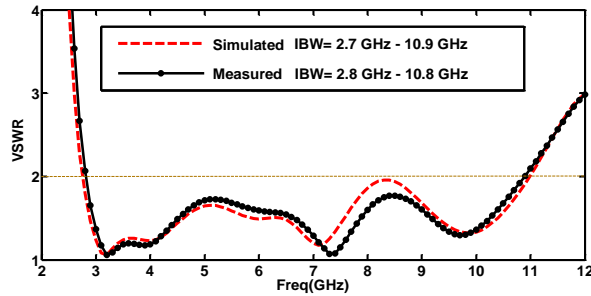
Fig. 5. Measured and simulated VSWR response of the proposed antenna.
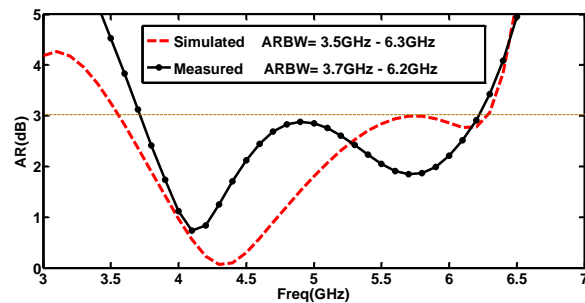
Fig. 6. Measured and simulated CP AR of the proposed antenna.

Indeed, by applying the inverted L-shaped grounded strips, and providing redistribution of the magnetic currents in the slots so that the two orthogonal resonant modes with equal amplitude and 90° phase difference can be excited. It is lead to a wide ARBW. The structure of inverted L grounded strips has been first proposed in [7]. In addition, by carving the two square slits at the two other opposite corners of the slot and providing more current paths, the wide IBW is achieved. The correlation between the simulated and measured results of the final antenna prototype is excellent as shown in the figures. The numerical results have been accomplished by using the Ansoft High Frequency Structure Simulator (HFSS Ver.11). For more understanding about the CP radiation, the surface current distribution of the antenna is discussed.

The surface current distribution over the antenna at 4.5 GHz, at the minimum point of AR, is shown in Fig. 7. It is observed that the surface current distribution at

180° and 270° is equal in the magnitude and opposite in the phase at 0° and 90°. When the current rotates in the clockwise/counter clockwise direction, the antenna correspondingly radiates in the RHCP/LHCP. The proposed CPSSA is able to generate an RHCP in the +z direction, whereas an LHCP is produced in the -z direction. Also, the normalized right-hand circular polarization (RHCP) and left-hand circular polarization (LHCP) radiation patterns of the CPSSA at the frequencies of 5 GHz and 6 GHz are given in Fig. 8.
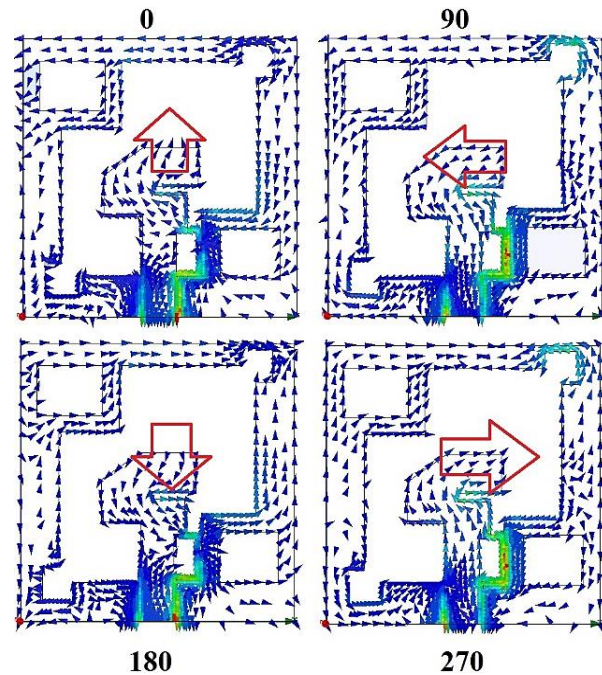
Fig. 7. Distribution of the surface current on the CPSS antenna at 4.4 GHz in 0°, 90°, 180°, and 270°.
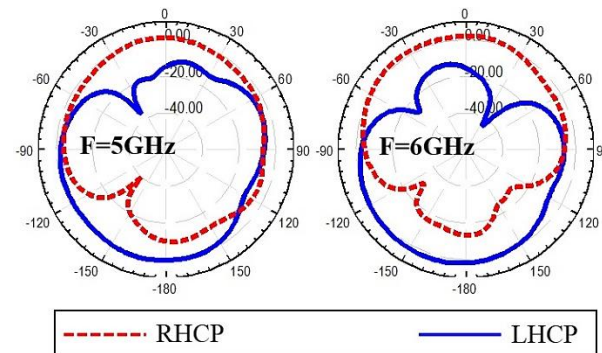
Fig. 8. Simulated radiation patterns of the proposed antenna at 5 and 6 GHz.

It shows the antenna exhibits omnidirectional radiation characteristics, but whose gain variation is evident over certain angular directions. For more explanation about the antenna radiation, 3D polar plot of

antenna gain in RHCP/LHCP states are given in Fig. 9. Furthermore, the simulated and measured gain curves of the proposed antenna are shown in Fig. 10.
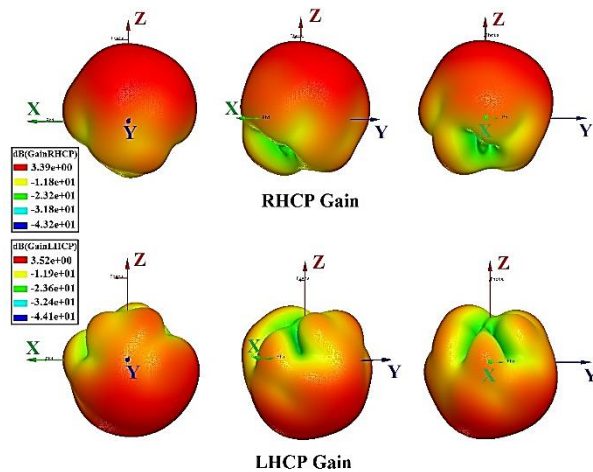
Fig. 9. Simulated 3D RHCP/LHCP gain of the proposed antenna at 4.4 GHz.
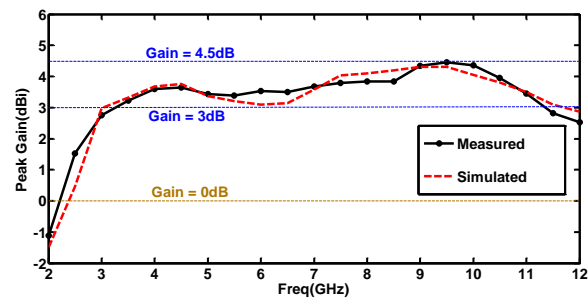
Fig. 10. Measured and simulated gain of the proposed antenna.

It shows a well agreed simulated and measured antenna gains in the antenna band whose maximum gain is about 4.5 dBi and its fluctuation is between 3 dBi and 4.5 dBi. Photograph of the fabricated antenna is shown in Fig.11.
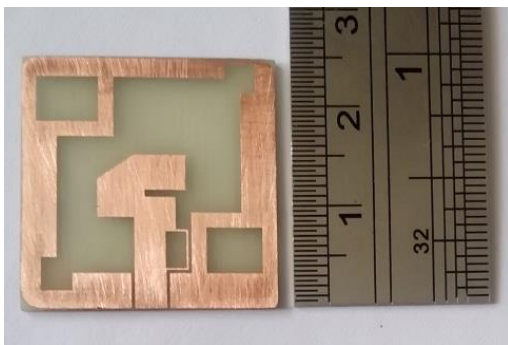
Fig. 11. Photograph of the fabricated antenna prototype.

IV. CONCLUSION

A new CPW-fed CPSSA has been proposed. The measured AR bandwidth can be enhanced to over than 50.5% with a wide IBW of greater than 117.6% that exactly covers the UWB band. The designed antenna has a very compact size of $25 \times 25 \times 0.8$ mm^3.

According to the impedance bandwidth and axial ratio bandwidth, the proposed antenna is suitable for WLAN, WiMAX and C-bands systems application.

ACKNOWLEDGMENT

REFERENCES

[1] Y. F. Lin, H. M. Chen, and S. C. Lin, "A new coupling mechanism for circularly polarized annular-ring patch antenna," *IEEE Trans. Antennas Propag.*, vol. 56, pp. 11-16, 2008.

[2] C. C. Chou, K. H. Lin, and H. L. Su, "Broadband circularly polarized cross-patch-loaded square slot antenna," *Electron. Lett.*, vol. 43, no. 9, pp. 485-486, 2007.

[3] J. Y. Sze, J. C. Wang, and C. C. Chang, "Axial-ratio bandwidth enhancement of asymmetric-CPW-fed circularly-polarized square slot antenna," *Electron. Lett.*, vo. 44, no. 18, pp. 1048-1049, 2008.

[4] C.-H. Chen and E. K. N. Yung, "Dual-band circularly-polarized CPW-fed slot antenna with a small frequency ratio and wide bandwidths," *IEEE Trans. Antennas Propag.*, vol. 59, no. 4, pp. 1379-1384, 2011.

[5] J.-Y. Jan, C.-Y. Pan, K.-Y. Chiu, and H.-M. Chen, "Broadband CPW-fed circularly-polarized slot antenna with an open slot," *IEEE Trans. Antennas Propag.*, vol. 61, no. 3, pp. 1418-1422, 2013.

[6] N. Felegari, J. Nourinia, C. Ghobadi, and J. Pourahmadazar, "Broadband CPW-fed circularly polarized square slot antenna with three inverted-L shape grounded strips," *IEEE Antenna Wireless Propag. Lett.*, vol. 10, pp. 274-277, 2011.

[7] J. Y. Sze and C. C. Chang, "Circularly polarized square slot antenna with a pair of inverted-L grounded strips," *IEEE Antennas Wireless Propag. Lett.*, vol. 7, pp. 149-151, 2008.

[8] J.-Y. Sze, C. Hsu, Z. Chen, and C. C. Chang, "Broadband CPW-fed circularly polarized square slot antenna whit lightening shaped feed line and inverted-L grounded strips," *IEEE Trans. Antenna Propag.*, vol. 58, pp. 973-977, 2010.

[9] J.-Y. Sze, K.-L. Wong, and C. Huang, "Coplanar waveguide-fed square slot antenna for broadband circularly polarized radiation," *IEEE Trans. Antennas Propag.*, vol. 51, pp. 2141-2144, 2003.

[10] C. Chen and E. Yung, "Dual-band dual-sense

circularly-polarized CPW-fed slot antenna with two spiral slots loaded," *IEEE Trans. Antennas Propag.*, vol. 57, pp. 1829-1833, 2009.

[11] M. Chiang, T. Hing, and S. Bor, "Dual-band circular slot antenna design for circularly and linearly polarized operations," *Microwave Opt. Technol. Lett.*, vol. 52, pp. 2717-2721, 2010.

[12] C. Chou, K. Lin, and H. Su, "Broadband circularly polarized crosspatch-loaded square slot antenna," *Electron. Lett.*, vol. 43, pp. 485-486, 2007.

[13] S. Karamzadeh, V. Rafii, M. Kartal, and M. Dibayi, "Circularly polarized square slot antenna using crooked T-shape technique," *Microw. Opt. Technol. Lett.*, vol. 56, pp. 229-233, 2015.

[14] K. M. Chang, R. J. Lin, I. C. Deng, B. Chen, K. Q. Xiang, and C. J. Rong, "A novel design of a CPW-fed square slot antenna with broadband circular polarization," *Microwave Opt. Technol. Lett.*, vol. 48, pp. 2456-2459, 2006.

[15] Y. B. Chen, X. F. Liu, Y. C. Jiao, and F. S. Zhang, "CPW-fed broadband circularly polarised square slot antenna," *Electron. Lett.*, vol. 42, pp. 1074-1075, 2006.

[16] I. C. Deng, R. J. Lin, K. M. Chang, and J. B. Chen, "Study of a circularly polarized CPW-fed inductive square slot antenna," *Microwave Opt. Technol. Lett.*, vol. 48, pp. 1665-1667, 2006.

[17] K. ElMahgoub, "Slotted triangular monopole antenna for UHF RFID readers," *ACES Express Journal*, vol. 1, no. 1, pp. 24-27, 2016.

[18] S. I. Rosaline and S. Raghavan, "Metamaterial-inspired split ring monopole antenna for WLAN applications," *ACES Express Journal*, vol. 1, no. 5, pp. 153-156, 2016.

[19] M. Shokri, Z. Amiri, M. Pilevari, M. Masoumi, S. Asiaban, and B. Virdee Raghavan, "Compact UWB antenna with dual functionality," *ACES Journal*, vol. 29, no. 7, pp. 479-485, 2014.

[20] M. Shokri, Z. Amiri, S. Asiaban, and B. Virdee, "Diamond shaped ring antenna for UWB applications with inherent band-notched functionality," *ACES Journal*, vol. 29, no. 11, pp. 911-915, 2014.

Modal Analysis of Wave Propagation in Straight and Curved Arched Tunnel Based on Equivalent Rectangular Tunnel Model

Hany M. El-Maghrabi [1], Samir F. Mahmoud [2], and Mostafa El-Said [2]

[1] Institute of Electromechanical Research
Housing and National Research Center, Cairo, Egypt
helmaghrabi@hbrc.edu.eg

[2] Department of Electronics and Electrical Communication
Cairo University, Cairo, Egypt

Abstract ─ In this paper, a model is presented to simulate wave propagation in straight and curved tunnels with arched cross section with imperfectly conducting walls. The model is based on treating the tunnels as a rectangular waveguide with imperfectly conducting walls, where the arched cross section of the tunnels is approximated with equivalent rectangular cross section. A scenario is considered to check the accuracy of this model. This scenario is verified by comparing experimental and numerical simulation results. Good agreement between the proposed model and the experimental results is obtained.

Index Terms ─ Arched tunnels, curved waveguide, imperfect conducting walls, wave propagation.

I. INTRODUCTION

Understanding the electromagnetic waves propagation in tunnels becomes increasingly important as a large number of communication systems, including GSM (Global System for Mobile Communications), 3G (3rd Generation), Wi-Fi systems are expected to support continuous service in subway tunnels to guarantee user experience. Since the early seventies of the last century till now, there has been a continued interest in radio communication through tunnels [1-28], since signaling within working areas in mine tunnels or road tunnels has been of prime importance [8–20]. A tunnel can act as a waveguide for radio waves of sufficiently high frequency, as the wavelength is much smaller than the tunnel linear dimensions, whence attenuation occurs only due to the surrounding rocks [8–11]. It should be noted that at frequencies of few hundred MHz, the earth rocks will act as a dielectric material with low loss tangent. In this case, the attenuation of the electromagnetic waves propagating in the tunnel occurs mainly due to leakage of waves into the rocks rather than Ohmic losses. In the presence of longitudinal conductors such as electricity cables, low frequency waves can also propagate

in the form of a coaxial like mode [12–16]. Intentionally placed leaky cables have been placed inside tunnels in order to control the signal level inside the tunnel [15–19]. A typical straight tunnel with cross sectional linear dimensions of few meters can act as a waveguide to electromagnetic waves at UHF and upper VHF bands [10,15].

Modal propagation in arched tunnel has been considered by Mahmoud [3, 21], showing a considerable increase in the attenuation due to arch. Tunnels with regular cross sections such as the circular or rectangular shape are amenable to analytical analysis that lead to full characterization of their main modes of propagation [5], [27]. However, most existing tunnels do not have regular cross sections and their study may require exhaustive numerical methods [28]. In this paper we consider arched tunnels whose cross-section comprise an incomplete circle with a flat base as shown in Fig. 1. We assess previously obtained closed forms of the attenuation rates of the low order modes by Mahmoud [3]. The attenuation rate of straight arched tunnel is approximated by equivalent rectangular straight tunnel. The curved arched tunnels is approximated with an equivalent rectangular curved tunnel and attenuation rate is calculated based on the same approach proposed in [4]. Finally, experimental results are conducted in order to verify the presented theory.

II. MODAL ANALYSIS OF STRIAGHT ARCHED TUNNEL

Most of existing tunnels do not have regular cross sections and their analysis may require numerical methods. One of the widely existing tunnels is a tunnel with cross-section that comprise a circular arch with a flat base as shown in Fig. 1.

This can be approximated as a circular tunnel whose shape is perturbed into a flat-based tunnel. So, perturbation theory can be used to predict attenuation and phase velocity of the dominant modes of arched

tunnel from the corresponding attenuation of a circular tunnel as shown in Fig. 2. Full details about the perturbation analysis is discussed in [3, 23]. As perturbation analysis requires numerical efforts, analytical model is proposed in the next section as a fast solution which requires low computing resources.
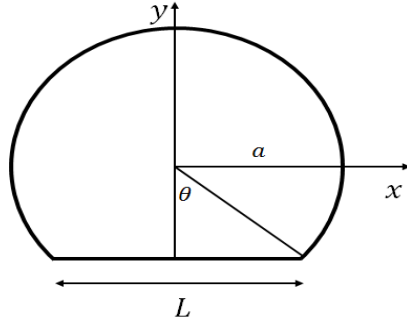
Fig. 1. Arched tunnel with radius a and flat base L.
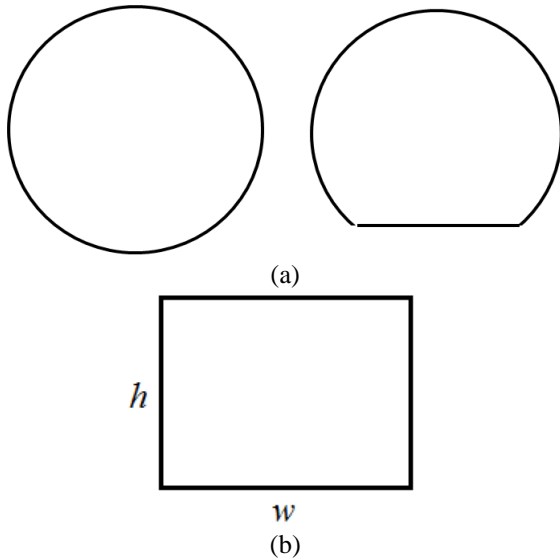
Fig. 2. (a) A circular tunnel and a perturbed circular tunnel with a flat base [3], and (b) equivalent rectangular model.

A. An equivalent rectangular tunnel model

It is shown in [3] that we can model the arched tunnel of Fig. 2 (a) by a rectangular tunnel as shown in Fig. 2 (b). Starting with the previously proposed model in [3], the arched tunnel is simulated here by using equivalent rectangular tunnel. Then an enhancement of the model is proposed.

For the circular tunnel with radius a, the attenuation factor for HE_{nm} is obtained as [3, 23]:

$$\alpha_{HE_{nm}} = \frac{Z_s/\eta_0 + Y_s\eta_0}{2k_0^2 a^3}[x_m^{n-1}]^2, \qquad (1)$$

where x_m^{n-1} is the mth zero of Bessel function $J_{n-1}(x)$ and the walls of the tunnel are characterized by constant

surface impedance and admittance Zs and Ys where their normalized values are given by [5]:

$$Y_S = (\varepsilon_r - i\sigma/\omega\varepsilon_0)/\sqrt{\varepsilon_r - 1 - i\sigma/\omega\varepsilon_0}, \qquad (2)$$

and,

$$Z_S = 1/\sqrt{\varepsilon_r - 1 - i\sigma/\omega\varepsilon_0}, \qquad (3)$$

where ε_r is the tunnel walls relative permittivity and σ is the walls conductivity. The proposed formula (1) is based on the condition: $k_0 a \gg x_m^{n-1}$[3]. For a rectangular tunnel with width w and height h the attenuation of HE_{nm} mode with vertical polarization is obtained as [23]:

$$\alpha_{HE_{nm}} = \frac{2\pi^2}{k_0^2}\left[\frac{m^2 Z_s/\eta_0}{w^3} + \frac{n^2 Y_s/\eta_0}{h^3}\right]. \qquad (4)$$

Substituting in (1) and (4) for HE_{11} (m = n = 1) mode in circular and square tunnel with $w = h$ and equating the attenuation rates we obtain:

$$w = h = (4\pi^2/2.4048^2)^{1/3}a = 1.897a. \qquad (5)$$

This means that the area of the equivalent square tunnel is equal to 1.145 times the area of the circular tunnel [3] for same attenuation rate. It should be noted that this equivalence is valid only for the HE_{11} mode in both tunnels; while for other modes the attenuation in the circular and the square tunnels are generally not equal.

Using the same approach for the case of the arched tunnel [3] by maintaining the ratio of areas as obtained from the square and circular tunnels; it can be deduced that the arched tunnel is approximated with an equivalent rectangular tunnel with area [3],

$$wh = 1.145[(\pi - \theta)a^2 + (La/2)\cos\theta]. \qquad (6)$$

The ratio h/w; equal to the arched tunnel height to its diameter is given by [3]:

$$\frac{h}{w} = (1 + \cos\theta)/2, \qquad (7)$$

where

$$\theta = \sin^{-1}(L/2a). \qquad (8)$$

Equations (6), (7) define a rectangular tunnel which is equivalent to the arched tunnel regarding the HE_{11} mode.

The proposed analysis assumes that for all dimensions of the arched tunnels, the ratio of the equivalent rectangular area to the arched tunnel area is a fixed number which is 1.145. As an enhancement in the present paper, a new approach is proposed by introducing a more general formula which accounts for the dimensions of the arched tunnel in the equivalence ratio. The proposed modification of Eq. (6) for best ratio of the equivalent rectangular area to the arched tunnel area is obtained as:

$$Area|_{rectangular} = R \times Area|_{arched}, \qquad (9)$$

where R is the areas ratio obtained as:

$$R = 1.145 C^n, \qquad (10)$$

where $C = (1 + \cos\theta)/2$ is the arched tunnel height to its diameter and θ is obtained by (8), while n is the tuning factor for best fitting between arched tunnel and equivalent rectangular model. Equation (9) can be written as:

$$wh = R[(\pi - \theta)a^2 + (La/2)\cos\theta]. \qquad (11)$$

In order to check the validity of this equivalence,

the proposed model is compared with the previously published results of [3]. The attenuation for HE_{11} mode is calculated in an arched tunnel of radius a = 2m with a flat base of width L. The surrounding earth has a relative permittivity of $\varepsilon_r = 6$ and the operating frequency is 500 MHz. The modal attenuation factor is plotted in Fig. 3 for HE_{11} mode as a function of the L/a. The attenuation factor is computed by using the perturbation analysis in [3] and the equivalent rectangular model for two cases. The first case: with $n = 0$ which is corresponding to the original proposed rectangular model by [3], and $n = 0.33$ which is corresponding to the best fitting of the proposed model of this work. It can be noted that the proposed modification with $n = 0.33$ has better agreement with the perturbation analysis. By changing the arched dimensions, the ratio R of equivalent rectangular area to arched tunnel area is changed according to Eq. (9), while the in old model the ratio is fixed for all cases. This will introduce a more general formula which accounts for the dimensions of the arched tunnel in the equivalence ratio.
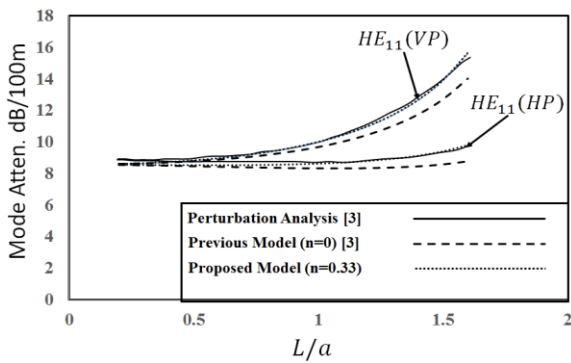
Fig. 3. Attenuation of the HE_{11} mode in the arched tunnel using perturbation analysis [3], rectangular equivalent tunnel [3] and proposed rectangular equivalent tunnel for Vertical Polarization (VP) and Horizontal Polarization (HP).

Full wave numerical analysis based on FEKO Ray Launching Geometrical Optics (RL‑GO) [29] simulator is used to verify the proposed equivalent rectangular model of arched tunnel. FEKO's RL‑GO [29] method is a ray‑based technique that models objects based on optical propagation, reflection and refraction theory [29]. GO (ray launching) is formulated for use in instances where electrically very large (>20λ) metallic or dielectric structures are modelled. Ray‑interactions with metallic and dielectric structures are modelled using Huygens sources, placed at each ray, contact point on material boundaries. The ray‑launching process is easily controlled, based on the angular spacing (for localized sources) or transverse spacing (for plane wave sources) of the rays and the number of multiple interactions

allowed. The tunnel as shown in Fig. 1 has radius $a = 2m$ while $L = a$. Figure 4 shows the normalized electric field distribution across the center line of the tunnel for the arched and the equivalent rectangular tunnels. The width and the height of the equivalent rectangular tunnel are calculated by using (11) and (7) with $n = 0.33$ in (10). The width of the equivalent rectangular tunnel is $w = 3.52m$ while the height is $h = 3.8$. The operating frequency is assumed to be 500 MHz. The length of the tunnel is assumed to be 60m while the relative permittivity of the walls is 6 and conductivity is σ=0.01 S/m [3]. Both the emitter and receiver are kept vertically polarized. Good agreement is obtained between the electric field in arched tunnel and the one in the equivalent rectangular tunnel. The field decay rate in both tunnels is also in good agreement. The calculated mean squared error between the proposed model and the arched tunnel results is about 12.42%. Also, it can be noted that in addition to the expected decrease in the electric field strength with distance from the transmitter, the interference between the direct rays and the reflected rays from the walls creates peaks and troughs where their positions depend on the phase difference between the electric field of the direct ray and that of the rays reflected from the walls.
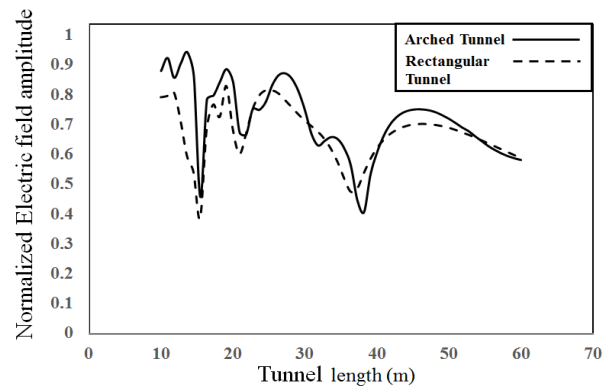
Fig. 4. Normalized electric field amplitude in arched and equivalent rectangular tunnel.

III. MODAL ANALYSIS OF CURVED ARCHED TUNNEL

In this section, curved tunnels with arched cross section are analyzed. The approach is based on approximating the arched cross section with the proposed equivalent rectangular, then the tunnel will be analyzed as curved rectangular tunnel using the same approach as in [4,5] for curved rectangular tunnel modal analysis.

First, the equivalent rectangular dimensions w and h are obtained from the corresponding arch dimensions as proposed in Section II. Then following [5], let us consider a curved tunnel with rectangular cross section as in Fig. 5 (b). Using a cylindrical coordinates frame

with the z-axis along the vertical direction, the side surfaces of the tunnel coincide with $\rho = R - w/2$ and $\rho = R + w/2$, where R is the mean radius of curvature. The main assumptions in the analysis are [5]: (i) the frequency is high so that $k_0 w/2 \gg 1$ and therefore the walls can be characterized by constant surface impedance and admittance Zs and Ys where their normalized values are given by (2) and (3), and (ii) slow curvature such that $2R/w \gg 1$. The waveguide modes are either TM or TE to z. Considering E_z for the low order TMz modes and ignoring field variation along z as the electric field is vertical, the field is almost constant in z-direction (since $k_z \ll k_0$), the electric field is given as [5]:

$$E_z = f_v(k_0\rho)exp(-jv\emptyset), \qquad (12)$$

where $f_v(k_0\rho)$ is a linear combination of Bessel functions of first and second kind with complex order v. However, with low curvature $R \gg w/2$, and high frequency excitation, it is expected that v and $k_0\rho$ are both large ($\gg 1$) while their difference is much less than v. Under these conditions, the modal equations for lower order TE_z and TM_z are derived in terms of the Airy functions instead of the Bessel function of complex order v and solved numerically for the propagation constant along the ϕ-direction [5]. Full analysis of the model is presented in [4].

The total approximate attenuation rate of wave propagating inside rectangular curved tunnel is obtained by [4] for VP modes as:

$$\alpha_{Total}^{VP} = \pi^2 Re(Y_s)/4k_0^2(h/2)^3 + (-\text{Im}\left[\frac{v}{R}\right]), \quad (13)$$

and using same analysis, the HP total attenuation rate can be obtained.

The electric field and attenuation rate inside the arched tunnel is obtained by (12) and (13) with equivalent rectangular curved tunnel of width w and height h.
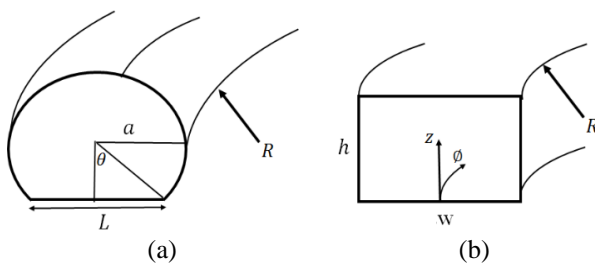
Fig. 5. Curved tunnel: (a) with arched cross section and (b) with rectangular cross section.

The electric field for arched and equivalent rectangular curved tunnels is implemented in Matlab which runs on a laptop with 8 GB of RAM, Intel 2.6 GHz processor, and operating system is Windows 8 64-bit. The tunnel has an arched cross section with radius $a = 2m$ and arch base $L = 2m$. The tunnel radius of curvature $R = 20a$ and the operating frequency is 950 MHz corresponding to GSM-900 band. The relative

permittivity of the walls is considered equal to 6 and the conductivity is 0.01 S/m [3]. The equivalent rectangular tunnel has width = 3.86m and height is = 3.54m. The transmitting and receiving antennas are kept vertically polarized. The height of both transmitting and receiving antennas is kept 1.5m above the ground.
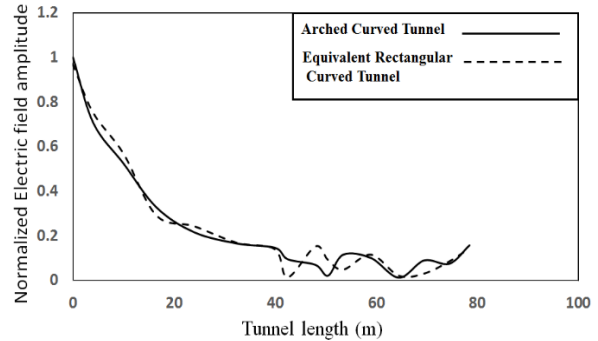
Fig. 6. Electric field in a curved arched tunnel with horizontally polarized mode. R = 20a, freq = 950 MHz, arch base L = 2.1m and arch radius = 2m, L/a = 1.05, where equivalent rectangular tunnel width dimensions are width = 3.86m, height = 3.54 m, error is 12.7%.

The total program runtime for the above example is about 12 minutes. On the other hand, the same example is simulated using FEKO version 7.0 with the same computer resources. It is found that the simulation takes about 60 minutes using FEKO RL-GO solver. So, the proposed model is faster than the simulation package and the differences will be increased by increasing the dimensions of the corridor or operating frequency. Figure 6 shows a comparison between the calculated normalized electric field along the tunnel center line using the proposed model and simulation results. It can be noted that good agreement is obtained and the calculated error between the model and simulation results is about 12.7%.

IV. MEASUREMENTS

In this section, sample results are presented to verify the accuracy of the proposed model for the signal attenuation rate in arched tunnel. The proposed measurements are used to study simple wave propagating inside straight arched tunnel for cars.

This simple scenario of a curved tunnel is verified experimentally in the frequency range 450 MHz corresponding to GSM-450 band. The scenario was done in arched tunnel for cars with concrete walls as shown in Fig. 7. The experimental setup consists of Handheld RF Signal Generator (RFEGEN 1.12) with dipole antenna with gain of 2.2 dBi used as transmitter, while the receiver is RF Viewer wireless USB dongle and data is collected using computer software package RF spectrum analyzer (TOUCHSTONE PRO); as shown in Fig. 8.

The transmitting and receiving antennas are kept horizontally polarized at 1m above the ground and measurements' samples are collected every 10m for 70m across the center line of the tunnel. The tunnel consist of three plane walls with arched roof. The arched radius is 7.3m and the tunnel width is 14m. The height at the tunnel center is 10.35m. The width of the equivalent rectangular tunnel is $w = 13.2\ m$, while the height is $h = 8.4\ m$. The tunnel is approximated as two sections where the upper section represents the arched roof while the lower one represents the three plane walls. The equivalent rectangular tunnel width is calculated by the proposed model for the arched roof, while the total height is the one calculated by the proposed model for arched roof in addition to the height of the plane walls.

Fig. 7. Arched tunnel for cars, flat base (L) = 14m, radius a = 7.3m, and height at center = 10.35m.

(a)
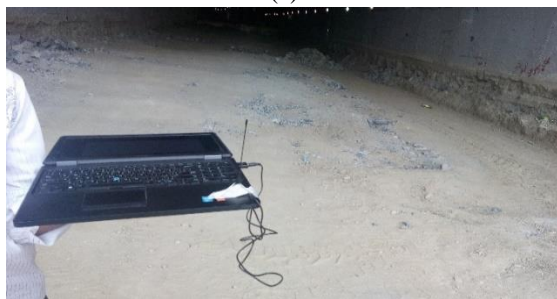
(b)

Fig. 8. Measurement setup: (a) transmitter (RF signal generator, and (b) receiver (computer software package RF spectrum analyzer).

Figure 9 shows a comparison between measured total received power in dBm and the calculated one by using the proposed model. Good agreement between the measured and calculated results is obtained. The slight differences can be explained due to errors in the manual positioning of the receiving antenna and differences due to the boundary conditions of the actual tunnel and the existence of the small metal sheets. The calculated error between the model and measured results is about 3.9%.
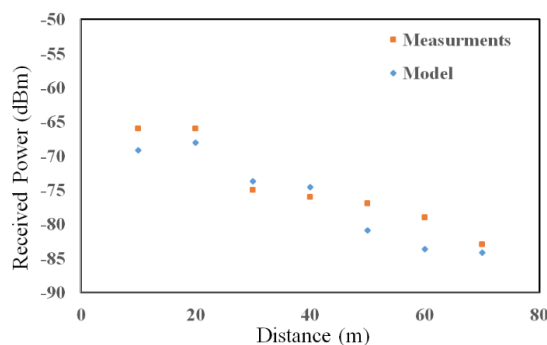
Fig. 9. Received power in arched tunnel with HP modes, tunnel dimensions are: $a = 7.3$m, L = 14m and equivalent rectangular tunnel $w = 13.2$m and h = 8.4m.

V. CONCLUSION

A new approach is proposed to model the wave propagation in straight and curved arched tunnels with an equivalent rectangular tunnel. The walls of the tunnels are considered imperfectly conducting walls. The proposed model introduces a more general formula which accounts for the dimensions of the arched tunnel in the equivalence ratio. The proposed model is verified by comparison with experimental results. Good agreements are obtained from these comparisons.

REFERENCES

[1] K. Guan, B. Ai, Z. Zhong, C. Lopez, L. Zhang, C. Briso, A. Haovat, and B. Zhang, "Measurements and analysis of large-scale fading characteristics in curved subway tunnels at 920 MHz, 2400 MHz, and 5705 MHz," *IEEE Trans. on Intelligent Transportation System*, vol. 16, no. 5, pp. 2393-2405, Oct. 2015.

[2] B. Zhang, Z. Zhong, K. Guan, R. He, and C. Briso, "Shadow fading correlation of multi-frequencies in curved subway tunnels," *Proc. IEEE Conf. ITSC*, Qingdao, China, pp. 1111-1116, Nov. 2014.

[3] S. Mahmoud, "Wireless transmission in tunnels with non-circular cross section," *IEEE Trans. on Antennas and Propagation*, vol. 58, no. 2, pp. 613-616, Feb. 2010.

[4] H. El-Maghrabi, A. Attiya, S. Mahmoud, M. El-Said, and E. Hashish, "Approximate calculation of the total attenuation rate of propagating wave

inside curved tunnel," *Applied Computational Electromagnetics Society (ACES) Journal*, vol. 31, pp. 1265-1270, Nov. 2016.

[5]   S. F. Mahmoud, "Modal propagation of high frequency electromagnetic waves in straight and curved tunnels within the earth," *J. of Electromagn. Waves and Appl.*, vol. 19, no. 12, pp. 1611-1627, 2005.

[6]   M. Lienard, J. M. Molina-Garcia-Pardo, P. Laly, C. Sanchis-Borras, and P. Degauque, "Communication in tunnel: Channel characteristics and performance of diversity schemes," *General Assembly and Scientific Symposium (URSI GASS), 2014 URSI*, Aug. 2014.

[7]   M. Lienard, C. Sanchis-Borras, J.-M. Molina-Garcia-Pardo, D. P. Gaillot, P. Laly, and P. Degauque, "Performance analysis of antenna arrays in tunnel Environment," *IEEE Antennas and Wireless Propagation Letters*, vol. 13, pp. 12-125, Jan. 2014.

[8]   M. Lienard, J. M. Molina-Garcia-Pardo, P. Laly, C. Sanchis-Borras, and P. Degauque, "MIMO and diversity techniques in tunnels," *International Conference on Computing, Management and Telecommunications (ComManTel)*, Apr. 2014.

[9]   C. Garcia-Pardo, J.-M. Molina-Garcia-Pardo, M. Lienard, D. P. Gaillot, and P. Degauque, "Double directional channel measurements in an arched tunnel and interpretation using ray tracing in a rectangular tunnel," *Progress In Electromagnetics Research M*, vol. 22, pp. 91-107, Apr. 2012.

[10] A. G. Emslie and R. L. Lagace, "Theory of the propagation of UHF radio waves in coal mine tunnels," *IEEE Trans. AP*, vol. 23, no. 2, pp. 192-205, Mar. 1975.

[11] S. F. Mahmoud and J. R. Wait, "Geometrical optical approach for electromagnetic wave propagation in rectangular mine tunnels," *Radio Science*, vol. 9, no. 12, pp. 1147-1158, Dec. 1974.

[12] P. Delogne, "Basic mechanisms of tunnel propagation," *Radio Science*, vol. 11, pp. 299-303, Apr. 1976.

[13] J. R Wait and D. A. Hill, "Guided electromagnetic waves along an axial conductor in a circular tunnel," *IEEE Trans. AP*, vol. 22, pp. 627-630, July 1974.

[14] S. F Mahmoud and J. R. Wait, "Theory of wave propagation along a thin wire inside a rectangular waveguide," *Radio Science*, pp. 417-420, Mar. 1974.

[15] S. F. Mahmoud, "Characteristics of electromagnetic guided waves for communication in coal mine tunnels," *IEEE Trans. COM*, vol. 22, pp. 1547-1554, Oct. 1974.

[16] J. R. Wait and D. A. Hill, "Propagation along a braided coaxial cable in a circular tunnel," *IEEE Trans. MTT*, vol. 23, pp. 401-405, May 1975.

[17] J. R. Wait, "EM theory of the loosely braided coaxial cable: Part I," *IEEE Trans. MTT*, vol. 24, pp. 262-265, July 1976.

[18] D. A. Hill and J. R. Wait, "EM theory of the loosely braided coaxial cable: Part II-Numerical results," *IEEE Trans. MTT*, vol. 28, pp. 262-265, Apr. 1980.

[19] S. F. Mahmoud and J. R. Wait, "Calculated channel characteristics of a braided coaxial cable in a mine tunnel," *IEEE Trans. COM*, vol. 24, pp. 82-87, Jan. 1976.

[20] P. Degauque, B. Demoulin, J. Fontaine, and R. Gabillard, "Theory and experiment of a mobile communication in tunnels by means of a leaky braided coaxial cable," *Radio Science*, vol. 11, pp. 305-314, Apr. 1976.

[21] P. Delogne, *Leaky Feeders and Subsurface Radio Communication*. IEE Electromagnetic Series 14, Peter Peregrinus Ltd., 1982.

[22] M. Lienard and P. Degauque, "Propagation in wide tunnels at 2 GHz: A statistical analysis," *IEEE Trans. on Vehicular Technology*, vol. 47, no. 4, pp. 1322-1328, Nov. 1998.

[23] S. F. Mahmoud, *Wireless Transmission in Tunnels*, *Mobile and Wireless Communications Physical Layer Development and Implementation*. InTech, 2010.

[24] M. Lienard and P. Degauque, "Natural wave propagation in mine environment," *IEEE Trans. on AP*, vol. 48, no. 9, pp. 1326-1339, Sep. 2002.

[25] S. F. Mahmoud and J. R. Wait, "Guided electromagnetic waves in a curved rectangular mine tunnel," *Radio Science*, pp. 567-572, May 1974.

[26] J. R Wait and D. A. Hill, "Guided electromagnetic waves along an axial conductor in a circular tunnel," *IEEE Transactions on Antennas and Propagation*, vol. 22, pp. 627-630, July 1974.

[27] D. G. Dudley, M. Lienard, S. F. Mahmoud, and P. Degauque, "Wireless propagation in tunnels," *IEEE Antennas Propag. Mag.*, vol. 49, no. 2, pp. 11-26, Apr. 2007.

[28] J. Pingenot, R. N. Rieben, D. A. White, and D. G. Dudley, "Full wave analysis of RF signal attenuation in a lossy rough surface cave using high order time domain vector finite element method," *J. Electromagn. Wave Applicat.*, vol. 20, no. 12, pp. 1695-1705, 2006.

[29] FEKO Suite 7.0, Altair Engineering, 2014.

Hany M. El-Maghrabi, M.Sc. and Ph.D. Electronics and Electrical Communications, Faculty of Engineering, Cairo University at 2011 and 2017, respectively. El-Maghrabi received position of Research Assistant in Housing and Building National Research Center (HBNRC), Institute of Electromechanical, Department of Communication (Egypt) in 2005. He became Assistant Researcher at HBNRC in 2011 and Researcher in 2017. He has co-authored technical journal articles and conference papers. El-Maghrabi has experience in electromagnetics, antennas, microstrip structures, numerical methods, wave propgation and their applications in microwave. El-Maghrabi was awarded the Best Paper in NRSC 2015.

Samir F. Mahmoud graduated from the Electronic Engineering Dept., Cairo University, Egypt in 1964. He received the M.Sc. and Ph.D. degrees in the Electrical Engineering Department, Queen's University, Kingston, Ontario, Canada in 1970 and 1973. During the academic year 1973-1974, he was a Visiting Research Fellow at the Cooperative Institute for Research in Environmental Sciences (CIRES), Boulder, CO, doing research on Communication in Tunnels. He spent two sabbatical years, 1980-1982, between Queen Mary College, London and the British Aerospace, Stevenage, where he was involved in design of antennas for satellite communication. He spent several years as Professor at the EE Department, Kuwait University. Currently Mahmoud is a Full Professor at the Electronic and Telecommunication Engineering Department, Cairo University. His research activities have been in the areas of antennas, geophysics, tunnel communication, and e.m wave interaction with composite materials. Mahmoud is a Fellow of IET and one of the recipients of the Best IEEE/MTT Paper for 2003.

Mostafa El-Said graduated from the Electronic Engineering Dept., Cairo University, Egypt in 1963. He received the Dipl.Ing. and Dr.Ing. degrees from Karlsruhe University, West Germany, in 1970 and 1974. Since 1992, he is Professor at the Electronic Engineering and Telecommunication Department Cairo University. His research activities have been in the areas of microstrip, wave propagation and nano technology.

Improper Integrals Calculations for Fourier Boundary Element Method

Jan Sikora [1], Krzysztof Polakowski [2], and Beata Pańczyk [1]

[1] Electrical Engineering and Computer Science Faculty
Lublin University of Technology, 20-618 Lublin 38A Nadbystrzycka str., Poland
sik59@wp.pl, b.panczyk@pollub.pl

[2] The Faculty of Electrical Engineering
Warsaw University of Technology, 00-661 Warszawa, Pl. Politechniki 1, Poland
Krzysztof.Polakowski@ee.pw.edu.pl

Abstract ─ This paper presents a method of regularization for the numerical calculation of improper integrals used in different formulations of Boundary Element Method (BEM). The main attention of the readers we would like to focus on Fourier Formulation of BEM. The singular integrals arise when for discretization the elements of a higher order than zero are used. Very often in the Diffusive Optical Tomography for infant head modeling, triangular or square curvilinear boundary elements of the second order are used [12,14], hence, our interest in the subject of effective and accurate calculation of singular integrals. Even for the classical formulation of BEM such a problem is extremely difficult [1]. Some authors believe that the practical application possesses only flat triangular boundary elements of zero-order, and although there is some truth in this statement, the elements of the second order show a significant advantage [10,12] in Diffusion Optical Tomography (DOT) for example.

This issue becomes even more interesting when we deal with the Galerkin BEM formulation offering the possibility of matrix of coefficients symmetrisation, which has fundamental importance for inverse problems. This matter becomes critical when we start to consider the Fourier BEM formulation, introduced by Duddeck [5]. His approach provides the possibility of a solution in the case which has no fundamental solution. The light propagation, which is described by the Boltzmann equation (see Arridge [2]) is such a case.

Currently and most commonly, the Boltzmann equation is approximated by the diffusion equation in strongly light scattering media [10]. In the author's opinion, the problem of numerical integration of improper integrals has not yet been fully exhausted in the classic and Galerkin BEM formulation but the Fourier BEM formulation still expects the proposals of the effective solutions. Such an offer we would like to present in this paper.

I. INTRODUCTION

In the field of digital modeling, two methods are used at present: the Finite Element Method (FEM) and the Boundary Element Method (BEM). The latter is less common since there is much less the professional computer software that uses the BEM compared to FEM.

For a few decades rapid development of BEM can be observed [1,5-7,9-12,14,15] resulting in an increase in BEM's application over time to, among other things, electromagnetic, thermal, and optical analysis [1,5–7, 11]. Nevertheless, it is not easy to find ready-to-use BEM implementations. The situation becomes even more difficult if we try to find free open source software and worse still if we need specialized BEM software applicable, for example, to Diffusion Optical Tomography. One of the reasons why this state is maintained might be the complexity of integration (in particular singular integrals) which needs to be done using BEM calculations. Of course, this is not a problem which cannot be overcome [12,14,15]. The need for the BEM calculations software exists and is unquestionable, but it has been only insignificantly implemented (Table 1 [10]). The other software packages for Boundary Element Methods is listed in Table 1. It is worth to emphasize that this list by no means is no complete.

It appears that industrial and scientific groups would like to have a well-designed platform for BEM calculations which should be universal but at the same time have modularity that easily enables application [8,14,15]. Such a software is collected in Table 2.

The plan of this article is as follows. In Section I, review the foundations of boundary element methods and standard methods for integration of singular integrals

is presented. Section II is devoted to a presentation of the major features of numerical integration for Fourier Boundary Element Method (FBEM). Finally, in Section III we discuss plans for further directions of our research.

Table 1: Commercial software implementing BEM [11,12]

Library (Programme)	Environment (Language)	Application
BEASY	Windows or Unix binaries	Construction engineering
Integrated Engineering Software	Windows only	Fields, wave, thermal analysis
GPBEST	Windows or Unix	Acoustics, thermal analysis
Concept analysis	Windows	Stress analysis

Table 2: Free software implementing BEM [8,14,15]

Library	Language	Distribution Conditions	Application
ABEM (by Kirkup)	Fortran	Commercial, open source	Acoustics, Laplace and Helmholz problems
LibBem	C++	Semi-commercial	Laplace equation
BEMLIB (Pozrikidis)	Fortran	GPL	Laplace, Helmholtz equations and Stokes flow
BIEPACK	Fortran	free open source	Laplace equation
BEA	Fortran	Distributed with the book	Acoustics
MaiProgs [8]	Fortran	Copyright © 2007 Matthias Maischak. Designed by Free CSS Templates. All templates are licensed under the Creative Commons Attribution 3.0 license.	Galerkin BEM for Laplace, Helmholtz, Lam´e and Stokes equations
HyENA (Hyperbolic and Elliptic Numerical Analysis [16])	C++	Provided under the GNU Lesser General Public License	Laplace, Helmholtz and Lam´e equations in 2D and 3D using the Galerkin or collocation approaches
BETL (Boundary Element Template Library [Hiptmair and Kielhorn 2012; Kielhorn 2012])	C++	BETL is free for academic use in research and teaching	Laplace, Helmholtz and Maxwell equations in 3D using the Galerkin approach
BEM++ [13]	C++ Phyton	Open-source	Laplace, Helmholtz and Maxwell problems in three space dimensions
BEMlab [3]	C++	Open-source	Laplace, Helmholtz and Maxwell problems in three space dimensions

A. Standard 3D boundary element method and numerical integration of singular integrals

Let's consider Poisson's equation in three–dimensional space:

$$\nabla^2 \Phi(r) = b, \tag{1}$$

where Φ stands for the arbitrary potential function for temperature or electric potential.

On the surface of the volume under consideration, the Robin boundary conditions are imposed:

$$\frac{\partial \Phi(r)}{\partial n} = m_R \Phi(r) + n_R, \tag{2}$$

where m_R and n_R are known coefficients for the Robin boundary condition [2].

The fundamental solution for 3D space is:

$$G(|r-r'|) = \frac{1}{4\pi R}, \tag{3}$$

where $R = |\mathbf{r} - \mathbf{r'}|$ is a distance between $\mathbf{r}$ (the source point) and $\mathbf{r'}$ (the field point).

The integral form for the Eq. (1) is:

$$c(r)\Phi(r) + \int_\Gamma \frac{\partial G(|r-r'|)}{\partial n} \Phi(r') d\Gamma(r') =$$
$$\int_\Gamma G(|r-r'|) \frac{\partial \Phi(r')}{\partial n} d\Gamma(r') + \int_\Omega bG(|r-r'|) d\Omega(r'). \tag{4}$$

When the distance between the source point and the element over which the integration is performed is sufficiently large relative to the element size, the standard Gauss–Legendre quadrature formula works efficiently. But when the distance tends to zero than integrals became singular and special integration strategy should be applied.

Let us consider Quadrilateral boundary elements. The strategy used for integration rectangular boundary elements is as follows: mapping them at first onto 2D curvilinear coordinates and then dividing them into two

or three triangles and subsequently onto the standardized square. The whole procedure is shown in Fig. 1.
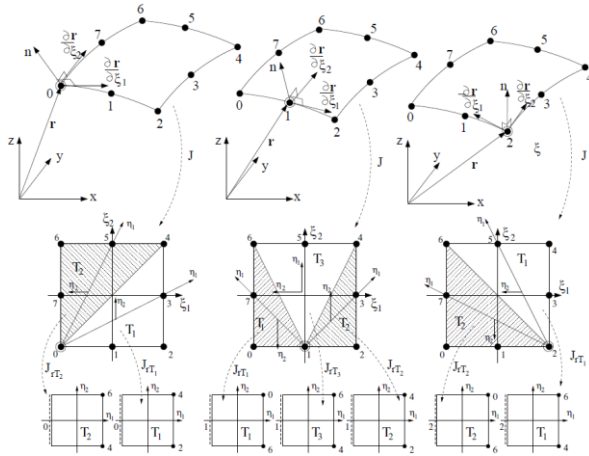
Fig. 1. Local coordinates of the quadrilateral boundary element and a mapping strategy [12].

Finally in all the above cases the Gauss – Legendre method of numerical integration was used [4]. The coordinates of the numerical integration points and the weights are available in the literature or in the internet, for example, [4,12].

II. FOURIER BOUNDARY ELEMENT METHOD (FBEM) AND NUMERICAL INTEGRATION

Let us briefly introduce some elements of basics of Fourier approach to BEM[1].

To obtain the Fourier transform of the Galerkin BEM, all quantities have to be extended from domain Ω to the space R^n. This can be achieved by defining a cutoff distribution χ [5], multiplying all quantities by χ and finally transforming the quantities into Fourier space:

$$F(u)=\hat{u}, \quad u \in L_1(R^n), \quad i=\sqrt{-1}\,.$$

The n-dimension Fourier transform is defined as:

$$\hat{u}(\hat{x}) = \int_{R^n} u(x)\, e^{-i\langle x,\hat{x}\rangle} dx, \qquad (5)$$

$$\langle x,\hat{x}\rangle = \sum_{k=1} x_k \hat{x}_k. \qquad (6)$$

The discretized Fourier BEM leads to an algebraic system identical to that obtained in the original space:

$$\sum_i K_u^{ji} u^i = F_u^j + \sum_i H_u^{ji} t^i - \sum_i G_u^{ji} u^i, \qquad (7)$$

where now, the matrices and vectors are computed in the transformed space,

---

[1] Based on F.M.E. Duddeck. Fourier BEM. Springer–Verlag, 2002. Lecture Notes in Applied Mechanics, vol. 5.

$$F_u^j = \frac{1}{(2\pi)^n}\left\langle \hat{\Phi}_t^j(-\hat{x}), \hat{f}(\hat{x})\hat{U}(\hat{x})\right\rangle,$$

$$G_u^{ji} = \frac{1}{(2\pi)^n}\left\langle \hat{\Phi}_t^j(-\hat{x}), \hat{\Phi}_u^i(\hat{x})\hat{A}_i^i\,\hat{U}(\hat{x})\right\rangle,$$

$$H_u^{ji} = \frac{1}{(2\pi)^n}\left\langle \hat{\Phi}_t^j(-\hat{x}), \hat{\Phi}_t^i(\hat{x})\hat{U}(\hat{x})\right\rangle,$$

$$K_u^{ji} = \frac{1}{(2\pi)^n}\left\langle \hat{\Phi}_t^j(-\hat{x}), \hat{p}_u^i(\hat{x})\right\rangle. \qquad (8)$$

A. Numerical example

The Fourier formulation of BEM is only presented for the boundary integral equations limited to constant elements and 2D space. As the test example, the Dirichlet problem of the Poisson equation is considered:

$$\Delta u(x) = -f(x), \quad x\in\Omega, \quad u(x)=u_\Gamma=0, \quad x\in\Gamma. \quad (9)$$

The Dirichlet problem is solved in a quadratic two-dimensional domain Ω [0, 1]x[0, 1]. At the boundaries, $u=0$ is imposed. The interior is subjected to stationary heat source f. The boundary Γ is divided into 16 elements. In our case when the source function $f=1$ the exemplary entries are:

$$H^{12} = \frac{1}{(2\pi)^2}\left\langle \hat{\Phi}_t^1(-\hat{x}), \hat{\Phi}_t^2(\hat{x})\hat{U}(\hat{x})\right\rangle =$$

$$\frac{1}{(2\pi)^2}\int_{R^2} \frac{\left[i\left(e^{i\hat{x}_1/4}-1\right)\right]\left[i\left(e^{-i\hat{x}_1/2}-e^{-i\hat{x}_1/4}\right)\right]}{-\hat{x}_1\hat{x}_1\left(-\hat{x}_1^2-\hat{x}_2^2\right)}d\hat{x}_1 d\hat{x}_2,$$

$$F^1 = \frac{1}{(2\pi)^2}\int_{R^2} \hat{\Phi}_t^2(-\hat{x})\hat{U}(\hat{x})\, d\hat{x} =$$

$$\frac{-1}{(2\pi)^2}\int_{R^2} \frac{\left[i\left(e^{i\hat{x}_1/4}-1\right)\right]}{-\hat{x}_1\left(-\hat{x}_1^2-\hat{x}_2^2\right)}d\hat{x}_1 d\hat{x}_2, \quad \text{for } f_0=1. \quad (10)$$
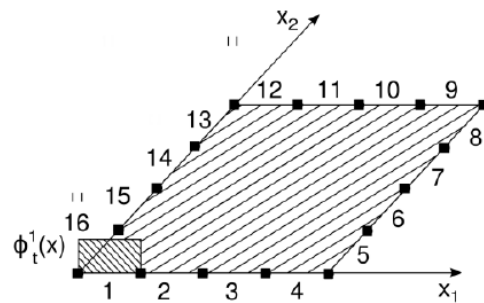
Fig. 2. Quadratic domain under consideration.

B. The integration in R^2 space and numerical challenges of improper integrals

Improper integrals present great challenges for numerical integration, but they are important in certain parts of science, like for example physics [13,14].

The trapezoidal and Simpson's methods use the value of the integrand at the endpoints of the domain of

integration. If the function is not defined there, these methods cannot be used. The midpoint and Gauss-Legendre methods use only interior points, so these are better suited to improper integrals.

However, as we will see, that these methods always return a result is not necessarily a good thing. Interior point methods return finite values when applied to both convergent and divergent integrals. It is something of an art to decide when an integral is divergent or how accurately the numerical value returned matches the integral.

C. Changing from infinite domains to finite domains of integration

Process of numerical integration in such a case of R^2 space could be divided into several steps.

STEP No. 1

The integrand (see Eq. (10)) has a singularity along the axis of the coordinate system x_1, x_2 as it is shown in Fig. 3. Therefore, in order to successfully integrate such a function numerically, we divide the space R^2 into four quarter in accordance with Fig. 4.
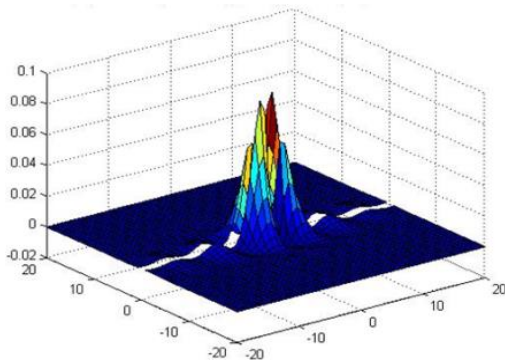
Fig. 3. Function being integrated in R^2 according to Eq. (10).
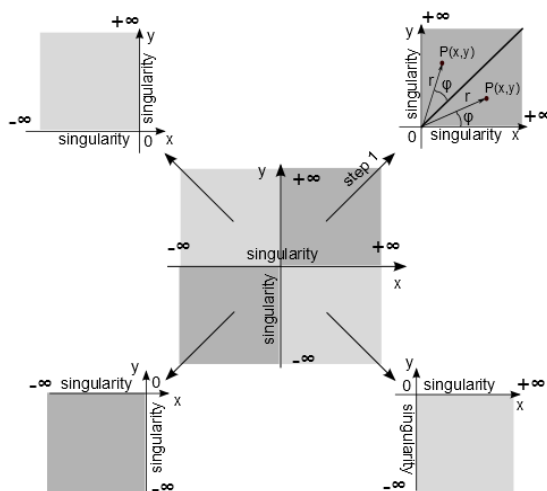
Fig. 4. R^2 space partition onto four quarters.

STEP No. 2

After dividing the area into four infinite subareas and unifying the limits of integration (for easier algorithmization) we have:

$$\int_{-\infty}^{\infty}\int_{-\infty}^{\infty} f(x_1,x_2)dx_1dx_2 =$$

$$\int_{0}^{\infty}\int_{0}^{\infty} f(x_1,x_2)dx_1dx_2 + \int_{0}^{\infty}\int_{-\infty}^{0} f(x_1,x_2)dx_1dx_2 +$$

$$\int_{-\infty}^{0}\int_{-\infty}^{0} f(x_1,x_2)dx_1dx_2 + \int_{-\infty}^{0}\int_{0}^{\infty} f(x_1,x_2)dx_1dx_2 = \qquad (11)$$

$$\int_{0}^{\infty}\int_{0}^{\infty} f(x_1,x_2)dx_1dx_2 + \int_{0}^{\infty}\int_{0}^{\infty} f(-x_1,x_2)dx_1dx_2 +$$

$$\int_{0}^{\infty}\int_{0}^{\infty} f(-x_1,-x_2)dx_1dx_2 + \int_{0}^{\infty}\int_{0}^{\infty} f(x_1,-x_2)dx_1dx_2.$$

After dividing the area into four infinite subareas and unifying the limits of integration, for easier algorithmization according to the last row of Eq. (11).

Every subarea was transformed into a local coordinate system using the transformation T (the same for both x_1 and x_2 coordinates):

$$x_i(\xi_i) = \frac{2\xi_i}{(1-\xi_i)^2}, \quad i = 1, 2, \qquad (12)$$

where ξ_1, ξ_2 are the local coordinates.

Double integrals in local coordinates ξ_1, ξ_2 corresponds to the integration under square domain as it is shown in Fig. 5.
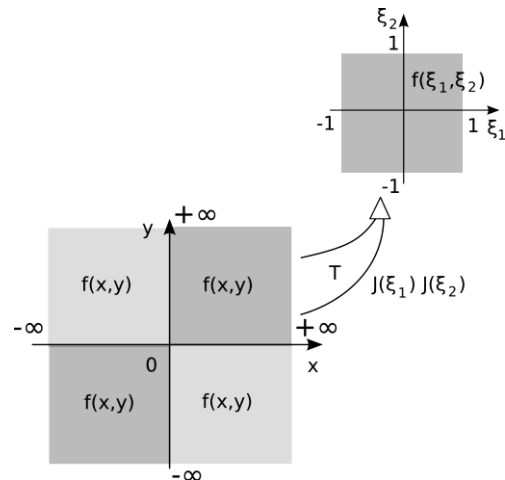
Fig. 5. One of the quarters after mapping into the normalized square.

The integrals can be calculated in a similar way as for the conventional BEM using twice Gauss-Legendre integration rules.

After transformation the numerical integration in the local coordinate system over each boundary element

is equal to:

$$I = \int_{-1}^{1}\int_{-1}^{1} f\left(x_1(\xi_1), x_2(\xi_2)\right) J(\xi_1)J(\xi_2)\, d\xi_1 d\xi_2, \quad (13)$$

where, f means any function for example the integrand from Eq. (10):

$$J(\xi_i) = \frac{dx_i}{d\xi} = \frac{2(1+\xi_i)^2}{(1-\xi_i^2)^2}, \quad i = 1, 2, \quad (14)$$

$J(\xi_i)$ for $i = 1, 2,$ are the Jacobians of the transformation.

After transformation of one quarter of the integration space to the normalized square (see Fig. 5) the integrand from the Eq. 10 is presented in Fig. 6 (a). Unfortunately, we can observe a big oscillation close to the boundaries of the square. Oscillating functions are the most difficult for numerical integrations. That is why the 80 integration points were used (Fig. 6 (b)) to achieve satisfactory results.

(a)   (b)
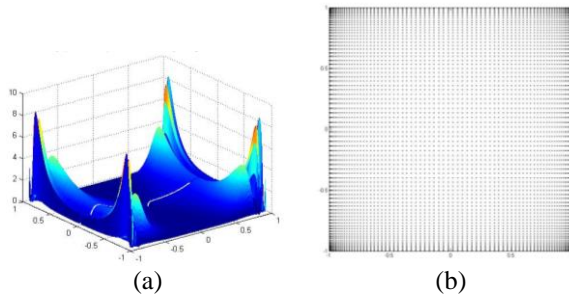
Fig. 6. (a) Function being integrated (see Eq. (10) after mapping into square. (b) For numerical calculation - the 80 integration points were used.

The 16 elements the coefficients matrix H (size of 4x4, see Eq. 8) were calculated numerically and the results of calculations are shown in Table 3 for the region and its discretization shown in Fig. 2. As we can see the discretization is not particularly dense – only 16 elements. As a reference solution, the analytical integration was treated (see Table 3).

Table 3: Comparison between exact and numerical integration

Exact Solution	Numerical Solution	Relative Error [%]
0.166736	0.166059	0.41
0.336249	0.343520	2.16
0.336249	0.343520	2.16
0.166736	0.166059	0.41

In Fig. 7 the relative error of the final solution is presented.

One can say that the errors reported in the Table 3 are quite satisfactory. But still two problems remain. The first one that we are forced to use a vast number of integration points what has a profound influence on the computation time for BEM. And the second problem that for the BEM such a level of relative error could not be sufficient in some applications like the DOT.

That is why we decided to develop the next steps of the integration procedure.
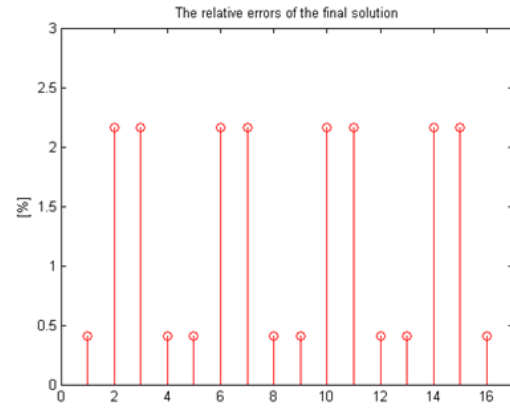
Fig.7. The relative error of the final solution.

STEP No. 3
Each quarter of the R^2 space is split onto two subspaces for which only one edge possess singularity as it is shown in Fig. 8.
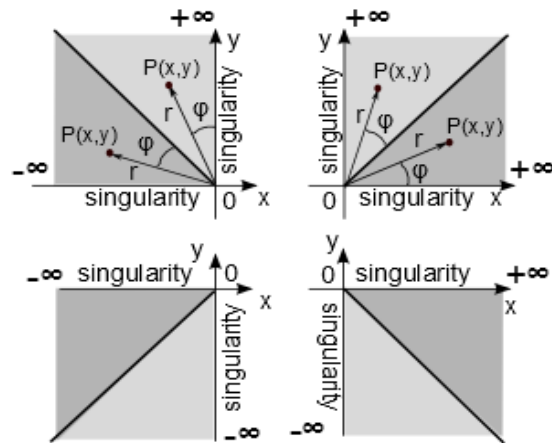
Fig. 8. Quarters are split onto eight parts.

STEP No. 4
Eight subspaces are mapped into the polar coordinate system. The polar coordinate system reduces infinity to one dimension only. In the Fig. 9 only the first two quarters of the R^2 space are presented but the rest is mapped in the similar way:

$$x(r, \Theta) = r\cos\Theta,$$
$$y(r, \Theta) = r\sin\Theta. \quad (15)$$

Now, the Eq. (11) become more complicated as it is expressed in Eq. (16):

$$\int_0^\infty\int_0^\infty f(x_1,x_2)dx_1dx_2+\int_0^\infty\int_0^\infty f(-x_1,x_2)dx_1dx_2+$$

$$\int_0^\infty\int_0^\infty f(-x_1,-x_2)dx_1dx_2+\int_0^\infty\int_0^\infty f(x_1,-x_2)dx_1dx_2=$$

$$\int_0^\infty\int_0^{\pi/4} f(\,r\cos\Theta,\ r\sin\Theta)\,r\,dr d\Theta+$$

$$\int_0^\infty\int_{\pi/4}^{\pi/2} f(\,r\cos\Theta,\ r\sin\Theta)\,r\,dr d\Theta+$$

$$\int_0^\infty\int_{\pi/2}^{3\pi/4} f(-r\cos\Theta,\ r\sin\Theta)\,r\,dr d\Theta+$$

$$\int_0^\infty\int_{3\pi/4}^{\pi} f(-r\cos\Theta,\ r\sin\Theta)\,r\,dr d\Theta+ \qquad (16)$$

$$\int_0^\infty\int_{\pi}^{5\pi/4} f(-r\cos\Theta,-r\sin\Theta)\,r\,dr d\Theta+$$

$$\int_0^\infty\int_{5\pi/4}^{3\pi/2} f(-r\cos\Theta,-r\sin\Theta)\,r\,dr d\Theta+$$

$$\int_0^\infty\int_{3\pi/2}^{7\pi/4} f(\,r\cos\Theta,-r\sin\Theta)\,r\,dr d\Theta+$$

$$\int_0^\infty\int_{7\pi/4}^{2\pi} f(\,r\cos\Theta,-r\sin\Theta)\,r\,dr d\Theta\,.$$
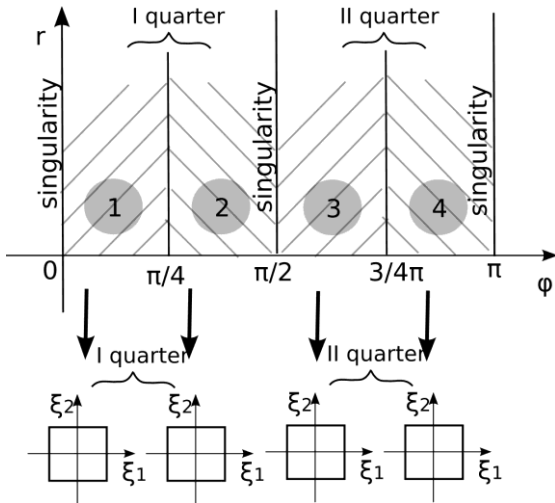
Fig. 9. The first two quarters are presented in polar coordinate system and next are mapped into normalized squares in local ξ_1,ξ_2 coordinate system.

STEP No. 5

Each of the eight subareas are transformed into a local coordinate system using the transformation *T*:

$$\Theta(\xi_1)=\frac{\pi}{8}\Big[\xi_1+(2k-1)\Big],$$

$$r(\xi_2)=\frac{2\xi_2}{(1-\xi_2)^2}, \qquad (17)$$

where ξ_1,ξ_2 are the local coordinates, $k=1\div 8$ is the number of considered sub areas.

D. Using the Gauss-Legendre method of improper integrals with finite domains

After transformation, the numerical integration in the local coordinate system over each boundary element is equal to:

$$\int_0^\infty\int_0^{\pi/4} f(\,r\cos\Theta,\ r\sin\Theta)\,r dr d\Theta=$$

$$\int_{-1}^1\int_{-1}^1 f\big(r(\xi_2)\cos\Theta(\xi_1),r(\xi_2)\sin\Theta(\xi_1)\big) \qquad (18)$$

$$r(\xi_2)J_\Theta(\xi_1)J_r(\xi_2)\,d\xi_1 d\xi_2,$$

where, *f* means any function,

$$J_\Theta(\xi_1)=\frac{d\Theta}{d\xi_1}=\frac{\pi}{8},$$

$$J_r(\xi_2)=\frac{dr}{d\xi_2}=\frac{2(1+\xi_2)^2}{(1-\xi_2{}^2)^2}, \qquad (19)$$

are the Jacobians of transformation and are the same for all eight subareas.

Next, we import the Gauss-Legendre coefficients from the following webpage:
http://www.math.ntnu.no/num/nnm/Program/Numlibc/g auss_co.c

III. CONCLUSION

This paper presents the regularization method for the integration of singular integrals for Fourier formulation of BEM. With the help of numerical experimentation, the effectiveness of the proposed method of integration was proven. Additionally, the authors tried to demonstrate that the degree of difficulty increases in the direction from the classical to the Fourier approach.

A very interesting formulation of the BEM was presented by Duddeck in his monograph [1], however the problem of integration was not considered thoroughly. One of the main goals of this paper was to address this gap. Without effective numerical integration, the Fourier approach to BEM becomes useless.

The authors believe that the Fourier's formulation holds enormous potential, for the Diffusion Optical Tomography. The light propagates in accordance with the Boltzmann equation [2]. The Boltzmann equation does not have a fundamental solution. Therefore, classical formulation of BEM becomes useless. Usually in case of environments strongly dissipative the Boltzmann equation is approximated by the diffusion equation [2,12].

The authors are aware that this work on numerical integration particularly in the R^2 space still required further work to improve the accuracy and reduce the number of integration points. This will be a critical

issue for real discretization with the aid of thousands of boundary elements.

ACKNOWLEDGMENT

REFERENCES

[1] M. H. Aliabadi and W. S. Hall, "The regularizing transformation integration method for boundary element kernels. Comparison with series expansion and weighted Gaussian integration methods," *Engineering Analysis with Boundary Elements*, vol. 6. No. 2, pp. 66-70, 1989.

[2] S. R. Arridge, "Optical tomography in medical imaging," *Inverse Problems*, vol. 15, no. 2, pp. R41-R93, 1999.

[3] BEMlab web page address: http://bemlab.org/wiki/Main_Page

[4] C. Bond, "A new integration method providing the accuracy of Gauss–Legendre with error estimation capability." http://www.crbond.com/papers/gbint.pdf

[5] F. M. E. Duddeck, *Fourier BEM*. Springer–Verlag, 2002. Lecture Notes in 258 Applied Mechanics, vol. 5.

[6] T. Grzywacz, J. Sikora, and S. Wojtowicz, "Substructuring methods for 3-D BEM multilayered model for diffuse optical tomography problems," *IEEE Transactions on Magnetics*, vol. 44, no. 6, pp. 1374-1377, June 2008.

[7] E. Łukasik, B. Pańczyk, and J. Sikora, "Calculation of the improper integrals for Fourier boundary element method," *Informatics Control Measurement in Economy and Environmental Protection (IAPGOS)*, ISBN 2083-0157, no. 3, pp. 7-10, 2013.

[8] M. Maischak, Maiprogs, 2013. http://www.ifam.uni-hannover.de/~maiprogs

[9] K. Polakowski, "Tomography visualization methods for monitoring gases in the automotive systems," Chapter in: *New Trends and Developments in Automotive Industry*, Edited by M. Chiaberge, (ISBN: 978-953-307-999-8), INTECH, pp. 193-208, 2011.

[10] T. Rymarczyk, S. F. Filipowicz, J. Sikora, and K. Polakowski, "Applying the level set methods and the immersed interface method in EIT," *Electrical Review (PRZEGLĄD ELEKTROTECHNICZNY)*, R. 85, no. 4, pp. 68-70, 2009.

[11] J. Sikora, A. Zacharopoulos, A. Douiri, M. Schweiger, L. Horesh, S. R. Arridge, and J. Ripoll, "Diffuse photon propagation in multilayered geometries," *Physics in Medicine and Biology*, vol. 51, pp. 497-516, 2006.

[12] J. Sikora, *Boundary Element Method for Impedance and Optical Tomography*. Warsaw University of Technology Publisher, 2007.

[13] W. Śmigaj, T. Betcke, S. R. Arridge, J. Phillips, and M. Schweiger, "Solving boundary integral problems with BEM++," *ACM Transactions on Mathematical Software*, vol. 41, no. 2, article 6, Publication date: January 2015, DOI: http://dx.doi.org/ 10.1145/2590830

[14] P. Wieleba and J. Sikora, "Open source BEM library," *Advances in Engineering Software*, 2008, issn. 0965-9978, doi. 10.1016/j.advengsoft.2008.10.007.

[15] P. Wieleba and J. Sikora, *BEMLAB – Universal, Open Source, Boundary Element Method Library Applied in Micro-Electro-Mechanical Systems*, Studies in Applied Electromagnetics and Mechanics 35, Electromagnetic Nondestructive Evaluation (XIV) Eds. T. Chady et. al., IOS Press, pp. 173-182, 2011.

[16] http://portal.tugraz.at/portal/page/portal/Files/i2610/files/Forschung/Software/HyENA/html/index.html

Jan Sikora graduated from Warsaw University of Technology Faculty of Electrical Engineering. During 40 years of professional work he has proceeded all grades, including the position of Full Professor at his alma mater. Since 1998 he has worked for the Institute of Electrical Engineering in Warsaw. In 2008 he has joined Electrical Engineering and Computer Science Faculty in Lublin University of Technology. His research interests are focused on numerical methods for electromagnetic field.

Krzysztof Polakowski graduated from Warsaw University of Technology Faculty of Electrical Engineering. During his studies, he has joined the Institute of Electrical Machines where he has achieved Ph.D. and defended Habilitatus work. His scientific interests are concentrated on CAD method applied for numerical modelling in 3D space. Just recently his interests are focused on electromobility and industrial application of electrical tomography.

Beata Pańczyk graduated from mathematics at the Maria Curie-Skłodowska University in Lublin. Since 1989 she has been working at the Lublin University of Technology (LTU), where she completed a Ph.D. in 1996. The doctoral thesis title was "Construction of the Physical Properties Distribution Image using Impedance Computer Tomography". Currently she is the Senior Lecturer at the Institute of Computer Science of the LTU. Her didactic and research interest are: object oriented programming, web application development and application of numerical methods in engineering.

Towards Wideband Hyperthermia Treatment System

**N. Nizam-Uddin, Wazie Alkadri, Waqar Ahmad Malik, Ibrahim Elshafiey,
and Abdel Fattah Sheta**

Department of Electrical Engineering
King Saud University, Riyadh, Kingdom of Saudi Arabia
{enizamuddin, walkadri, wmalik, ishafiey, asheta}@ksu.edu.sa

Abstract ─ This paper presents an overview of design and functionality of the essential modules proposed to build a wideband hyperthermia system. Description is provided of the waveform shaper, power amplifier and applicator array modules. Big data analysis is presented to accelerate energy localization depending on a time reversal technique. Simulation results are provided assuming a cylindrical head phantom characterized with wideband dispersive tissue properties, and the obtained field maps are shown in different planes to visualize energy localization process. Results reveal that wideband operation has the potential to enhance energy localization in deep tumor regions while eradicating hot spots, as compared to conventional narrowband systems.

Index Terms ─ Big data, double-ridge horn antenna, hyperthermia treatment, time reversal focusing, wideband power amplifier.

I. INTRODUCTION

Hyperthermia is known to be a promising therapeutic modality for curing cancer. In electromagnetic (EM) hyperthermia systems, the induced EM energy is used to elevate the temperature of malignant tissues to 40-45C° [1, 2]. Used in adjunct with radiotherapy and chemotherapy, hyperthermia treatment can reduce the vitality of malignant tissues and increase the effectiveness of therapeutic plans [3, 4]. Energy localization is required to be achieved onto intended regions without affecting the surrounding healthy tissues [5]. An effective hyperthermia treatment planning that caters for variations in age, size, tumor location and tissue properties is challenging. Development of a patient-specific treatment plan can be achieved, depending on robust energy focusing techniques along with high flexibility in system technical parameters. This research aims at enhancing the degrees of freedom of hyperthermia treatment system by using various channels and adopting wideband operation. Elevating the number of degrees of freedom allows the optimization of system performance on the expense of augmenting the complexity of data processing and analysis. Progress in big data analysis however, can be used to alleviate the complexity of developing patient-specific hyperthermia treatment systems.

With exponential growth of associated data in health care domains, big data is gaining considerable attention in terms of reducing cost, enhancing performance, developing standards and improving patient care [6, 7]. Characterizing data by volume, veracity, variety and velocity, big data analysis accelerates innovations in health care units [8, 9]. The evaluation tools associated with big data allow shifting from population based to patient specific plans. Patient specific planning allows improving the efficacy and specificity of treatment, and enhances patient care and comfort.

This research proposes a modular treatment system that can be used for patient specific treatment of brain tumors. The main modules include head model, applicator array, power amplifier PA array, and waveform shaper. The modular nature of the proposed system provides flexibility of system parameters to allow optimizing energy localization to required regions, while reducing associated hot spots in healthy tissues.

From big data perspective, the *volume* represents the complexity of our system related to the parameters of various modules. This includes the patient head model that identifies the size and location of each tumor as well as the wideband dispersive model of brain tissues. Data volume is also related to the characteristics of antenna element of the applicator array linked with system channels. Each channel is also associated with a PA that is characterized by frequency band of operation, maximum power, linearity and efficiency. In order to ensure the *veracity* of the proposed system we characterize each module under wideband operation. The waveform-shaping module is concerned with data *variety*. This module is associated with identifying the number of enabled channels as well as designing the excitation signal for each channel. The optimization tool associated with waveform-shaping module controls the *velocity* of the system, and we devise a robust wideband time reversal optimization tool to meet the velocity

requirements of the proposed system.

II. PROTOTYPE OF WIDEBAND HYPERTHERMIA SYSTEM

The proposed multi-channel wideband hyperthermia system for enhanced energy localization is shown in Fig. 1. The waveform-shaping module depends upon an optimization tool to obtain digital form of the excitation signal of each channel. The optimization tool estimates the optimum values of the phase and magnitude of each frequency subcarrier to achieve constructive interference or EM energy at the tumor region and destructive interference elsewhere.

The optimization tool depends on accurate patient specific head model to account for the wideband dispersive properties of various tissues. A linearization tool is also integrated with the waveform-shaping module in order to equalize the distortion introduced by the power amplifier under wideband excitation, which can diminish the process of energy localization.

Each channel consists of a digital to analog converter (DAC), and high power wideband amplifier to provide enough power to maintain required temperature levels at tissues. The wideband applicator elements should maintain appropriate radiation in the frequency band of operation. A feedback mechanism is added to monitor temperature maps and control the waveform-shaping module. Description of our proposed system is described next.
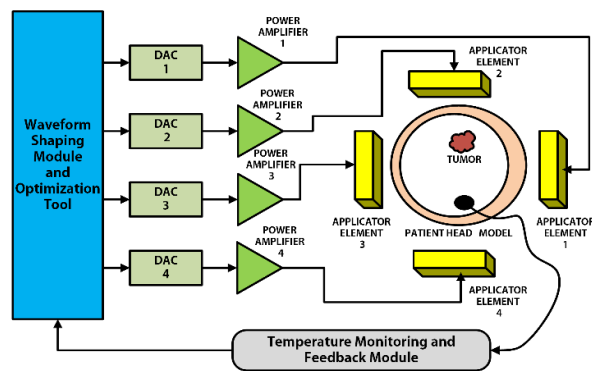
Fig. 1. Prototype of four-channel wideband hyperthermia treatment system.

III. MODULAR DESCRIPTION OF THE PROPOSED SYSTEM

Based on Fig. 1, we present an overview of the design and functionality of each module independently with a focus on the response of each module under wideband excitation.

A. The head model module

Patient-specific model and properties of head tissue can be utilized to optimize system performance. In this research, the analysis depends on heterogeneous head phantom represented by a four-layered cylinder of radius 10 cm is developed in CST Microwave Studio [10]. The inner four layers depicts brain tissue (radius = 8cm), gray matter (radius = 8.4cm), cerebrospinal fluid (CSF) (radius = 8.9cm) and skull (radius = 9.4cm) respectively. This model is shown in Fig. 2.
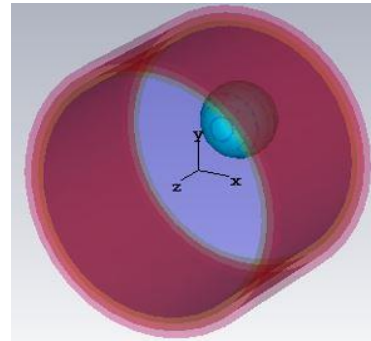
Fig. 2. Illustration of head phantom with an embedded tumor.

The tumor is taken to be of spherical shape (radius is 2.5 cm), and is located at x = 3 cm, y = 4 cm and z = 0, where the origin is set at the center of the phantom. The dispersive dielectric properties of brain tissue and tumor under wideband excitation are chosen in accordance with [11-13].

B. The applicator module

Several designs have been considered as heating applicators for hyperthermia treatment over the past few years. It includes Vivaldi [14], antipodal [15], microstrip [16, 17] and horn [18] antennas. Double ridge horn antenna can be designed to provide good performance in a very large bandwidth. Therefore, the traditional horn antenna has been replaced by double ridge horn antennas (DRHA) because of high gain, good directivity performance, low back radiation, low voltage standing wave ratio, and high peak power handling capability in wide bandwidth, which makes it a promising heating source for hyperthermia treatment [19, 20]. Recent developments in DRHA design are reported in [21, 22].

Here in this research we propose a double ridge horn antenna comprising of coaxial feeding, waveguide part, and two side ridges made of base ridges and flares as shown in Fig. 3.

The exponential section of the ridge profile is approximated by the following exponential equation:
$$f(x) = 0.02x + 2.5e^{0.0305x}. \qquad (1)$$
Where x is the axial length in millimeter along the horn from the straight section of the ridge, and f(x) is the perpendicular distance in millimeter from the centerline of the horn. The physical dimensions of the proposed DRHA are aperture width = 100 mm, aperture height =

100 mm and antenna length = 111 mm. We choose a minimum distance of 5 mm between proposed antenna and head phantom illustrated in Fig. 4 for simulation purpose.

(a)

(b)
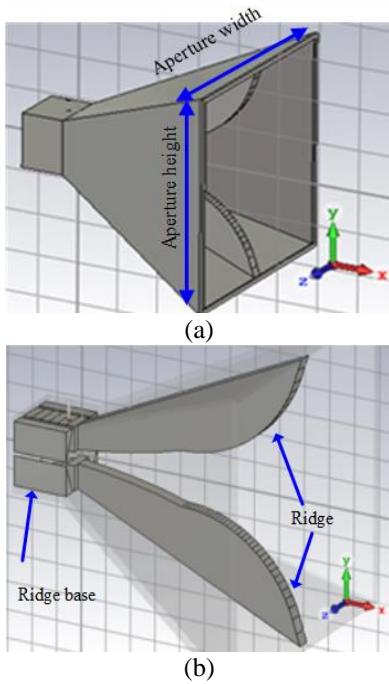
Fig. 3. (a) Geometry of the proposed DRHA, and (b) illustration of adopted ridges.
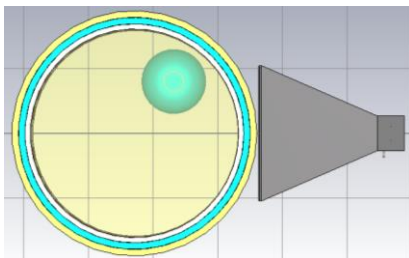
Fig. 4. DRHA with head phantom model.

The simulated S_{11} and VSWR characteristics of the proposed DRHA antenna with and without head phantom model are shown in Figs. 5 and 6 respectively. It is evident from the figures that S_{11} (<10 dB) is achieved for frequency band of 0.48 GHz to 1.24 GHz and the VSWR is almost below a value of two for the observed band. The resulting E-field maps by exciting the antenna with different frequency subcarriers are shown in Figs. 7 to 10. The radiation patterns corresponding to the chosen frequencies are presented in Figs. 11 to 14. In order to evaluate values of specific absorption rate SAR inside the head phantom, we compute the power loss density and then acquire the SAR maps for different frequencies as depicted in Figs. 15 to 18.
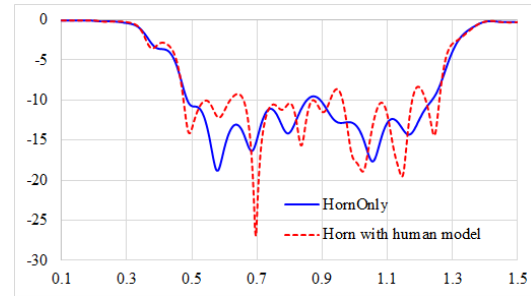
Fig. 5. Simulated S_{11} (dB) (y-axis) versus frequency (GHz) (x-axis) of the proposed antenna with and without phantom.
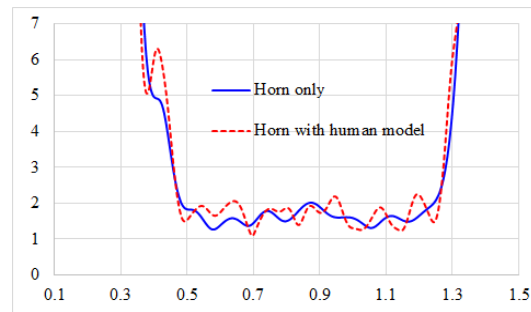
Fig. 6. Simulated VSWR (y-axis) versus frequency (GHz) (x-axis) of the proposed antenna with and without phantom.
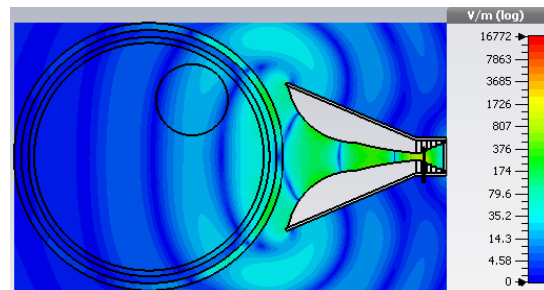
Fig. 7. E-field map of the proposed DRHA antenna in the vicinity of head phantom at 0.5 GHz.
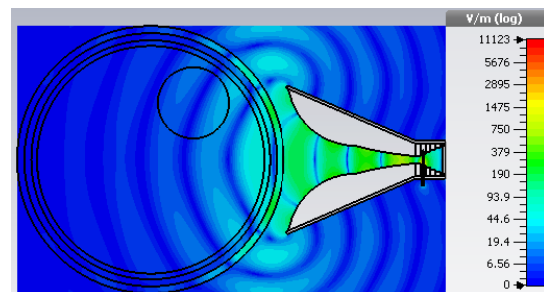
Fig. 8. E-field map of the proposed DRHA antenna in the vicinity of head phantom at 0.75 GHz.
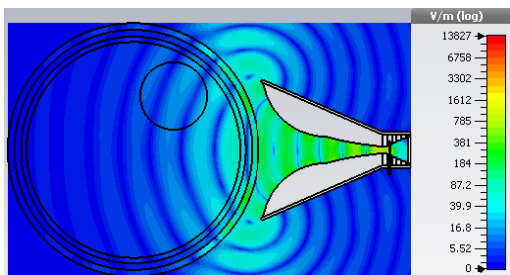
Fig. 9. E-field map of the proposed DRHA antenna in the vicinity of head phantom at 1 GHz.

Fig. 10. E-field map of the proposed DRHA antenna in the vicinity of head phantom at 1.25 GHz.

Fig. 11. Simulated radiation pattern of the proposed DRHA antenna at 0.5 GHz.
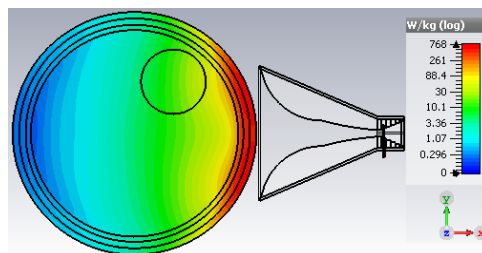
Fig. 12. Simulated radiation pattern of the proposed DRHA antenna at 0.75 GHz.

Fig. 13. Simulated radiation pattern of the proposed DRHA antenna at 1 GHz.

Fig. 14. Simulated radiation pattern of the proposed DRHA antenna at 1.25 GHz.

Fig. 15. Simulated SAR map inside the head phantom when the proposed DRHA antenna operates at frequecny of 0.5 GHz.
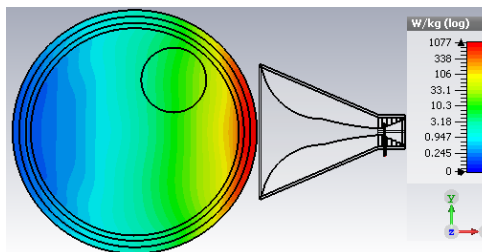
Fig. 16. Simulated SAR map inside the head phantom when the proposed DRHA antenna operates at frequecny of 0.75 GHz.
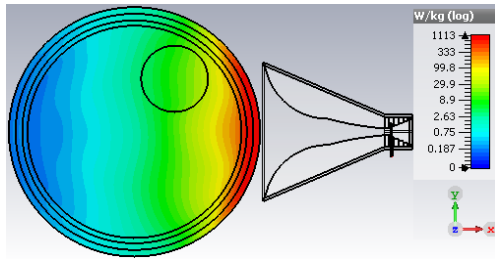
Fig. 17. Simulated SAR map inside the head phantom when the proposed DRHA antenna operates at frequecny 1 GHz.
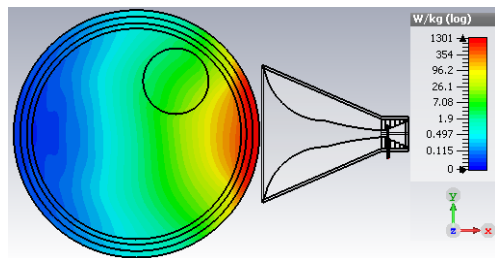
Fig. 18. Simulated SAR map inside the head phantom when the proposed DRHA antenna operates at frequecny 1.25 GHz.

As apparent from the figures, appropriate levels of SAR distribution can be achieved inside the phantom for different frequencies. However, to maximize SAR at tumor location and minimize outside the tumor, it requires wave-shaping of wideband energy radiated from an applicator array. This can be accomplished using energy localization methods such as time reversal technique.

C. Power amplifier (PA) module

The introduction of power amplifier in each channel is essential to allow deposition of enough energy into the intended tissue to raise the temperature and achieve hyperthermia therapeutic level. Wideband channels allows targeting superficial as well as deep-seated tumors. This invokes the requirement of PA providing high power levels, wideband and high efficiency characteristics. To achieve high efficiency, the PA has to be operated near its saturation, which causes the amplifier to behave non-linearly and yield harmonics and intermodulation products. This can severely degrade the performance of the energy localization. In this research, we devise a power amplifier that can exhibit high efficiency while maintaining good degree of linearity for a wideband frequency range of operation.

The recent research trend in the area of wideband power amplifier design is the use GaN HEMT field effect transistors because of its high breakdown voltage level and current density as compared to its counterpart

GaAs transistors. With the aim to achieve high power, several GaN HEMT based distributed power amplifiers are reported by researchers. It includes a wideband distributed power amplifier using a GaN HEMT to give 40.4 dBm of maximum output power with a small signal gain of 10 dB and power added efficiency (PAE) of greater than 35% when operated in 700 MHz to 4.5 GHz frequency [23]. In another research effort, an ultra-wideband GaN HEMT DA with a frequency range of 20 MHz to 3 GHz, 37 dBm output power and PAE of 27% is achieved using three GaN HEMT transistors [24]. A 5-W GaN HEMT, 0.35-8 GHz ultra-wideband power amplifier with average gain of 9 dB and PAE of 20% throughout the band is reported in [25].

In this paper we present the design of multi-octave GaN HEMT based wideband distributed power amplifier with almost flat gain of 10 dB from 0.2 GHz to 1.2 GHz. The maximum PAE achieved is 50%. This design is based on conventional distributed amplifier also known as travelling wave amplifier, consists of multiple FETs connected through drain and gate transmission lines as shown in Fig. 19.
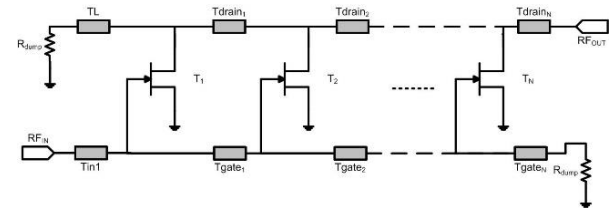
Fig. 19. Conventional distributed power amplifier.

The power is amplified at each FET and it adds up in phase with the signal at each section. Since the gain is almost the same for each amplifier, higher gain-bandwidth product can be achieved. The main disadvantage of the distributed power amplifier is its efficiency, which is typically in the range of 20-35%. The efficiency however can be increased using different techniques. One approach is to reduce losses at the gate of FET by introducing a series capacitance [26]. Another approach is based on tapering of the drain line with no termination as proposed by [27]. We included both techniques in our design.

In order to meet the output power requirement for hyperthermia treatment which typically varies between 90-110W for each channel, we choose a CREE manufactured 120 watts bare-die GaN HEMT FET (CGH60120D) [28]. A three-cell cascade topology of the distributed amplifier (DA) is adopted based on conventional design of DA and then optimized for high efficiency, gain and power. The schematic of the designed DA is shown in Fig. 20. The structure is simulated using Advance Design System (ADS) simulation software by Keysight's technologies. The values of lumped components used in the schematic are given in Table 1.
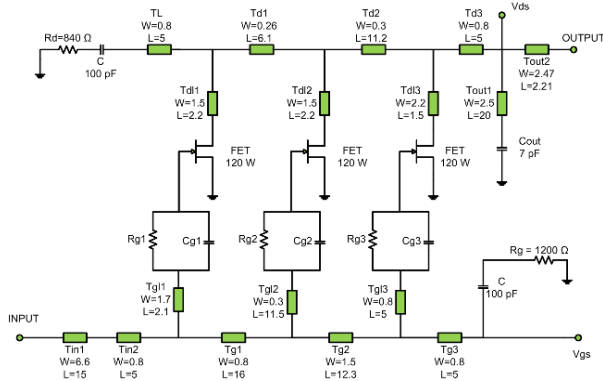
Fig. 20. Component level schematic of the proposed power amplifier.

Table 1: Lumped parameters used in schematic

Capacitors	Value (pF)	Resistors	Value (Ohms)
C	100	Rg1	710
Cout	7	Rg2	830
Cg1	0.3	Rg3	15
Cg2	5.7	Rd	840
Cg3	3	Rg	1200

The small signal simulations are carried out with the biasing conditions of Vgs = -2.5 Volts and Vds = 28 Volts. The HEMT has typically a larger gate-to-source capacitance 'Cgs' than its drain-to-source capacitance 'Cds'. In our case Cgs value is 34 pF, while, Cds is 7.7 pF at -8 Volts of Vgs as stated in the datasheet of the HEMT.

The bandwidth and efficiency can be improved by adding a series gate capacitance to lower the value of HEMT's Cgs. The simulations therefore involved two steps: firstly, without the series capacitance and secondly, with an optimized series capacitance. The values of the optimized capacitances are listed in Table 1. By adding the series capacitances to our HEMTs, their equivalent input capacitances which are directly proportional to its bandwidth can be approximated as; Ceq1 = Cgs ‖ Cg1 = 0.29 pF, Ceq2 = Cgs ‖ Cg2 = 4.88 pF, and Ceq3 = Cgs ‖ Cg3 = 2.75 pF. Thus, S_{11} and transducer power gain both are improved by adding the series gate capacitance C_{g1}, C_{g2}, and C_{g3} as illustrated in Figs. 21 and 22, respectively.

To improve output power and power added efficiency R_d and R_g are chosen to be 840 Ω, while the optimized capacitances 'C' along with drain and gate line is chosen to be 100 pF. With this configuration, maximum efficiency achieved at 1.2 GHz is 50% with maximum output power of 49 dBm as shown in Fig. 23, which corresponds to 80 watts, approximately making it suffice to be used in each channel of the proposed hyperthermia treatment system.
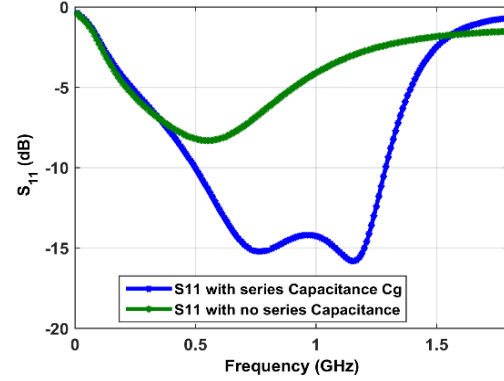
Fig. 21. S_{11} (dB) versus frequency (GHz), with and without series gate capacitance Cg.
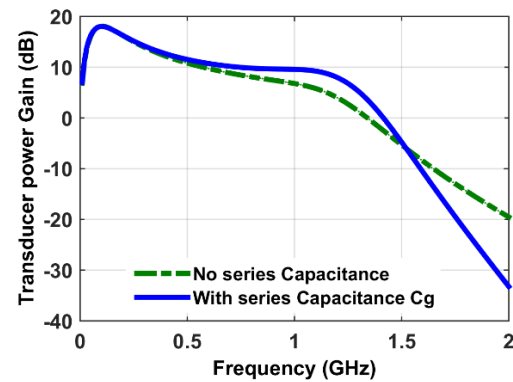
Fig. 22. Transducer gian S_{21} (dB) versus frequency (GHz), with and without series gate capacitance Cg.
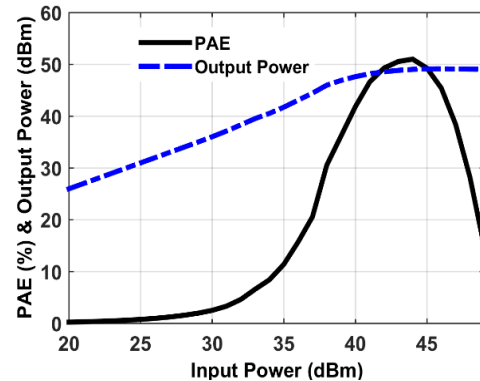
Fig. 23. Output power (dBm) & power added efficiency (%) versus input power (dBm) at 1.2 GHz.

D. Waveform shaping module

Energy localization in hyperthermia treatment is reported to be achieved using various techniques such as phased-arrays [29, 30], ultra-wideband beamforming approach [10], multi-frequency technique [31], transmission line approach [32, 33], time reversal techniques [34, 35],

temperature control feedback approach [36], projection algorithm [37], eigenvalue analysis [38] and SAR optimization techniques reported in [39-42].

We chose time reversal (TR) optimization technique to achieve energy localization at tumor region. As compared to other SAR or temperature optimization techniques, it is more robust, as it estimates the phases and magnitudes of E-fields directly from wave simulation rather than measured data [35]. It also allows the use of sinusoidal or pulse form of input excitation signals. Typically, TR operation involves two steps [43, 44]. In the first step, a virtual excitation source is placed at desired focusing position and energy is allowed to propagate through the heterogeneous head model. These field values are recorded at model surface and are processed in a time-reversed order, corresponding to conjugation in frequency domain. In the second step, the virtual source is removed and antenna applicators are placed at points of maximum field and are driven by the time-reversed signals. Because of the time invariance characteristics of EM field, the back-propagated time-reversed fields has the capability to refocus at the initial position of the virtual source. Here in this study, we use a plane of virtual source at tumor center. This plane has a dimension of 1cm x 1cm and can be considered as grid of point sources, excited by each of the subcarriers.

Mathematically, the field measured by an applicator at the phantom surface from the mth excitation point is given by:

$$f(t) = \sum_{m=1}^{M} h_m(t) \otimes e_m(t), \quad (2)$$

or

$$f(t) = \int_{-\infty}^{+\infty} \sum_{m=1}^{M} h_m(t) e_m(t - \tau) d\tau, \quad (3)$$

Where $\otimes$ represents the temporal convolution and $h_m(t)$ is the linear propagation operator defined by Green's function. This term includes the propagation effects of the medium from the mth excitation point to applicator. $e_m(t)$ corresponds to excitation signal of point source and $f(t)$ is the signal measured by the applicator. In frequency domain, Equation (3) can be written in matrix form as:

$$F(\omega) = H_m(\omega) E_m(\omega). \quad (4)$$

The matrix $H_m(\omega)$ is the Fourier transform of the Green's function. By assuming spatial reciprocity condition, the propagation between applicator and virtual point sources can be represented as:

$$E_m(\omega) = H_m^T(\omega) F(\omega). \quad (5)$$

Here H_m^T is the transpose of H_m. For the time reversal step, the time reversal operation of Green's function $[h_m(-t)]$ in time domain is equivalent to complex conjugate in frequency domain. Therefore, the time reversing the spectrum of applicator's output yields:

$$F^*(\omega) = H_m^*(\omega) E_m^*(\omega) = H_m^*(\omega) E_m(\omega). \quad (6)$$

Here E_m is real and '*' represents the complex conjugate. By combing the previous two equations, the back-propagated signal at the initial source location can be achieved as:

$$E_{TR}(\omega) = H_m^T(\omega) F^*(\omega), \quad (7)$$

or

$$E_{TR}(\omega) = H_m^T(\omega) H_m^*(\omega) E_m(\omega). \quad (8)$$

Where $H_m^T(\omega) H_m^*(\omega)$ is known as time reversal (TR) operator. In this research, a time reversal (TR) tool is developed using MATLAB [45], which has the capability to interface with CST simulating environment to automate the process of field acquisition, TR processing and feeding back to the applicators.

We investigate step 2 of the TR method by considering three planes xmax, ymax and zmin located on phantom surface at maximum value of x, maximum value of y and minimum value of z positions, respectively. The field resulted by excitation of the source at tumor center are collected at these planes, and TR tool is invoked to acquire field values, calculate the conjugate, and feed it back at planes positions. The fields are then ready to be back propagated towards tumor center, which is step 2 of the TR technique. In order to visualize energy localization at tumor region, we made three cut planes at tumor center located parallel to yz, xz and xy planes. The results are shown in Figs. 24 to 27, respectively.

Figure 24 demonstrates that energy localization is more prominent in the tumor yz plane when xmax plane is chosen for step 2 of TR. When ymax plane is chosen, good energy localization is achieved in tumor xz plane as shown in Fig. 25. The focus of energy localization shifts to tumor xy plane when zmin is chosen as excitation plane for step 2 of TR. This is illustrated in Fig. 26.

(a)   (b)

(c)   (d)
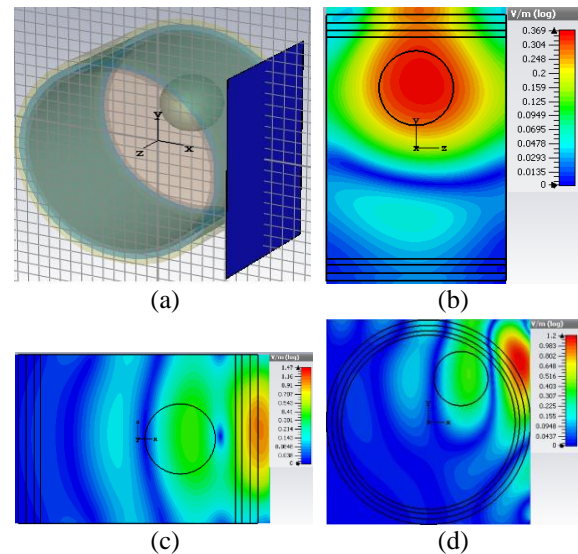
Fig. 24. Step 2 of TR energy locaization when (a) field from xmax plane is back-propagated towards tumor. Energy localization is shown at tumor center in yz (b), xz (c), and xy (d) planes.

(a)   (b)

(c)   (d)
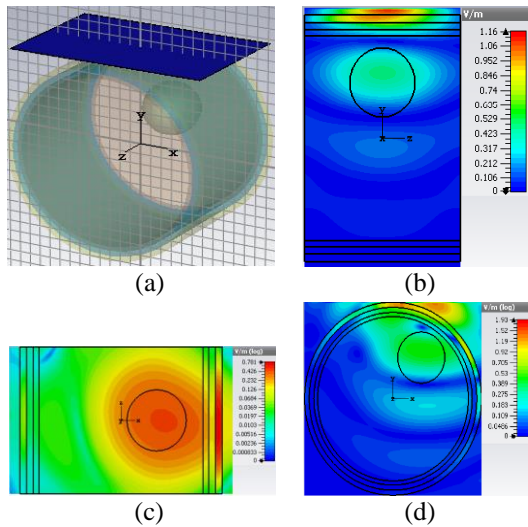
Fig. 25. Step 2 of TR energy locaization when (a) field from ymax plane is back propogated towards tumor. Energy localization is shown at tumor center in yz (b), xz (c), and xy (d) planes.

(a)   (b)

(c)   (d)
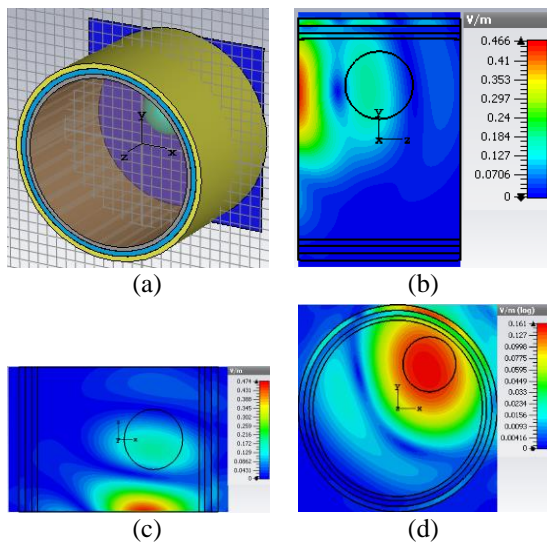
Fig. 26. Step 2 of TR energy locaization when (a) field from zmin plane is back propogated towards tumor. Energy localization is shown at tumor center in yz (b), xz (c), and xy (d) planes.

For the case when all fields at phantom surface is propagated backward to phantom in time reversal mode, the results are shown in Fig. 27. We now extend the results achieved in Fig. 27 to 3D visualization by considering two cases: narrowband and wideband excitation and investigating the results of TR energy localization for both cases. The results achieved for narrowband case is shown in Fig. 28, when all the four planes at phantom surface are excited with a single frequency carrier of 0.5, 0.75, 1 and 1.25 GHz respectively.

The figure reveals the fact that good penetration of EM signal is achieved for low frequencies while sharp focus is accomplished for high frequencies. It implies that adopting a wideband TR approach can deliver enhanced localization of energy. Results for the wideband TR energy localization are shown in Figs. 29 and 30.

For wideband operation, the results demonstrate the fact that increasing the number of frequency subcarriers can further improve energy localization. Heat generated, because of hotspots at the head interface, can be cooled down by the water coupling medium present between the applicator and the head.

(a)   (b)

(c)   (d)
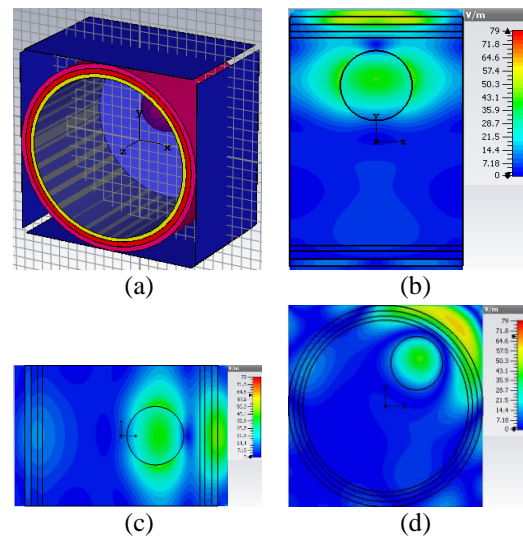
Fig. 27. Step 2 of TR energy locaization when (a) fields from four planes are back propogated towards tumor. Energy localization is shown at tumor center in yz (b), xz (c), and xy (d) planes.

(a)   (b)

(c)   (d)
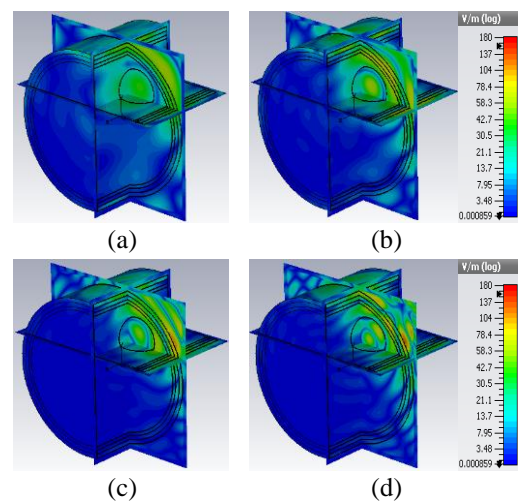
Fig. 28. 3D view of energy localization at tumor center for narrowband TR case when frequency is (a) 0.5 GHz, (b) 0.75 GHz, (c) 1 GHz, and (d) 1.25 GHz.
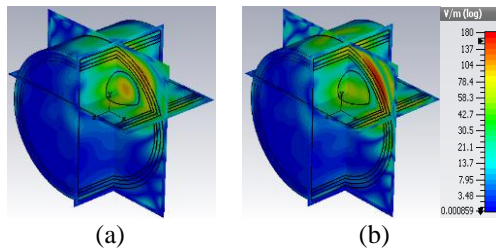
Fig. 29. 3D view of energy localization at tumor center for wideband TR case when (a) two frequency subcarriers 0.5 and 0.75 GHz are combined, and (b) three frequency subcarriers 0.5, 0.75, and 1 GHz are combined.
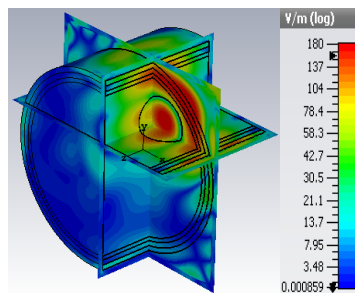
Fig. 30. 3D view of energy localization at tumor center for wideband TR case when four frequency subcarriers 0.5, 0.75, 1.0 and 1.25 GHz are combined.

IV. DISCUSSION AND CONCLUSIONS

A wideband, hyperthermia treatment system with the potential of enhancing energy localization is investigated and presented. The incorporated multi-channel configuration allows enhancement in energy focus. The proposed system is described in big data domain with the aim to identify system parameters to expedite energy accumulation process with precision and accuracy. A modular description of the proposed system is presented focusing on the functionality of each module under wideband excitation. With the adopted modular approach, the system provides an increase in the number of degrees of freedom to allow performance improvement. A robust wideband waveform shaping technique is proposed based on an optimization tool to maximize SAR values at the affected regions and minimize the values in healthy tissues. The achieved results show that wideband energy can be controlled to target deep-seated tumor effectively.

Clinical adaptation of such systems requires the development of real time optimization tool, which can be achieved using hardware acceleration and cluster computing techniques. Robust real time temperature monitoring is needed to provide a feedback mechanism to control energy excitation. With addressing of clinical challenges, the proposed system can improve the efficacy of hyperthermia treatment and enhance patient comfort and safety.

REFERENCES

[1] A. Shitzer and R. C. Eberhart, *Heat Transfer in Medicine and Biology: Analysis and Applications*. vol. 1, Plenum Press, 1985.

[2] H. Trefna and M. Persson, "Heating of deep seated tumours using microwaves radiation," in *ACES*, Verona, Italy, 2007.

[3] X. Wu, B. Liu, and B. Xu, "Theoretical evaluation of high frequency microwave ablation applied in cancer therapy," *Applied Thermal Engineering*, vol. 107, pp. 501-507, 2016.

[4] J. Mallorqui, A. Broquetas, L. Jofre, and A. Cardama, "Non-invasive active thermometry with a microwave tomographic scanner in hyperthermia treatments," *Applied Computational Electromagnetics Society (ACES) Journal*, vol. 7, pp. 121-127, 1992.

[5] M. M. Paulides, P. R. Stauffer, E. Neufeld, P. F. Maccarini, A. Kyriakou, R. A. Canters, C. J. Diederich, J. F. Bakker, and G. C. Van Rhoon, "Simulation techniques in hyperthermia treatment planning," *International Journal of Hyperthermia*, vol. 29, pp. 346-357, 2013.

[6] S. Fodeh and Q. Zeng, "Mining big data in biomedicine and health care," *Journal of Biomedical Informatics*, vol. 63, p. 400, 2016.

[7] K. J. Archer, K. Dobbin, S. Biswas, R. S. Day, D. C. Wheeler, and H. Wu, "Computer simulation, bioinformatics, and statistical analysis of cancer data and processes," *Cancer Informatics*, vol. 14, p. 247, 2015.

[8] J. Roski, G. W. Bo-Linn, and T. A. Andrews, "Creating value in health care through big data: Opportunities and policy implications," *Health Affairs*, vol. 33, pp. 1115-1122, 2014.

[9] P. Groves, B. Kayyali, D. Knott, and S. V. Kuiken, "*The 'big data' revolution in healthcare: Accelerating value and innovation*," Center for US Health System Reform, McKinsey & Company, 2013.

[10] M. Converse, E. J. Bond, B. Veen, and S. C. Hagness, "A computational study of ultra-wideband versus narrowband microwave hyperthermia for breast cancer treatment," *IEEE Transactions on Microwave Theory and Techniques*, vol. 54, pp. 2169-2180, 2006.

[11] M. N. Tabassum, I. Elshafiey, and M. Alam, "Enhanced noninvasive imaging system for dispersive highly coherent space," in *IEEE International Conference on Acoustics, Speech and Signal Processing (ICASSP)*, pp. 912-916, 2015.

[12] M. N. Tabassum, I. Elshafiey, and M. Alam, "Efficient techniques to enhance nearfield imaging of human head for anomaly detection," in *IEEE International Symposium Medical Measurements and Applications (MeMeA)*, pp. 565-569, 2015.

[13] M. N. Tabassum, I. Elshafiey, and M. Alam, "Compressed sensing based nearfield electromagnetic imaging," in *IEEE International Conference on Control System, Computing and Engineering (ICCSCE)*, pp. 571-575, 2014.

[14] M. Aldhaeebi and I. Elshafiey, "New antenna design for hyperthermia treatment of human head," in *IEEE 16th International Conference on Computer Modelling and Simulation, UKSim-AMSS*, 2014, pp. 96-100.

[15] A. Alkhaibari, A. F. Sheta, and I. Elshafiey, "Notched anti-podal Vivaldi antenna for biomedical applications," in *IEEE 7th International Conference on Modeling, Simulation, and Applied Optimization (ICMSAO)*, pp. 1-4, 2017.

[16] M. M. M. Ali, O. Haraz, I. Elshafiey, S. Alshebeili, and A.-R. Sebak, "Efficient single-band and dual-band antennas for microwave imaging and hyperthermia treatment of brain tumors," in *IEEE International Conference on Control System, Computing and Engineering (ICCSCE)*, pp. 597-600, 2014.

[17] G. Chakaravarthi and K. Arunachalam, "Design and characterisation of miniaturised cavity-backed patch antenna for microwave hyperthermia," *International Journal of Hyperthermia*, vol. 31, pp. 737-748, Mar. 10, 2015.

[18] S. Singh and S. P. Singh, "Theoretical and simulation studies on water-loaded metal diagonal horn antenna for hyperthermia application," *Progress In Electromagnetics Research C*, vol. 58, pp. 105-115, 2015.

[19] A. Mallahzadeh and A. Imani, "Modified double-ridged antenna for 2-18 GHz," *Applied Computational Electromagnetics Society (ACES) Journal*, vol. 25, p. 137, 2010.

[20] Q. Yang, X. Zhao, and Y. Zhang, "Electromagnetic analysis on propagation characteristics of CRLH waveguide loaded with double ridge corrugations," *Progress In Electromagnetics Research C*, vol. 75, pp. 1-11, 2017.

[21] M. Botello-Perez, H. Jardon-Aguilar, and I. G. Ruíz, "Design and simulation of a 1 to 14 GHz broadband electromagnetic compatibility DRGH antenna," in I*EEE 2nd International Conference on Electrical and Electronics Engineering*, pp. 118-121, 2005.

[22] S. I. Latif, D. Flores-Tapia, S. Pistorius, and L. Shafai, "Design and performance analysis of the miniaturised water-filled double-ridged horn antenna for active microwave imaging applications,"

[23] H. Y. Amin and B. Yarman, "Distributed wideband power amplifier using reactive coupled line feedback structure," in *IEEE 2nd International Conference on Knowledge-Based Engineering and Innovation (KBEI)*, pp. 91-94, 2015.

[24] S. Lin, M. Eron, and A. E. Fathy, "Development of ultra wideband, high efficiency, distributed power amplifiers using discrete GaN HEMTs," *IET Circuits, Devices & Systems*, vol. 3, pp. 135-142, 2009.

[25] A. Sayed, A. A. Tanany, and G. Boeck, "5W, 0.35-8 GHz linear power amplifier using GaN HEMT," in *European Microwave Conference (EuMC)*, pp. 488-491, 2009.

[26] Y. Ayasli, J. Vorhaus, R. Mozzi, and L. Reynolds, "Monolithic GaAs travelling-wave amplifier," *Electronics Letters*, vol. 17, p. 413, 1981.

[27] E. L. Ginzton, W. R. Hewlett, J. H. Jasberg, and J. D. Noe, "Distributed amplification," *Proceedings of the IRE*, vol. 36, pp. 956-969, 1948.

[28] Wolfspeed A Cree Company. 120 Watts RF GaN HEMT (CGH60120D). Available: http://www.wolfspeed. com/cgh60120d

[29] A. J. Fenn, V. Sathiaseelan, G. A. King, and P. R. Stauffer, "Improved localization of energy deposition in adaptive phased-array hyperthermia treatment of cancer," *Lincoln Laboratory Journa*l, vol. 9, 1996.

[30] C. M. Furse, "A survey of phased arrays for medical applications," *Applied Computational Electromagnetics Society (ACES) Journal*, vol. 21, pp. 365-379, 2006.

[31] S. Jacobsen and F. Melandsø, "The concept of using multifrequency energy transmission to reduce hot spots during deep-body hyperthermia," *Annals of Biomedical Engineering*, vol. 30, pp. 34-43, 2002.

[32] N. Nizam-Uddin and I. Elshafiey, "Transmission line approach for energy localization in wideband hyperthermia treatment system," in *IEEE 5th International Conference on Electronic Devices, Systems and Applications (ICEDSA)*, pp. 1-4, 2016.

[33] N. Nizam-Uddin and I. Elshafiey, "Enhanced energy localization with wideband hyperthermia treatment system," *Applied Computational Electromagnetics Society Journal*, vol. 32, pp. 389-396, 2017.

[34] P. Takook, H. D. Trefná, A. Fhager, and M. Persson, "Evaluation of the 3D time reversal method for hyperthermia treatment planning in head and neck tumors," in *9th European Conference on Antennas and Propagation (EuCAP)*, pp. 1-5, 2015.

[35] H. D. Trefná, J. Vrba, and M. Persson, "Time-

reversal focusing in microwave hyperthermia for deep-seated tumors," *Physics in Medicine and Biology*, vol. 55, p. 2167, 2010.

[36] F. Bardati, A. Borrani, A. Gerardino, and G. A. Lovisolo, "SAR optimization in a phased array radiofrequency hyperthermia system," *IEEE Transactions on Biomedical Engineering*, vol. 42, pp. 1201-1207, 1995.

[37] C. A. Liontas and P. Knott, "An alternating projections algorithm for optimizing electromagnetic fields in regional hyperthermia," in *IEEE 10th European Conference on Antennas and Propagation (EuCAP)*, pp. 1-5, 2016.

[38] R. M. C. Mestrom, J. P. van Engelen, M. C. van Beurden, M. M. Paulides, W. C. M. Numan, and A. G. Tijhuis, "A refined eigenvalue-based optimization technique for hyperthermia treatment planning," in *IEEE 8th European Conference on Antennas and Propagation (EuCAP)*, pp. 2010-2013, 2014.

[39] M. Aldhaeebi, M. Alzabidi, and I. Elshafiey, "Genetic algorithm optimization of SAR distribution in hyperthermia treatment of human head," in *IEEE 1st International Conference on Artificial Intelligence, Modelling and Simulation (AIMS)*, pp. 92-97, 2013.

[40] M. Aldhaeebi, M. Alzabidi, and I. Elshafiey, "Optimization of UWB antenna array for hyperthermia treatment of brain tumor," in *IEEE Saudi International Electronics, Communications and Photonics Conference (SIECPC)*, pp. 1-6, 2013.

[41] P. T. Nguyen, A. Abbosh, and S. Crozier, "Three-dimensional microwave hyperthermia for breast cancer treatment in a realistic environment using particle wwarm optimization," *IEEE Transactions on Biomedical Engineering*, 2016.

[42] N. Nizam-Uddin and I. Elshafiey, "Enhanced energy localization in hyperthermia treatment based on hybrid electromagnetic and ultrasonic system: Proof of concept with numerical simulations," *BioMed Research International*, vol. 2017, p. 18, 2017.

[43] R. Carminati, R. Pierrat, J. De Rosny, and M. Fink, "Theory of the time reversal cavity for electromagnetic fields," *Optics Letters*, vol. 32, pp. 3107-3109, 2007.

[44] D. Cassereau and M. Fink, "Time-reversal of ultrasonic fields. III. Theory of the closed time-reversal cavity," *IEEE Transactions on Ultrasonics, Ferroelectrics, and Frequency Control*, vol. 39, pp. 579-592, 1992.

[45] MathWorks. MATLAB: The Language of Technical Computing. Available: http://www.mathworks.com/

N. Nizam-Uddin received his B.S. degree in Electrical Engineering from NWFP University of Engineering & Technology Peshawar, Pakistan in 2002 and M.S. from Edinburgh Napier University, UK in 2005, majoring Communication. He is currently pursuing Ph.D. in Electrical Engineering at King Saud University. His research interest includes antenna theory, bio-electromagnetics, biomedical physics and microwave engineering.

Wazie M. Abdulkawi is currently pursuing Ph.D. at Electrical Engineering Department in King Saud University. He received M.S. in Electrical Engineering from King Saud University in 2013 and B.Sc. in Communication Engineering from Ibb University, Ibb, Yemen in 2007. His research interest includes antenna theory, RFID design, electromagnetics and microwave engineering.

Waqar Ahmad Malik received his B.S. degree in Electrical Engineering from NWFP University of Engineering & Technology Peshawar, Pakistan in 2004 and M.S. from The University of Hull, UK in 2006, majoring Radio Systems Engineering. He is currently pursuing Ph.D. in Electrical Engineering at King Saud University. His research interest includes optimization of microwave circuits, broadband matching circuits, and microwave amplifiers design.

Ibrahim Elshafiey received his B.S. degree in Communications and Electronics Engineering from Cairo University in 1985. He obtained his M.S. and Ph.D. degrees from Iowa State University in 1992 and 1994 respectively. He is currently a Professor in the Electrical Engineering Department at King Saud University. His research interests include computational electromagnetics, biomedical imaging, communication systems and non-destructive evaluation.

Abdel Fattah Sheta graduated from the Faculty of Engineering, Alexandria University, Egypt in 1985. He received the M.Sc. degree in Electrical Engineering from Cairo University, Egypt, in 1991. In 1996, he received the Ph.D. degree in Microwave Circuits Analysis and Design from ENST, Université de Bretagne Occidentale, France. He is a Full Professor at Electrical Engineering Department at King Saud University. His current research interests include reconfigurable RF system, UWB systems, microstrip antennas, antennas for hyperthermia applications, microstrip filters, planar and uniplanar MIC's and MMIC's, and power amplifiers.

Parallel Higher-Order Method of Moments with Efficient Out-of-GPU Memory Schemes for Solving Electromagnetic Problems

Zhongchao Lin, Yan Chen, Xunwang Zhao*, Daniel Garcia-Donoro, Yu Zhang, and Huanhuan Zhang

School of Electronic Engineering
Xidian University, Xi'an, Shaanxi 710071, China
xwzhao@mail.xidian.edu.cn

Abstract ─ A distributed parallel Higher-order Method of Moments (HoMoM) for solving electromagnetic problems on CPU/GPU clusters is presented. An MPI/OpenMP/CUDA parallel framework based on the GPU context technique is designed. An out-of-GPU memory scheme is employed to break the limitation of the GPU memory. To improve the performance of data transferring between main memory and GPU memory, an overlapping scheme based on asynchronous technique and CUDA streams is adopted. In comparison with the parallel CPU version only, numerical results including a metallic airplane and an airborne array with dielectric structures demonstrate the high performance of the proposed method.

Index Terms ─ GPU-based HoMoM, GPU context, out-of-GPU memory, overlapping, parallel framework.

I. INTRODUCTION

In the field of computational electromagnetics (CEM), the method of moments (MoM) is widely used for solving electromagnetic radiation and scattering problems [1]. It is well known that direct lower/upper (LU) decomposition solvers and iterative solvers are the most common ways to solve the matrix equations of MoM. In order to avoid slow convergence rates or divergence issues of iterative solvers, direct LU decomposition algorithms are utilized as matrix equation solvers. Unfortunately, with the electrical size of problems increasing, the solution time of LU solver increases rapidly due to the computational complexity of $O(N^3)$, where N is the number of unknowns. With the rapid development in computer hardware capabilities, parallel computing technique has been an efficiently approach for solving extremely complicated engineering problems. In recent years, the Graphics Processing Unit (GPU) has become a prevalent commodity in parallel computing due to its powerful computational capability.

Since the Nvidia GPUs programmed through the CUDA API was introduced in 2006 [2], the GPUs provide a very attractive, low-cost hardware platform for

CEM. The application of GPU in the area of CEM started in the finite-difference time-domain method (FDTD). In [3-5], the GPU-accelerated FDTD was implemented to deal with the 2D and 3D simulation problems, a good acceleration ratio can be obtained. However, MoM has received relatively little attention in the GPU context. The application of GPU acceleration using CUDA to MoM is presented in [6-8], and an iterative solution scheme for the linear system was adopted rather than a direct solving scheme. In [9-11], a GPU-accelerated implementation using Nvidia CUDA for the matrix assembly of the MoM using Rao-Wilton-Glisson (RWG) basis functions [12] was presented. However, the utilization of MAGMA library [13] prohibits its application on a distributed memory platform. In [14], an out-of-core scalable approach that can break the restrictions of GPU memory was introduced, but its performance get worse without the optimization of data-movement between GPU and CPU. In [15], an approach integrating the CUDA computing directly into the ScaLAPACK framework was presented and good speedup was obtained. However, the scale of matrix can be factorized is limited by the GPU memory. In very recent papers by Topa [16] and Mu [17], some efficient out-of-core techniques of GPU-accelerated MoM were presented, but these work are also developed on a single CPU/GPU computing platform.

Under this situation, a hybrid parallel CPU/GPU version of a higher-order method of moments (HoMoM) is presented in this paper. The proposed technique makes use of procedures with efficient out-of-GPU memory schemes and able to run on distributed memory systems with multiple CPU/GPU computing nodes. In the particular case of this paper, the GPU is used to accelerate the calculations of the LU decomposition during the matrix factorization step. The scattering of an airplane and the radiation of an airborne array are simulated to demonstrate the acceleration performance of the proposed algorithm. The implementation of the proposed hybrid CPU/GPU technique is summarized as: 1) an efficient MPI/OpenMP/CUDA parallel framework based on GPU

context technique is adopted to implement the hybrid parallel CPU/GPU procedures; 2) an efficient out-of-GPU memory scheme is utilized to break the limitation of GPU memory, thus offering a possibility of handling complex EM problems; and 3) the asynchronous data transfer and CUDA streams techniques are used to overlap the data-movement and computation, which can effectively avoid the time of data transfer between CPU and GPU. Details about all these procedures are given in Section III.

II. PARALLEL HIGHER-ORDER METHOD OF MOMENTS

A brief review regarding the basic principles of the integral equation theory, higher-order basis functions and the LU decomposition algorithm is given in this section. Readers are referred to [1] for an in-depth discussion of the theory.

A. Integral equations

The electromagnetic theory employed in this paper is based on the so-called Surface Integral Equations (SIEs) [18] in the frequency domain for equivalent electric and magnetic currents over dielectric boundary surfaces and electric currents over Perfect Electric Conductors (PECs). The set of integral equations obtained are solved by using MoM, and specifically using the Galerkin's method. The code is able to handle inhomogeneous dielectrics categorized by a combination of various homogeneous dielectrics. Therefore, any composite metallic and dielectric structure can be represented as an electromagnetic system consisting of a finite number of finite-size linear, homogeneous and isotropic regions situated in an unbounded linear, homogeneous and isotropic environment.

For general models, the integral equation employed by the code is the well-known Poggio-Miller-Chang-Harrington-Wu (PMCHW) formulation [1, 19]. However, when one of the boundary surfaces between two different regions is PEC, the magnetic currents are equal to zero at the boundary surface and that equation degenerates into the electric field integral equation (EFIE) [20].

B. Higher-order basis functions

In order to approximate the solution to the aforementioned integral equation, higher-order polynomials over wires and quadrilateral patches are used as basis functions over relatively large subdomains [1]. Typically, the number of unknowns for the HOBs is reduced by a factor of 10 compared with that for RWGs, and thus the use of HOBs significantly reduces the computational complexity and memory requirement.

There are also some other advantages in using the polynomial basis functions. For example, the intermediate results obtained in evaluating the elements of the impedance matrix for lower-order can be used in the computation of the elements of the impedance matrix when using higher-order polynomials. In addition, Green's function for each pair of integration points belonging to two patches is only evaluated once. These advantages improve the efficiency of the matrix filling for the HOBs presenting a straightforward implementation.

C. LU decomposition algorithm

Once the system of equations is obtained, the code makes use of the LU decomposition algorithm to solve the problem and obtain the solution. Specifically, the code uses the LU right-looking algorithm. This decomposition technique mainly includes the pivoting step, the panel column factorization, the panel row update and, finally, the trailing submatrix update. Given deeper details about the code involved on the LU decomposition, the routines pzgetrf2, pztrsm and pzgemm are the ones responsible of each of the steps. It is worth noting that the update operations contribute more than 80% of the computation time for a large scale dense complex matrix.
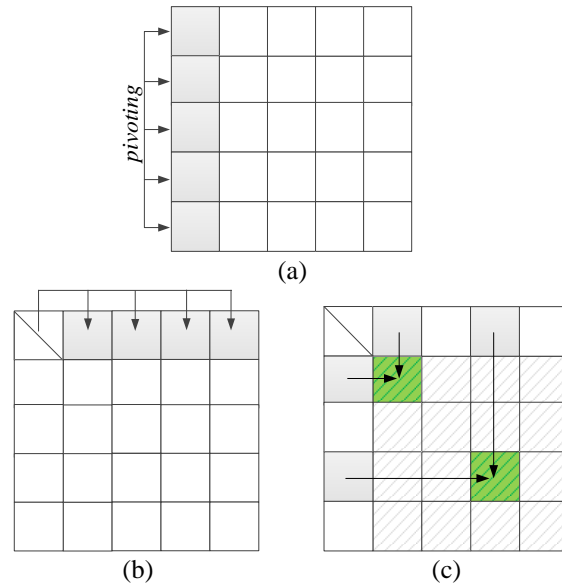
Fig. 1. Processes of LU Decomposition in ScaLAPACK or Intel MKL: (a) panel column factorization, (b) panel row update, and (c) trailing update.

Figure 1 shows a summary of the algorithm where the arrows indicate the data dependency on each step. In this way, for example, during the pivoting step, all the coefficients of the panel column have to be known by all the MPI processes involved on the decomposition. Then, network communication is required between these processes degrading the parallel performance. This behavior can be extrapolated to the rest decomposition steps which are repeatedly executed until the factorization is completed.

III. HYBRID PARALLEL CPU/GPU IMPLEMENTATION

Details about the implementation of the proposed hybrid parallel CPU/GPU technique are given in this section. The parallel implementation of the method is described next meanwhile the out-of-GPU memory scheme is detailed later. It is worth to mention that, only using an MPI-based multi-node processing is not enough to achieve good parallel performance. It is also required an optimization on the data-movement between GPU and CPU memory. All these details are described in the next subsections.

A. Parallel framework based on GPU context

As any other computational technique running on distributed memory CPU/GPU clusters, the proposed GPU HoMoM implementation makes use of MPI to perform the internode communication.

The simplest parallel framework one can consider is to assign one CPU core and one GPU card to each MPI process. However, typically, the number of GPU cards is usually less than that of CPU cores available in the system. Under this scenario, there is an unmatched situation between MPI processes and GPU cards, which would lead to an unbalanced computing power in the different MPI processes. In order to alleviate this issue, different techniques reduce the number of MPI processes of each node to match with the number of GPU cards, meanwhile, multi-threads techniques (*i.e.*, OpenMP) are adopted to make full use of the CPU cores of each node. This improved scheme assigns multiple CPU cores and one GPU card to each MPI process, ensuring a good balance between the computes nodes. However, due to the low number of MPI processes involved on the execution (typically, CPU/GPU cluster has only one GPU card per compute node), the amount of communication needed increases rapidly reducing the performances of the implementation. Therefore, the implementation of an efficient parallel framework with good balance and performance is not straightforward. Fortunately, the context technique of CUDA makes this possible.

Based on the CUDA context technique, multiple MPI processes can use a GPU card simultaneously. Each MPI process opens a CUDA context on the GPU card, and the resources of the GPU card are averagely distributed to each MPI process. It is equivalent to partition one GPU card into several virtual GPU cards. Each MPI process can use its own virtual GPU resources to accelerate the computing tasks. Note that the OpenMP technique can also be adopted in this framework and the communication between CPU cores and GPU context is implemented by PCI-E system bus. The efficient parallel framework based on GPU context is shown in Fig. 2.

It is worth noting that, in systems where only few CPU cores are available per node, the number of virtual GPU card can be equal to the number of CPU cores. In this case, the OpenMP technique is not required to provide a good power balance. However, when the number of CPU cores available per node is larger, the GPU context technique will consume a large amount of GPU resources. Thus, the total performance of the implementation will be drastically degraded. Then, the number of virtual GPU card must be reduced and the OpenMPI technique used.
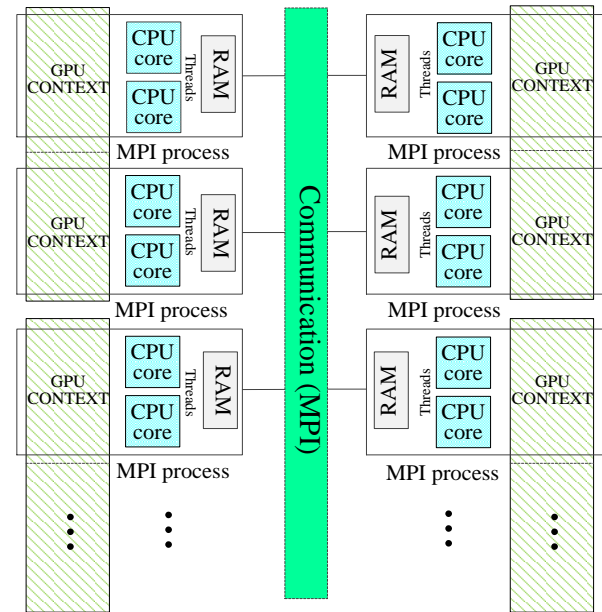
Fig. 2. MPI/OpenMP/CUDA parallel framework base on GPU context technique.

B. Out-of-GPU memory scheme

As mentioned previously, the trailing update operation in the LU decomposition algorithm contributes in more than 80% of the computation time for a large scale dense complex matrix. The, it seems appropriate to accelerate the pzgemm routine employing the GPU power. In this phase, the computing task of each process is reduced to perform matrix multiplication in the form: C=C-AB (see Fig. 3 (a)). The matrix C is located on the process that executes the matrix multiplication, while the matrices A and B are obtained through MPI communication.

The data required for GPU to complete certain compute tasks should be uploaded to it, so the size of the uploaded data has influence on the performances. Thus, in order to accelerate the whole matrix multiplication, the matrices B and C are divided into two parts C_1 and C_2, and B_1 and B_2, respectively. Then, the operation $C_1=C_1-AB_1$ is performed in the CPU cores, meanwhile the operation $C_2=C_2-AB_2$ is performed in GPU cards. Fig. 3 (b) illustrates this process.

Note that when matrices B_2 and C_2 are too large to fit in GPU memory, the previous scheme must be

improved and this memory limitation has to be broken. Thus, an out-of-GPU memory scheme is implemented where matrices B_2 and C_2 are split into smaller matrices that can fit into the GPU memory. Then, through multiple data transfer and calculation, the process of trailing update is completed. Figure 3 (c) shows a sketch of this out-of-GPU scheme.
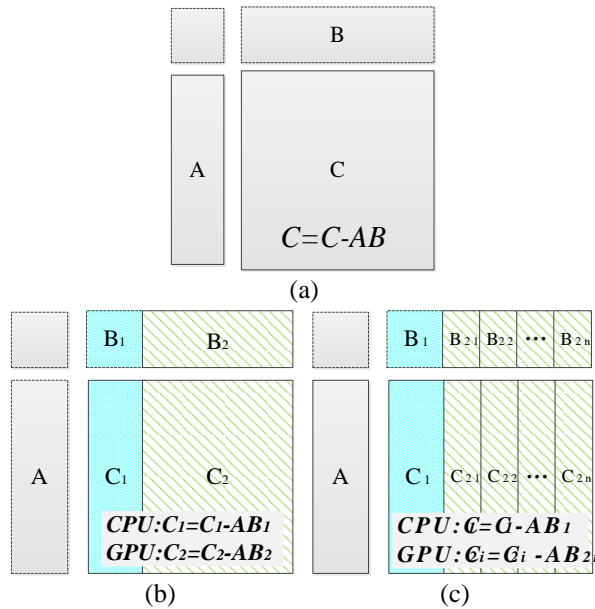
Fig. 3. The out-of-GPU memory scheme.

C. Overlapping scheme

The previous out-of-GPU memory scheme overcomes the restriction of GPU memory, offering the possibility of handling complex electromagnetics (EM) problems. However, the data transfer between CPU and GPU is a time consuming process. Fortunately, the asynchronous technique and CUDA streams can be used to overlap it with the calculation.

Each MPI process opens several CUDA streams [21] on the GPU context (see Fig. 4). The CUDA stream are similar to a CPU pipeline operation queue. Then, matrices B_2 and C_2 are split into smaller matrices according to Fig. 3 (c). These smaller matrices will be transferred to the GPU memory thought different CUDA streams using the CUDA asynchronous data transfer function. After the GPU calculation is completed, the results will be transferred back to RAM in the same way. Note that this transfer process must be executed when the number of CUDA streams is less than the number of smaller matrices.

This overlapping scheme consists of three different operations: data transfer from CPU to GPU, GPU calculation and data transfer from GPU to CPU, these operations are performed by different hardware units. To control the time sequence, the operations in the same CUDA stream must be performed once at a time. However, different operation in different CUDA streams can be done in parallel. Note that the same operation cannot be executed at the same time in two different CUDA streams since they are performed by the same hardware unit.
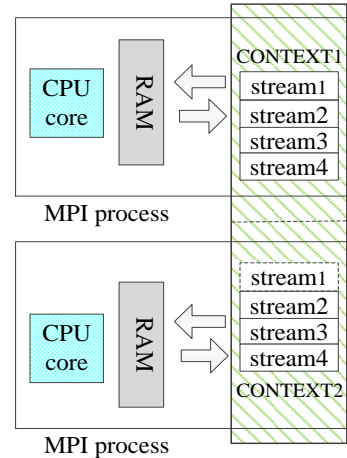
Fig. 4. MPI process opens CUDA streams on GPU context.

For example, in Fig. 5, we have four CUDA streams and the three operation marked with different colors. When one of the streams is involved in data transferring, another can be used for calculations at the same time. The data transfer and calculation of different CUDA streams can be executed in parallel, so the communication time is hidden. Moreover, the only work that CPU does is to start the GPU kernel function. Then CPU will do its own work without waiting for the ending of the GPU computing.
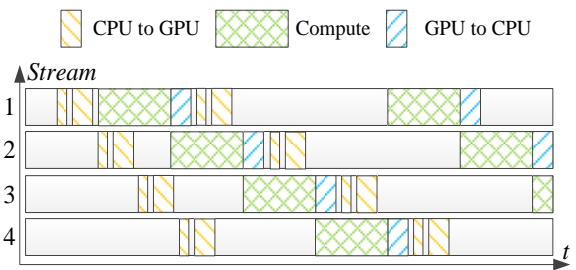
Fig. 5. Overlapping scheme of communication and computation on GPU context.

IV. NUMERICAL RESULTS

In order to demonstrate the correctness and the parallel performance of the proposed hybrid parallel CPU/GPU technique different benchmarks are run. The first test consists of the scattering analysis of PEC sphere used to check the correctness of the implementation.

The second test consists of the analysis of a perfectly conducting cylinder. This test is used to check the parallel performance of the method. Finally, some analysis of a real airplanes and antennas are presented to demonstrate that the method can solve real electromagnetic challenging problems.

The computational platform used for these benchmarks is a high performance GPU cluster with seven computing nodes. Each computing node has two Intel Xeon two 12-core Intel Xeon E5-2692v2 2.2 GHz EM64T processors (12×256 KB L2 Cache and 30 MB L3 Cache), one NVIDIA Tesla K20c GPU card (4.6 GB memory of available) and 64 GB RAM. The nodes are connected with Infiniband switches. The code is developed using the FORTRAN/C/C++ hybrid languages based on MPI.

A. Correctness of the implementation

To validate the accuracy and efficiency of the proposed hybrid parallel CPU/GPU technique the analysis of a PEC sphere with radius of 10 λ is performed. The excitation is a z-axis polarized plane wave propagating along the x-axis direction. The sphere model (see Fig. 6) is discretized into 3258 bilinear patches given a total number of unknowns of 27,528. The bistatic RCS results are given in Fig. 7. A comparison with the analytic Mie solution is performed showing an excellent agreement.

B. Performance testing

The second test consists of the analysis of a perfectly conducting cylinder that is infinitely long along one direction and is illuminated by a transverse magnetic (TM)-polarized plane wave. This benchmark is used to check the performance of the method under different configurations: (1) a single node with 4 MPI processes (each MPI process opens 6 OpenMP threads) and one GPU and (2) two nodes with 8 MPI processes (each MPI process opens 6 OpenMP threads) and two GPUs.

Figure 8 shows the benchmarking results for double precision complex matrices ranging from 1024×1024 to 56320×56320 elements in size. The K20c GPU with 4.6 GB of memory is limited to about 17000 unknowns. Figure 9 shows the benchmarking results for double precision complex matrices ranging from 1024×1024 to 78848×78848 elements in size. The two K20c GPUs with 2×4.6 GB of memory is limited to about 24000 unknowns.
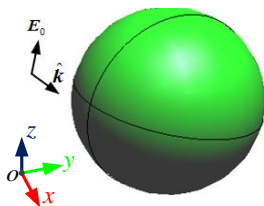
Fig. 6. The model of a PEC sphere.
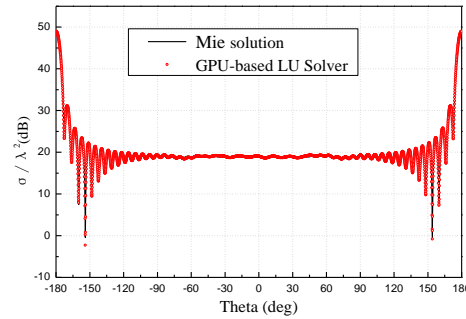
Fig. 7. RCS results in *xoz* plane from the PEC sphere with radius of 10 λ.
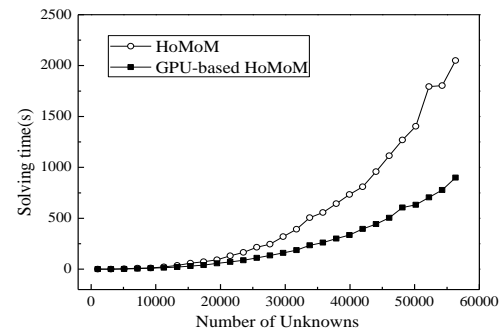
Fig. 8. Performance against matrix size for two versions of LU decomposition using a single node.
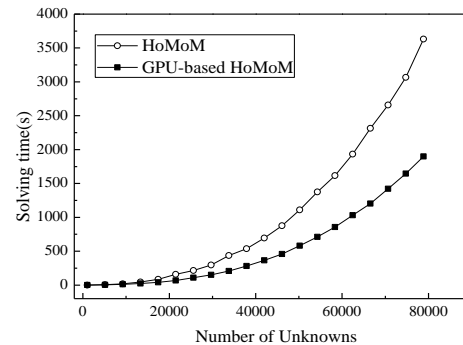
Fig. 9. Performance against matrix size for two versions of LU decomposition using two nodes.

A comparison between the results given by the proposed hybrid parallel CPU/GPU technique and the CPU version only are given in both figures. On a single node, the computing speed of the 24 CPU cores with a single GPU is about 2.3 times than that obtained by using 24 CPU cores alone. On two nodes configuration, the computing speed of the 48 CPU cores with two GPUs is about twice of that from using 48 CPU cores alone. The results show that the proposed technique can save at least 50% of computation time on both distributed and shared memory systems.

C. Performance analysis for metallic structures

This section contains the scattering results of a real airplane. This benchmark demonstrates that the proposed method can solve electromagnetic challenging problem as well. The airplane model is shown in Fig. 10. The airplane is 30.6 m long, 29.0 m wide and 11.8 m high. The bistatic RCS of airplane is simulated at the frequency 440 MHz. The excitation is a z-axis polarized plane wave propagating along the negative x-axis direction. The airplane is discretized into 16,980 bilinear patches, and the total number of unknowns is 135,501.
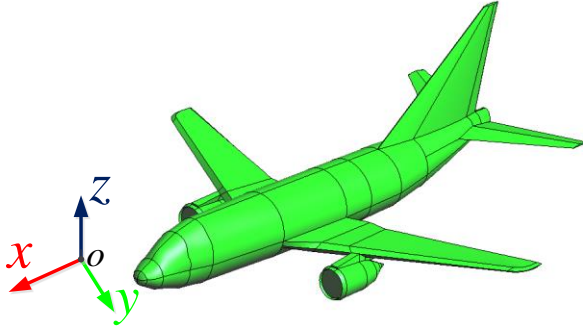
Fig. 10. The model of an airplane.

The two-dimensional (2D) RCS results are shown in Fig. 11. The 2D results computed by the parallel CPU version only are also given for comparison. Note that θ coordinate is measured from xoy plane to z axis and φ coordinate is measured from $+x$ axis to y axis in this paper. The computation parameters are listed in Table 1. For this simulation, seven compute node of the described computational platform were used.

Table 1: Computational parameters for the airplane

Computational Resources	Solving Time (s)	Speedup
24 CPU cores×7	2499.298	1
(24 CPU cores and 1 GPUs) ×7	1089.444	2.294

From the comparisons, one can see that the results of both CPU version only and the proposed hybrid CPU/ GPU technique present a very good agreement. The required memory of this simulation is about 274 GB when the memory provided by the GPUs is less than 34 GB. Thus, the proposed algorithm breaks the limitation of the memory of the GPUs as it was described previously. Regarding, the speedup between both codes, the hybrid CPU/GPU code is over 2 times faster, while a speedup of over 380 times is achieved compared to the sequential CPU version only.

(a)

(b)
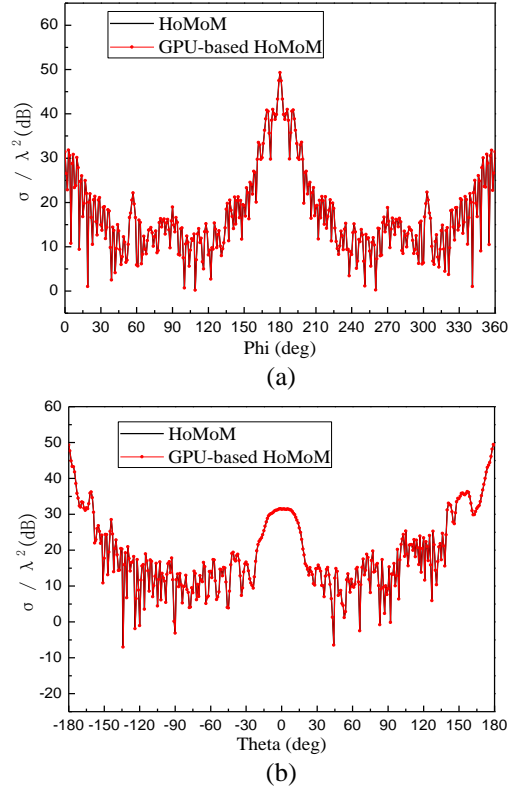
Fig. 11. 2D RCS of the airplane: (a) xoy plane and (b) xoz plane.

D. Performance analysis for composite metallic and dielectric structures

Finally, the radiation pattern of an airborne array is presented. A microstrip array (20x4) is printed on a substrate $\varepsilon_r = 4.5$ and $\mu_r = 1.0$ and is housed in a 5.27 m by 0.9524 m by 0.018 m cavity in a ground plane, as shown in Fig. 12 (a). The feeding line for each patch has the radius of 1.8 mm. The dimensions of each patch element are 0.2056 m by 0.1548 m, and the gaps between any two neighboring elements are 0.0579 m by 0.0833 m along the length and width directions. The microstrip array is installed 4.0 m above the airplane, as shown in Fig. 12, and the distance between the center of the array and the nose of the airplane is 15.4 m. A -30 dB Taylor amplitude distribution is utilized in the array feed along the y-direction and the mainlobe is also directed towards the tail. The operation frequency of the array is 440 MHz. The airborne model is discretized into 21,602 bilinear patches, and the total number of unknowns is 155,494.

The 2D and 3D gain patterns obtained by the proposed method are shown in Fig. 13. The 2D gain patterns computed by the CPU version only are also given for comparison where a very good agreement is clearly seen. In addition, the computation parameters

are listed in Table 2.

(a)

(b)
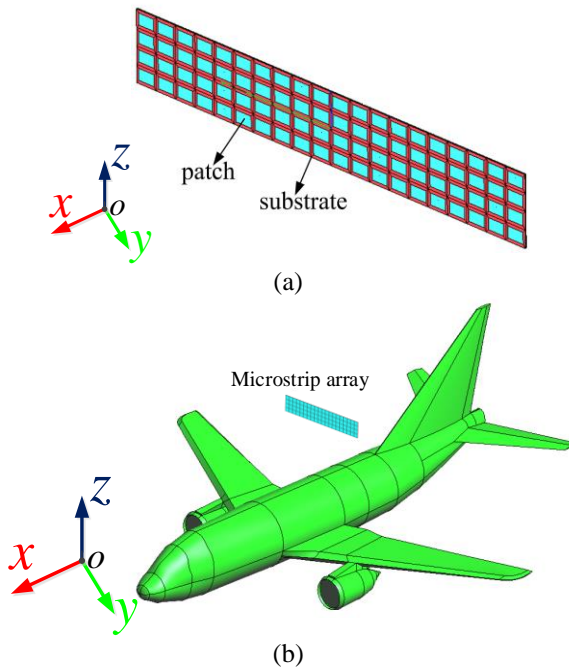
Fig. 12. The airborne array model: (a) the microstrip patch array with 20×4 elements, and (b) the airborne microstrip patch array.

(a)

(b)

(c)
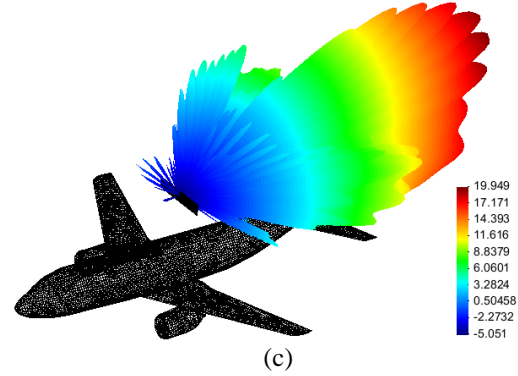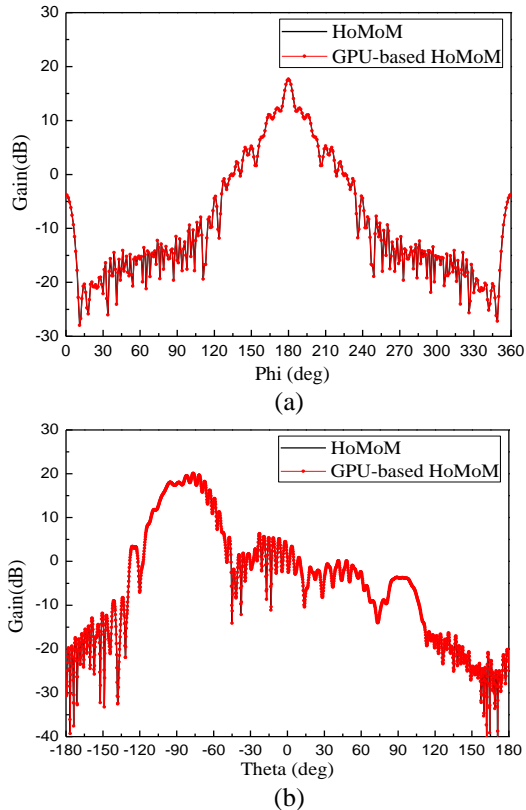
Fig. 13. 2D and 3D gain patterns of the airborne array antenna: (a) *xoy* plane, (b) *xoz* plane, and (c) 3D pattern.

Table 2: Computational parameters for the airborne array

Computational Resources	Solving Time (s)	Speedup
24 CPU cores×7	3749.444	1
(24 CPU cores and 1 GPUs) ×7	1577.735	2.376

In this simulation, we can also see that the limitation of the memory of the GPUs is broken. The required memory of the airborne array (about 360 GB) is quite larger than the available memory of the GPUs (about 34 GB). Moreover, a speedup of over 2 times is achieved compared to the parallel CPU version only, while compared with the sequential HoMoM version, the speedup of the hybrid CPU/GPU technique is about 400 times.

V. CONCLUSION

In this paper, a hybrid parallel CPU/GPU HoMoM method is presented and used to simulate the scattering of an airplane and the radiation pattern of an airborne array. The hybrid parallel CPU/GPU procedure is proved to have a good speedup in the same degree of accuracy compared with the parallel HoMoM using the Intel MKL LU solver. The MPI/OpenMP/CUDA parallel framework base on GPU context technique can support a large scale of parallelism, which can fully exploit the computing power of current distributed CPU/GPU clusters. The out-of-GPU memory scheme overcomes the GPU memory limitation is to utilize both the CPU and GPU memory, which offering a possibility of handling complex electrically large objects.

REFERENCES

[1] Y. Zhang and T. K. Sarkar, *Parallel Solution of Integral Equation Based EM Problems in the Frequency Domain*. Hoboken, NJ: Wiley, 2009.

[2] "NVIDIA GeForce 8800 GPU architecture overview," NVIDIA Corporation, Santa Clara, CA, Tech. Brief TB-02787-001_v0.9, Nov. 2006.

[3] S. E. Krakiwsky, L. E. Turner, and M. M. M. Okoniewski, "Acceleration of finite-difference time-domain (FDTD) using graphics processor units (GPU)," *in IEEE MTT-S Int. Microwave Symp. Digest*, pp. 1033-1036, 2004.

[4] M. J. Inman and A. Z. Elsherbeni, "Programming video cards for computational electromagnetics applications," *IEEE Antennas Propag. Mag.*, vol. 47, pp. 71-78, 2005.

[5] M. J. Inman, A. Z. Elsherbeni, J. G. Maloney, and B. N. Baker, "Practical implementation of a CPML absorbing boundary for GPU accelerated FDTD technique," *ACES Journal*, vol. 23, no. 1, pp. 16-22, Dec. 2008.

[6] T. Takahashi and T. Hamada, "GPU-accelerated boundary element method for Helmholtz' equation in three dimensions," *International Journal for Numerical Methods in Engineering*, vol. 80, pp. 1295-1321, 2009.

[7] S. Peng and Z. Nie, "Acceleration of the method of moments calculations by using graphics processing units," *IEEE Trans. Antennas Propag.*, vol. 56, no. 7, pp. 2130-2133, May 2008.

[8] M. J. Inman, A. Z. Elsherbeni, and C. J. Reddy, "CUDA based LU decomposition solvers for CEM applications," *ACES Journal*, vol. 25, no. 4, pp. 339-347, Dec. 2010.

[9] E. Lezar and D. Davidson, "GPU acceleration of method of moments matrix assembly using Rao-Wilton-Glisson basis functions," *in Proc. ICEIE*, Kyoto, Japan, pp. V1-56-V1-60, 2010.

[10] E. Lezar and D. Davidson, "GPU-accelerated method of moments by example: Monostatic scattering," *IEEE Antennas Propag. Mag.*, vol. 52, no. 6, pp. 120-135, Dec. 2010.

[11] E. Lezar and D. B. Davidson, "GPU-based LU decomposition for large method of moments problems," *Electronics Letters*, vol. 46, no. 17, pp. 1194-1196, 2010.

[12] S. M. Rao, D. R. Wilton, and A. W. Glisson, "Electromagnetic scattering by surfaces of arbitrary shape," *IEEE Trans. Antennas Propag.*, vol. AP-30, no. 3, pp. 409-418, May 1982.

[13] Innovative Computing Laboratory, University Tennessee, Knoxville, "MAGMA: Matrix Algebra on GPU and Multicore Architectures,"2009. [Online]. Available: http://icl.cs.utk.edu/magma/index.html

[14] E. DAzevedo and JC Hill, "Parallel LU factorization on GPU cluster," *Procedia Computer Science*, 9, pp. 67-75, 2012.

[15] P. Du, S. Tomov, and J. Dongarra, "Providing GPU Capability to LU and QR within the ScaLAPACK Framework," 2012. [Online] Available: http://www.netlib.org/lapack/lawnspdf/ lawn272.pdf

[16] T. Topa, "Efficient out-of-GPU memory strategies for solving matrix equation generated by method of moments," *Electronics Letters*, vol. 51, no. 19, pp. 1542-1544, 2015.

[17] X. Mu, H.-X. Zhou, K. Chen, and W. Hong, "Higher order method of moments with a parallel out-of-core LU solver on GPU/CPU platform," *IEEE Trans. Antennas Propag.*, vol. 62, no. 11, pp. 5634-5646, 2014.

[18] P. Ylä-Oijala, M. Taskinen, and S. Järvenpää, "Analysis of surface integral equations in electromagnetic scattering and radiation problems," *Engineering Analysis with Boundary Elements*, vol. 32, no. 3, pp. 196-209, 2008.

[19] R. F. Harrington, "Boundary integral formulations for homogenous material bodies," *Journal of Electromagnetic Waves and Applications*, vol. 3, no. 1, pp. 1-15, 1989.

[20] John L. Volakis and Kubilay Sertel, *Integral Equation Methods for Electromagnetics*. Raleigh, NC: SciTech Pub., 2012.

[21] NVIDIA Corporation, "CUDA API REFERENCE MANUAL Version 5.0", Oct. 2012.

Circularly Polarized Aperture Coupled Zeroth Order Resonance Antenna for mm-Wave Applications

Saeid Karamzadeh [1,2], Vahid Rafiei [1], and Hasan Saygin [2]

[1] Department of Electric and Electronics Engineering, Istanbul Aydin University, Istanbul, Turkey
karamzadeh@itu.edu.tr, vahidrafiei@aydin.edu.tr

[2] Application & Research Center for Advanced Studies, Istanbul Aydin University, Istanbul, Turkey
hasansaygin@aydin.edu.tr

Abstract ─ In this work, a millimetre-wave aperture–coupled antenna was offered by mode synthesis. In order to increase half power beam width (HPBW), the present study united a TM_{010} mode, which was generated by aperture slot of substrate integrated waveguide (SIW), and a zeroth-order resonance (ZOR) mode of a metamaterial polarizer mushroom. The results were confirmed by an equivalent circuit and a full wave simulator. Moreover, to prevent mm-wave fed loss, the study made use of a SIW feed with a slot which reduced the interference between a feed and a mushroom metamaterial structure as a polarizer antenna. The proposed antenna was fabricated and measured at 35 GHz. The simulated results roughly agreed with the measured results.

Index Terms ─ Aperture–coupled antenna, Substrate Integrated Waveguide (SIW), Zeroth-Order Resonance (ZOR).

I. INTRODUCTION

In recent years, having a high data rate and a small size, millimetre-wave systems have provided access to less-crowded spectrums. They are a good alternative to be considered for future telecommunication systems. To enhance the accessibility and capability of mm-wave systems, the use of antennas with broad bands and high gain has become widespread [1–8]. Two main issues in designing mm-wave antenna must be considered. The first problem in designing an antenna in mm-wave application is high atmospheric debilitation, which reduces communication range [1–8]. Thus, the antenna in mm-wave application must follow either beam forming or broadside patterns. As is well known, designing beam forming feed network antenna is difficult and the risk of losing in the feed network is very high. On the other hand, despite that ordinary patch antennas follow a broadside pattern, their large size and low gain are important problems of these antennas. Second problem in designing mm-wave antennas is the high loss of feed network. Although, using a substrate with high relative permittivity can compensate microstrip radiation loss, it cannot compensate for higher losses. Additionally, making the overall system more resistant in the case of multipath propagation is another problem which must be considered in mm-wave application. Hitherto, to overcome each of the mentioned problems, previous studies have reported different methods. In [2], for example, an E-shape patch antenna was proposed for millimetre wave frequencies. This technique, though causing the bandwidth and broadside pattern to increase, has lower gain. On the other hand, the microstrip feed line and patch created in same layer lead to loss increase. Combining an aperture–coupled and a zeroth-order resonance, [3] reported a mode of a metamaterial antenna at the millimetre-wave frequency band that could almost solve the problem faced in [2]. However, there are still the problems of multipath effect and radiation loss of microstrip line. [4] employed the metallic waveguide fed microstrip array to alleviate the radiation loss. The substrate integrated waveguide (SIW) fed planar microstrip array has been introduced in [5] to overcome the limitations of conventional metallic waveguide, where a higher radiation efficiency was obtained. Nevertheless, the feed network and patch array were integrated onto the same layer; hence, the spurious radiation from the feed network was not completely suppressed [6]. The present study attempted to solve the mentioned problems by offering a solution for each. In order to have a broad side pattern with a high gain and low loss feed network, the study used a SIW cavity backed slot antenna which combining novel circularly polarizer mushroom and parasitic ring, produced a zeroth order resonance (ZOR) that was capable of increasing the broadside and gain even at a small size.

II. ANTENNA STRUCTURE

Figure 1 displays the geometry of the proposed CP SIW ZOR antenna. The antenna consists of two substrates isolated by a ground with an aperture. The top substrate is RT/Duroid 5880 with relative permittivity of ε_r=2.2,

loss tangent of tanδ=0.0009, and thickness of h_1=0.508 mm. It contains the ZOR polarizer radiating element, while the other substrate, with the SIW fed line, is Rogers 4003 (ε_r=3.55, tanδ=0.002). The polarizer includes a mushroom antenna and a parasitic ring patch, the two opposite corners of each are etched by S_1 and S_2, respectively, to attain CP feature. The antenna produces two modes of TM_{01} and TM_{10} with a directional radiation pattern leading to the emergence of CP characteristic, and a ZOR mode with an omnidirectional radiation pattern, respectively. The optimal dimensions of the antenna are as follows: W_p=2 mm, W_h=1.3 mm, radius of the via V_r=0.1 mm, L_a=2 mm, and W_a=0.1 mm. The parameters were derived from full wave simulation (ANSYS HFSS). The size of the patch antenna (W_p) and that of the etched hole (W_h) are determined to set the resonance frequency at 35 GHz, while the size of the aperture (L_a) and the radius of via (V_r) are set to optimize the radiation efficiency of the mushroom antenna [3].

(a)

(b)
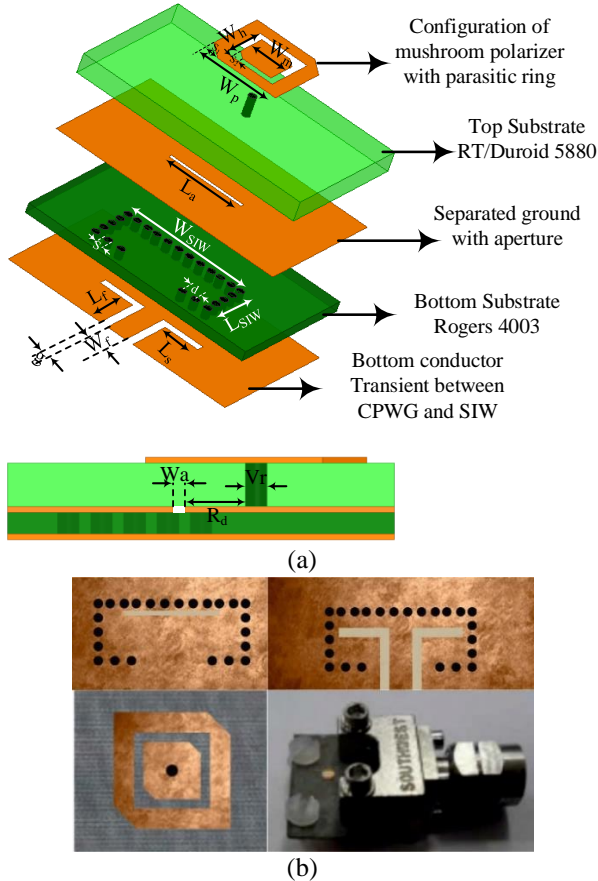
Fig. 1. (a) Configuration of antenna structure, and (b) fabricated photo.

III. EQUIVALENT CIRCUIT

The equivalent circuit of the antenna is shown in Fig. 2. It consists of an aperture (C_1, C_a, L_a, and R_a), a parasitic ring patch antenna (C_p, L_p, and R_p), and a mushroom (C_R, L_L, and R_m). Γ_m, Γ_p, and Γ_{pm} are the coupling coefficients between an aperture and a mushroom, an aperture and a parasitic ring patch, and a mushroom and a patch, respectively. The equivalent circuit is calculated as follows in Ref. [1-4].

The first step is to model the mushroom with a RLC network. The formulas to represent a resonator as a parallel resonant circuit can be found in [1-4] and [9] when the resonator is coupled to the excitation source:

$$Z_{surface} = \frac{j\omega L}{1-\omega^2 LC}, \quad (1)$$

where ω=2πf and f define the angular frequency and frequency of the wave, respectively. The equivalent sheet inductance, L_L, and the equivalent sheet capacitance, C_R, are given as follows:

$$L_L = \frac{\eta_s}{\omega}\tan(\beta h); \; and \; C_R = \frac{w\varepsilon_0(\varepsilon_{r1}+\varepsilon_{r2})}{\pi}\cosh^{-1}\left(\frac{D}{g}\right).(2)$$

The properties of the characteristic parasitic patch can be obtained by using:

$$L_P = \frac{\frac{\mu_0}{2}l_{avg}}{4}\left[Ln\left(\frac{l_{avg}}{w}\right)-2\right], \quad (3)$$

where μ_0 is the vacuum permeability, l_{avg} is the average strip length calculated over all the rings and,

$$C_P = 2\varepsilon_0\varepsilon_r^{sub}\frac{2w+\sqrt{2}g}{\pi}\text{arccosh}\left[\frac{2w+g}{g}\right]; and \; \varepsilon_r^{sub} = 1 +$$
$$\frac{2}{\pi}arctg\left[\frac{h}{2\pi(w+s)}\right](\varepsilon_r-1). \quad (4)$$

Where in (3) and (4), g, s and w are the gap between patch and parasitic patch (W_h - W_p), width of parasitic patch (W_p - W_h), and patch width (W_p), respectively. The second step is to find the input impedance of the slot. When the transmission line is terminated by a stub length, the input impedance is simply put under the rectangular waveguide supposition and this result is added as series reactance, X. The total impedance is then:

$$Z_{slot} = Z_c\frac{2R}{1-R} + X. \quad (5)$$

As is well known, the impedance of an SIW, Z_0, can be calculated by:

$$Z_0 = \frac{\frac{h}{w}\eta}{\sqrt{1-\left(\frac{\lambda}{\lambda_c}\right)}} \; and \; \eta = \frac{120\pi}{\sqrt{\varepsilon_r}}, \quad (6)$$

where Z_c is the characteristic impedance of transmission line and R is voltage reflection coefficient.

The mutual inductance between the microstrip patch and the slot is:

$$M = \left(\frac{\mu_0 W_a}{2\pi}\right) Ln\,(sec\,\theta_0)\,; \; \theta_0 = \; arctan\left(\frac{L_a}{2h}\right), \quad (7)$$

where W_a, L_a and h are the slot width, the slot length, and the substrate height, respectively.

The mutual inductance between the microstrip patch and parasitic patch is:

$$M = \frac{\mu_0 x_1}{2\pi}\left[0.467 + \frac{0.059w^2}{x_1^2}\right], \quad (8)$$

where w is the patch width(W_p) and x_1 is the effective parasitic patch length.

From the equivalent circuit, the total incident power

to the proposed antenna can be expressed by:

$$P_{inc-t} = P_{inc-ZOR} + P_{inc-TM010}, \quad (9)$$

where $P_{inc-ZOR}$ and $P_{inc-TM010}$ are the incident powers to the inner mushroom ZOR antenna and the outer patch antenna, respectively. Hence, $P_{inc-ZOR}$ and $P_{inc-TM010}$ can be written by [10]:

$$P_{inc-ZOR} = \frac{1}{2} R_m |i_1|^2, \quad (10)$$

$$P_{inc-TM010} = \frac{1}{2} R_p (|i_2|^2 + |i_3|^2). \quad (11)$$

By using the injected power to each antenna, the incident power ratio (P_r) can be defined as:

$$P_r = \frac{P_{inc-ZOR}}{P_{inc-ZOR} + P_{inc-TM010}}. \quad (12)$$

Consequently, in (1)-(12), the equivalent elements of the antenna are extracted as follows: C_1=12.63 fF, C_a=126.47 fF, L_a=163.91 nH, R_a=3126 Ω, C_p=49.61 pF, L_p=842.26 nH, R_p=884 Ω, C_R=84.62 pF, L_L=276.01 nH, R_m=796 Ω, Γ_m=0.146, Γ_p=0.103, and Γ_{pm}=0.078.
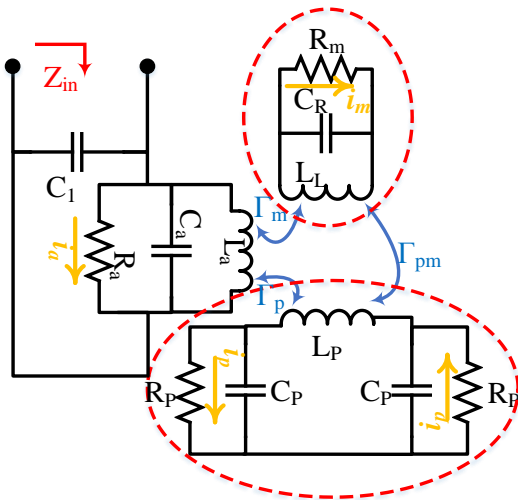
Fig. 2. Equivalent circuit of the proposed antenna.

Fig. 3. Studying the effect of changing parameter R_d on impedance matching.
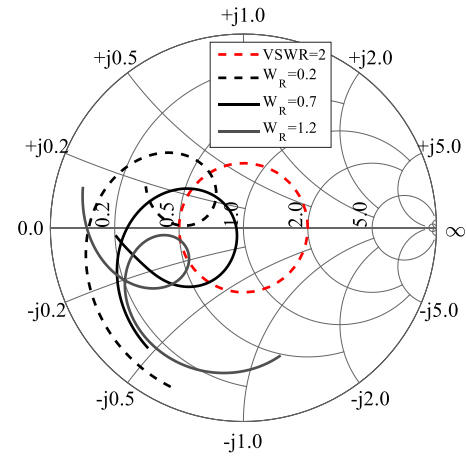
Fig. 4. Studying the effect of changing parameter W_R on impedance matching.

IV. RESULTS AND DISCUSSION

All parameters of the antenna have been optimized by using commercial software high frequency structure simulator (HFSS ver. 14). In order to investigate the effect of each parameter, two parameters of Rd and WR=Wp-Wh have been studied. By changing Rd value from 0.5 to 0.55 mm, inductance effect increases and impedance matching changes, but by changing Rd value from 0.55 to 0.6 mm, the capacitance effect increases again and causes a decrease in impedance bandwidth. Results of these changes are demonstrated in Fig. 3.

As mentioned, another parameter which has important effect on the antenna results is WR. In Fig. 4, by changing this parameter from 0.2 to 0.7, the capacitance effect is reduced which leads to an increase in impedance bandwidth but by increasing inductance effect via changing W_R from 0.7 to 1.2 mm, impedance matching was disturbed.

The proposed SIW fed CP ZOR antenna was fabricated and measured. The scattering parameters of the proposed antenna were performed with an Agilent 8510XF (E7340A) vector network analyzer. As specified in Fig. 5, the measured result for the S_{11} is in reasonable agreement with the simulated one, except for a little frequency shift [7-8] for the most ranges of the impedance bandwidth. From the measured results, a good impedance bandwidth over the frequency range of 33.82-36.37 GHz can be attained (as shown in Fig. 5).

As is well known, since an equivalent horizontal magnetic loop current is generated inside the mushroom structure at the ZOR mode, the power radiates with an omni-directional pattern [3]. If the directional radiation pattern of the combination of TM_{01} and TM_{10} modes and the omni-directional radiation pattern of the ZOR mode are combined at the same frequency, it is possible for the HPBW of the total radiation pattern to improve. On the

other hand, since TM_{01} and TM_{10} are two modes with the same magnitudes and 90-degree phase difference, the proposed antenna radiated as CP antenna. In order to prove the performance principle of the design theory of the antenna, the study displayed the simulated surface current distribution on the antenna peripheral as well as the E-field distribution at the center frequency for different phases (Fig. 6). The direction of the wave in the presented antenna configuration leads to the counter clockwise rotated current distribution which results in right-handed CP (RHCP) radiation. Left-handed CP (LHCP) radiation can be obtained by changing chamber location of the presented configuration. The comparison between simulated and measured radiation patterns of the proposed antenna is demonstrated in Fig. 7. As proved in Fig. 7, this antenna with a broadside pattern radiates RHCP in +Z direction and because the loss of feed line is reduced and antenna is operated with SIW cavity backed slot, the gain is increased to 9.2 dB.
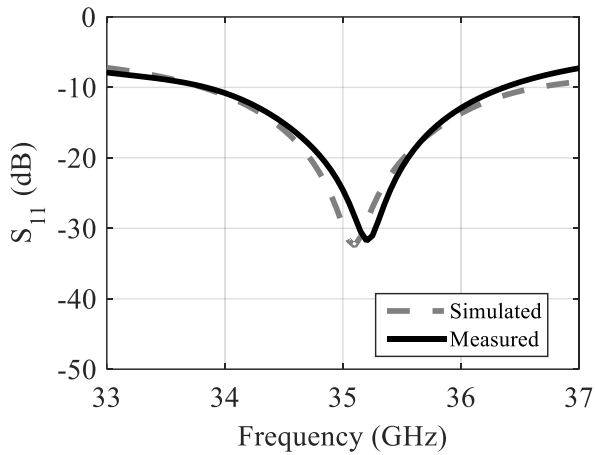
Fig. 5. The comparison between simulated and measured S_{11}.
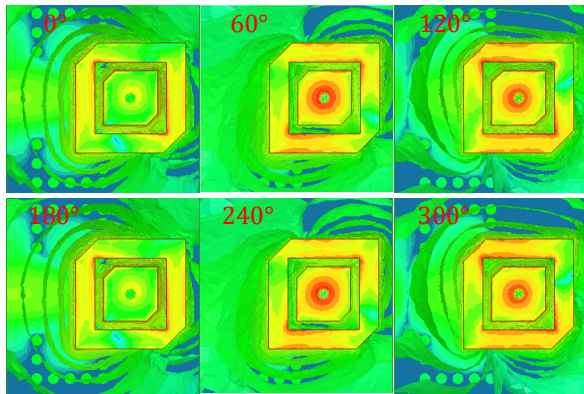
Fig. 6. Simulated current and E-field distributions on the surface of the proposed CP planar aperture ZOR antenna at 35 GHz for different phases.
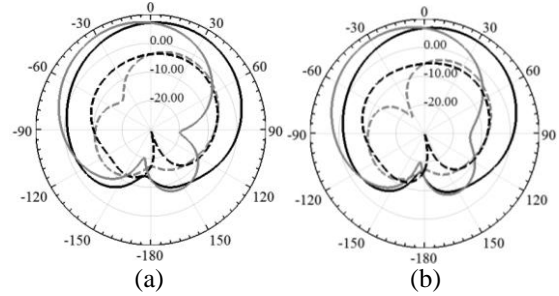
Fig. 7. The comparison between (a) simulated and (b) measured radiation patterns at 35 GHz (solid line is RHCP, dash line is LHCP, black line is $\varphi=0°$, and grey line is $\varphi=90°$).

In addition, using mushroom polarizer leads to an increase in gain with a broadside pattern. The simulated and measured half power bandwidths of antenna are 105 and 103.8 degrees, respectively. The comparison between simulated and measured results of axial ratio and gain of ZOR antenna versus frequency is illustrated in Fig. 8. The simulated 3-dB axial ratio is from 34.27 to 35.87 GHz and measured axial ratio, while matching well with simulated results, has 4.7% (34.32-35.94 GHz) bandwidth. The gain of antenna in all frequency ranges has low variant value which suggests that this antenna possesses stable pattern and results. The measured average gain of the antenna is 8.93 dBic.
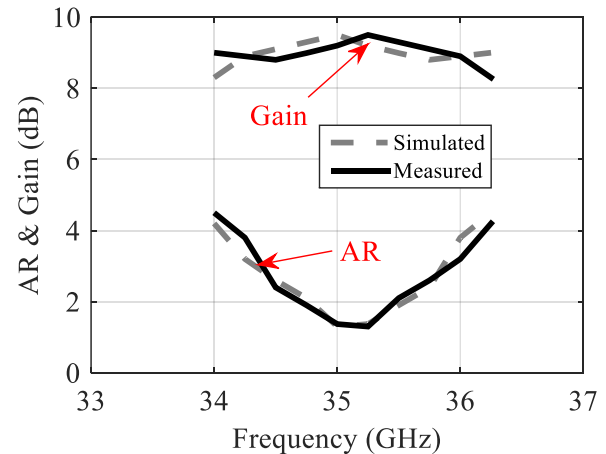
Fig. 8. The simulated and measured ARs and gains of proposed CP ZOR antenna.

V. CONCLUSION

In this work, a SIW mm-wave antenna with wide HPBW was presented. The combination between a SIW aperture-coupled antenna (with TM_{010}) and a mushroom polarizer metamaterial antenna helps develop HPBW. In order to increase the antenna performance and generate two orthogonal modes simultaneously to attain CP, the

study applied a modified mushroom with etching corner on SIW slot. The antenna has the advantages such as a simple structure, and planar configuration in spite of using two radiators. In conclusion, in the present study, an antenna with 7.3% BW, 4.7% 3-dB axial ratio BW, the maximum gain of 8.93 dBic, and 103.8° HPBW was designed.

REFERENCES

[1] B. Biglarbegian, M. Fakharzadeh, D. Busuioc, M.-R. Nezhad-Ahmadi, and S. Safavi-Naeini, "Optimized microstrip antenna arrays for emerging millimeter-wave wireless applications," *IEEE Trans. Antennas Propag.*, vol. 59, no. 5, pp. 1742-1747, May 2011.

[2] W. He, R. Jin, and J. Geng, "E-shape patch with wideband and circular polarization for millimeter-wave communication," in *IEEE Transactions on Antennas and Propagation*, vol. 56, no. 3, pp. 893-895, Mar. 2008.

[3] C.-H. Lee and J.-H. Lee, "Millimeter-wave wide beamwidth aperture–coupled antenna designed by mode synthesis," *Microw. Opt. Technol. Lett.*, vol, 57, pp. 1255-1259, 2015.

[4] M. Shahabadi, D. Busuioc, A. Borji, and S. Safavi-Naeini, "Low-cost high-efficiency quasi-planar array of waveguide-fed circularly polarized microstrip antennas," *IEEE Trans. Antennas Propag.*, vol. 53, no. 6, pp. 2036-2043, June 2005.

[5] A. Borji, D. Busuioc, and S. Safavi-Naeini, "Efficient low-cost integrated waveguide-fed planar antenna array for ku-band applications," *IEEE Antennas Wireless Propag. Lett.*, vol. 8, pp. 336-339, 2009.

[6] B. Guntupalli, T. Djerafi, and K. Wu, "Two-dimensional scanning antenna array driven by integrated waveguide phase shifter," in *IEEE Transactions on Antennas and Propagation*, vol. 62, no. 3, pp. 1117-1124, Mar. 2014.

[7] S. Karamzadeh, V. Rafii, M. Kartal, and B. S. Virdee, "Compact and broadband 4×4 SIW butler matrix with phase and magnitude error reduction," in *IEEE Microwave and Wireless Components Letters*, vol. 25, no. 12, pp. 772-774, Dec. 2015. doi: 10.1109/LMWC.2015.2496785

[8] S. Karamzadeh, V. Rafii, M. Kartal, and B. S. Virdee, "Modified circularly polarised beam steering array antenna by utilised broadband coupler and 4 × 4 butler matrix," in *IET Microwaves, Antennas & Propagation*, vol. 9, no. 9, pp. 975-981, June 18, 2015. doi: 10.1049/iet-map.2014.0768

[9] S. S. Mohan, "Design, Modeling and Optimization of OnChip Inductor and Transformer Circuits," *Ph.D. Dissertation*, Stanford University, Palo Alto, 1999.

[10] S. T. Ko and J. H. Lee, "Hybrid zeroth-order resonance patch antenna with broad E-plane beam-width," in *IEEE Transactions on Antennas and Propagation*, vol. 61, no. 1, pp. 19-25, Jan. 2013. doi: 10.1109/TAP.2012.2220315

Saeid Karamzadeh, received his M.S. and Ph.D. degrees in Department of Communication Systems, Satellite Communication & Remote Sensing program at Istanbul Technical University in 2013 and 2015 respectively. He won the most successful Ph.D. Thesis Award of Istanbul Technical University. Currently, he is an Assistant Professor in the Istanbul Aydin University, Department of Electrical and Electronics Engineering. He is also with Application & Research Center for Advanced Studies in the Istanbul Aydin University, Turkey. His research interests include remote sensing, radar, microwave, and Antenna design.

Vahid Rafiei, was born in Naghadeh, IRAN in 1986. He is author and co-author more than a dozen articles about CP array and beam steering antenna. He is selected as Top Iranian Young Research in 2014-2016. Now, he is working with Advance Electromagnetics, Microwave and Antenna Research Group at Istanbul Aydin University and at the same time as Faculty Member of Istanbul Aydin University. His main areas of interest in research are microstrip array antenna, beam steering and beam shaping feed networks, computational methods, microwave passive and active circuits graphene base nano structure microwave and antenna application, and RF MEMS.

Hasan Saygin, Professor of Engineering, specializing in Applied Sciences, and Advisor to the Chairman of the Board of Trustees at the Istanbul Aydin University. He received his Ph.D. from École Polytechnique de Montréal, Institut de génie énergétique at the Université de Montréal, and his M.Sc. in Nuclear Energy from Istanbul Technical University. His working area are Nuclear Energy, Thermodynamic, Computational Fluid Mechanics, Energy Policy, microwave and Antenna application.

An Improved Design of Equal-Split Filtering Divider with Integrated Coupled-Line Band-Pass Filter

Zafar Bedar Khan and Huiling Zhao

Department of Electronics and Information, Northwestern Polytechnical University, Xian, 710072, P. R. China
zafarbedarkhan@mail.nwpu.edu.cn, zhhl@nwpu.edu.cn

Abstract ─ A novel methodology is proposed for achieving good output port isolation and return loss in a micro-strip filtering divider design with integrated coupled-line (CPL) band-pass filter (BPF). The designed filtering divider shows improved performance parameters as compared to previously reported work. It is proposed that by incorporating an extended transmission line (TL) and a conventional resistor as isolation elements, in addition to good even mode response (i.e., insertion loss IL, and input port return loss RL), the odd mode response (i.e., output port RL and isolation) can simultaneously be improved. In addition, two transmission zeros are realized in the vicinity of the pass band providing a reasonable skirt. Firstly, the coupled-line filter (CPLF) is matched to 70.7Ω and subsequently integrated in place of conventional quarter wavelength transformers in a Wilkinson Power Divider (WPD) for equal division. Under these matched conditions, it is shown that a TL section and isolation resistor sufficed to achieve a reasonable output port return loss (RL) and isolation in the resulting filtering divider. Experimental validation of the proposed methodology comes from the measurements results of the fabricated CPL filtering divider designed at 3 GHz conforming reasonably to the simulated ones. For instance, 1 dB fractional bandwidth of 15.3%, port isolation of better than 31 dB and good out-of-band performance up to 2.67f_0 were experimentally achieved.

Index Terms ─ Band-pass filter, coupled line filter, equal split, filtering divider.

I. INTRODUCTION

Integration of band-pass filter (BPF) in a Wilkinson power divider (WPD) has drawn much research interest for realization of a filtering divider with low insertion loss (IL) and compact area as compared to when implemented separately in most RF front-ends (RFFE). The idea is to effectively replace the quarter wavelength transformers ($\lambda_g/4$, where λ_g is the guided wavelength) with a BPF (with certain fractional bandwidth (FBW)) in a power divider (PD) to improve the frequency selectivity, which is otherwise poor in a conventional WPD [1]. In addition, different isolation elements/techniques are employed between the output ports to achieve an acceptable port isolation and output return loss (RL). Many types of band pass filters have been used for the purpose for unequal/equal power division [2-8] with different isolation elements. For instance quasi-elliptical BPF was used in [2-3] with a single resistor as isolation element. In [2], a FBW of 4% was achieved with improved out of band rejection but output port isolation (using a resistor as isolation element) was only at 15 dB with high insertion loss of 6.4 dB. In [3], IL was improved to 3.99 dB with output port RL and isolation of 20 dB each, by employing a $\lambda_g/2$ resonator, four $\lambda_g/4$ resonators and an isolation resistor. The achieved FBW was 6.5% with a very high value of the isolation resistor (3.2 KΩ), deviating considerably from the conventional value of 100Ω. Coupled-line (CPL) structures and BPF have been extensively used to improve the frequency selectivity in WPD [4-8]. Unequal power division was addressed in [4-5]. For equal-split, a CPL structure with an isolation resistor was used in [6] to achieve a FBW of 16% but out-of-band response was not catered for and there were no transmission zeros. A coupled-line filter (CPLF) was used with a 3-dB hybrid as isolating element in [7]. Two prototypes were designed with port isolation of 24 dB. Here, although two transmission zeros were realized, but the IL was higher at 5.2 dB and 5.4 dB over a FBW 9.8% and 8.6% respectively. Moreover out-of-band rejection was less than 2f_0 (where f_0 is the design frequency). A CPL section with defected ground structure (DGS) was used in [8] to achieve input port match and IL of 30 dB 3.15 dB respectively (even mode response). For effective output isolation, inductor, capacitor and resistor (LCR) were used and 23 dB of isolation and output port RL of 30 dB (odd mode response) was achieved. It may be noted here that third harmonic rejection was achieved with no transmission zeros. Two prototypes of filtering divider were presented in [9] by integrating second-order and fourth-order CPLF with a 3 dB FBW of 14.9% and 15.2% respectively. A port isolation of about 24 dB in both prototypes was achieved by employing a single resistor at the outputs. The IL however was high at 5.5 dB and 6.8 dB respectively. From the afore-said, there appears to be a tradeoff between the even mode response (Input

port RL and IL) and odd mode response (output port RL and port isolation) of the filtering divider.

In this paper, a new methodology is presented which integrates a CPLF in WPD with an extended transmission line (TL) and resistor as isolation elements for improved performance parameters. It was previously established in our work [10-11] that a 50Ω extended TL section and a 100Ω resistor were sufficient to provide good isolation and output port RL in two and three TL dual band WPD. Here the concept is implemented on single-band filtering divider design to achieve simultaneous good even and odd mode response. A second order CPLF with a FBW of 16%, matched to 70.7Ω, has been shown to be effectively integrated in WPD maintaining low IL and good input matching as well as good output port matching and isolation. In addition, two transmission zeros are realized for a reasonably sharp skirt and good out-of-band rejection is achieved. For micro-strip implementation, using the proposed approach avoids usage of reactive elements. Moreover easily available SMD packages may be used to implement the conventional 100Ω resistor.

II. PROPOSED DESIGN DETAILS

A. Coupled-line filter (CPLF) design

Coupled lines/coupled line filters have been one of the famous choices for integration in the PD [4-9] as stated earlier. It is well established that even ordered filters are more appropriate to replace the conventional $\lambda_g/4$ transformers [4, 9]. In this subsection, design of a second order coupled line filter with Chebyshev response, pass-band ripple of 0.1 dB and FBW of 16% at a center frequency (CF) of 3 GHz is presented. Although design procedure of such CPLFs is well known [12], a brief design description is provided for brevity. For the laid down specification of the CPLF, firstly low pass filter prototype elements were calculated to be $g_0=1$, $g_1=0.843$, $g_2=0.622$ and $g_3=1.355$. By calculating the admittance (J) inverter values from Equations (1-3), band-pass conversion was carried out as a next step. Subsequently, form Equations (4-5), even and odd mode impedances were calculated. An important point to note here is that while designing the CPLF, the system impedance was taken to be 70.7Ω instead of 50Ω, in order to match the BPF in the PD circuit. This point is explained in detail in the next sub section.

With the values of impedances known and F4BM-2 taken as substrate with dielectric constant of 2.2 and height of 0.8 mm, widths (w) and distances (s) were calculated for each coupled line section as shown in Fig. 1 (a). Agilent's Advance Design System software (ADS) was used to carry out all simulations of the CPLF and CPLF divider. In order to get the desired response, the dimensions of the CPLF were slightly optimized and the final parameters are given in Table 1.

$$\frac{J_{01}}{Y_0} = \sqrt{\frac{\pi FBW}{2 g_0 g_1}} \, , \qquad (1)$$

$$\frac{J_{j,j+1}}{Y_0} = \frac{\pi FBW}{2} \frac{1}{\sqrt{g_j g_{j+1}}} \ (j = 1 \text{ to } n-1), \qquad (2)$$

$$\frac{J_{n,n+1}}{Y_0} = \sqrt{\frac{\pi FBW}{2 g_n g_{n+1}}} \, , \qquad (3)$$

$$(Z_{0e})_{j,j+1} = \frac{1}{Y_0}\left[1 + \frac{J_{j,j+1}}{Y_0} + \left(\frac{J_{j,j+1}}{Y_0}\right)^2\right], \qquad (4)$$

$$(Z_{0o})_{j,j+1} = \frac{1}{Y_0}\left[1 - \frac{J_{j,j+1}}{Y_0} + \left(\frac{J_{j,j+1}}{Y_0}\right)^2\right] \ (j=0 \text{ to } n). \ (5)$$

Where:
$J_{j, j+1}$ = Admittance (J) inverter parameters
Y_0 = Characteristic admittance of the terminating line (with Z0 = 70.7Ω)
FBW   = Fractional Bandwidth = BW/centre frequency
N   = Order of the filter
$(Z_{0e})_{j,j+1}$ = Even mode impedance
$(Z_{0o})_{j,j+1}$ = Odd mode impedance

Table 1: Calculated design parameters of the CPLF

j	$J_{j, j+1}$	$(Z_{0e})_{j,j+1}$	$(Z_{0o})_{j,j+1}$	$w_{j,j+1}$ (mm)	$s_{j,j+1}$ (mm)
0	0.557	132.05	53.25	0.715	0.18
1	0.362	105.5	54.9	1.012	0.24
2	0.557	132.05	53.25	0.715	0.18

Please note that Z_0 was taken as 70.7Ω in the CPLF design equations for subsequent good match in the filtering divider. Simulation of the CPLF was carried out by setting the port impedance to 70.7Ω, due to which the width w_f of the feeding TLs at both connecting ends was taken equal to 1.386 mm (corresponding to 70.7Ω). Length L of each coupled line section was kept equal at $\lambda_g/4$ as shown in Fig. 1 (a). Figure 1 (b) depicts the simulated S-parameters response of the CPLF at 3 GHz with a 1 dB BW from 2.7 GHz to 3.2 GHz (FBW of 16.7%) achieving the desired specifications.

(a)
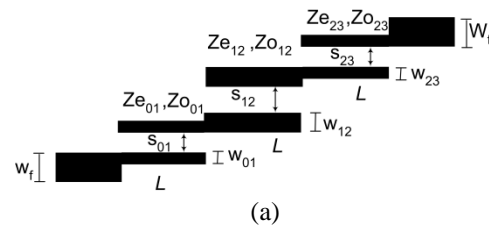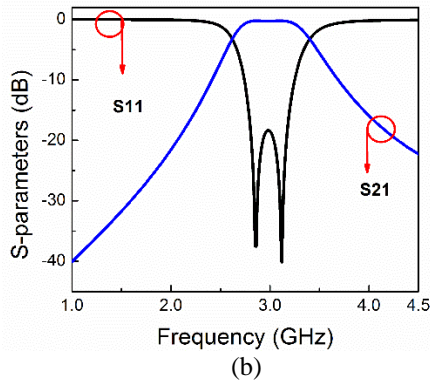
Fig. 1. (a) Second order coupled-line filter (CPLF) structure, and (b) simulated response of second order CPLF at 3 GHz.

B. Coupled-line filter divider (CPLFD) design

Proposed filtering divider circuit with a TL section and an isolation resistor is shown in Fig. 2 (a). The conventional $\lambda_g/4$ transformers have been replaced by second order CPLFs. A 50Ω extended TL section of length l_{TL} and a resistor R have been employed for effective output ports isolation and return loss (RL) [10, 11]. In order to get a simultaneous good even mode and odd mode response of the filtering PD, the TL length l_{TL} was optimized. Please note (refer to Fig. 3) that the outputs were tapped form zero position (the point where the BPFs end). Symmetry of the circuit in Fig. 2 (a) allows the even–odd mode analysis to be applied resulting in the half circuits as depicted in Figs. 2 (b) & (c) for even mode and odd mode respectively.

Under even mode excitations at the outputs, the proposed circuit can be bisected in the middle due to open circuit (magnetic wall) at the symmetric plane as shown in Fig. 2 (b). The isolation resistor R becomes superfluous and is shown as open circuit (OC). Assuming a system impedance of 50Ω, the input port 1 resistance doubles to a value of 100Ω in the bisected even mode circuit [1, 3]. Since the output port 2 is kept at 50Ω (system impedance), a transformation of 70.7Ω is required to achieve a perfect match between the input port and output port, as in conventional PD design [1]. In order to effectively replace the $\lambda_g/4$ transformer by a BPF, the latter must be matched to 70.7Ω so that Z_{in} = 50Ω as shown in Fig. 2 (b). This is exactly the reason that in the previous sub section, the port impedance was set to 70.7Ω instead of 50Ω for the CPLF simulation. Thus, under even mode condition, the proposed structure is expected to equally divide the signal with the filtering functionality as well, implying good IL and input port match (good RL).

Good output ports isolation and RL can be ensured through odd mode half circuit as shown in Fig. 2 (c) which results due to odd mode excitation at the output

ports, forming a short circuit (electric wall) at the symmetric plane. Thus, port 1 is shorted and if port 2 is perfectly matched then, maximum power is delivered to the isolation resistor which is half of its original value and no (or very little) power is transferred to port 2 [1, 3]. Thus, for good isolation between the output ports 2 & 3 (each of 50Ω), the resistor value was taken to be 100Ω (R = 2 x 50 Ω). Best output port RL and isolation is achieved by optimizing l_{TL} of the TL which acts as an extension of the output port.

(a)

(b)

(c)
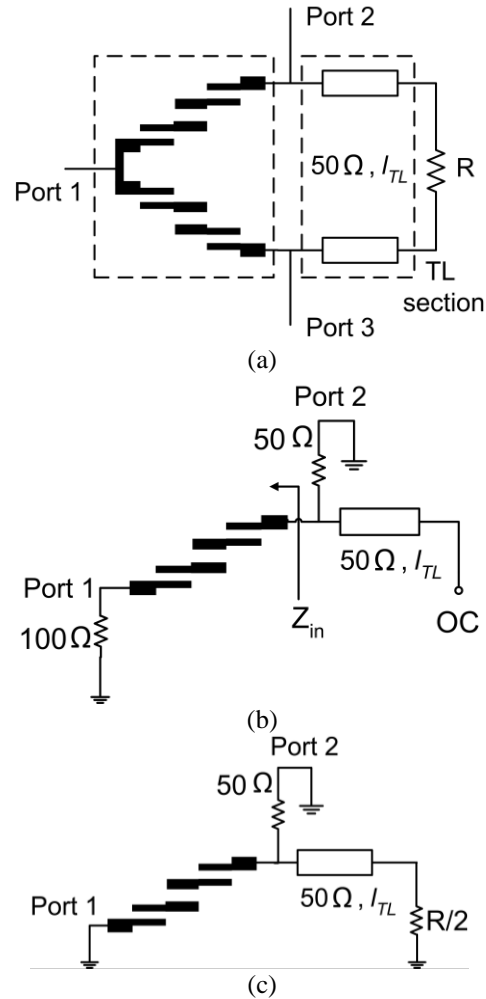
Fig. 2. (a) Proposed filtering divider, (b) even mode half circuit, and (c) odd mode half circuit.

It is imperative to mention here that the optimization of the TL length was carried out through the 'optimization tool' of the ADS in which the optimization goals were to achieve minimum value of S22/S33 and S23 by setting l_{TL} as variable (to be optimized in the range of $\lambda_g/8 < l_{TL} < \lambda_g/2$). This enabled accomplishing our purpose of attaining minimum S22/S33 and S23 just by optimizing the l_{TL} and keeping the R at a conventional value.

III. IMPLEMENTED FILTERING DIVIDER CIRCUIT

The designed filtering divider was fabricated on a F4BM-2 substrate with dielectric constant of 2.2 and height of 0.8 mm. Figure 3 shows the photo of the fabricated CPLFD. Please note that the TL length l_{TL} was optimized in the range of $\lambda_g/8 < l_{TL} < \lambda_g/2$ to get the best simultaneous even and odd mode response. Moreover, the output ports are shown to be tapped from zero position as marked in Fig. 3. Good functional response of the circuit was achieved at $l_{TL} = \lambda_g/2 = 37$ mm. The dimensions of the manufactured CPLFD are reported to be 10.1 cm × 2.4 cm (24.24 cm^2) or $1.3\lambda_g \times 0.3\lambda_g$. Although the size is slightly bigger in one dimension, but as will be shown in the results section, good simultaneous even and odd mode responses are achieved.
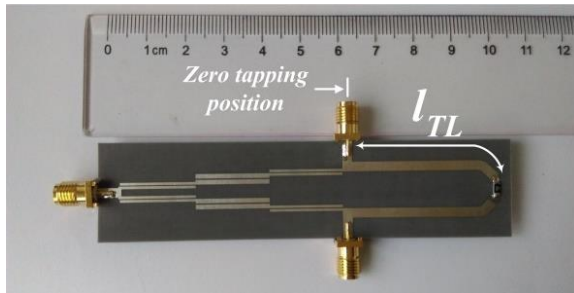
Fig. 3. Photograph of the manufactured CPLFD at 3 GHz.

IV. RESULTS AND DISCUSSION

All measurements of the fabricated CPLFD prototype were carried out on Agilent's PNA model no. E8363B. Figure 4 manifests the functional validity of the proposed technique which is evident through good conformance of measured and simulated S-parameter results at the design frequency of 3 GHz. Figure 4 (a) illustrates wide-band transmission response of the CPLFD with two transmission zeros at 1.4 GHz and 4 GHz. Moreover an out-of-band rejection of better than 15.8 dB was achieved up to $2.67f_0$ (8 GHz), since the first spurious pass-band appeared centered at about 8.5 GHz. Narrow band transmission characteristics are shown in Fig. 4 (b). Good symmetry of the designed circuit can be observed due to a fairly overlapping response of measured IL (S21 & S31). For even mode response, good input port match (S11) is reported to be at a measured value of 25 dB, while the insertion loss (S21 & S31) is at 3.45 dB (ideal value is 3 dB for equal division). Figures 4 (c) & (d) illustrate the odd mode response. From Fig. 4 (c), it is clear that the output port RL, (S22 and S33) stand at 29 dB each manifesting good match. Measured output port isolation (another very important performance parameter) is at 31 dB as shown in Fig. 4 (d). The designed CPLFD is operational over a measured 1 dB BW from 2.71 GHz to 3.17 GHz (1 dB FBW of 15.3%).
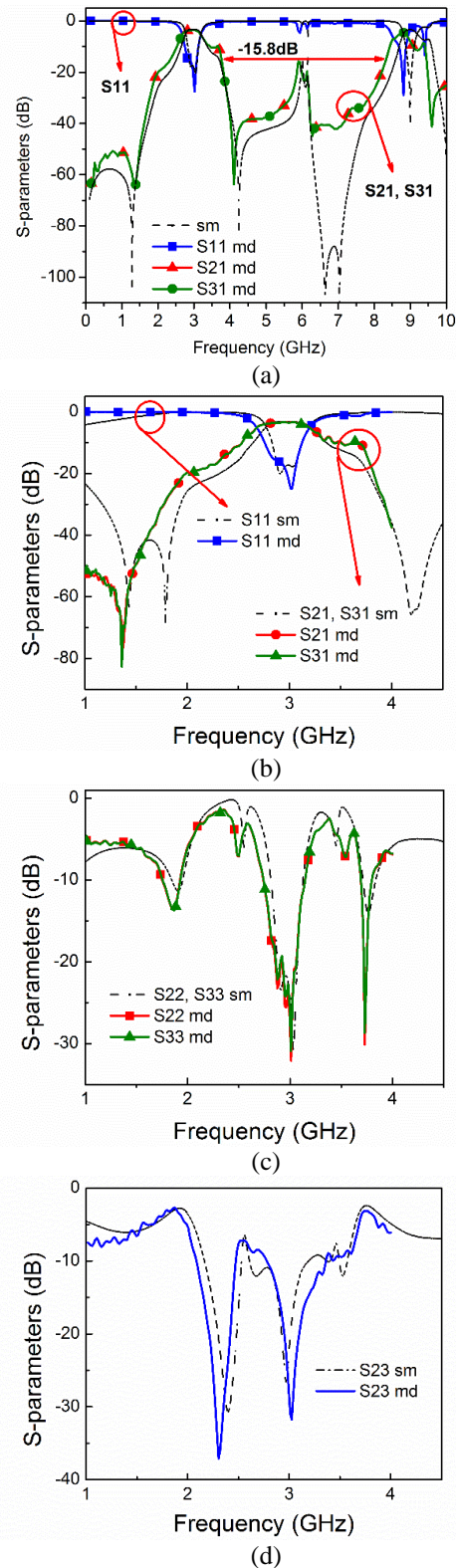
Fig. 4. Measured vs. Simulation response of CPLFD (sm = simulated, md = measured). (a) Wide-band response, (b) transmission characteristics in narrow band, (c) output port return loss, and (d) output port isolation.

Figure 5 depicts the measured amplitude imbalance/difference (|S21| - |S31|) and phase imbalance/difference (∠S21 - ∠S31) at the output ports of the CPLFD over the achieved operational FBW. At 3 GHz, the amplitude difference is 0.036 dB and phase difference is -0.59° which implies that the divided signals at the two output ports have almost same amplitude and phase. Simultaneous good even and odd mode responses can be noted in the circuit designed through proposed methodology.

Table 2 presents a comparison of the presented work with some previous works. It may be noted from Table 2 that [2, 3, 7] offer sharp skirt (having transmission zeros) at the cost of bigger order of the filter and higher IL. The IL in [8] is low with no transmission zeros and reactive elements have been employed. Similarly in [9], even and odd mode responses are not simultaneously good. The work presented here achieves good input port match and

low IL while maintaining reasonable output port match and return loss with two transmission zeros.
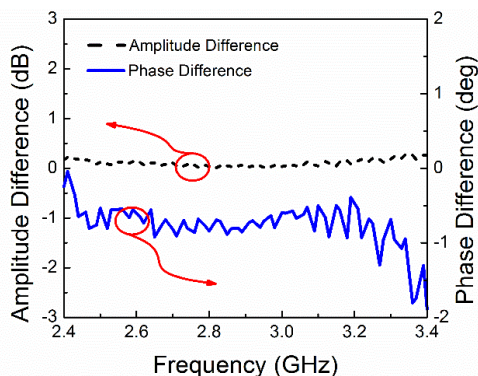
Fig. 5. Amplitude and phase imbalance at output port.

Table 2. Comparison of proposed work with previous work

Works	Parameters								
	Order	BPF Type	Isolation Elements	Input Port RL (dB)	IL (dB)	Output Port RL (dB)	Isolation (dB)	FBW (%)	Transmission Zeros
[2]	4	Quasi-elliptical filter	R	~25	6.4	~25	15	4	4
[3]	3	Quasi-elliptical filter	R	20	3.99	20	20	6.5	2
[7]	5	Coupled line filter	3dB Hybrid	30	5.2	30	25	9.8	2
[8]	-	Single coupled line section	LCR	30	3.15	30	23	Not given	None
[9]	2	Coupled line filter	R	27	5.5	27	24	14.9	None
	4	Coupled line filter	R	25	6.8	25	24	15.2	2
This work CPLFD	2	Coupled line filter	TL, R	25	3.45	29	31	15.3	2

V. CONCLUSION

A new design methodology has been proposed for filtering divider with a transmission line and resistor as isolation elements which ensures simultaneous good even and odd mode response. As a first step, coupled line filter (CPLF) was designed and matched to 70.7Ω in the simulation and was subsequently integrated in the PD with a 50Ω extended TL and a 100Ω resistor as isolation elements. The designed coupled line filtering divider (CPLFD) was fabricated and measured response was good over a FBW of 15.3% at the design frequency of 3 GHz. A sufficiently wide out-of-band response was achieved for most practical purposes with two transmission zeros in the vicinity of the pass-band. The achieved S-parameters (S11/S22/S33, S21/S31, S23) in the designed prototype were in reasonably good agreement with simulation

results, authenticating the proposed technique.

REFERENCES

[1] D. M. Pozar, *Microwave Engineering*. Second edition, Wiley, New York, 2009.
[2] J.-Y. Shao, S.-C. Huang, and Y.-H. Pang, "Wilkinson power divider incorporating quasi-elliptical filters for improved out-of-band rejection," *Electron. Lett.*, vol. 47, no. 23, pp. 1288-1289, 2011.
[3] X. Y. Zhang, K.-X. Wang, and B.-J. Hu, "Compact filtering power divider with enhanced second-harmonic suppression," *IEEE Microw. Wireless Compon. Lett.*, vol. 23, no. 9, pp. 483-485, 2013.
[4] P.-H. Deng and L.-C. Dai, "Unequal Wilkinson power dividers with favorable selectivity and high-isolation using coupled-line filter transformers,"

IEEE Trans. Microw. Theory Techn., vol. 60, no. 6, pp. 1520-1529, 2012.

[5] B. Li, X. Wu, and W. Wu, "A 10:1 unequal-split Wilkinson power divider using coupled line with two shorts," *IEEE Microwave Wireless Compon. Lett.*, vol. 19, no. 12, pp. 781-791, Dec. 2009.

[6] Y. Wu, J. Li, and Y. Liu, "A simple coupled-line Wilkinson power divider for arbitrary complex input and output terminated impedances," *Applied Computational Electromagnetics Society (ACES) Journal*, vol. 29, no. 7, pp. 565-570, 2014.

[7] S. L. Romano, A. G. Lamperez, M. S. Palma, A. I. D. Eusebiot, J. S. G. Villasantet, and M. J. P. Cruzin, "Microstrip filter and power divider with improved out-of-band rejection for a Ku-band input multiplexer," *In Proc. 33rd European Microwave Conference*, Munich, pp. 315-318, 2003.

[8] J. Yang, C. Gu, and W. Wu, "Design of novel compact coupled microstrip power divider with harmonic suppression," *IEEE Microw. Wireless Compon. Lett.*, vol. 18, no. 9, pp. 572-574, Sep. 2008.

[9] P. H. Deng, L. C. Dai, and Y. D. Chen, "Integrating equal-split Wilkinson power dividers and coupled-line bandpass filters," *in Symposium Proceedings Progress In Electromagnetics Research*, Moscow Russia, pp. 1249-1253, 2012.

[10] Z. B. Khan, H. Zhao, and Y. Zhang, "Simplified approach for design of dual-band Wilkinson power divider with three transmission line sections," *Microwave Opt. Technol. Lett.*, vol. 58, no. 10, pp. 2374-2377, Oct. 2016.

[11] Z. B. Khan, H. Zhao, and Y. Zhang, "A new simplified approach for design of dual-band Wilkinson power divider with two and three transmission line sections using only even-mode analysis," *Journal of Microwaves, Optoelectronics and Electromagnetic Applications*, vol. 15, no. 4, pp. 390-401, Dec. 2016.

[12] J. S. Hong, *Microstrip Filters for RF/Microwave Applications*. Wiley, New York, 2011.

Zafar Bedar Khan received his B.E. (Avionics) degree from National University of Sciences and Technology, Pakistan and M.S. (Electronics & Comm.) degree from Hanyang University, South Korea in 2002 and 2010 respectively. Khan has been working as a Research Engineer in an R&D organization in Pakistan in the field of RF front-end design. He is currently pursuing his Ph.D. degree in Northwestern Polytechnical University, Xian, China. His research interests include RF passive component design for RF front-end application in Radar and communication systems.

Huiling Zhao received her Ph.D. Degree in Circuit and System from Northwestern Polytechnical University, Xian, China in 2002. Zhao is currently a Professor in the Department of Electronics and Information, Northwestern Polytechnical University, China. She has been a visiting Associate Professor in the Duke University, USA from 2006 to 2007. Zhao's main research interests include optimization algorithm development for beam forming, computational electromagnetics, microwave and millimeter wave circuit and antenna design.

High Selectivity Dual-band Bandpass Filters Using Dual-mode Resonators

Rui Yin [1], Wenjie Feng [1*,2], and Wenquan Che [1]

[1] Department of Communication Engineering, Nanjing University of Science & Technology, Nanjing, China

[2] State Key Laboratory of Millimeter Waves, Southeast University, Nanjing, China
fengwenjie1985@163.com

Abstract – Two high selectivity dual-band bandpass filters using dual-mode resonators are proposed in this paper. Four and six transmission zeros near the passbands can be easily achieved for two dual-band bandpass filters. A transmission zero located in the two passbands is used to realize good isolation for the two passbands. Two prototypes with center frequencies located at 1.93, 2.42 GHz, and 2.04, 2.32 GHz with upper stopband insertion loss greater than 20 dB are designed and fabricated. The two proposed dual-band bandpass filters show high passband selectivity, good out-of-band suppression.

Index Terms – Bandpass filter, dual-band, dual-mode, transmission zeros.

I. INTRODUCTION

Dual-band bandpass filters are becoming more and more important with the rapid development microwave communication systems [1]-[6]. The main attentions for dual-band bandpass filter design are the passband selectivity, passband isolation, upper stopband, and bandwidth control. Dual-mode ring resonators have a lot of attractive features such as compact circuit size, transmission zeros near passbands, which are firstly proposed by Wolff [7]. The dual-mode ring resonators have been introduced to design different bandpass filters, balanced circuits, power dividers [8]-[12] in the past few years. As discussed in [9], coupled ring resonators can be easily used to design high performance dual-band bandpass filters, several resonators can be configured in series, in parallel or both to realize different transmission characteristic. However, the dual-band bandpass filters have only two transmission zeros near each passband, cascaded ring resonators can only increase the passband-order, the out-of-band transmission zeros are difficult to increase.

In this paper, two novel dual-band bandpass filters with multiple transmission zeros are proposed, two dual-mode ring resonators are used to realize the two passbands, and loaded shorted stubs and coupled lines are used to increase the numbers of transmission zeros. Pairs of independently adjusted transmission zeros can

be easily realized for the two dual-band filters. Two prototypes of the dual-band bandpass filters are constructed on the dielectric substrate with $\varepsilon_r = 2.65$, $h = 1.0$ mm, and $\tan \delta = 0.003$.

II. ANALYSIS OF PROPOSED DUAL-BAND FILTERS

A. Bandpass filters using dual-mode resonators

Figures 1 (a)-(b) shows the ideal circuits of the bandpass filters using dual-mode ring resonators, and the dual-mode ring resonators are attached to two quarter-wavelength side-coupled lines (electrical length θ, even/odd-mode characteristic impedance Z_{e1}, Z_{o1}). Two transmission lines (Z_1, θ) are located in the middle of the filter circuits, two microstrip lines with characteristic impedance $Z_0 = 50$ Ω are connected to ports 1, 2.

(a)

(b)
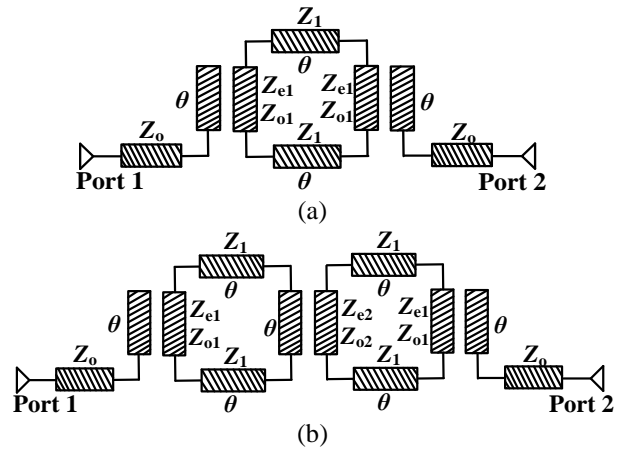
Fig. 1. (a) Bandpass filter circuit using single dual-mode ring resonator [8], and (b) dual-band filter using series dual-mode ring resonators [9].

The simulated results of Figs. 1 (a)-(b) are shown in Fig. 2, the two transmission zeros near the passband can be calculated as:

$$\theta_{tz1} = \arccos \sqrt{\frac{Z_{e1}+Z_{o1}-2Z_1}{Z_{e1}+Z_{o1}+2Z_1}} \ , \ \theta_{tz2} = \pi - \theta_{tz1} . \quad (1)$$

And when two dual-mode ring resonators are in series, a transmission zero (f_0) can be realized in the center frequency of the bandpass filter, and two passbands can be easily realized [9]. In addition, due to the cascaded dual-mode ring resonators, the out-of-band performance rejection has been further improved. However, due to the circuit limitation, the out-of-band performance cannot be further improved for lack of transmission zeros out-of-band. Next, two improved dual-band filters with four and six transmission zeros will be given.
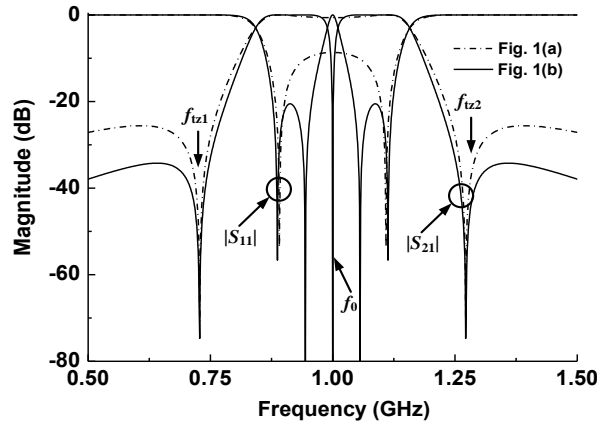
Fig. 2. Simulated results of the bandpass filters of Fig. 1, ($Z_1 = 90/90$ Ω, $Z_{e1} = 182$ Ω, $Z_{o1} = 72$ Ω, $Z_{e2} = 182$ Ω, $Z_{o2} = 72$ Ω, $Z_0 = 50$ Ω).

B. Proposed two dual-band bandpass filters

The ideal circuit of the dual-band bandpass filter with four transmission zeros are shown in Fig. 3 (a), and two shorted stubs (Z_2, θ) are located in the end of the side-coupled lines. The other parts are the same as Fig. 1 (b). The simulated frequency responses of the dual-band bandpass filter with five transmission zeros are shown in Figs. 3 (b)-(e), and besides the transmission zeros located at f_0, four transmission zeros (f_{z1}, f_{z2}, f_{z3}, f_{z4}, $f_{z1}+f_{z4}=2f_0$, $f_{z2}+f_{z3}=2f_0$) are realized due to the loaded shorted stubs Z_2. Due to the complex transmission matrix of the cascaded two dual-mode ring resonators, the equations of transmission zeros of the center frequencies of Fig. 3 (a) are difficult to solve out directly. From the simulated results of Figs. 3 (b)-(e), we can find that, the center frequency of the two passbands move towards f_0 as Z_1 increases, and the bandwidth of the two passband increases as the sum of Z_{e2}, and Z_{o2} increases. Moreover, the two transmission zeros f_{z1}, f_{z4} move away from f_0 as sum of Z_{e1}, and Z_{o1} decreases, and the two transmission zeros f_{z2}, f_{z3} move away from f_0 as the sum of Z_{e2}, and Z_{o2} increases. The passband selectivity and out-of-band harmonic suppression have been improved due to the

increased transmission zeros.

(a)

(b)

(c)

(d)

(e)
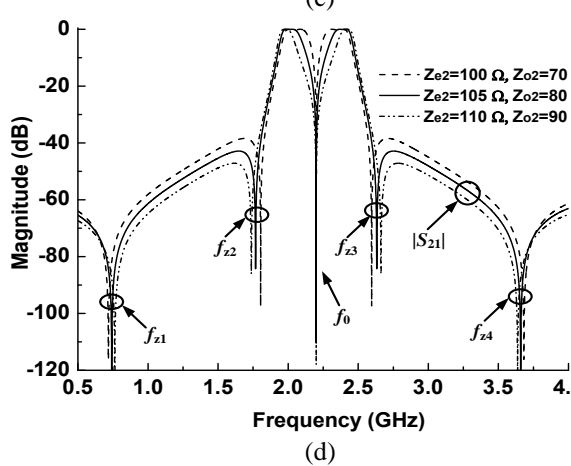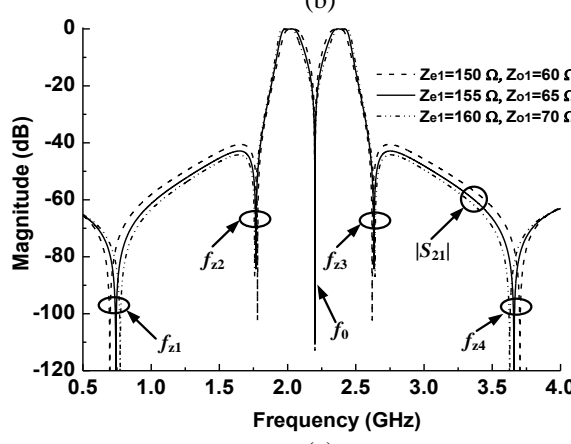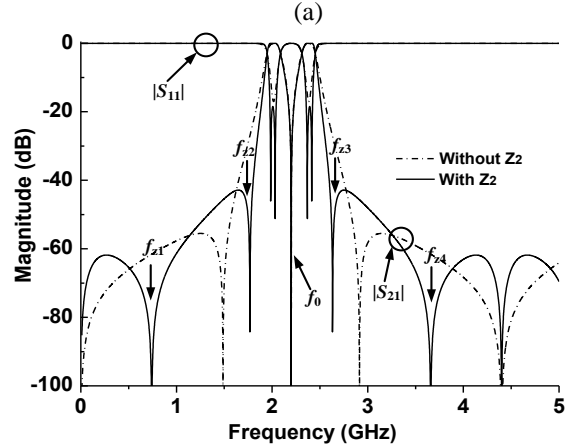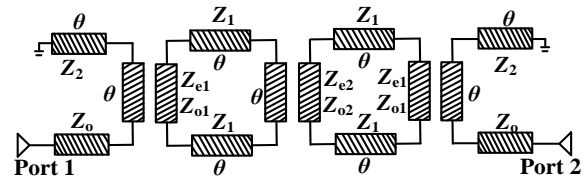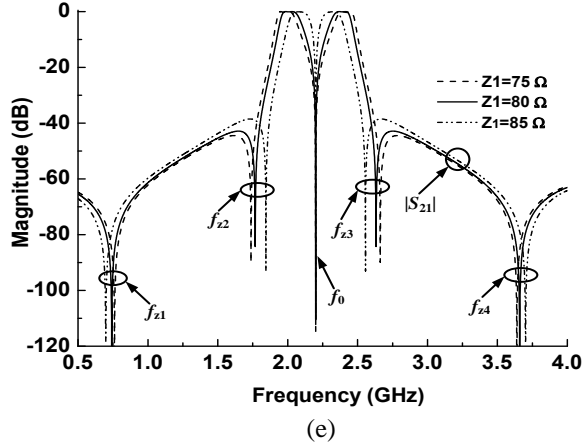
Fig. 3. (a) Ideal circuit of the dual-band filter with five transmission zeros, (b) simulated results of Fig. 1 (b) and Fig. 3 (a), (c) $|S_{21}|$ versus Z_{e1}, Z_{o1}, (d) $|S_{21}|$ versus Z_{e2}, Z_{o2}, and (e) $|S_{21}|$ versus Z_1, ($Z_1 = 80$ Ω, $Z_2 = 120$ Ω, $Z_{e1} = 155$ Ω, $Z_{o1} = 65$ Ω, $Z_{e2} = 105$ Ω, $Z_{o2} = 80$ Ω, $Z_0 = 50$ Ω).

The proposed dual-band bandpass filter with seven transmission zeros is illustrated in Fig. 4 (a), and two open/shorted coupled lines (electrical length θ, even/odd-mode characteristic impedance Z_{e3}, Z_{o3}), and the input impedance of the open/shorted coupled lines is:

$$Z_{in} = j\frac{(Z_{e3}+Z_{o3})^2 \cos^2 \theta - (Z_{e3}-Z_{o3})^2}{(Z_{e3}+Z_{o3})\sin 2\theta}. \qquad (2)$$

When $Z_{in} = 0$, two transmission zeros can be obtained as:

$$\theta_{z5} = \arccos\sqrt{\frac{Z_{e3}-Z_{o3}}{Z_{e3}+Z_{o3}}}, \quad \theta_{z6} = \pi - \theta_{z5}, \qquad (3)$$

and the two transmission zeros (f_{z5}, f_{z6}) have only relationship with Z_{e3}, Z_{o3}, which are two independently adjusted transmission zeros for the dual-band bandpass filter with seven transmission zeros.

The simulated frequency responses of the two dual-band bandpass filters are shown in Figs. 4 (b)-(c), and the two transmission zeros f_{z5}, f_{z6} are located in the center of f_{z1}, f_{z2}, f_{z3}, f_{z4}, the out-of-band harmonic suppression can be easily improved, and the bandwidth of the two passbands and center frequencies do not change with f_{z5}, f_{z6} [8], which can supply more freedom for the bandpass filter design.

Based on the above discussions and analysis, the center frequencies of the two dual-band filters are chosen as: 1.94 and 2.42 GHz, 2.04 and 2.34 GHz, and the prototypes of the proposed two dual-band bandpass filters are shown in Figs. 5 (a)-(b), and the final parameter for the two dual-band bandpass filters are shown in Table 1. The simulated results of the two dual-band bandpass filters are shown in Figs. 6 (a)-(b), for the dual-band bandpass filter with five transmission zeros, the center frequencies are located at 1.93 GHz and 2.42 GHz, the 3-dB bandwidths of the two passbands are 8.3% (1.86-2.02 GHz) and 5.0% (2.35-2.47 GHz), and five

transmission zeros are located at 0.70 GHz, 1.64 GHz, 2.21 GHz, 2.60 GHz, and 3.53 GHz, and the upper stopband insertion loss is greater than 35 dB from 2.57 GHz to 6.0 GHz. For the dual-band bandpass filter with seven transmission zeros, the 3-dB bandwidths of the two passbands are 8.1% (1.965-2.13 GHz), 5.1% (2.26-2.38 GHz), seven transmission zeros are located at 0.55 GHz, 1.49 GHz, 1.68 GHz, 2.21 GHz, 2.51 GHz, 3.58 GHz, and 4.18 GHz, and the upper stopband insertion loss is greater than 30 dB from 2.48 to 6.1 GHz, compared with the dual-band filter with five transmission zeros, the passband selectivity have been further improved.

(a)

(b)

(c)
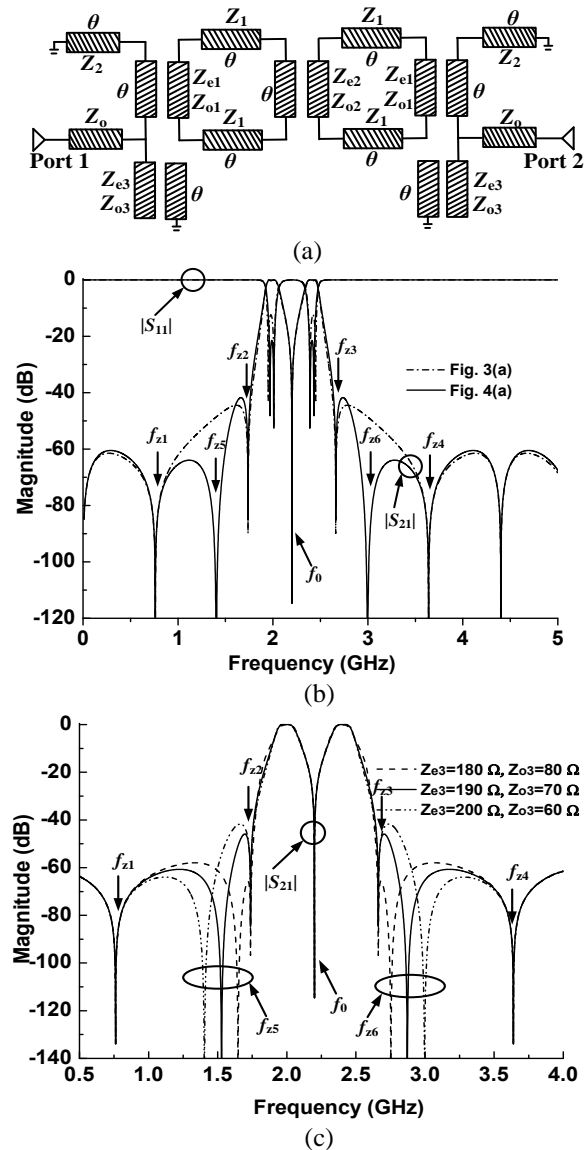
Fig. 4. (a) Ideal circuit of the dual-band filter with seven transmission zeros, (b) simulated results of Fig. 3 (a) and Fig. 4 (a), (c) $|S_{21}|$ versus Z_{e3}, Z_{o3}, ($Z_1 = 80$ Ω, $Z_2 = 120$ Ω, $Z_{e1} = 155$ Ω, $Z_{o1} = 65$ Ω, $Z_{e2} = 105$ Ω, $Z_{o2} = 80$ Ω, $Z_{e3} = 200$ Ω, $Z_{o3} = 60$ Ω, $Z_0 = 50$ Ω).
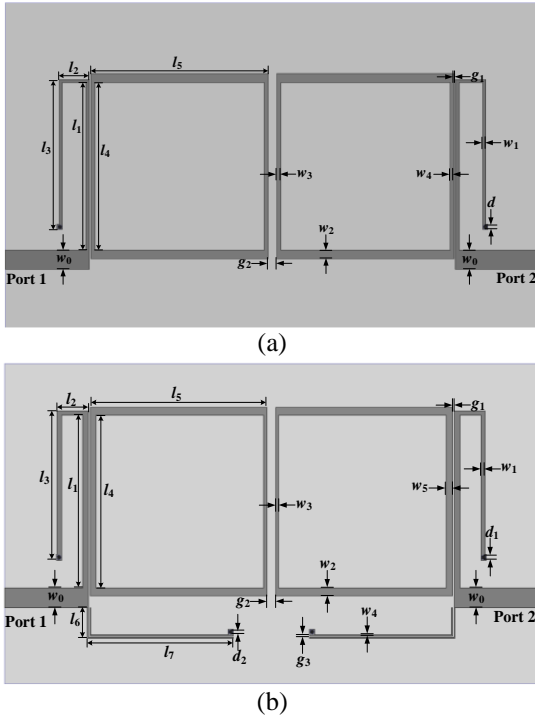
Fig. 5. Geometries of the two dual-band bandpass filters, (a) five zeros and (b) seven zeros.
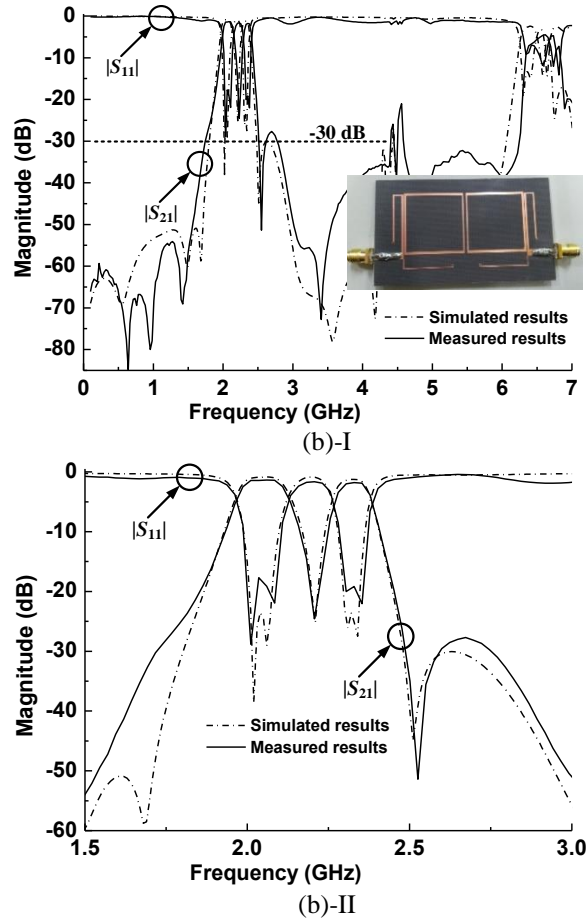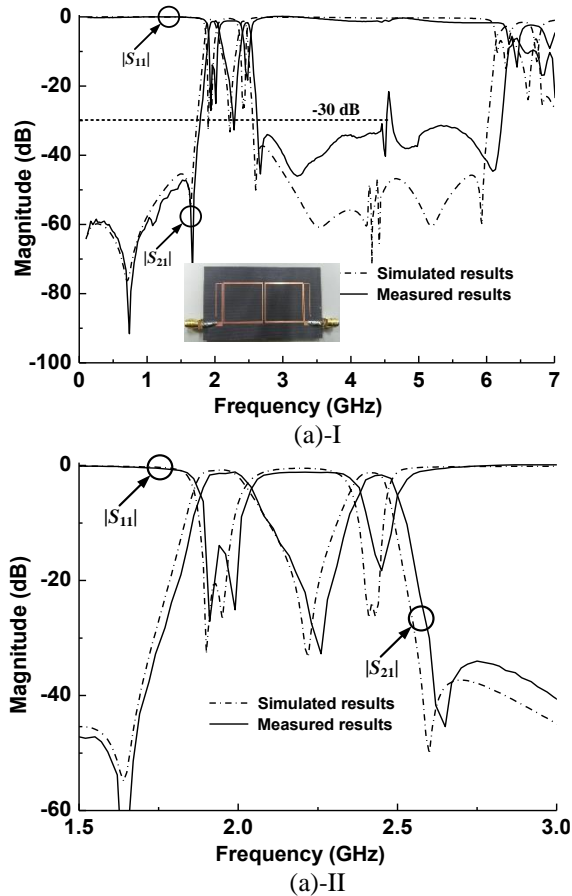
Fig. 6. Photographs, simulated and measured results of the two dual-band bandpass filters, (a) five zeros and (b) seven zeros.

Table 1: Parameters of the proposed two filters ($\varepsilon_r = 2.65$, $h = 1.0$ mm, and tan $\delta = 0.003$)

Proposed Filters	Circuit Parameters (Ω)	Structure Parameters (mm)
Five zeros	$Z_0 = 50$, $Z_1 = 80$, $Z_2 = 125$, $Z_{e1} = 151$, $Z_{o1} = 60$, $Z_{e2} = 125$, $Z_{o2} = 95$	$l_1 = 23.6$, $l_2 = 4.2$, $l_3 = 20.4$, $l_4 = 23.6$, $l_5 = 24.7$, $w_0 = 2.7$, $w_1 = 0.42$, $w_2 = 1.24$, $w_3 = 0.56$, $w_4 = 0.56$, $g_1 = 0.19$, $g_2 = 1.2$, $d = 0.6$
Seven zeros	$Z_0 = 50$, $Z_1 = 85$, $Z_2 = 11$, $Z_{e1} = 135$, $Z_{o1} = 55$, $Z_{e2} = 135$, $Z_{o2} = 100$, $Z_{e3} = 230$, $Z_{o3} = 88$	$l_1 = 23.6$, $l_2 = 4.4$, $l_3 = 20.0$, $l_4 = 23.6$, $l_5 = 24.9$, $l_6 = 4.2$, $l_7 = 20.5$, $w_0 = 2.7$, $w_1 = 0.6$, $w_2 = 1.06$, $w_3 = 0.46$, $w_4 = 0.15$, $w_5 = 0.84$, $g_1 = 0.24$, $g_2 = 1.2$, $g_3 = 0.2$, $d_1 = 0.6$, $d_2 = 0.6$

III. EXPERIMENT AND RESULTS DISCUSSIONS

The photographs, measured results of the two dual-band bandpass filters are also illustrated in Fig. 6. Good agreements can be observed between the simulation and the experiments. For the dual-band bandpass filters with five transmission zeros, five transmission zeros are located at 0.74 GHz, 1.67 GHz, 2.28 GHz, 2.67 GHz, and 3.21 GHz, the 3-dB bandwidths of the two passbands are 8.1% (1.90-2.06 GHz) and 5.3% (2.40-2.53 GHz), and the upper stopband insertion loss greater than 20 dB from 2.6 GHz to 6.26 GHz; for the dual-band bandpass filter with seven transmission zeros, the 3-dB bandwidths of the two passbands are 8.2% (1.99-2.16 GHz) and 5.1% (2.29-2.41 GHz), seven transmission zeros are located at 0.64 GHz, 0.96 GHz, 1.42 GHz, 2.23 GHz, 2.55 GHz, 3.15 GHz, and 3.41 GHz, the upper stopband insertion loss is greater than 20 dB from 2.46 GHz to 6.28 GHz.

Moreover, Table 2 illustrates the comparisons of measured results for several dual-band bandpass filter structures. Compared with other balanced filters [1], [2], [3], [6], [9], the proposed two dual-band bandpass filters have more transmission zeros near the passbands, and the upper stopband for the two bandpass filters can stretch up to $3.3f_1$ ($|S_{21}| < $ -20 dB) and $3.1f_1$ ($|S_{21}| < $ -20 dB), respectively. Further circuit size reduction can be also realized by using folded lines in multi-layer circuits.

Table 2: Comparisons of measured results for some dual-band filters

Filter Structures	TZs, $\lvert S_{21}\rvert$	Bandwidth (%)	Stopband $\lvert S_{21}\rvert$, dB	Center Frequencies (GHz)
Ref. [1]	5	14%,10%	<-20, $3.0f_1$	1.80, 3.50
Ref. [2]	2	2.0%, 3.0%	<-20, $1.6f_1$	0.87, 1.27
Ref. [3]	3	25.7%, 15.3%	< -20, $3.0f_1$	1.32, 2.67
Ref. [6]-I	4	8.55%, 5.93%	<-20, $2.7f_1$	1.87, 2.53
Ref. [9]	3	5.3%, --	<-20, $3.0f_1$	2.0, 4.0
These works	5	8.1%, 5.3%	<-20, $3.3f_1$	1.93, 2.42
	7	8.2%, 5.1%	<-20, $3.1f_0$	2.04, 2.32

IV. CONCLUSION

In this paper, two novel high selectivity dual-band bandpass filters with multiple transmission zeros using dual-mode resonators are proposed. Five and seven transmission zeros from direct current to second harmonic can be used to realize high passband selectivity, and the bandwidth and center frequencies of the two passbands can be adjusted independently by changing the coupling even/odd mode of the coupled lines and characteristic impedance of the ring resonators. The proposed dual-band bandpass filters have advantages of high selectivity, wide upper stopband, simple structure, and high passband

isolation. Good agreements between simulated and measured responses of the structures are demonstrated, indicating good candidates for planar microwave dual-band circuits and systems.

ACKONWLEGEMENT

REFERENCES

[1] L. Gao and X. Y. Zhang, "High-selectivity dual-band bandpass filter using a quad-mode resonator with source-load coupling," *IEEE Microw. Wireless Compon. Lett.*, vol. 23, no. 9, pp. 474-476, Sep. 2013.

[2] A. Genc, R. Baktur, and R. J. Jost, "Dual-bandpass filters with individually controllable passbands," *IEEE Trans. Compon. Packag. Manuf. Technol.*, vol. 3, no. 1, pp. 105-112, Jan. 2013.

[3] Y. L. Wu, S. Y. Zhou, W. W. Zhang, M. B. Liao, and Y. A. Liu, "Coupled-line dual-band bandpass filter with compact structure and wide stopband," *IET Electron. Lett.*, vol. 50, no. 3, pp. 187-189, Feb. 2014.

[4] C. Zhao, W. Feng, and W. Che, "Ultra-wideband balanced bandpass filters based on transversal signal-interference concepts," *The Applied Computational Electromagnetics Society Journal*, vol. 30, no. 10, pp. 1232-1237, Oct. 2016.

[5] W. Feng, M. Hong, and W. Che, "High selectivity balanced filter based on transversal signal-interaction concepts," *The Applied Computational Electromagnetics Society Journal*, vol. 30, no. 10, pp. 1257-1264, Oct. 2016.

[6] Y. M. Chang, W. Feng, and W. Che, "Dual-band bandpass filters with high isolation using coupled lines," *International Journal of Electron.*, vol. 101 no. 3, pp. 372-383, Feb. 2016.

[7] I. Wolff, "Microstrip bandpass filter using degenerate modes of a microstrip ring resonator," *IET Electron. Lett.*, vol. 8, pp. 302-303, 1972.

[8] W. J. Feng, W. Q. Che, and Q. Xue, "Balanced filters with wideband common mode suppression using dual-mode ring resonators," *IEEE Trans. Circuits Syst. I: Regular Papers*, vol. 62, no. 6, pp. 1499-1507, June 2015.

[9] M. K. Mohd Salleh, M. T. Ali, M. K. Hamzah, and G. Prigent, "Series coupled microwave ring resonators," *2011 IEEE International Conference on Sys. Engin. and Techn. (ICSET)*, pp. 125-127, 2011.

[10] R. G.García, R. L. Sánchez, D. Psychogiou, and D. Peroulis, "Single/multi-band Wilkinson-type power

dividers with embedded transversal filtering sections and application to channelized filters," *IEEE Trans. Circuits Syst. I: Regular Papers*, vol. 62, no. 6, pp. 1518-1527, June 2015.

[11] M. K. Mohd Salleh, G. Prigent, O. Pigaglio, and R. Crampagne, "Quarter-wavelength side-coupled ring resonator for bandpass filters," *IEEE Trans. Microw. Theory Techn.*, vol. 56, no. 1, pp. 156-162, Jan. 2008.

[12] W. J. Feng, X. Gao, W. Q. Che, and Q. Xue, "Bandpass filter loaded with open stubs using dual-mode ring resonator," *IEEE Microw. Wireless Compon. Lett.*, vol. 25, no. 5, pp. 295-297, May 2015.

Rui Yin was born in Chenzhou, Hunan Province, China, in 1993. She received the B.E. degree from the Hunan Institute of Humanities, Science and Technology, Loudi, China, in 2014. From October 2015, she went to Nanjing University of Science and Technology (NUST), Nanjing, China, for further study as a postgraduate.

Her research interests include power dividers and planar microstrip filters.

Wenjie Feng was born in Shangqiu, Henan Province, China, in 1985. He received the B.Sc. degree from the First Aeronautic College of the Airforce, Xinyang, China, in 2008, the M.Sc. and Ph.D. degrees from the Nanjing University of Science and Technology (NUST), Nanjing, China, in 2010, 2013.

From November 2009 to February 2010, March 2013 to September 2013, he was a Research Assistant with the City University of Hong Kong. From October 2010 to March 2011, he was an exchange student with the Institute of High-Frequency Engineering, Technische Universität München, Munich, Germany. He is currently a Professor with the Nanjing University of Science and Technology, Nanjing, China. He has authored or co-authored over 120 internationally referred journal and conference papers. His research interests include ultra-wideband (UWB) circuits and technologies, substrate integrated components and systems, planar microstrip filters and power dividers, LTCC circuits.

Feng is a Reviewer for over ten internationally referred journal and conference papers, including eight IEEE Transactions and IEEE Letters. He now serves as an Associate Editor for *IET Electronics Letters*, *IEEE Access and International Journal of Electronics*.

Wenquan Che received the B.Sc. degree from the East China Institute of Science and Technology, Nanjing, China, in 1990, the M.Sc. degree from the Nanjing University of Science and Technology (NUST), Nanjing, China, in 1995, and the Ph.D. degree from the City University of Hong Kong (CITYU), Kowloon, Hong Kong, in 2003.

In 1999, she was a Research Assistant with the City University of Hong Kong. From March 2002 to September 2002, she was a Visiting Scholar with the Polytechnique de Montréal, Montréal, QC, Canada. She is currently a Professor with the Nanjing University of Science and Technology, Nanjing, China. From 2007 to 2008, she conducted academic research with the Institute of High Frequency Technology, Technische Universität München. During the summers of 2005–2006 and 2009–2012, she was with the City University of Hong Kong, as Research Fellow and Visiting Professor. She has authored or co-authored over 200 internationally referred journal papers and international conference papers. She has been a Reviewer for *IET Microwaves*, *Antennas and Propagation*. Her research interests include electromagnetic computation, planar/coplanar circuits and subsystems in RF/microwave frequency, microwave monolithic integrated circuits (MMICs) and medical application of microwave technology.

Che is a Reviewer for the IEEE Transactions on Microwave Theory and Techniques, IEEE Transactions on Antennas and Propagation, IEEE Transactions on Industrial Electronics, and IEEE Microwave and Wireless Components Letters. She was the recipient of the 2007 Humboldt Research Fellowship presented by the Alexander von Humboldt Foundation of Germany, the 5th China Young Female Scientists Award in 2008 and the recipient of Distinguished Young Scientist awarded by the National Natural Science Foundation Committee (NSFC) of China in 2012.

Optimization of Wireless Power Transmission Systems with Parasitic Wires

K. H. Yeap, A. R. C. Cheah, K. Hirasawa, K. C. Yeong, K. C. Lai, and H. Nisar

Universiti Tunku Abdul Rahman, Kampar, Perak 31900, Malaysia
yeapkh@utar.edu.my, agnescheah_91@hotmail.com, hirasawa@ieee.org, yeongkc@utar.edu.my,
laikc@utar.edu.my, humaira@utar.edu.my

Abstract − We present a rigorous optimization method to design wireless power transmission (WPT) systems. In order to optimize the power coupled to the receiver, reactive parasitic components are integrated into the system. Simulated annealing is implemented in conjunction with the method of moments to determine the optimum parameters for the design. By carefully adjusting the geometry, size, position and properties of the parasitic wires, it could be seen that the peak efficiency and effective distance for power coupling could be significantly improved. The result shows that the implementation of a square parasitic wire gives better performance than a circular one. A WPT system with a square reactive wire gives respectively a 0.79% and 0.07λ improvement in peak efficiency and effective distance compared to its zero-impedance counterpart. By inserting two square reactive wires with the transmitter sandwiched in between, the peak efficiency and effective distance are found to have increased respectively by 3.37% and 0.18λ, compared to that with a single reactive wire.

Index Terms − Antennas, method of moments, simulated annealing, wireless power transmission.

I. INTRODUCTION

Throughout years of research and development, workable wireless power transmission (WPT) systems have already been made available [1]. However, there are still open issues and challenges yet to be overcome. According to the findings by Kurs et al. [2], the power efficiency of a WPT system operating at 9.9 MHz deteriorates below 50% at a distance greater than 2 m. It is apparent that the power transmission efficiency of a WPT system is constrained by the distance the power can be effectively transferred to the receiver. As a result of this, existing WPT devices can only operate at very close proximity. The rapid attenuation of the propagating energy is clearly one of the critical issues which require an immediate and effective solution.

The installation of parasitic elements into a wireless communication system is found to have significantly reduced signal attenuation and increase signal quality. In [3], a comparison was made between the performance of a conventional Yagi-Uda transmitting antenna and that with parasitic elements constructed around it. It is found that the system installed with parasitic elements outperformed the conventional Yagi-Uda system -- the signal to interference noise ratio (SINR) and the voltage standing wave ratio (VSWR) were both significantly minimized.

In this paper, parasitic components with different geometries and designs are introduced into a near field WPT system (henceforth referred to as the PWPT system). Analyses are performed to investigate their effectiveness in enhancing the efficiency of the system. To obtain the optimum parameters for the designs, Simulated Annealing or SA optimization algorithm has been applied in conjunction with the method of moments (MoM) when computing the parameters.

In order to present a complete scheme, brief overview on the MoM and SA are first given in the subsequent sections. This is followed by a detailed elucidation on the design of the PWPT systems. Analyses based on the results obtained from the MoM and SA are discussed. A summary is then provided at the final section of the paper.

II. METHOD OF MOMENTS

The MoM is used to solve an *E*-field integral equation on the transmitting, receiving and loaded parasitic wire. The radius of the wire is assumed to be much smaller than the operating wavelength ($a << \lambda$) and the antenna length ($a << L$). The surface current on the wire is therefore axially directed, i.e., only the component flowing along the *z*-axis is considered.

The current *J* along the wire is approximated as the summation of piecewise sinusoidal expansion functions as:

$$J = \sum_{n=1}^{M} I_n J_n, \qquad (1)$$

where J_n denotes the current on the nth segment, *M* the number of expansion functions and I_n is the unknown coefficient to be obtained [4]. Then, the *E*-field integral equation on the wire is solved by the MoM and the following matrix equation is obtained:

$$[Z + Z_L][I] = [V], \qquad (2)$$

where $[Z]$ is an M x M impedance matrix and the element Z_{ij} is the mutual impedance between the i th and j th segment. The M x M matrix $[Z_L]$ has only non-zero diagonal elements equal to impedance values at a receiving and a loading point [4]. Also, the unknown current $[I]$ and known feed voltage $[V]$ are an M-dimensional column vector. The element of $[V]$ corresponding to a feed point is only non-zero and is assumed 1 V. By solving (2), the antenna characteristics, including currents at the feed point I_t and receiving point I_r can then be obtained.

In this paper the efficiency is defined as:

$$e_f = \frac{P_r}{P_t} = \frac{\text{Re}(V_r I_r)}{\text{Re}(V_t I_t)}, \qquad (3)$$

where $V_t = 1$ V at the feed point and,

$$V_r = -R_r I_r, \qquad (4)$$

at the receiving point (R_r Ω is loaded). At the inductive load on the parasitic wire we have:

$$V_p = -jX_p I_p, \qquad (5)$$

where jX_p is a loaded reactance on a parasitic wire. Load values R_r and jX_p in (4) and (5) are included in $[Z_L]$ in (2). The efficiency in (3) is then calculated by including the mutual coupling effects between all wires rigorously.

III. SIMULATED ANNEALING

The minimization search process in SA starts by generating an arbitrary initial point, x^0. Based on the cost function C defined with respect to a scale proportional to the temperature T, the initial temperature TI and the temperature length TL are set. The function of TL is to determine the extent of search for the algorithm. The algorithm will then start by generating a random neighboring solution, x'. Once the two points – $C(x')$ and $C(x^{new})$ – are obtained, the cost function difference ΔC, which shows the difference between the existing point and the new point, can be determined by [5]:

$$\Delta C = C(x') - C(x^{new}). \qquad (6)$$

If ΔC is greater than 0, that means the current point x^{new} is better than the initial point x' and x^{new} will overwrite x'. Otherwise, the program will generate a variable q, where the value of q will be randomly picked between 0 and 1. It then decides to accept or reject the inferior point. The decision to accept or reject the inferior point is based on the result obtained from the comparison between the calculated acceptance probability and the variable q. The calculated acceptance function A_p is given in (7) below:

$$A_p = \exp\left(\frac{\Delta C}{T}\right), \qquad (7)$$

where T denotes the temperature. If the calculated value is near 1.0, then the new solution is taken to be better than its previous one. Otherwise, a value which is near 0 indicates that the new solution is worse. After each iteration, the temperature T will decrease systematically according to the annealing schedule defined by the user. When T approaches zero, the probability the algorithm accepts a worse solution decreases correspondingly as well. The process will then repeat starting from generating a random neighboring solution until the algorithm reaches its termination condition, i.e., maximum number of iterations, computational time or maximum number of evaluations of the objective function.

IV. WIRELESS POWER TRANSMISSION

In this section, analyses on the performance of various WPT systems are performed. These include the conventional WPT (CWPT) system and the systems with parasitic elements installed into them (PWPT). Various designs of the PWPT system are proposed. The operating frequency used throughout the research work here is 1 GHz, voltage source at the transmitter V_s is 1 V and the load at the receiver R_L is 100 Ω.

A. Conventional WPT systems

In a CWPT system, energy is transferred via free space from an antenna connected to the source and it is then collected by the antenna at the receiving end [6]. A simplified schematic for the system is shown in Fig. 1. As can be observed from the figure, the transmitting antenna T_X is separated from the receiving antenna R_X by certain distance. The efficiency of wireless power transfer is determined when R_X is placed at different distance away from T_X. Here, center-fed half-wave dipoles are used for both antennas. The parameters used in the CWPT system are summarized in Table 1.

Figure 2 depicts the efficiency of the CWPT system, computed based on the MoM. As can be observed from the figure, the efficiency of the system decreases proportionately with distance as expected. This is to say that, the farther the receiver is placed away from the transmitting source, the more drastic the energy coupled to the antenna degrades. This has clearly restricted the distance for effective energy transmission in a CWPT system. Table 2 summarizes the peak efficiency and the effective distance of the CWPT system. Since the energy of the CWPT system deteriorates along with distance, the peak efficiency for wireless transmission is taken at the starting point where R_X is placed at distance 0.3λ away from the transmitter. For effective energy transmission, the minimum efficiency is set to be at 5%. This is to say that, the effective distance is taken at the position where the efficiency drops to 5%.

B. WPT systems with single parasitic wire

Figures 3 and 4 depict, respectively, the design configurations of the PWPT systems with a square and a circular parasitic wire installed into them. The distance between T_x and P_x is given as D_{Px} and that between P_x and R_x is given as D_{Rx}. To give a fair comparison between

the two PWPT systems, the sizes of both parasitic wires are set to be identical.
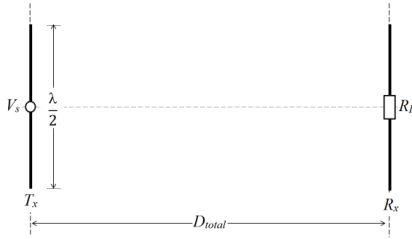
Fig. 1. A conventional WPT system, with half-wave dipole antennas.
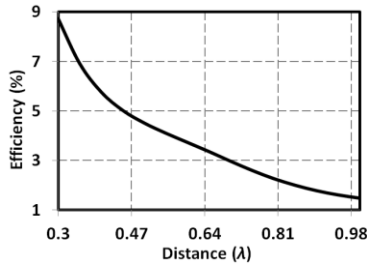
Fig. 2. Power efficiency of a conventional WPT system as a function of distance from the transmitter.
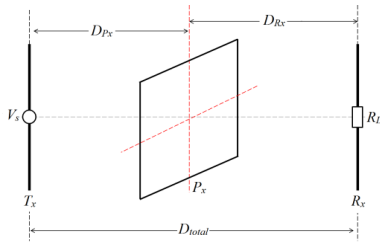
Fig. 3. A WPT system with a square parasitic wire.
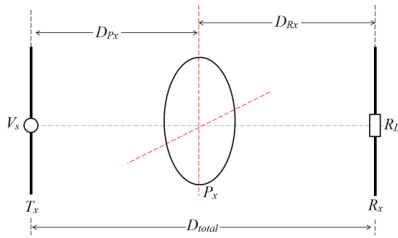
Fig. 4. A WPT system with a circular parasitic wire.

Table 1: Parameters of a CWPT system

Variables	Dimensions
T_X height (λ)	0.5
T_X radius (λ)	0.005
R_X height (λ)	0.5
R_X radius (λ)	0.01

Table 2: Performance of the CWPT system

Performance	CWPT
Peak efficiency (%)	8.72
Effective distance (λ)	0.45

In order to determine the optimum parameters for the design, the geometry, size, properties and position of the parasitic wires are taken as variables for optimization. Like the case of the CWPT system, the receiving antenna R_x is allowed to vary so as to compute the efficiency of the power coupled to it at varying distances from T_x. When performing optimization, P_x has been set to be either no impedance loading (i.e., both resistance R_p and reactance X_p are zero) or impedance loading (i.e., R_p and X_p are allowed to vary). The parameters for a square and circular parasitic wire P_x, obtained using SA are summarized in Table 3. Upon close inspection on the table, it can be observed that the resistance value R_P obtained using SA is 0 Ω for optimum performance. Since resistance contributes to loss, it is therefore to be minimized in order to ensure efficient energy coupling. Reactance loading is one of the methods to improve antenna characteristics [4] and it is interesting to introduce it to optimize near-field power efficiency.

Figures 5 to 8 depict the power efficiency of the reactive WPT systems in terms of distance λ. The curves in the figures show that the system obtained its peak efficiencies at about 0.37λ using a square and circular P_x. The peak efficiency is some distance away from the transmitter because the receiver antenna may collect additional energy scattered from the parasitic wire in addition to the reception of direct electromagnetic energy from the transmitter [7]. The curves in the figures show that the system gives the highest power efficiency with the presence of an inductive P_x. Table 4 summarizes the peak efficiencies and effective distances found in Figs. 5 to 8. As shown in the table, the peak power efficiency when a reactive component is included in P_x is about 0.79% (for the square geometry) to 1.0% (for the circular geometry) higher than that of the zero-impedance case. It can also be seen that a square reactive P_x performs better than its circular counterpart. The peak efficiency attained using the square P_x is 0.69% higher than the circular P_x. When the receiver moves farther away from the transmitter, the power coupled to the receiver antenna tends to decrease. Hence, the power efficiency decreases accordingly as well. As depicted in Figs. 7 and 8, at a distance of 0.5λ to 1λ, the efficiencies using the square and circular P_x are comparable. By comparing Tables 2 and 4, it can be seen that the peak efficiency of the inductive square PWPT system is about 5.82% higher than that of the CWPT system. The effective distance of the square P_x is also approximately 0.32λ farther than that of the CWPT system.
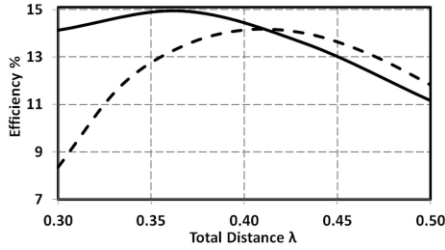
Fig. 5. Performance of WPT systems with zero-impedance (dashed line) and inductive (solid line) square parasitic wires, at distance 0.3λ to 0.5λ.
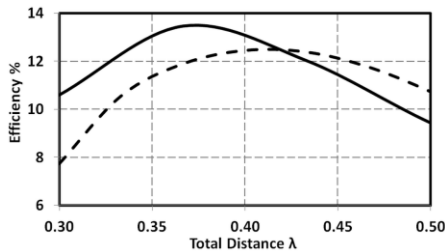
Fig. 6. Performance of WPT systems with zero-impedance (dashed line) and inductive (solid line) circular parasitic wires, at distance 0.3λ to 0.5λ.
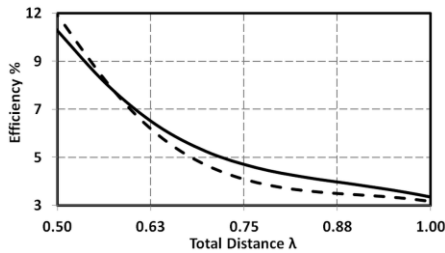
Fig. 7. Performance of WPT systems with zero-impedance (dashed line) and inductive (solid line) square parasitic wires, at distance 0.5λ to 1.0λ.
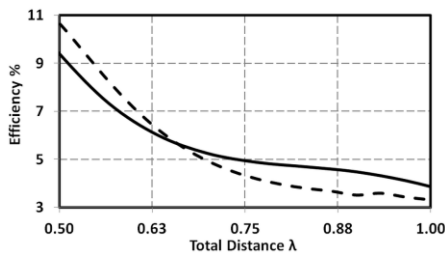
Fig. 8. Performance of WPT systems with zero-impedance (dashed line) and inductive (solid line) circular parasitic wires, at distance 0.5λ to 1.0λ.

In order to obtain a better insight on the effect of inductance in parasitic wires, the current generated at each part of the system is investigated. Figure 9 illustrates the points and expansion functions set up in the MoM to calculate the current in the square PWPT system. It is clear from the figure that each point and expansion function corresponds to different parts of the system. The impedances Z_p are placed at expansion function $n = 21$ and 33. It is to be noted that Z_p is a complex variable which consists of $R_p = 0$ Ω and $X_p = 17.26$ Ω, i.e., $Z_p = 0 + j17.26$ Ω.

Figures 10 to 12 depict the current distribution at the transmitter, receiver and parasitic wire when the receiver is 0.5λ away from the transmitter. According to the curves shown in Fig. 7, the efficiency of the power coupled to the receiver is about 10.76% when $D_{RX} = 0.5λ$. Due to the effect of the parasitic element the real part of I_t has a peak and the imaginary part of I_t has a notch to reduce the imaginary power which stores the energy. Then real power P_t is transferred efficiently to the receive antenna. Therefore the current at the feed has a notch as shown in Fig. 10. At the receive antenna the larger receive power is transferred and the current amplitude has a peak as shown in Fig. 11.

Table 3: Parameters of a PWPT system

Variables	Square P_X	Circular P_X
P_X length (λ)	1.0	1.00
P_X radius (λ)	0.005	0.005
D_{PX} (λ)	0.161	0.154
D_{RX} (λ)	0.189	0.209
R_P (λ)	0.00	0.00
X_P (λ)	17.26	13.27

Table 4: Performance of a PWPT system

Configuration	Peak Efficiency (%)	Effective Distance (λ)
Lossless square geometry ($R_P = X_P = 0$)	13.75	0.70
Inductive square geometry ($R_P = 0$, $X_P = 17.26$ Ω)	14.54	0.77
Lossless circular geometry ($R_P = X_P = 0$)	12.85	0.70
Inductive circular geometry ($R_P = 0$, $X_P = 13.27$ Ω)	13.85	0.77
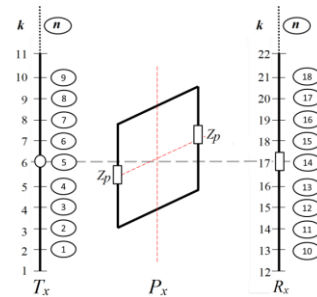
Fig. 9. Points (k) and expansion function (n) numbering of the PWPT system.
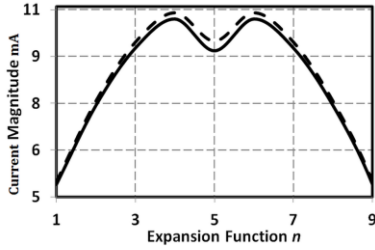
Fig. 10. Current distributions at the transmitter of a WPT system with an inductive (solid line) and zero-impedance (dashed line) parasitic wire.
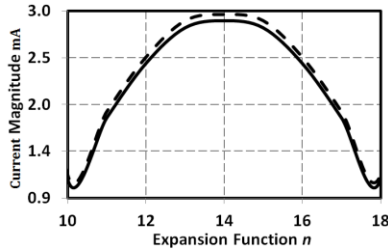
Fig. 11. Current distributions at the receiver of a WPT system with an inductive (solid line) and zero-impedance (dashed line) parasitic wire.
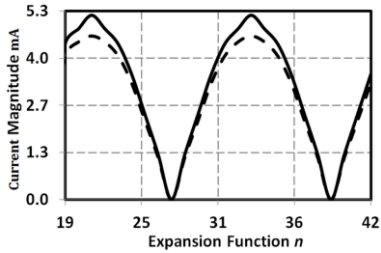
Fig. 12. Current distributions at the parasitic wire of a WPT system with an inductive (solid line) and a zero-impedance (dashed line) parasitic wire.

It can be seen from Fig. 12 that the current distributions produced at expansion functions ranging from $n = 19$ to 24 and 31 to 36 are higher than those at $n = 25$ to 30 and 37 to 42. The former two ranges of expansion functions correspond to the left and right parts of the wire which are in parallel with the antennas and the wave polarization; whereas, the latter two correspond to the top and bottom parts which are in orthogonal. The result indicates that higher current is produced at the wire when it is parallel to the direction of the wave polarization. With proper orientation, it can be seen that the wire in parallel with the direction of wave polarization is longer for a square wire compared to a circular one. Hence, the system with a square P_x exhibiting better performance than that with a circular P_x is to be expected. Figure 12

also shows that the current distributions found at the inductive wire are higher than those parts with zero impedance. Indeed, the current peaks at $n = 21$ and 33, i.e., the positions where both inductances are placed. It is therefore evident that the presence of inductance (which is an energy storage device) helps to enhance the current produced at the parasitic wire.

C. WPT systems with dual parasitic wires

Based on the results obtained in the previous section, it can be concluded that a PWPT system enhances both the peak efficiency and the effective distance of wireless power transmission and that a square (rather than a circular) P_x is a better option for the system. In this section, an additional square P_x is therefore proposed to be integrated into the system to study its impact on performance enhancement.

Figure 13 shows the configuration of a PWPT system with dual parasitic wires (henceforth referred to as the PPWPT system). Two parasitic wires P_{x1} and P_{x2} are placed along the same axis with the transmitting antenna T_x sandwiched in between both. The distance between P_{x1} and T_x is denoted as D_{Px1} and that between P_{x2} and T_x as D_{Px2}. Similarly, the distance between the receiving antenna and P_{x1} is denoted as D_{Rx}. The optimum parameters for an inductive system are tabulated in Table 5. The performance of the system with respect to the total distance D_{total} from R_x to P_{x2} is shown in Fig. 14. The peak efficiency and effective distance of the system are summarized in Table 6. It is apparent from the table that the effective distance of the system is found to have extended close to 1λ. This is to say that, the distance it takes for the efficiency of the system with dual P_x to drop below 5% is relatively longer than that with a single P_x. By comparing Tables 4 and 6, it can also be seen that the magnitude of the peak efficiencies and effective distances are about 3.37% higher and 0.18λ farther than those with a single P_x. Hence, it can be concluded here that the performance of the WPT system can be significantly improved when the number of parasitic wires increases. This is particularly so, when the wires are placed at the front and back of the transmitting antenna.
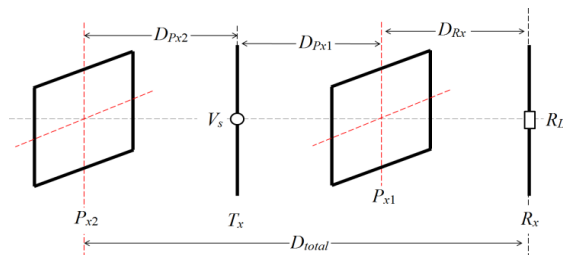
Fig. 13. A PPWPT system.
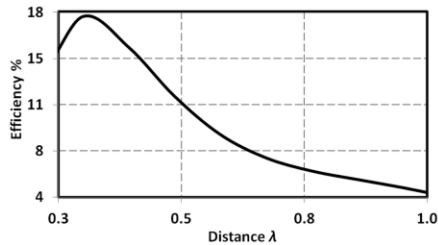
Fig. 14. Performance of a PPWPT system.

Table 5: Parameters of a PPWPT system

Variables	Dimensions
P_X length (λ)	1.0
P_X radius (λ)	0.005
D_{PX1} (λ)	0.173
D_{PX2} (λ)	0.30
D_{RX} (λ)	0.173
R_P (Ω)	0
X_P (Ω)	19.33

Table 6: Performance of a PPWPT system

Performance	Inductive Square PWPT
Peak efficiency (%)	17.91
Effective distance (λ)	0.95

V. CONCLUSION

In this paper, the optimization procedure of wireless power transmission systems with parasitic wires is presented in detail. By implementing the MoM in conjunction with SA, the geometry, size, properties and position of the parasitic wires are optimized. When a square inductive wire is integrated in between the transmitter and receiver, the result gives the highest peak power efficiency and longest effective distance for power coupling. The performance of the system can be further enhanced when an additional square wire is placed at the back of the transmitter.

REFERENCES

[1] X. Jin, J. M. Caicedo, and M. Ali, "Near-field wireless power transfer to embedded smart sensor antennas in concrete," *ACES J.*, vol. 30, no. 3, pp. 261-269, 2015.

[2] A. Kurs, A. Karalis, R. Moffatt, J. D. Joannopoulos, P. Fisher, and M. Soljacic, "Wireless power transfer via strongly coupled magnetic resonances," *Science Express*, vol. 317, no. 5834, pp. 83-86, 2007.

[3] M. D. Migliore, D. Pinchera, and F. Schettino, "A simple and robust adaptive parasitic antenna," *IEEE Transactions on Antennas and Propagation*, vol. 53, no. 10, pp. 3262-3272, 2005.

[4] K. Hirasawa and M. Haneishi, *Analysis, Design and Measurement of Small and Low-Profile Antennas*. 1st ed., Boston, USA, Artech House, 1992.

[5] D. Bertsimas and J. Tsitsiklis, "Simulated annealing," *Statistical Science*, vol. 8, no. 1, pp. 10-15, 1993.

[6] A. R. C. Cheah, K. H. Yeap, K. C. Yeong, and K. Hirasawa, "Biologically inspired wireless power transmission system: A review," In: V. Ponnusamy, N. Zaman, T. J. Low, and A. H. M. Amin, *Biologically-Inspired Energy Harvesting Through Wireless Sensor Technologies*. 1st ed., Hershey PA, USA, IGI Global, pp. 27-50, 2016.

[7] A. R. C. Cheah, K. H. Yeap, K. Hirasawa, K. C. Yeong, and H. Nisar, "Optimization of a wireless power transmission system", in Proc. of the Int. MultiConference of Engineers and Computer Scientists; Hong Kong, pp. 590-592, 2016.

Kim Ho Yeap received his Ph.D. from Universiti Tunku Abdul Rahman. He is currently an Associate Professor in Universiti Tunku Abdul Rahman.

Agnes Ruey Chyi Cheah received her B. Eng. (Hons) Electronics Engineering at Tunku Abdul Rahman University. She is currently pursuing her Master degree in the same university.

Kazuhiro Hirasawa received his Ph.D. from Syracuse University, USA in 1971. He is currently an Emeritus Professor in University of Tsukuba, Tsukuba, Japan. His research interests include wireless power transmission.

Kee Choon Yeong received his Ph.D. from Rensselaer Polytechnic Institute. He is currently an Assoc. Professor in Universiti Tunku Abdul Rahman.

Koon Chun Lai received his Ph.D. from Universiti Tunku Abdul Rahman. He is currently an Assistant Professor in Universiti Tunku Abdul Rahman.

Humaira Nisar received her Ph.D. from Gwangju Institute of Science and Technology. She is currently an Associate Professor at Universiti Tunku Abdul Rahman.

Low-profile Hybrid-mode Antenna Providing Near-hemispherical Field-of-view Coverage

Ren Wang, Bing-Zhong Wang, Xiao Ding, and Changhai Hu

Institute of Applied Physics
University of Electronic Science and Technology of China, Chengdu, 610054, China
rwang.uestc@hotmail.com, bzwang@uestc.edu.cn, xding@uestc.edu.cn

Abstract ─ The hybrid-mode model (HMM) combining monopole and dipole radiation modes can provide near-hemispherical coverage but has a high profile. To reduce the profile of HMM, a modified HMM is presented in this paper using a dipole radiator and a magnetic current loop radiator. Based on the modified model, a low-profile on-board antenna is proposed. When the side length of the ground is infinite, the 3-dB beamwidths in the *xz* plane and *yz* plane of the proposed antenna are both 180°. When the side length of the ground is finite, the proposed antenna can provide a near-hemispherical field-of-view coverage. The design example demonstrates the practicability of the modified HMM and the proposed antenna can be used in wide-angle scanning arrays and rich-multipath communication systems.

Index Terms ─ Broad beam, hemispherical coverage, hybrid modes, low profile, wide-angle scanning.

I. INTRODUCTION

The hybrid-mode model (HMM) combining monopole radiation mode and dipole radiation mode is a traditional and popular method to obtain near-hemispherical field-of-view coverage [1], [2]. The dipole model and monopole mode can provide horizontally polarized patterns and vertically polarized patterns [3]-[5], respectively. The peaks and nulls of the HMM can be controlled by adjusting the monopole height and dipole length. Therefore, the HMM is possible to achieve a near hemispherical field-of-view coverage [1], [2]. Recently, the hemispherical coverage was also obtained using half-loop antennas [6], [7], which can be considered as the transformation of HMM.

In wide-angle scanning arrays, the HMM has been used to design broad-beam elements. In [8], [9], two parasitic monopoles with reactive loads were placed near a driving dipole to broaden the E-plane pattern of dipole antennas. In [10]-[12], the dipole-mode radiator surrounded by monopoles was used to achieve near-hemispherical coverage for wide-angle scanning phased arrays. In wireless communication systems, a single antenna with dipole radiation mode and monopole

radiation mode can provide antenna diversity and improve system reliability in rich multipath environments [13], [14]. In radio astronomy systems (RAS), the HMM with near-hemispherical field-of-view coverage and polarization discrimination capability is particularly important [15], [16]. To use HMM antenna in RAS, a theoretical sensitivity analysis of HMM antennas was proposed in [17] and [18]. In addition, the HMM has been used to simplify hemispherical two-dimensional angular space null steering [19].

Although the HMM has been extensively investigated and widely used in several applications, the high profile of monopole radiator is an existing problem to this model and the mentioned HMM antennas have a profile of approximately λ/4, where λ is the wavelength corresponding to center operation frequency. To reduce the profile, the HMM is modified in this paper by using a dipole radiator and a magnetic current loop (MCL) radiator. The radiation patterns of MCL and dipole can cover the low elevation area and high elevation area, respectively. Therefore, a near-hemispherical coverage can be obtained by optimizing the weights of the two radiation modes. Based on the modified hybrid-mode model (MHMM), a low-profile on-board antenna with near-hemispherical field-of-view coverage is proposed. When the side length of the ground is infinite, the 3-dB beamwidths in the *xz* plane and *yz* plane of the proposed hybrid-mode antenna are both 180°. The design example demonstrates the practicability of the MHMM and the proposed antenna can be used in wide-angle scanning arrays and radio astronomy systems.

II. LOW-PROFILE ANTENNA WITH NEAR-HEMISPHERICAL COVERAGE

A. Low-profile hybrid-mode model

To lower the profile of HMM, a substitute with a similar radiation pattern of monopole radiator should be found firstly. According to [20] and [21], MCL has a monopole-like radiation pattern. Therefore, the MCL is used to replace the monopole radiator in this paper. The radiation pattern of MCL is shown in Fig. 1. The models are simulated by CST Microwave Studio. Because CST

software has no magnetic currents, the MCL on an electric wall is represented with an electric current loop with a radius of $\lambda/40$ placed on an infinite magnetic wall in the simulation, i.e., the complementary structure of MCL. The distance between the loop and the magnetic wall is $\lambda/40$, where λ is the free-space wavelength. From Fig. 1, we can see that the pattern of MCL and that of monopole are very similar. Therefore, a low-profile MHMM with near-hemispherical pattern may be obtained if the MCL and dipole can be excited at the same time.
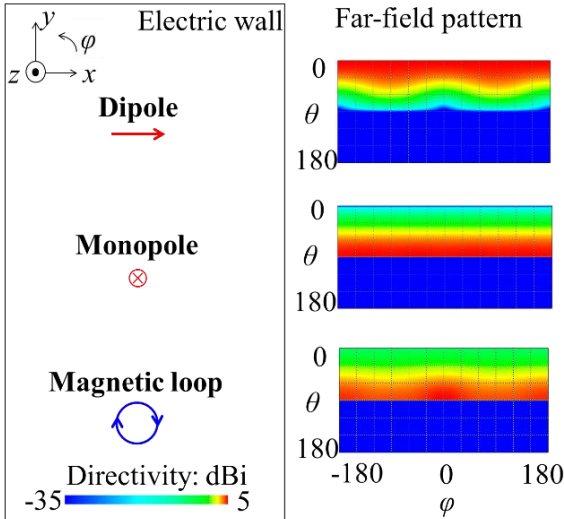
Fig. 1. Dipole, monopole, and magnetic current loop on an infinite electric wall and their radiation patterns. The models are simulated by CST Microwave Studio.

B. Antenna with near-hemispherical coverage

Based on the MHMM combining a dipole radiator and a MCL radiator, a microstrip on-board antenna at L band is proposed to provide a near-hemispherical pattern. Geometry of the proposed antenna is shown in Fig. 2 and its optimum dimensions are marked in the figure. This antenna is composed of two kinds of dielectric substrates and three layers of copper patches. The top substrate has a thickness of 4 mm and a relative dielectric constant of 2.65; the bottom substrate has a thickness of 1.6 mm and a relative dielectric constant of 4.4. A narrow rectangular patch and a circular patch are printed on the top and bottom substrates. The narrow patch can provide a radiation similar to a dipole on an electric wall. The circular patch with opened edge is fed from the center and the electric field is from the patch to the ground, therefore, the edge of the circular patch can be equivalent to a MCL radiator. The two patches are connected with a copper via and fed from the backside with a 50-Ω coaxial probe. The whole dimension of the radiation patches is approximately $0.2\lambda \times 0.1\lambda \times 0.03\lambda$.
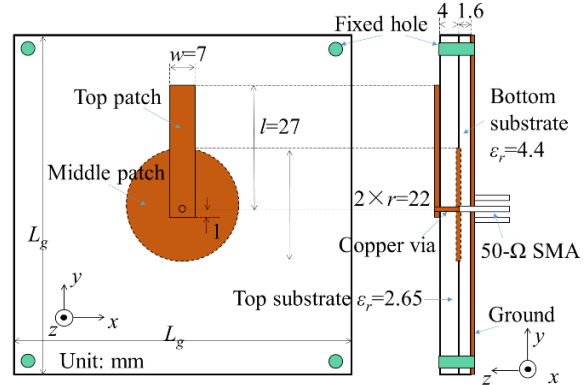
Fig. 2. Geometry of the hybrid-mode antenna. The color brown represents copper material. The dimensions are optimized by CST.

According to the boundary condition, the radiation pattern of MCL radiator, similar to monopole, can cover to the ground plane only when the ground is infinite. As a result, the HMM, as well as the MHMM, can potentially provide a hemispherical coverage only when the ground is infinite. To eliminate the effect of ground, the ground is set to be infinite when optimizing parameters. The simulated reflection coefficient of the proposed antenna with an infinite ground is shown in Fig. 3. The simulated band with S11 below -10 dB includes 1.6 GHz, which is the desired operating frequency.
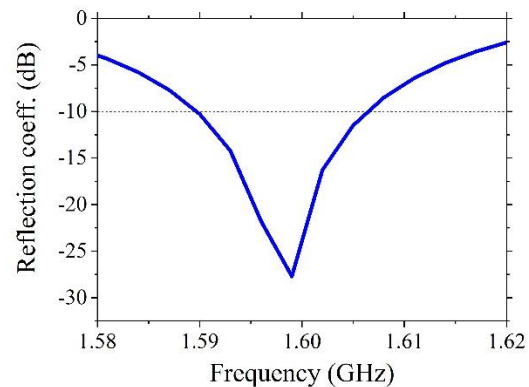
Fig. 3. Simulated reflection coefficient of the hybrid-mode antenna with an infinite ground.

For the hemispherical-pattern antenna, radiation on each direction should be equal. However, the exact condition is difficult to practically use in the numerically calculation. To simplify the hemispherical-pattern condition, a five-equal-points condition is used to optimize the radiation pattern. The five key control points of a hemispherical pattern are ($\theta=90°$, $\varphi=90°$), ($\theta=90°$, $\varphi=180°$), ($\theta=90°$, $\varphi=270°$), ($\theta=90°$, $\varphi=0°$), and

($\theta=0°$), respectively. Because the five-equal-points condition is a necessary but not sufficient condition for the hemispherical pattern, the radiation pattern should be checked after optimization. The simulated radiation patterns at 1.6 GHz of the proposed antenna with an infinite ground are shown in Fig. 4. When the ground is infinite, the 3-dB beamwidths in the *xz* plane and *yz* plane are both 180° and the pattern fluctuation in the *xy* plane is less than 5 dB. In the design process, we consider a hemispherical pattern is obtained when the 3-dB beamwidths in both *xz* plane and *yz* plane are 180°.
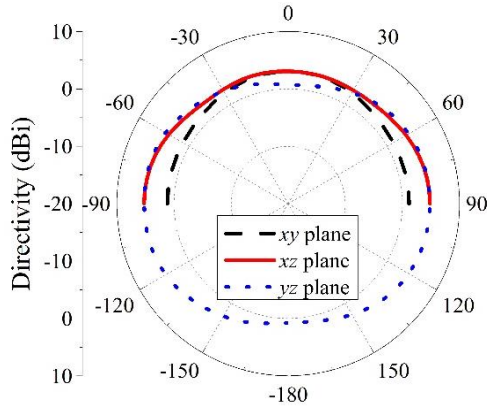
Fig. 4. Simulated patterns at 1.6 GHz of the hybrid-mode antenna with an infinite ground.

From the principle of the MHMM, the dipole can cover the high-elevation area and the MCL can cover the low-elevation area. A near-hemispherical coverage may obtained only when the appropriate weight factors of the two kinds of radiations are satisfied. For the proposed hybrid-mode antenna, the weight factor can be adjusted by structure parameters. Next, the effect of the length *l* of the narrow rectangular patch is analyzed as an example, as shown in Fig. 5 and Fig. 6.

The simulated patterns at 1.6 GHz in the *xz* plane of the proposed hybrid-mode antenna corresponding to different length *l* are shown in Fig. 5. From these figures, we can see that the φ component can cover the high-elevation area and the θ component can cover the low-elevation area. The polarization discrimination capability is particularly important to rich multipath environments [13], [14]. When the length *l* increases, the radiation of φ component is strengthened and the radiation of θ component is weakened. When *l* is less than 27 mm, the radiation maximum of θ component is larger than φ component and the sum radiation pattern has a depression around 0°. When *l* is more than 27 mm, the radiation maximum of θ component is smaller than φ component and sum radiation pattern has a narrow broadside pattern. When *l*=27 mm, the two components have similar radiation maximums and a broad coverage of the sum radiation is obtained.
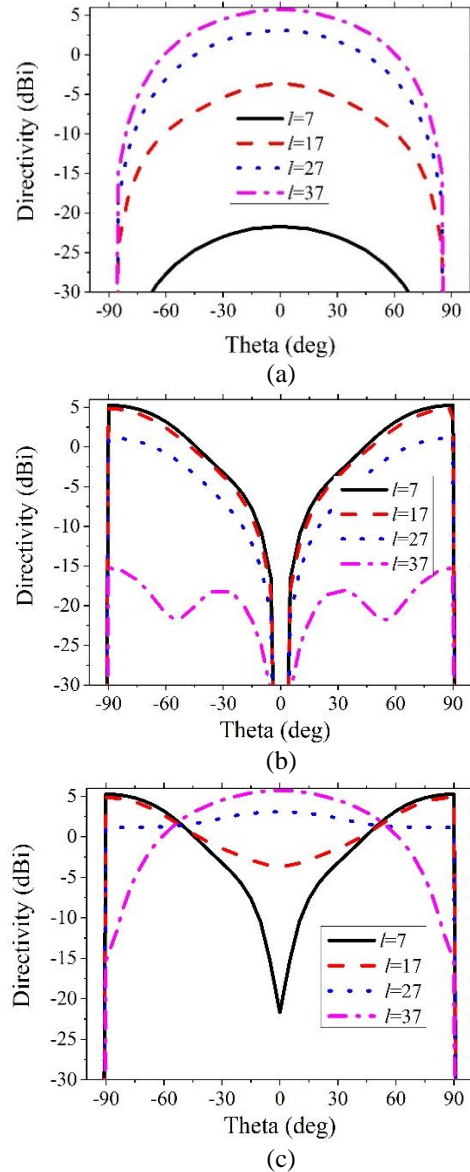
Fig. 5. Simulated patterns at 1.6 GHz in the *xz* plane corresponding to different length *l* of the narrow rectangular patch: (a) φ component, (b) θ component, and (c) vector sum of the two components. The unit of *l* is mm.

The simulated patterns at 1.6 GHz in the *yz* plane of the proposed hybrid-mode antenna corresponding to different length *l* are shown in Fig. 6. The radiation of θ component is much larger than φ component. The low cross polarization radiation in the *yz* plane of the MHMM antenna is similar to that of the monopole radiator in HMM, which indicates that the MCL will not cause cross polarization in the H-plane of dipoles [8], [9]. This phenomenon is appropriate for wide-angle scanning arrays. When *l*=27 mm, a 180° coverage of θ component is obtained. Therefore, the radiations of

the proposed antenna can be controlled by adjusting structure parameters to realize a near-hemispherical coverage.
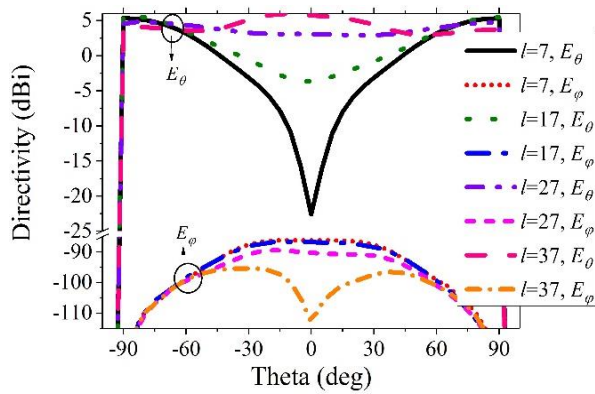
Fig. 6. Simulated patterns at 1.6 GHz in the *yz* plane corresponding to different length *l* of the narrow rectangular patch. The unit of *l* is mm.

The above discussions are under the circumstance of infinite ground. The performances of the proposed hybrid-mode antenna with finite ground are shown in the following. Two prototypes of the proposed antenna, with $L_g=\lambda$ and $L_g=4\lambda$ respectively, are fabricated. Two photographs of unassembled and assembled antenna with $L_g=\lambda$ are shown in Fig. 7.

(a)

(b)
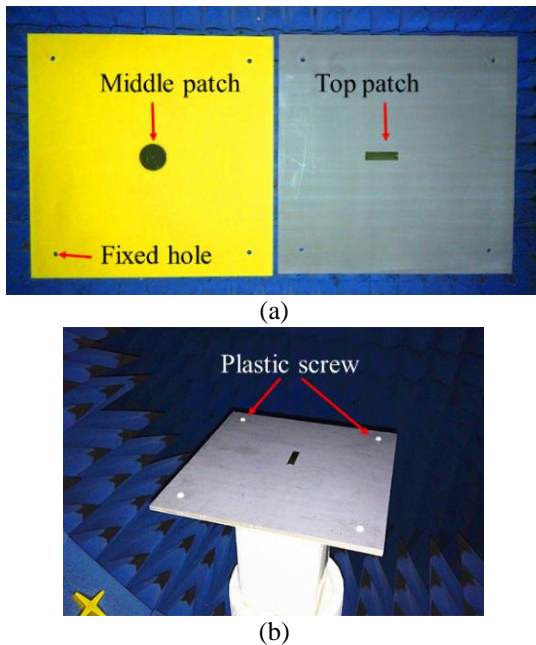
Fig. 7. Photographs of the hybrid-mode antenna with $L_g=\lambda$: (a) unassembled antenna and (b) assembled antenna.

The simulated and measured reflection coefficients of the proposed antenna are shown in Fig. 8. From Fig. 8, we can see that the resonant frequency changes little with L_g. The ground size has little effect on the resonant frequency in both simulated results and the measured results. The simulated and measured bands with S_{11} below -10 dB both include 1.6 GHz. The measured resonant frequency has a little move toward the high frequency because of the machining error, which includes the soldering error, the assembled error, and parameters error of practical substrate.
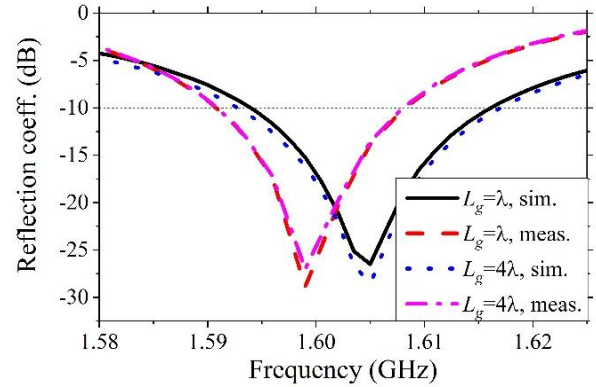
Fig. 8. Simulated and measured reflection coefficients of the hybrid-mode antenna when $L_g=\lambda$ and $L_g=4\lambda$. The resonant frequency changes little with L_g.

The far-field radiation pattern is measured in a microwave anechoic chamber. The simulated and measured radiation patterns of the proposed antenna with different L_g are shown in Fig. 9. When L_g is λ, the simulated 3-dB beamwidth in the *xz* plane is 128° and the measured one is 130°; the simulated 3-dB beamwidth in the *yz* plane is 147° and the measured one is 140°. When $L_g=4\lambda$, the simulated 3-dB beamwidth in the *xz* plane is 152° and the measured one is 161°; the simulated 3-dB beamwidth in the *yz* plane is 175° and the measured one is 172°. The 3-dB beamwidths in the *xz* plane and *yz* plane both increase with L_g. From the simulated and measured results, we can also see that when $L_g=4\lambda$, the side lobe level is significantly lower than that in the case of $L_g=\lambda$. The proposed antenna has a broad beam and can provide a near-hemispherical coverage with a finite ground.

The measured efficiencies and peak gains of the proposed antenna are shown in Fig. 10. When $L_g=\lambda$ and $L_g=4\lambda$, the measured efficiencies are both more than 60% in the frequency band of 1.59 GHz-1.62 GHz. The peak gain in the case of $L_g=\lambda$ is a little higher than that in the case of $L_g=4\lambda$ because the radiation beam is broader when $L_g=4\lambda$.

(a)

(b)
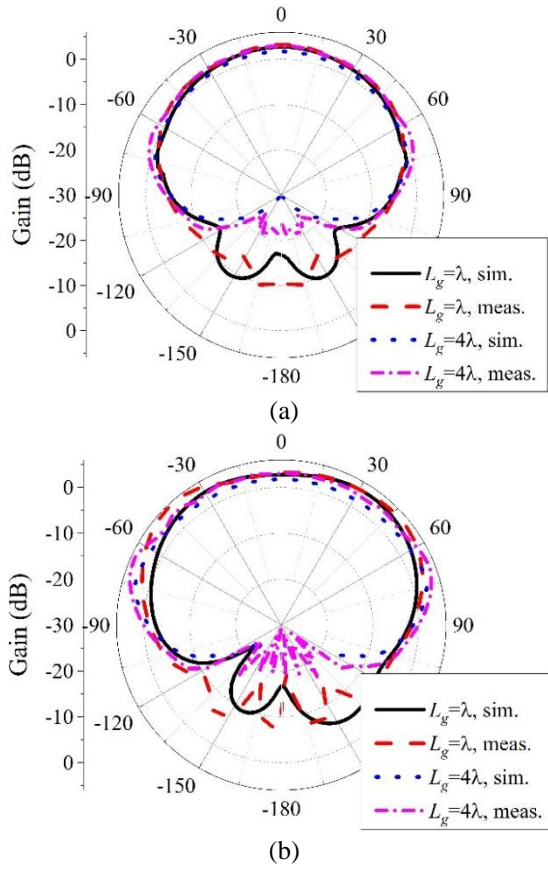
Fig. 9. Simulated and measured: (a) *xz* plane patterns and (b) *yz* plane patterns at 1.6 GHz of the hybrid-mode antenna. The 3-dB beamwidths in the *xz* plane and *yz* plane both increase with L_g.
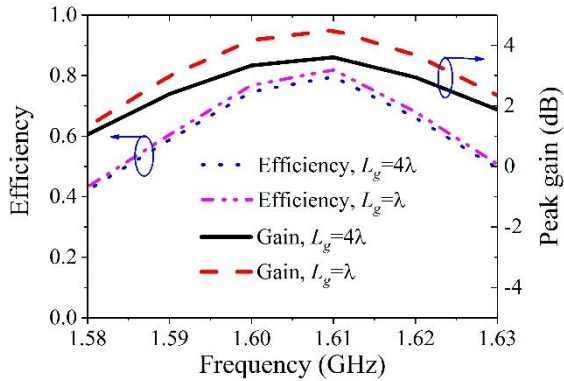
Fig. 10. Measured efficiencies and peak gains of the hybrid-mode antenna when $L_g=\lambda$ and $L_g=4\lambda$. The peak gain in the case of $L_g=\lambda$ is a little higher than that in the case of $L_g=4\lambda$ because the radiation beam is broader when $L_g=4\lambda$.

III. CONCLUSION

In this paper, a low-profile hybrid-mode model is proposed to obtain a near-hemispherical coverage. Based on this model, an on-board antenna is designed. When the side length of the ground is infinite, the 3-dB beamwidths in the *xz* plane and *yz* plane are both 180°. When the side length of the ground is finite, the proposed antenna can provide a near-hemispherical coverage. The design example demonstrates the practicability of the proposed model and the proposed antenna can be used in wide-angle scanning arrays and rich-multipath communication systems.

REFERENCES

[1] E. E. Altshuler, "A monopole loaded with a loop antenna," *IEEE Trans. Antennas Propag.*, vol. 44, no. 6, pp. 787-791, June 1996.

[2] E. E. Altshuler and D. S. Linden, "Design of a loaded monopole having hemispherical coverage using a genetic algorithm," *IEEE Trans. Antennas Propag.*, vol. 45, no. 1, pp. 1-4, Jan. 1997.

[3] H. L. Sneha, S. Hema, and R. M. Jha, "Analytical estimation of radar cross section of arbitrary compact dipole array," *ACES Journal*, vol. 29, no. 9, pp. 726-734, 2014.

[4] N. Ojaroudi, G. Noradin, and O. Yasser, "Bandwidth improvement of omni-directional monopole antenna with a modified ground plane," *ACES Journal*, vol. 29, no. 4, pp. 328-334, 2014.

[5] P. Zibadoost, J. Nourinia, C. Ghobadi, S. Mohammadi, A. Mousazadeh, and B. Mohammadi, "Full band MIMO monopole antenna for LTE systems," *ACES Journal*, vol. 29, no. 1, pp. 54-61, 2014.

[6] P. A. Turalchuk, D. V. Kholodnyak, and O. G. Vendik, "A novel low-profile antenna with hemispherical coverage suitable for wireless and mobile communications applications," in *Proc. IEEE LAPC*, Loughborough, UK, pp. 337-340, Mar. 2008.

[7] P. Nayeri, A. Z. Elsherbeni, R. Hasse, and D. Kajfez, "Half-loop segmented antenna with omni-directional hemispherical coverage for wireless communications," *ACES Express Journal*, vol. 1, no. 3, pp. 88-91, Mar. 2016.

[8] K. Nishizawa, H. Miyashita, S. Makino, and K. Sawaya, "Broadening beamwidth of E-plane radiation pattern of a dipole antenna with loaded monopole elements," in *Proc. IEEE Antennas Propag. Society Int. Symposium*, Monterey, USA, pp. 3984-3987, June 2004.

[9] K. Nishizawa, H. Miyashita, S. Makino, and K.

Sawaya, "Broad beamwidth and cross polarization free dipole antennas with reactive loaded monopoles," *IEEE Trans. Antennas Propag.*, vol. 55, no. 5, pp. 1230-1238, May 2007.

[10] C. N. Hu, C. S. Chuang, D. C. Chou, and K. J. Liu, "Design of the cross-dipole antenna with near-hemispherical coverage in finite-element phased array by using genetic algorithms," in *Proc. IEEE Int. Conference Phased Array Systems Technol.*, Dana Point, USA, pp. 303-306, June 2000.

[11] M. Scott, "A printed dipole for wide-scanning array application," in *Proc. 11th Int. Conference Antennas Propag.*, Manchester, UK, pp. 37-40, Apr. 2001.

[12] R. Wang, B.-Z. Wang, X. Ding, Z.-S. Gong, Y. Yang, and Y.-Q. Wen, "A wide-angle scanning array based on image theory and time reversal synthesis method," in *Proc. 2015 IEEE Int. Symposium Antennas Propag.*, Vancouver, Canada, pp. 2495-2496, July 2015.

[13] P. S. Kildal, C. Orlenius, and J. Carlsson, "OTA testing in multipath of antennas and wireless devices with MIMO and OFDM," *Proc. IEEE*, vol. 100, no. 7, pp. 2145-2157, July 2012.

[14] A. Hussain, P. Kildal, and A. Al-Rawi, "Efficiency, correlation, and diversity gain of UWB multiport self-grounded bow-tie antenna in rich isotropic multipath environment," in *Proc. 9th Int. Workshop Antenna Technol.*, Karlsruhe, Germany, pp. 336-339, Mar. 2013.

[15] R. Karlsson, "Theory and applications of tri-axial electromagnetic field measurements," Ph.D. dissertation, Dept. Astronomy Space Phys., Uppsala University, Uppsala, 2005.

[16] T. D. Carozzi and G. Woan, "A generalized measurement equation and van Cittert-Zernike theorem for wide-field radio astronomical interferometry," *Monthly Notices Royal Astron. Soc.*, vol. 395, no. 3, pp. 1558-1568, May 2009.

[17] D. S. Prinsloo, P. Meyer, R. Maaskant, and M. Ivashina, "Design of an active dual-mode antenna with near hemispherical field of view coverage," in *Proc. Int. Conference Electromagnetics Advanced App.*, Torino, Italy, pp. 1064-1067, Sep. 2013.

[18] D. S. Prinsloo, R. Maaskant, M. V. Ivashina, and P. Meyer, "Mixed-mode sensitivity analysis of a combined differential and common mode active receiving antenna providing near-hemispherical field-of-view coverage," *IEEE Trans. Antennas Propag.*, vol. 62, no. 8, pp. 3951-3961, Aug. 2014.

[19] Y. Li, Z. Zhang, C. Deng, and Z. Feng, "A simplified hemispherical 2-D angular space null steering approach for linearly polarization," *IEEE Antennas Wireless Propag. Lett.*, vol. 13, pp. 1628-1631, 2014.

[20] L. Economou and R. J. Langley, "Patch antenna equivalent to simple monopole," *Electron. Lett.*, vol. 33, no. 9, pp. 727-729, Apr. 1997.

[21] T. Kaufmann and C. Fumeaux, "Low-profile magnetic loop monopole antenna based on a square substrate-integrated cavity," *Int. Journal Antennas Propag.*, vol. 3, pp. 1-6, 2015.

Ren Wang was born in Anhui Province, China, in 1990. He received the B.S. degree in Electronic Information Science and Technology from University of Electronic Science and Technology of China (UESTC), Chengdu, in 2014. He is currently working toward the Ph.D. degree in Radio Physics at UESTC. His main research interests include time-reversed technique, compact multiport antenna, and phased array.

Bing-Zhong Wang received the Ph.D. degree in Electrical Engineering from the University of Electronic Science and Technology of China (UESTC), Chengdu, in 1988.

He joined UESTC in 1984 and is currently a Professor there. He has been a Visiting Scholar at the University of Wisconsin-Milwaukee, a Research Fellow at the City University of Hong Kong, and a Visiting Professor at the Pennsylvania State University, University Park. His current research interests are in the areas of computational electromagnetics, antenna theory and techniques, and time-reversed electromagnetics.

Xiao Ding received the B.S. and M.S. degrees in the Communication Engineering and Electromagnetic Field and Microwave Engineering, respectively, from Guilin University of Electronic Science and Technology (GUET), Guilin, China, in 2004 and 2007, respectively, and the Ph.D. degree in Radio Physics from University of Electronic Science and Technology of China (UESTC), Chengdu, China, in 2014. He joined the UESTC in 2014. In 2013, he was a Visiting Scholar at the South Dakota School of Mines and Technology, SD, USA. His research interests include short-wave, ultrashort-wave wire antennas and reconfigurable antenna and its' applications.

Changhai Hu was born in Chongqing City, China, in 1987. He received the B.S. and M.S. degrees in the Computer Science and Technology and Electromagnetic Field and Microwave Technology, from Southwest Jiaotong University (SWJTU), Chengdu, China, in 2010 and 2014, respectively. He is currently working toward the Ph.D. degree in Radio Physics at University of Electronic Science and Technology of China (UESTC), Chengdu, China. His main research interests include ultra-wide band antenna and phased array.

A Comparative Study of Opposition-Based Differential Evolution and Meta-Particle Swarm Optimization on Reconstruction of Three Dimensional Conducting Scatterers

Mojtaba Maddahali [1], Ahad Tavakoli [1], and Mojtaba Dehmollaian [2]

[1] Department of Electrical Engineering
Amirkabir University of Technology, Tehran, 15875-4413, Iran
tavakoli@aut.ac.ir, maddahali@aut.ac.ir

[2] School of Electrical and Computer Engineering
University of Tehran, Tehran, 14395-515, Iran
m.dehmollaian@ece.ut.ac.ir

Abstract ─ In this paper, opposition-based differential evolution and Meta-particle swarm optimization is applied to reconstruct three dimensional conducting scatterers. Rational Bezier surfaces are utilized to model the shape of the scatterers. The mathematical representation of this surfaces are expanded in terms of Bernstein polynomials. The unknown coefficients of these polynomials depend on a few control points in space. An optimization method is used to find the location of the control points such that a specific measure of the difference between radar cross section (RCS) of the reconstructed and the original target is minimized. Physical optics (PO) approximation is used to find the RCS of a reconstructed scatterer in each iteration of the proposed algorithm. Simulation results show that these algorithms are very stable in the presence of noise.

Index Terms ─ Differential evolution, inverse scattering, particle swarm optimization, physical optics approximation, rational Bezier surfaces.

I. INTRODUCTION

Shape reconstruction of two and three dimensional conducting targets by using electromagnetic scattered field is a typical problem in inverse scattering and has many applications in radar target detection and identification and remote sensing. Several algorithms and approaches have been developed to deal with problem of inverse scattering such as level set schemes [1], linear sampling [2], time reversal [3]. Employing optimization methods to reconstruct the targets is another approach which have been widely used in recent years, mainly because of their simplicity of implementation [4]. Optimization methods are categorized into two main approaches of deterministic and stochastic methods.

The main drawback of the deterministic methods is that they may trap in a local minimum. However, in stochastic algorithms, population of a random solution is used and therefore, better solutions help other members to emerge from local minima. Differential evolution (DE), particle swarm optimization (PSO), and genetic algorithm (GA) are the most popular schemes among stochastic algorithms. A comparative study of the performance of DE and PSO, to reconstrcut two dimensional conducting cases is reported in [4]. The performance of the genetic algorithm to reconstrcut two and three dimensional conducting scatterers has been reported in [5-6]. However, there is no report on the performance of DE and PSO for three dimensional conducting scatterers.

The main purpose of this paper is to compare a variant of DE, known as opposition-based differntial evoloution (ODE) and a version of PSO known as Meta-PSO when applied to three dimensional problems. These two algorithms have a good peformance over traditional optimization methods [12-13]. In reconstruction of two and three dimensional scatterers, the shape of the scatterers could be parameterized in terms of some specific polynomials. In the inverse problem [6], the coefficients of these polynomials are optimized such that electromagnetic scattered fields of the reconstructed shape and the original shape approach each other.

One of the few commonly used polynomials in this field are Bernstain polynomials [8]. In this paper, we also use Bernstein polynomials as the basis to expand the surface equation. The coefficients of this polynomial are extracted in the inverse problem using two approaches of ODE and Meta-PSO.

In summary, the novelty of this paper is two folds: (i) in the previous paper DE and PSO methods are discussed and compared for reconstruction of two-

dimensional objects, but in this paper, we analysize and compare those algorithms to deal with three-dimensional structures, (ii) in this comparison, we use more recent versions of DE and PSO methods, namely ODE and Meta-PSO. These newer approaches are more efficient compared with traditional ones that are discussed in the litreture.

This paper is organized as follows. Section II presents the forward formulation. The inverse formulation is discussed in Section III. The two optimization algorithms are briefly reviewed in Section IV. Simulation results and concluding remarks are represented in Sections V and VI respectively.

II. FORWARD FORMULATION

The back scattered electromagnetic field from a large conducting scatterer can be expressed by physical optics approximation as follows [7]:

$$\vec{E}_s(r) = -\frac{j}{\lambda}\frac{\exp^{-jk_0 r}}{r}(\hat{k}.\vec{I})\vec{E}_0, \vec{I} = \int \hat{n}(r') \exp^{j2\vec{k}.\vec{r}'} ds', \quad (1)$$

where λ is the operating wavelength, $\vec{E}_0$ is the polarization of the incident field, $\hat{k}$ is the wave vector, $\vec{r}'$ is the source point position vector, ds' is the surface differential element, $\hat{n}$ is the surface normal vector at the source, k_0 is the free space wave number and $\vec{I}$ is the physical optics integral. In order to compute the PO integral, the surface geometry is modeled by rational Bezier patches. These patches are parametric and can be expressed in terms of Bernstein polynomials as follows [8]:

$$\vec{r}(u,v) = \frac{\sum_{i=0}^{m}\sum_{j=0}^{n} w_{ij}\vec{b}_{ij} B_i^m(u) B_j^n(v)}{\sum_{i=0}^{m}\sum_{j=0}^{n} w_{ij} B_i^m(u) B_j^n(v) w_{ij}}, \quad (2)$$

where $\vec{b}_{ij} \in R^3$, $i = 0,\ldots,m$, $j = 0,\ldots,n$, are the Bezier patches control points, $w_{ij} \in R$, $i = 0,\ldots,m$, $j = 0,\ldots,n$, are the associated weights, the integers m and n are degrees of the surface, and u and v are the parameters that shape the surface. The Bernstein polynomial, $B_i^m(u)$ is expressed as:

$$B_i^m(u) = \frac{m!}{i!(m-i)!} u^i (1-u)^{m-i}, 0 \le u \le 1. \quad (3)$$

Geometrical parameters of Bezier surfaces such as orthogonal and position vectors could be easily calculated in terms of Bernstein polynomials. In the literature, these surfaces are categorized into three groups of singly–curved, doubly–curved and plane patches. The PO integral over these surfaces could be simply evaluated by the stationary phase method and analytical techniques [9], [10] and [11].

III. INVERSE FORMULATION

The objective of the shape reconstruction process is to find the shape of the scatterer such that the difference between radar cross section of the reconstructed and the original shape is minimized. For this purpose, the shape of the scatterer is represented by Bernstein polynomials and the coefficients of these polynomials are calculated through optimization. More precisely, the coefficients of these polynomials are determined such that the cost function is minimized with respect to some specific control points. The cost function is defined as:

$$f(p) = \frac{\sum_{\omega}\sum_{\theta}\sum_{\phi} | \sigma_{\theta\phi\omega}^{true} - \sigma_{\theta\phi\omega}^{rec} |}{\sum_{\omega}\sum_{\theta}\sum_{\phi} | \sigma_{\theta\phi\omega}^{true} |}, \quad (4)$$

where $\sigma_{\theta\phi\omega}^{true}$ and $\sigma_{\theta\phi\omega}^{rec}$ are radar-cross sections of the original and the reconstructed scatterer, respectively. In this paper, opposition-based differential evolution and Meta-particle swarm optimization algorithm are used as the optimization techniques.

A. Opposition-based differential evolution algorithm

In the first step of this algorithm NP parameter vectors of D-dimension are created, that NP is the population of optimization algorithm and D is the number of unknown parameters. Also the opposite of this parameter vecors are produced as follows [12]:

$$ox_{i,j} = a_j + b_j - x_{i,j}, \quad (6)$$

where the minimum and maximum of the jth dimension of the parameter vector are a_j and b_j. Then $ox_{i,j}$ is replaced by $x_{i,j}$ If the cost function of $ox_{i,j}$ is lower than $x_{i,j}$. Next, a mutant vector and a trial vector are created for each target as follows:

$$v_i^{G+1} = x_{r1}^G + F.(x_{r2}^G - x_{r3}^G), \quad (7)$$

$$u_i^{G+1} = (u_{1i}^{G+1}, u_{2i}^{G+1}, \ldots, u_{Di}^{G+1}), \quad (8)$$

where

$$u_{ji,G+1} = \begin{cases} v_{ji}^{G+1} & if \quad h_j \leqslant H \quad or \quad j = l \\ x_{ji}^{G+1} & if \quad h_j > H \quad and \quad j \ne l \end{cases}. \quad (9)$$

In these equations, G is the generation index, r_1, r_2, r_3 are three mutually different integers that also differ from target index i, F is the mutuant constant that is taken to be 0.8, h_j is a random number in the interval [0,1], $H\varepsilon(0,1)$ is a crossover constant selected by the user, and l is a random integer $\in [1,2,\ldots,D]$.

If the cost function of u_i^{G+1} is lesser than x_i^{G+1}, then x_i^{G+1} is changed by the trial vector. In the last step a random number between [0,1] is generated and if it is lower than the preselected jumping rate J_r then $x_{i,j}^G$ is compared with the opposite of it and the one with a

lower cost function is selected as the member of the current population.

B. Opposition-based Meta particle swarm algorithm

For simplicity, first, ordinary PSO is explained and then it is generalized to Meta PSO. If a problem has D unknown parameters, a group of NP_1 parameter vectors x_i, $i = 1,....,NP_1$, each with dimension D are produced. Each vector has an initial random velocity to search the solution space. This velocity is updated in each iteration of the optimization algorithm as:

$$v_t = w \times v_{t-1} + c_1(pbest_{t-1} - x_{t-1}) + c_2(gbest_{t-1} - x_{t-1}), \quad (11)$$

where w is the inertial weight that scale the old velocity, $pbest_{t-1}$ is the previous best solution of each member before iteration t, and $gbest_{t-1}$ is the previous best solution of all members before iteration t. Moreover, c_1 and c_2 are the two preselected numbers that are usually chosen to be 0.49, 1.49, or 2 [13]. With this velocity, the position of the members are updated in each iteration as:

$$x_t = x_{t-1} + v_t. \quad (12)$$

If the current member has a lower cost function than $pbest_{t-1}$, then, $pbest_{t-1}$ is replaced by this member. The same procedure is used to update $gbest_{t-1}$.

In Meta-PSO, several groups are randomly generated. The velocity of one particle from each group is changed as follows [9]:

$$v_t = w \times v_{t-1} + c_1(pbest_{t-1} - x_{t-1}) + c_2(gbest_{t-1} - x_{t-1}) + c_3(sbest_{t-1} - x_{t-1}), \quad (13)$$

where $sbest_{t-1}$ is the best previous location of all members of all groups. c_1, c_2, and c_3 are three preselected numbers that are selected to be 2 here. In this problem, NS groups, where each group has NP_1 members are considered. For the purpose of comparing Meta-PSO with ODE, we choose $NS \times NP_1$ as equal to the population of ODE. Similarly to the previous algorithm a random number between [0,1] is generated and if it is lower than the preselected jumping rate J_r, then $x_{i,j}^G$ is compared with the opposite of it and the one with a lower cost function is selected as the member of the current population.

V. NUMERICAL RESULTS

For the first example, the reconstruction of a perfectly conducting conical curved sector with the height of 1 m, the bottom radius of 1m, and the top radius of 0.5 m is presented. In the reconstruction procedure, the degree of the surface and weight coefficients are selected a-priori. In addition, we assume that the surface curvature is negative. This cone is modeled by 3x2 control points.

The parameters of the Meta-PSO and the opposition-based differential evolution are listed in Table 1 and Table 2. The original cone is compared with the ODE and the Meta-PSO reconstructed cones in Fig. 1 (a) and Fig. 1 (b) respectively. A comparison between the cost function of these two algorithms at various iterations are depicted in Fig. 1 (c). The scattered filed is evaluated at 45 points that are located at $\theta = 60°, 75°, 90°, 105°, 120°$ and at frequencies of $0.4, 0.8, 1.2 GHz$. As shown, ODE converges better than Meta-PSO. The RCS of the original and the reconstructed cones for $45° < \theta < 120°$ and $\phi = 45°$ are presented in Fig. 1 (d). A very good agreement is observed between the RCS of the original cone and the reconstructed one. Also for comparison purpose, the RCS simulated with the moment method is depicted in the same figure. The good agrement between the full wave method and physical optic method can be seen. To measure the accuracy of the reconstruction procedure, the shape error function is defined as [6]:

$$RECP = \frac{1}{N_{vnet}} \left(\sum_{i=0}^{m} \sum_{j=0}^{n} \frac{\| \Delta^{0,1} p_{i,j}^{true} - \Delta^{0,1} p_{i,j}^{reco} \|^2}{\| \Delta^{0,1} p_{i,j}^{true} \|^2} + \frac{\| \Delta^{1,0} p_{i,j}^{true} - \Delta^{1,0} p_{i,j}^{reco} \|^2}{\| \Delta^{1,0} p_{i,j}^{true} \|^2} \right)^{1/2}, \quad (14)$$

where $N_{vnet} = 2mn + m + n$ is the number of elements in the vector net and $\| p_{i,j} \|$ is the Euclidean norm given by:

$$\| p_{i,j} \| = \sqrt{x_{i,j}^2 + y_{i,j}^2 + z_{i,j}^2}. \quad (15)$$

$\Delta^{0,1} p_{i,j}$ and $\Delta^{1,0} p_{i,j}$ are related to the control points as:

$$\Delta^{0,1} p_{i,j} = p_{i,j+1} - p_{i,j} \quad \Delta^{1,0} p_{i,j} = p_{i+1,j} - p_{i,j}. \quad (16)$$

The cost function in this problem is defined on RCS. Because the RCS does not change with the displacement of the shape, we obtain a transformation of the object in the reconstruction. Finally, we define the reconstruction error in a form that does not change with the displacement of the shape.

Table 1: Opposition-based differential evolution parameters

Jumping Rate	Mutant Constant	Crossover Rate
0.5	0.8	0.5

Table 2: Meta-particle swarm optimization parameters

Jumping Rate	w	c1	c2	c3
0.5	0.9-0.4	2	2	2

(a)

(b)

(c)

(d)
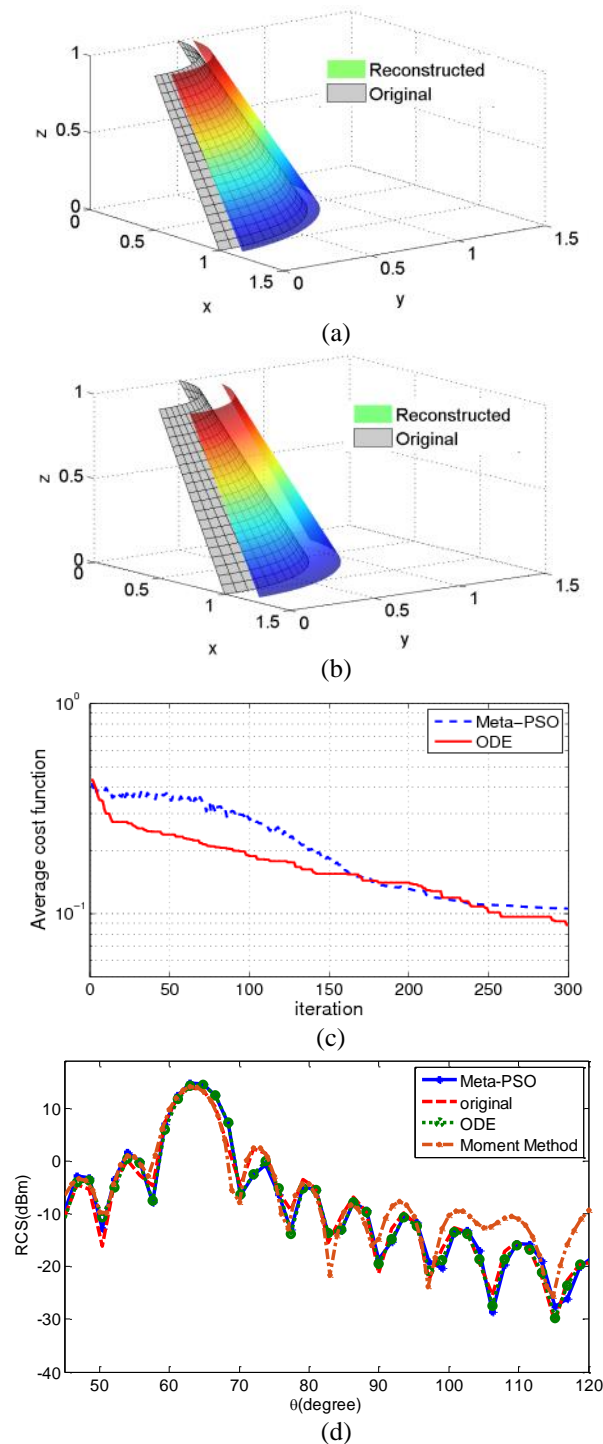
Fig. 1. (a) Comparison between original and reconstructed target by ODE, (b) comparison between original and reconstructed target by Meta-PSO, (c) cost function of ODE and Meta-PSO, and (d) comparison between RCS of reconstructed and original shape at $f = 1.2 GHZ$.

In the simulation, the average reconstruction errors for five simulation of ODE and Meta-PSO are 0.16 and

0.07 respectively. The stability of the algorithm is tested in the presence of an additive noise of [6]:

$$\sigma^n_{\theta,\varphi,\omega} = \sigma_{\theta,\varphi,\omega} + \sqrt{\overline{\sigma^2_{\theta,\varphi,\omega}}} \times (NL) \times (rand), \qquad (17)$$

where $\sigma_{\theta,\phi,\omega}$ is the RCS of the original shape, *NL* is the noise level, *rand* is a random number between [0,1], and is the root mean square of the original RCS. The reconstruction error with an additive noise level of 0.1 is 0.1764 for ODE and 0.1532 for Meta-PSO. Therefore, given that the reconstruction method is stable in the presence of additive noise in the radar cross-section, it can be concluded that if we use the measurement data for reconstruction, this method is also usable.

For the second example, the reconstruction of perfectly conducting $90°$–cylindrical sector, with the height and radius of 1m is considered. Similarly, Fig. 2 shows the target and the simulation results. The average shape error obtained by ODE is 0.2174 and by Met-PSO is 0.2138. If the number of optimization steps was increased, the radar cross section of the reconstructed body would be closer to the original object.

(a)

(b)

(c)

(d)
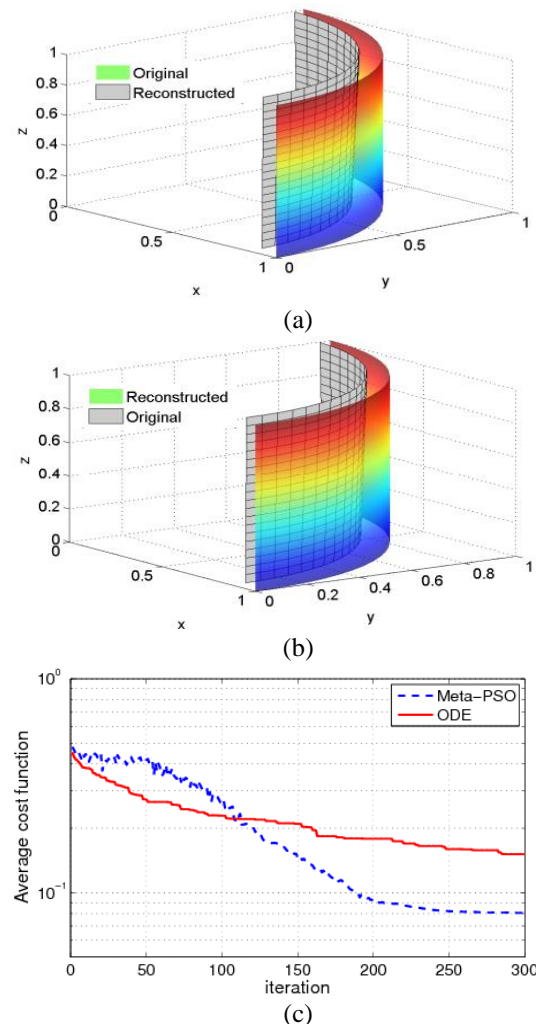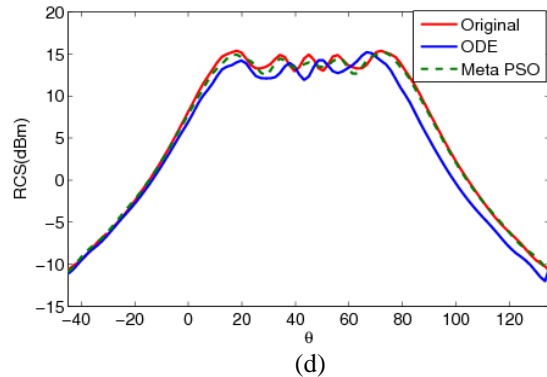
Fig. 2. (a) Comparison between original and reconstructed target by ODE, (b) comparison between original and reconstructed target by Meta-PSO, (c) cost function of ODE and Meta-PSO, and (d) comparison between RCS of reconstructed and original shape at $f = 1.2GHZ$.

VI. CONCLUSION

ODE and Meta-PSO algorithms are compared for shape reconstruction of three dimensional conducting objectst. In both cases, a good agreement between the reconstructed and the original shape is observed. Bezier surfaces are utilized to model the target and PO approximation is used to compute the scattered field. In addition, the stability of this algorithm in the presence of noise is investigated. Finally from the results we find that Meta-PSO is better than ODE for reconstruction of the target.

ACKNOWLEDGMENT

REFERENCES

[1] P. Kosmas and C. M. Rappaport, "An inverse scattering method based on contour deformation by meand of a level set method using frequency hopping technique," *IEEE Trans. Antennas Propagat.*, vol. 51, no. 5, pp. 1100-1113, May 2003.

[2] L. Crocco, I. Catapano, L. Di Donato, and T. Isernia, "The linear sampling method as a way to quantitative inverse scattering," *IEEE Trans. Antennas Propagat.*, vol. 60, no. 4, pp. 1844-1853, Apr. 2012.

[3] P. Kosmas and C. M. Rappaport, "Time reversal with the fdtd method for microwave breast cancer detection," *IEEE Transactions on Microwave Theory and Techniques*, vol. 53, no. 7, pp. 2317-2323, July 2005.

[4] I. T. Rekanos, "Shape reconstruction of a perfectly conducting scatterer using differential evolution and particle swarm optimization," *IEEE Trans. Geosci. Remote Sens.*, vol. 46, no. 7, pp. 1967-1974, July 2008.

[5] A. Qing, C. K. Lee, and L. Jen, "Electromagnetic inverse scattering of two-dimensional perfectly conducting objects by real-coded genetic algorithm," *Geoscience and Remote Sensing, IEEE Transactions on*, vol. 39, no. 3, pp. 665-676, Mar. 2001.

[6] A. Saeedfar and K. Barkeshli, "Shape reconstruction of three-dimensional conducting curved plates using physical optics, nurbs modeling, and genetic algorithm," *IEEE Trans. Antennas Propagat.*, vol. 54, no. 9, pp. 2497-2507, Sept. 2006.

[7] F. S. de Adana and O. Gutierrez, *Practical Applications of Asymptotic Techniques in Electromagnetics.* Artech House Electromagnetic Analysis Series, Artech House, 2010.

[8] G. E. Farin, *Curves and Surfaces for Computer-Aided Geometric Aesign: A Practical Guide.* Number v. 1 in Computer Science and Scientific Computing, Academic Press, 1997.

[9] J. Perez and M. F. Catedra, "Application of physical optics to the rcs computation of bodies modeled with nurbs surfaces," *IEEE Trans. Antennas Propagat.*, vol. 42, no. 10, pp. 1404-1411, Oct. 1994.

[10] O. M. Conde, J. Perez, and M. P. Catedra, "Stationary phase method application for the analysis of radiation of complex 3-D conducting structures," *IEEE Trans. Antennas Propag.*, vol. 49, no. 5, pp. 724-731, May 2001.

[11] F. S. de Adana, I. G. Diego, O. G. Blanco, P. Lozano, and M. F. Catedra, "Method based on physical optics for the computation of the radar cross section including diffraction and double effects of metallic and absorbing bodies modeled with parametric surfaces," *IEEE Trans. Antennas Propagat.*, vol. 52, no. 12, pp. 3295-3303, Dec. 2004.

[12] S. Rahnamayan, H. R. Tizhoosh, and M. M. A. Salama, "Opposition-based differential evolution," *IEEE Transactions on Evolutionary Computation*, vol. 12, no. 1, pp. 64-79, Feb. 2008.

[13] S. Selleri, M. Mussetta, P. Pirinoli, R. E. Zich, and L. Matekovits, "Differentiated meta-pso methods for array optimization," *Antennas and Propagation, IEEE Transactions on*, vol. 56, no. 1, pp. 67-75, Jan. 2008.

Mojtaba Maddah-ali was born in Isfahan, Iran, on December 5, 1987. He received B.Sc. degree in Electrical Engineering from Isfahan University of Technology, Isfahan, Iran, in 2009, the M.Sc. degrees from the Amirkabir University of Technology (Tehran Polytechnic), Tehran, Iran, in Electrical Engineering, in, 2013.

Currently, he is a Research Assistant with the Amirkabir University of Technology. His main interest lies in the electromagnetic wave propagation, scattering and inverse scattering in electromagnetic problems.

Ahad Tavakoli was born in Tehran, Iran, on March 8, 1959. He received the B.S. and M.S. degrees from the University of Kansas, Lawrence, and the Ph.D. degree from the University of Michigan, Ann Arbor, all in Electrical Engineering, in 1982, 1984, and 1991, respectively.

He is currently a Professor in the Department of Electrical Engineering at Amirkabir University of Technology. His research interests include EMC, scattering of electromagnetic waves and microstrip antennas.

Mojtaba Dehmollaian was born in Iran in 1978. He received the B.S. and M.S. degrees in Electrical Engineering from the University of Tehran, Tehran, Iran, in 2000 and 2002, respectively. He received the M.S. degree in Applied Mathematics and Ph.D. degree in Electrical Engineering from the University of Michigan, Ann Arbor, in 2007.

Currently, he is an Assistant Professor with the Department of Electrical and Computer Engineering, University of Tehran. His research interests are applied electromagnetics, radar remote sensing, electromagnetic wave propagation and scattering.

3-D Defect Profile Reconstruction from Magnetic Flux Leakage Signals in Pipeline Inspection Using a Hybrid Inversion Method

Junjie Chen

Electric Power Planning & Engineering Institute, Beijing, 100120, China
jjchen@eppei.com

Abstract ─ In this paper, we propose a hybrid inversion approach to reconstruct the profile of arbitrary three-dimensional (3-D) defect from magnetic flux leakage (MFL) signals in pipeline inspection. The region of pipe wall immediately around the defect is represented by an array of partial cylinder cells, and a reduced forward FE model is developed to predict MFL signals for any given defect. The neural network (NN) method is used at first to give a coarse prediction of the defect profile, and the prediction is then utilized as one original solution of the genetic algorithm (GA) to search for the global optimum estimate of the defect profile. To demonstrate the accuracy and efficiency of the proposed inversion technique, we reconstruct defects from both simulated and experimental MFL signals. In both cases, reconstruction results indicate that the hybrid inversion method is rather effective in view of both efficiency and accuracy.

Index Terms ─ Defect reconstruction, genetic algorithm, magnetic flux leakage, neural network, pipeline inspection.

I. INTRODUCTION

Magnetic flux leakage (MFL) inspection is widely used for detecting corrosion defects in pipelines for oil and gas [1]. The inspection devices, referred as in-line-inspection (ILI) tools, are designed for autonomous operation in the pipeline. Once defects have been identified, an equally important problem is the assessment of the size or severity of the defect [2].

In the past, inverse MFL problems were solved based on neural networks [3-5], gradient-based optimization methods [6, 7], GA-based optimization methods [8] and other methods [9, 10]. Neural networks are advantageous in cases where rapid inversions are required. However, their main drawback is that they require a large database for training. The performance of neural networks depends on the data used in training and testing. When the test signal is no longer similar to the training data, performance degrades. In contrast, methods embedding the physical model into the MFL signal inversion process do not require a large database. The physical model and the optimization procedure are crucial for these inversion methods. On the issue of convergence, gradient-based optimization often fails to converge to the global optimum in the presence of multiple local optima, since the optimization problem for defect reconstruction from MFL signals is not a unique solution one. The GA-based approach, on the other hand, begins with a large set of initial search points using well-defined probabilistic tools to guide a search towards regions in the search space that are more likely to contain the global optimum. The GA usually begins with a randomly generated set of original solutions, which may takes a long time to converge to the global optimum. Therefore, a suitable selection of the initial search points is rather important for the GA-based approach to improve the efficiency.

In this paper, we propose a hybrid method for 3-D defect reconstruction from MFL signals in pipeline inspection. We develop a reduced forward model of pipe in MFL inspection, and combine NN to GA in inversion process by applying the prediction result of NN as one initial solution of GA. Results of defect reconstruction show that the proposed method has outstanding performance for both simulated and real experimental MFL signals.

The organization this paper is as follows. In Section II, we introduce the reduced forward FE models of pipe and characterization of defect in MFL inspection. In Section III, we summarize the application of NN and GA to 3-D defect inversion. Section IV gives experimental results based on simulated and realistic experimental MFL data, and Section V gives the conclusions.

II. FORWARD MODEL OF MFL INSPECTION

Figure 1 depicts the corresponding magnetic circuit for an ILI tool for pipe inspection. Permanent magnets magnetize the pipe wall to saturation or near saturation flux density, typically in the axial direction. As shown, the magnetic leakage fields from the pipe wall are detected using uniformly-spaced Hall or coil sensors.
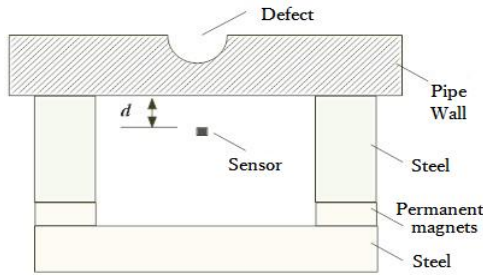
Fig. 1. Simplified magnetic circuit of an ILI tool.

A. Reduced forward model

Based on the magnetic circuit of the ILI tool, we create a 90-degree forward FE model of MFL inspection as shown in Fig. 2 (a), including pipe wall, steel, permanent magnets, air and defect [11, 12]. Compared with the complete 360-degree model, this model could reduce much computation work. Then, a further reduced forward model is proposed as shown in Fig. 2 (b). The reduced forward model only consists of air, nonlinear pipe material and permanent magnets embedded in the pipe wall. The size and distance of permanent magnets could be adjusted so that the simulated MFL signals agree with the real signals.
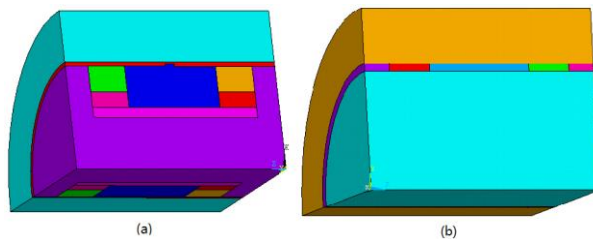
Fig. 2. (a) Basic 90-degree forward model. (b) Reduced forward model.

For the basic forward model and the reduced forward model, the related parameters together with detailed explanations are presented in Table 1, and the characteristic curves of nonlinear magnetic materials used in the forward model are presented in Fig. 3.
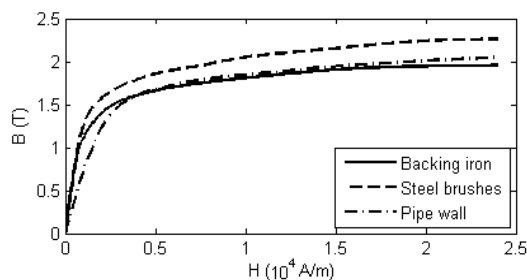
Fig. 3. Characteristic curves of nonlinear magnetic materials used in the forward model.

Table 1: Related parameters for the forward model

Parameter	Value	Unit
Pipe diameter	457	mm
Pipe thickness	14.3	mm
Permanent magnet width	80	mm
Permanent magnet height	30	mm
Brush width	80	mm
Brush height	50	mm
Back height	20	mm
Magnetic pole spacing	1000	mm
Relative permeability	1.26	-
Coercive force	836	KA/m
Lift off value	3	mm

The results of simulation show that, the reduced model only brings less than 5% error while taking one fifth time as the basic model does. Figure 4 shows two samples of MFL images of metal loss defects using the reduced model.
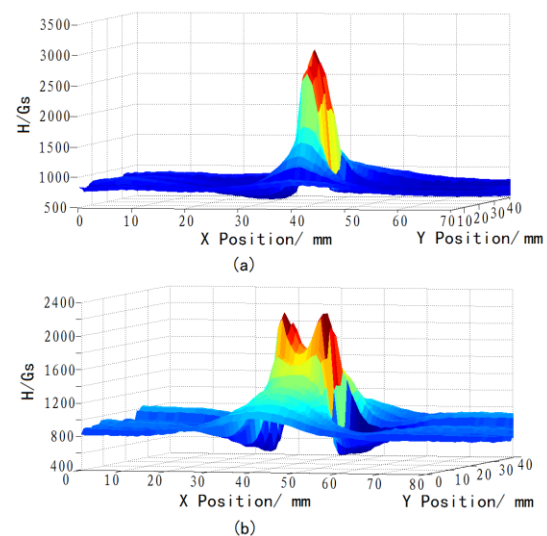
Fig. 4. Simulated MFL images for metal-loss defects using the reduced forward model. (a) Internal defect, 100.1mm×14.3mm×5.7mm; (b) external defect, 42.9mm× 42.9 mm×8.6 mm.

B. Defect characterization

The forward computational problem consists of using the reduced FE model to efficiently obtain the magnetic flux field profile for any defect in the pipe. The region of pipe wall immediately around the defect constitutes the 'region of interest' (ROI). To characterize different defect shapes, the radial depth, the tangential width and the axial length of ROI are divided into 7, 10 and 10 parts respectively. Consequently, the ROI could be represented by an array of 7×10×10 partial cylinder cells as illustrated in Fig. 5.
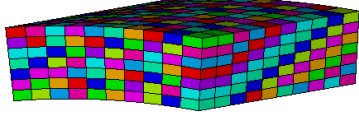
Fig. 5. Defect characterization with $7\times10\times10$ basic model for inversion.

The magnetic conductivity of each cell could be made equal to that of air or iron, resulting in different geometries of the defect. By doing this, any particular defect in the whole defect area could be characterized by a set of 100 depths: $d_1, d_2, ..., d_{100}$, where $d_i \in \{0,1,...,7\}$. Thus the value of a particular depth is encoded as a 3 bit binary string, and the parameter set for the whole defect area can be represented by a 300 bit binary string.

III. INVERSION PROCEDURE USING NN AND GA

In order to take full use of the advantages of both the NN and the GA method, we propose a hybrid method for the defect reconstruction from MFL signals, i.e., to use the results of NN inversion as one initial solution for the GA method.

A. NN prediction

As shown in Fig. 6, a feed-forward NN with a single hidden layer is used to predict the defect profile for the initial solution of GA. The input of the NN consists of feature parameters of MFL signals scanned over the test-pipe, and the output are the parameters of defects corresponding to the MFL signals. The databases of both MFL signals and corresponding defect parameters are separated into training, validation and verification sets.
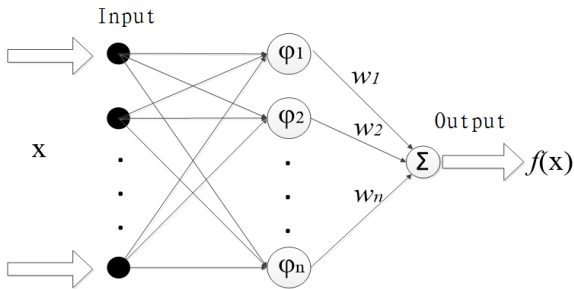
Fig. 6. The feed-forward NN used for prediction.

The training process starts with only one hidden node, and for each training epoch a new node is created. The new input-hidden connections receive random weights and the rest of the weights are obtained by solving (1) with the least square minimization based on the singular value decomposition:

$$A \cdot W_{io} + f_1(A \cdot W_{ih}) \cdot W_{ho} = f_2^{-1}(B), \qquad (1)$$

where A and B represent the input and output training data sets, f_1 and f_2 are nonlinear activation functions for hidden and output nodes, $[W_{ih}]$ the "randomly-fixed" input-hidden weights, and $[W_{io}], [W_{ho}]$ the matrices containing unknown weights, are the input-output and the hidden-output inter-connection weights, respectively.

To generate the training data sets, the reduced forward model shown in Fig. 2 (b) and the defect characterization shown in Fig. 5 were used to get simulated MFL signals. Considering the object for NN inversion result in this paper, only cuboid defects are simulated. Therefore, the trained NN could only provide a cuboid prediction for any arbitrary defect profile as one initial solution.

B. GA inversion process

The flowchart of iterative inversion process using GA for 3-D defect reconstruction is shown in Fig. 7. The inverse problem is solved by minimizing an objective function, representing the difference between the forward model predicted and the realistic measured MFL signal. When the difference is below a pre-set threshold, the defect profile represents the desired solution. The various issues related with the formulation of the inversion process are described below.
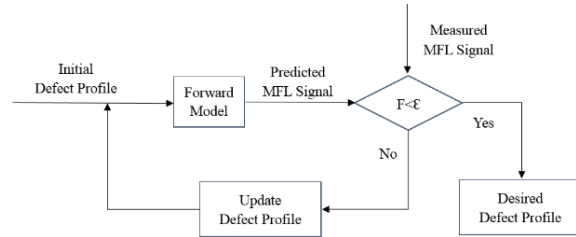
Fig. 7. Iterative inversion flowchart for 3-D defect reconstruction.

As all the three components (radial, tangential and axial) of magnetic flux density carry the information of defect profile, they are all chosen as input signals for the inverse optimization procedure when simulated MFL signals are used. However, only the axial component is used when the inversion is conducted based on realistic measured MFL data, because only the axial component is detected by the ILI tool.

The minimization of an error between measured and predicted MFL signals can be recast as maximizing of the following fitness function:

$$F = \frac{1}{1 + C\sum_{i=1}^{N} \| B_i^m - B_i^{FEM} \|}, \qquad (2)$$

Where N is the number of points taken on the signal

and C is constant. The global maximum value of F is 1, corresponding to the case the predicted and measured MFL signals are exactly the same. It should also be noted that in case of the error reaching a local minimum other than the global minimum of zero, the relative ratio between the corresponding local and global maximums of F is determined by the constant C.

As shown before, the results of NN inversion is taken as one initial solution for the GA inversion process. This will bring significant help in increasing both efficiency and possibility for the GA to reach the global optimum solution, which will be presented in Section IV. At the same time, 7 randomly generated original solutions are also used. Furthermore, 2 special 300-bit binary strings, composed of only '0' and only '1' respectively, are added to the initial population for GA in order to keep the diversity of population.

When the original solutions have been selected, a fitness function is used as a measure of closeness of each member in the population to the global optimum solution. Subsequently, a new population is generated by applying genetic operators including reproduction, crossover and mutation on the previous population. The selection mechanism for reproduction favors the highly fit members, so that the members more close to the global optimum are assigned higher probabilities for producing children. Crossover operations ensure that the new population inherits highly fit features, while mutation may add previously unexplored features into the new population. With this, the population drifts to a global or near global solution after a few number of generations in the iterative process.

IV. EXPERIMENTAL RESULTS

In this paper, reconstruction is implemented using biased Roulette-Wheel algorithm with a two-point crossover, and the mutation probability varies between 0.3 and 0.5. The iterative process is terminated when the population of the GA has been updated for 200 times, and at last smoothing is conducted to produce a better defect profile.

Experiments of 3-D defect reconstruction are conducted based on 3-D simulated MFL signals and 1-D measured MFL signals. An internal 100.1mm×14.3mm× 5.7mm cuboid defect (Fig. 8 (a)), an external 42.9mm× 42.9mm×8.6mm cuboid defect (Fig. 9 (a)), and an external 42.9mm×7.15mm globoid defect (Fig. 10 (a)) are simulated using the reduced forward model. At the same time, the ILI tool is used to measure the axial MFL signals of an 18-inch and 14.3mm-thick pipe, on which the same defects as the three simulated ones have been artificially made.

The reconstruction is firstly conducted using general GA with initial population composed of 10 randomly generated original solutions. Figure 8 (b), Fig. 9 (b), and Fig. 10 (b) depict the final predicted profiles of the three defects based on 3-D simulated MFL signals. As comparison, Fig. 8 (c), Fig. 9 (c), and Fig. 10 (c) show the predicted defect profiles based on 1-D measured MFL signals. It can be seen that the predicted profiles using 3-D simulated MFL signals match the real defects very well, while at the same time, the inversion results using 1-D measured MFL signals are not so good within a fixed number of iterations. Possible reasons could be lack of enough information carried by the radial and tangential components of magnetic flux density together with error between simulated and realistic MFL signals.

Then the reconstruction is conducted again using the proposed hybrid inversion method, with the prediction of NN as one original solution of the GA inversion. The prediction results for the three defects from NN are shown in Fig. 8 (d), Fig. 9 (d) and Fig. 10 (d). Figure 8 (e), Fig. 9 (e), and Fig. 10 (e) depict the final predicted profiles of the three defects based on 3-D simulated MFL signals. Similarly, Fig. 8 (f), Fig. 9 (f), and Fig. 10 (f) show the predicted defect profiles based on 1-D measured MFL signals. Compared with former inversion results using general GA, reconstructed defects match the real ones better when prediction results of NN are used as the original solutions of the GA in the hybrid inversion procedure. In fact, the efficiency of defect reconstruction has been improved significantly, and the accuracy of reconstruction has increased within same time.

The reconstruction errors in different situations are then calculated and summarized as Table 2. The larger errors of reconstructed results using general GA with randomly generated original solutions demonstrate that the optimization fails to converge to the global minimum solution within fixed number of iterations. When the prediction of NN is used as original solution in the hybrid inversion procedure, the iterative GA could produce obviously better results of defect reconstruction.

To further testify the robustness of the proposed hybrid inversion procedure, a randomly generated internal defect as Fig. 11 (a) is simulated using the reduced forward model to get corresponding 3-D simulated MFL signals. The reconstructed defect profile using the proposed hybrid inversion procedure, based on the basic 7×10×10 defect model shown in Fig. 5, is shown in Fig. 11 (b). Then the hybrid inversion procedure is conducted again, based on a refined 15×20×20 defect model, to get a new reconstructed defect profile (Fig. 11 (c)). The results of reconstruction show that the proposed hybrid inversion procedure is rather effective and robust even for randomly generated defect profile. Furthermore, the accuracy of reconstruction could get improved using a refined defect model extended from the basic one shown in Fig. 5.
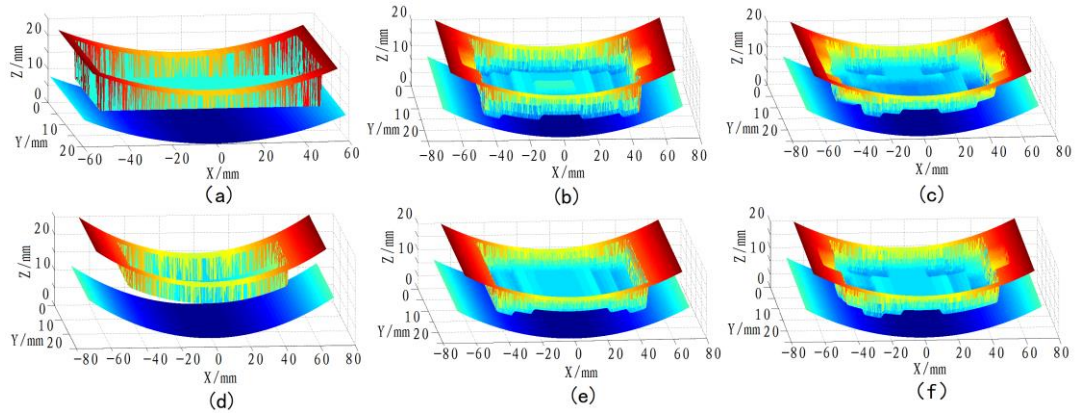
Fig. 8 Reconstruction of internal cuboid defect, 100.1mm×14.3mm×5.7mm. (a) Real defect profile; (b), (c) reconstructed defects based on 3-D simulated and 1-D measured signals, using general GA with randomly generated initial population; (d) prediction result of NN inversion; (e), (f) reconstructed defects based on 3-D simulated and 1-D measured signals, using GA with initial solution from NN inversion.
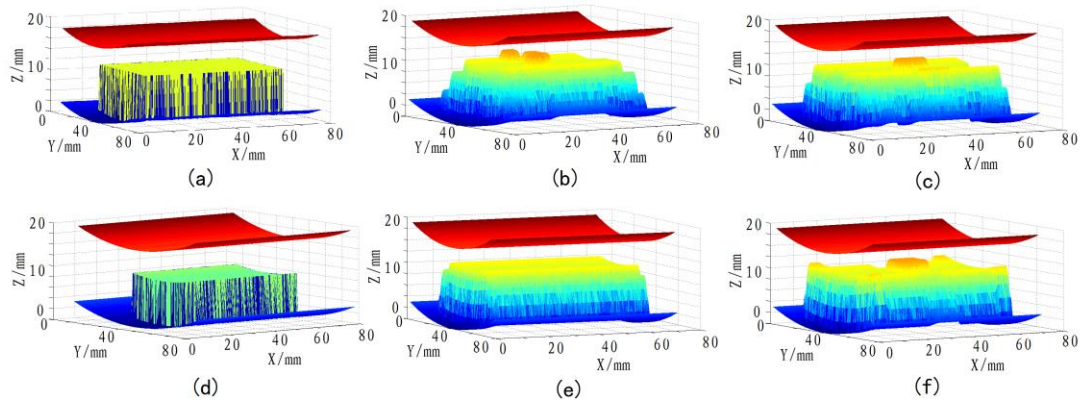
Fig. 9. Reconstruction of external cuboid defect, 42.9mm×42.9mm×8.6mm. (a) Real defect profile; (b), (c) reconstructed defects based on 3-D simulated and 1-D measured signals, using general GA with randomly generated initial population; (d) prediction result of NN inversion; (e), (f) reconstructed defects based on 3-D simulated and 1-D measured signals, using GA with initial solution from NN inversion.
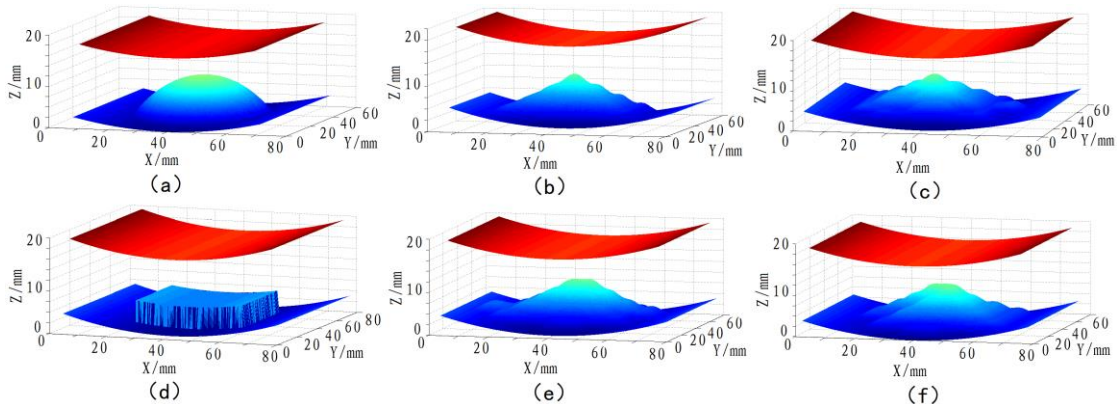
Fig. 10. Reconstruction of external globoid defect, 42.9mm×7.15mm. (a) Real defect profile; (b), (c) reconstructed defects based on 3-D simulated and 1-D measured signals, using general GA with randomly generated initial population; (d) prediction result of NN inversion; (e), (f) reconstructed defects based on 3-D simulated and 1-D measured signals, using GA with initial solution from NN inversion.

Table 2: Reconstruction errors of different defects

Defect/mm	Simulated Signals		Measured Signals	
	General GA	Hybrid	General GA	Hybrid
Internal cuboid 100.1×14.3×5.7	0.12	0.05	0.21	0.14
External cuboid 42.9×42.9×8.6	0.13	0.05	0.22	0.15
External globoid 42.9×7.15	0.25	0.12	0.41	0.28
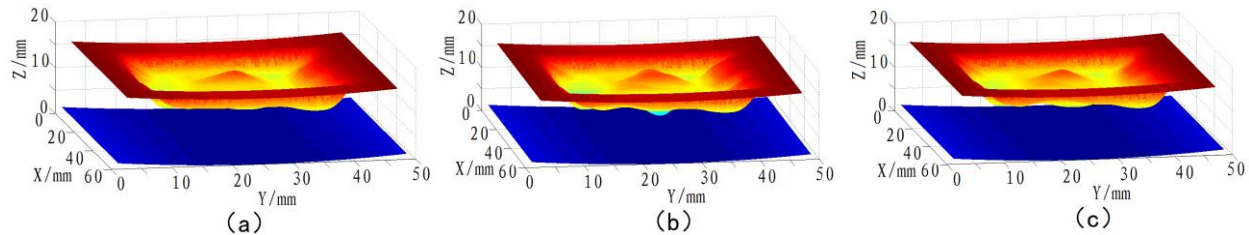
Fig. 11. Reconstruction of randomly generated defect using proposed hybrid inversion method based on 3-D simulated MFL signals. (a) Real defect profile; (b) reconstructed defect using basic 7×10×10 defect model; (c) reconstructed defect using refined 15×20×20 defect model.

V. CONCLUSION

In this paper, a hybrid inversion approach is presented to reconstruct the 3-D defect profile from MFL signals in pipeline inspection. The reduced FE forward model of MFL inspection is developed, and the defect area is represented by an array of 7×10×10 partial cylinder cells. The NN is used at first to get a prediction of the defect, which is then utilized as one original solution of the GA to search for the global optimum estimate of the defect profile. Accuracy and efficiency of the proposed hybrid inversion method is demonstrated by the reconstruction results from both simulated and experimental MFL signals. Comparison between results from simulated and measured MFL signals also show that all the three components, instead of only the axial or radial component, of MFL signals in pipeline inspection should be detected for better reconstruction results. Furthermore, the accuracy of reconstruction could get improved using a refined defect model.

Future work will concentrate on optimizing the forward model to reduce time consumption and refining the defect model to increase accuracy of defect prediction. Besides, more kinds of defect shape should be covered in the experiment to test the proposed inversion method.

REFERENCES

[1] A. Khodayari-Rostamabad, J. P. Reilly, N. K. Nikolova, et al., "Machine learning techniques for the analysis of magnetic flux leakage images in pipeline inspection," *IEEE Transactions on Magnetics*, vol. 45, no. 8, pp. 3073-3084, 2009.

[2] M. Ravan, R. K. Amineh, S. Koziel, et al., "Sizing of 3-D arbitrary defects using magnetic flux leakage measurements," *IEEE Transactions on Magnetics*, vol. 46, no. 4, pp. 1024-1033, 2010.

[3] P. Ramuhalli, L. Udpa, and S. S. Udpa, "Electromagnetic NDE signal inversion by function-approximation neural networks," *IEEE Transactions on Magnetics*, vol. 38, no. 6, pp. 3633-3642, 2002.

[4] A. Joshi, "Wavelet transform and neural network based 3D defect characterization using magnetic flux leakage," *International Journal of Applied Electromagnetics and Mechanics*, vol. 28, no. 1, pp. 149-153, 2008.

[5] S. R. H. Hoole, S. Subramaniam, R. Saldanha, et al., "Inverse problem methodology and finite elements in the identification of cracks, sources, materials, and their geometry in inaccessible locations," *IEEE Transactions on Magnetics*, vol. 27, no. 3, pp. 3433-3443, 1991.

[6] R. Priewald, C. Magele, P. Ledger, et al., "Fast magnetic flux leakage signal inversion for the reconstruction of arbitrary defect profiles in steel using finite elements," *IEEE Transactions on Magnetics*, vol. 49, no. 1, pp. 506-516, 2013.

[7] K. C. Hari, M. Nabi, and S. V. Kulkarni, "Improved FEM model for defect-shape construction from MFL signal by using genetic algorithm," *Science, Measurement & Technology, IET*, vol. 1, no. 4, pp. 196-200, 2007.

[8] M. Yan, S. Udpa, S. Mandayam, et al., "Solution of inverse problems in electromagnetic NDE using finite element methods," *IEEE Transactions on Magnetics*, vol. 34, no. 5, pp. 2924-2927, 1998.

[9] A. A. Adly and S. K. Abd-El-Hafiz, "Utilizing particle swarm optimization in the field computation of non-linear magnetic media," ACES *Journal*, vol. 18, no. 3, pp. 202-209, 2003.

[10] J. Chen, S. Huang, and W. Zhao, "Three-

dimensional defect reconstruction from magnetic flux leakage signals in pipeline inspection based on a dynamic taboo search procedure," *Insight-Non-Destructive Testing and Condition Monitoring*, vol. 56, no. 10, pp. 535-540, 2014.

[11] P. S. Kildal and A. Kishk, "EM Modeling of surfaces with STOP or GO characteristics-artificial magnetic conductors and soft and hard surfaces," ACES *Journal*, vol. 18, no. 1, pp. 32-40, 2003.

[12] M. M. Bibby and F. P. Andrew, "High accuracy calculation of the magnetic vector potential on surfaces," ACES *Journal*, vol. 18, no. 1, pp. 12-22, 2003.

Junjie Chen was born in 1988. He received his Ph.D. degree from Tsinghua University in 2015. He is currently working on problems in power system.

Optimal Design of Elliptical Array Antenna Using Opposition Based Differential Evolution Technique

Rajesh Bera [1], Durbadal Mandal [1], Rajib Kar [1], and Sakti Prasad Ghoshal [2]

[1] Department of Electronics and Communication Engineering
National Institute of Technology Durgapur-713209, West Bengal, India
rajeshkiit12@gmail.com, durbadal.bittu@gmail.com, rajibkarece@gmail.com

[2] Department of Electrical Engineering
National Institute of Technology Durgapur-713209, West Bengal, India
spghoshalnitdgp@gmail.com

Abstract ─ Radiation pattern synthesis of non-uniformly excited planar arrays with the lowest relative side lobe level (SLL) is presented in this paper. Opposition based differential evolution (ODE) scheme, which represents a novel parameter optimization technique in antenna engineering is applied for the parameter optimization of the single and the multi-ring circular array (CA), hexagonal array (HA) and elliptical array (EA) of isotropic elements. To overcome the problem of premature convergence of differential evolution (DE) algorithm, ODE is designed without significantly impairing the fast converging property of DE. Two design examples are presented which illustrate the effectiveness of the ODE based method, and the optimization goal for each example is easily achieved. The design results obtained using ODE are much more improved than those of the results obtained using the state of the art evolution algorithms like particle swarm optimization (PSO), harmonic search (HS) and differential evolution (DE) methods in a statistically significant way.

Index Terms ─ Concentric circular array, concentric elliptical array, concentric hexagonal array, opposition based differential evolution, side lobe level.

I. INTRODUCTION

Uniform circular array [1, 2] has the capability of 360 degree beam scanning without the significance change in SLL or beam width and it can be useful for smart antenna application [3, 4]. The mutual coupling effect is more significant in order to achieve low SLL by reducing the distance between elements in circular arrays. Hexagonal array is presented to overcome the problem of high SLL for smart antenna applications [5]. The comparison between CA and HA shows that the hexagonal array geometry provide deeper nulls and higher gain with the same beam width as circular array [6]. Also, best beam steering ability was found using a uniform hexagonal array of seven patch antennas with a central element [7] which can be applied to the wireless communication of advance generation. Elliptical shaped array and the combinations of elliptical and linear array with array factors are investigated in [8]. The effect of ellipse eccentricity, number of elements and element spacing are also investigated. Array hybridization (mixing two different arrays) approaches can also be used to improve the performance of antenna arrays in terms of SLL and directivity [9].

For optimization of complex, nonlinear and non-differentiable array factor of antenna array, various evolutionary optimization approaches such as firefly algorithm (FFA) [10], particle swarm optimization (PSO) [11], harmonic search (HS) [12], differential evolution (DE) [13] etc., have been widely used. It is accepted that, compared with the other state-of-art optimization techniques, the PSO is a powerful optimization scheme for antenna design problems [14], cluster based wireless sensor network design [15], wiring network diagnosis [16] etc.

Problems with the real valued variables can be solved by DE technique which is one of the finest genetic type process. In DE, mutation operation is used as a primary search mechanism and selection to direct the search toward a more promising region. Selection mechanism is used in genetic algorithm (GA) to generate a population sequence while crossover as principal operation for useful exchange of information of the solutions. This is the fundamental difference between GA and DE. The idea of opposition-based learning (OBL) is introduced in [17] by Tizhoosh. Based on the concept OBL, a new reinforcement learning algorithm is presented in [18, 19] to accelerate the convergence of the algorithm. OBL has been utilized to improve the global search ability and to accelerate the convergence rate of DE in this paper. Therefore, the proposed methodology of opposition based differential evolution (ODE) is used

to achieve a better estimation for the current candidate solution. In this paper, the array geometry synthesis is first formulated as an optimization problem with the goal of SLL reduction and then is solved using ODE algorithm for optimum current excitations.

II. DESIGN EQUATIONS

A. Array factors
1.1 Single-ring arrays
The general configuration of circular array (CA) with N number elements in x-y plane is shown in Fig. 1. The array factor $AF(\theta,\varphi)$ for CA is given by (1) [2]:

$$AF(\theta,\varphi) = \sum_{n=1}^{N} I_n e^{jkr\sin\theta(\cos\varphi_n\cos\varphi+\sin\varphi_n\sin\varphi)}, \quad (1)$$

where r = radius of circular array; k = wave number; θ = elevation angle; φ = azimuth angle; I_n = excitation coefficient of nth element; angular position of nth element, $\varphi_n = 2\pi(n-1)/N$.
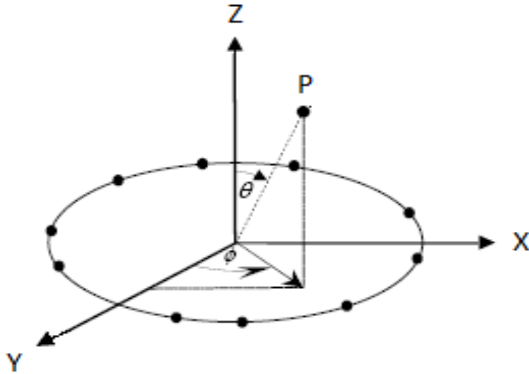
Fig. 1. Circular array (CA) structure.

Figure 2 displays the general configuration of a regular hexagonal array (HA) with 2×N elements (N=6). Here, half (N) of the array elements are situated at the angular points and another half are located at the middle edges of the hexagon.

The far-field pattern of HA can be expressed as array factor AF, given in (2) [4]:

$$AF(\theta,\varphi) = \sum_{n=1}^{N} [A_n e^{jkr_1\sin\theta(\cos\varphi_{1n}\cos\varphi+\sin\varphi_{1n}\sin\varphi)}$$
$$+ B_n e^{jkr_2\sin\theta(\cos\varphi_{2n}\cos\varphi+\sin\varphi_{2n}\sin\varphi)}] \quad (2)$$

where

$$\left.\begin{array}{l} r_2 = r_1\cos(\pi/N) \\ r_1 = d_e/\sin(\pi/N) \end{array}\right\}. \quad (3)$$

The array factor of an N-element elliptical array (Fig. 3) can be derived using (4) [4]:

$$AF(\theta,\varphi) = \sum_{n=1}^{N} A_n e^{jk\sin\theta(a\cos\varphi_n\cos\varphi+b\sin\varphi_n\sin\varphi)}, \quad (4)$$

where a is the semi-major axis and b is the semi-minor axis of the elliptical array.
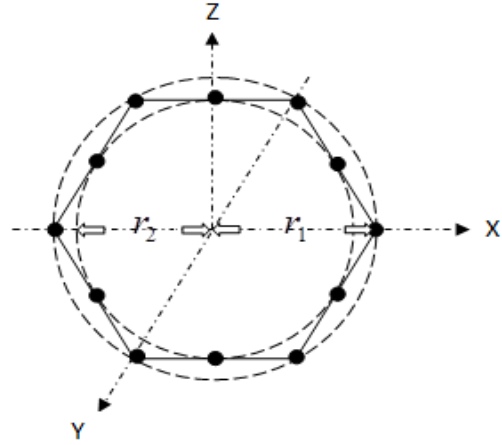
Fig. 2. Hexagonal array (HA) structure.
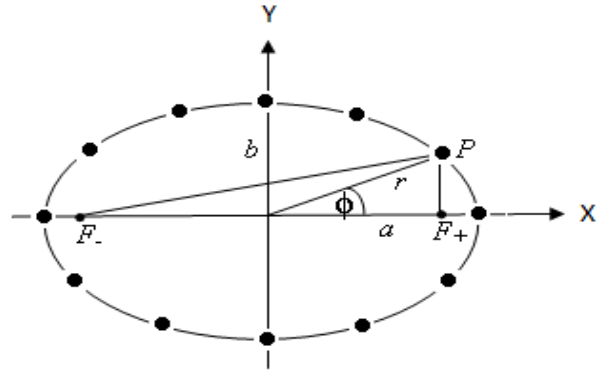
Fig. 3. Elliptical array (EA) structure.

1.2 Concentric-ring arrays
The array factor of M-ring concentric elliptical array (CEA) is given by (5) [4]:

$$AF(\theta,\varphi) = \sum_{m=1}^{M} \sum_{n=1}^{N_m} B_{nm} e^{jk\sin\theta(a_m\cos\varphi_n\cos\varphi+b_m\sin\varphi_n\sin\varphi)}, \quad (5)$$

where N_m is the number of elements lie on m^{th} elliptical ring, B_{nm} is the excitation amplitude and a_m is the semi-major axis and b_m is the semi-minor axis of mth ring. The values of a_m and b_m can be obtained from (6) for a given eccentricity e and inter-ring spacing d:

$$\left.\begin{array}{l} a_m = a+(m-1)d \\ b_m = a_m\sqrt{1-e^2} \end{array}\right\}. \quad (6)$$

In (6), innermost elliptical ring is having the semi-major axis a.

The expression for the array factor of concentric circular array (CCA) in the x-y plane is derived by

substituting $a_m = b_m = r_m$ in (5) and is given in (7):

$$AF(\theta, \varphi) = \sum_{m=1}^{M} \sum_{n=1}^{N} B_{nm} e^{jkr_m \sin\theta\cos(\varphi-\varphi_n)} . \qquad (7)$$

The array factor of concentric hexagonal array (CHA) can be found by the summation of the array factors of M concentric HAs, given in (8):

$$AF(\theta, \varphi) = \sum_{m=1}^{M} \sum_{n=1}^{N} [A_{nm} e^{jkr_{1m}\sin\theta(\cos\varphi_{1n}\cos\varphi+\sin\varphi_{1n}\sin\varphi)} +$$

$$B_{nm} e^{jkr_{2m}\sin\theta(\cos\varphi_{2n}\cos\varphi+\sin\varphi_{2n}\sin\varphi)}]$$

$$(8)$$

where

$$\begin{align} r_{1m} &= r + (m-1)d_h \\ r_{2m} &= r_{1m}\cos(\pi/N) \end{align} \qquad (9)$$

In (9), r is the radius of the smallest circle encompassing the smallest hexagon with the elements lying on its vertices and d_h is the spacing between the hexagons along x-axis.

B. Objective function formulation

For the synthesis of single and concentric ring arrays, cost function *CF* is formulated which is capable of generating pencil beam with lower SLL and higher directivity. *CF* is formulated to meet the corresponding design goal as follows:

$$CF = C_1[SLL_c - SLL_d] + C_2[FNBW_c - FNBW_d]. \quad (10)$$

In (10), SLL_c and $FNBW_c$ are the computed values (corresponding value of $I_n=1$) of SLL and first null beam width, respectively. SLL_d and $FNBW_d$ refer to the desired values of SLL and first null beam width, respectively, for non-uniform excitation case.

III. OPPOSITION-BASED DIFFERENTIAL EVOLUTION ALGORITHM

A. A brief description of differential evolution (DE) algorithm

For optimization problems over continuous domains, DE algorithm was first developed by R. Storn and K. Price in 1995. Scheme for generating trial parameter vectors is the fundamental idea behind DE algorithm. It produces new parameter vectors by adding the weighted difference vector between two populations. The details of DE algorithm can be found in [13].

B. Concept of opposition-based learning (OBL)

The computation time of any evolutionary optimization method is dependents on the distance between randomly chosen initial solutions (random guesses) and the optimal solution. The improvement of this starting phenomenon can be done with a nearby solution by consecutively testing the opposite solution [17]. Thus, to accelerate the convergence, the nearer of the two guesses (guess and opposite guess) is used as the

initial population. The same methodology can be applied continuously to every solution in the current population. The mathematical concept of opposite number and opposition based optimization is stated below:

Let $P = (x_i^1, \cdots\cdots, x_i^d, \cdots\cdots, x_i^n)$ be a point (guess) in *n*-dimensional space, where

$$\{x_i^1, \cdots\cdots, x_i^d, \cdots\cdots, x_i^n\} \in R,$$

and

$$x_i \in [A_i, B_i] \forall_i \in \{1, \cdots\cdots, d, \cdots\cdots, n\}.$$

The opposite point (opposite guess) $\hat{P} = (\hat{x}_1^1, \cdots\cdots, \hat{x}_1^d, \cdots\cdots, \hat{x}_1^n)$ is defined by its components as stated in (11):

$$\hat{x}_i = A_i + B_i - x_i . \qquad (11)$$

Assume $f = (.)$ is a fitness function which is used to measure the candidate's fitness.

Now, for a minimization problem, the point P can be replaced with $\hat{P}$ if $f(\hat{P}) \le f(P)$. Hence, to continue with the appropriate solution, the point and its opposite point are evaluated simultaneously.

C. Opposition-based differential evolution (ODE) algorithm

In this algorithm, opposition-based idea is implanted in DE which is selected as the parent algorithm to accelerate the convergence characteristics with near global optimal solution. The scheme of the OBL [17, 20] is merged in two steps such as initialization and opposition based generation in each iteration. The steps of the suggested ODE are discussed as follow:

Step 1: Generation of opposition based initial population P_0.

```
for (i = 0; i < S; i++)              %
Population size S
    for (j = 0; j < n; j++)          %
n-dimensional space
        OP_{0_{i,j}} = A_j + B_j - P_{0_{i,j}}    %
    initial population P_0 %  opposite
    population OP_0
    end
end
```

Selection of *S* suitable solutions from $\{P_0, OP_0\}$.

Step 2: Fitness calculations for each set of particles in the population.

Step 3: Follow the steps of Mutation, Crossover and Selection in DE.

Step 4: Checking for constraints of the problem.

Step 5: Generation jumping (opposition based).

```
if (rand(0, 1) < J_r)
    for (i = 0; i < S; i++)
```

$$\text{for } (\; j = 0; \; j < n; \; j++)$$

$$OP_{i,j} = \min{}^p_j + \max{}^p_j - P_{i,j}$$

end

end

Selection of S suitable solutions from $\{P, OP\}$ as current population, P

Step 6: Steps 2 to 5 are repeated until the stopping condition is met.

IV. RESULTS AND DISCUSIONS

CASE-1: **Simulation results of single ring arrays**

24-element single-ring CA, HA and EA each of which is placed on x-y plane symmetrically with respect to origin are considered. In order to place the elements symmetrically and equally spaced along the edges of the hexagonal geometry, the total number of elements in the array is taken as multiple of six (N=6×4=24). In the case of 24-element HA, 6 elements are placed at the vertices and the remaining 18 elements can be placed along the edges of the hexagon symmetrically. Different values of e (=0.2, 0.4 and 0.6) are considered for elliptical shaped array. So, the total number of arrays taken into account for comparison is five. Circular array can also be defined as elliptical array with eccentricity e=0. Cost function (objective function) *CF* in (10) is utilized in four algorithms in this case. Inter-element spacing *d* in each array is considered as 0.5λ.

A comparison is made among optimized CA, HA and EA in terms of SLL and Directivity (DIR) using PSO, HS, DE and ODE and is given in Table 1. Tables 2-4 present the optimal amplitudes coefficients for these three different array structures. Figures 4 (a) and 4 (b) depict the normalized power patterns for CA and HA, respectively, using PSO, HS, DE and ODE. Figures 4 (c), 4 (d) and 4 (e) represent the normalized power patterns of EA with three different values of eccentricity, respectively. From Table 1, it can be seen that ODE produces the best results as compared with other three state-of-art algorithms for the design of single ring arrays in terms of SLL reduction of approximately 5dB without affecting the directivity considerably.

(a)

(b)

(c)

(d)

(e)
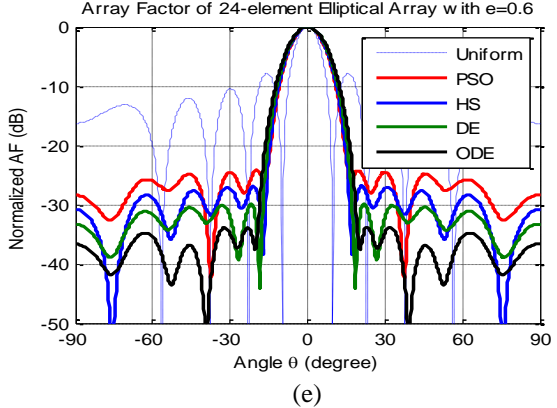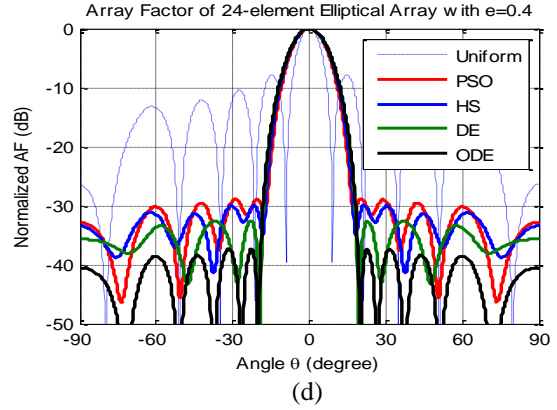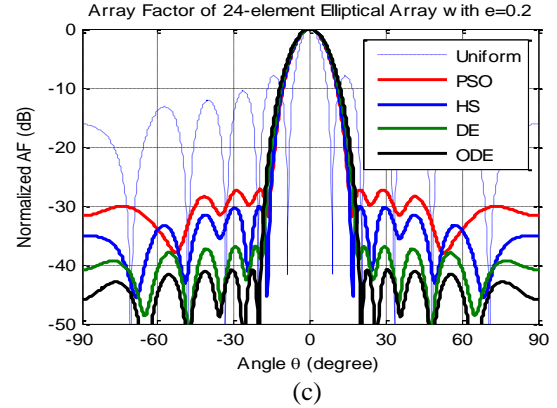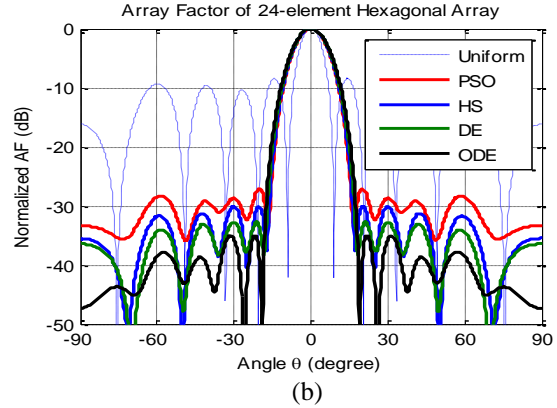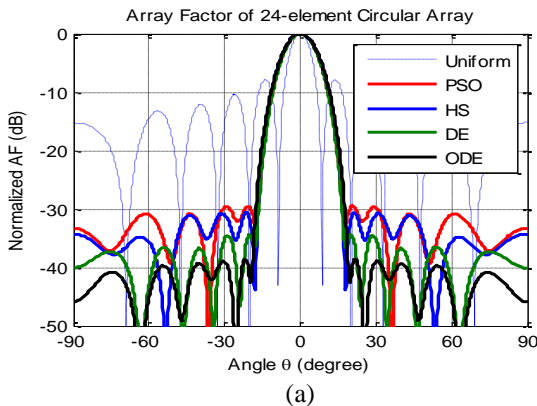
Fig. 4. Array patterns of: (a) CA, (b) HA, (c) EA with e=0.2, (d) EA with e=0.4, and (e) EA with e=0.6.

CASE-2: **Simulation results of concentric ring arrays**

CCA, CHA and CEA, each with four concentric rings are considered. Each ring having $N_i = (6\times i)$ number of uniformly spaced isotropic elements where i (=1, 2, 3, 4) denotes the ring number counted from the innermost ring. So, each array contains a total of 60 elements. CEA is considered for three different eccentricity values (e=0.2, 0.4, 0.6) where eccentricity value e=0 reveals that the array is the same as CCA. The spacing between two adjacent rings is constant with value d_e=0.5λ. The spacing between two adjacent elements in the innermost ring is also fixed at d_i=0.5λ for each array geometry. Inter-element spacing for the other rings can be calculated from d_e, d_i and N_i. In case of CEA, parameter a_m and b_m can be measured by (6) for a particular value of eccentricity.

Performances of CCA, CHA and CEA in terms of SLL and HPBW (3-dB BW) using PSO, HS, DE and ODE are tabulated in Table 5.

Table 1: Performances of 24-elements CA, HA and EA

Array Configuration		PSO		HS		DE		ODE	
		SLL (dB)	DIR	SLL (dB)	DIR	SLL (dB)	DIR	SLL (dB)	DIR
CA		-29.47	16.1532	-30.61	15.4240	-34.41	15.6591	-38.55	15.4166
HA		-27.09	16.1729	-30.01	14.8225	-32.67	14.9997	-35.00	14.9372
EA	e=0.2	-27.24	15.8365	-30.01	15.7854	-36.87	15.6439	-40.79	14.1663
	e=0.4	-28.83	15.9518	-29.88	15.6905	-32.52	15.5647	-37.35	15.6282
	e=0.6	-24.23	16.7684	-26.91	16.1146	-29.93	16.0594	-33.82	16.1673

Table 2: Excitation amplitude distribution of 24-element CA using three different optimization techniques

Algorithms	Amplitude Distributions	Max. SLL (dB)
PSO	1.0000 1.0000 0.9957 1.0000 0 0.0832 0.2912 0.0450 0.3357 0 0.4797 1.0000 1.0000 1.0000 0.8005 0.3889 0 0 0 0.0039 0.1913 0 0 0.5469	-29.47
HS	1.0000 1.0000 0.5650 0 0.2853 0.0702 0.2348 0 0 0.7194 0.7723 1.0000 1.0000 0.6363 1.0000 0 0.0034 0 0 0 0.1643 0.4550 0 1.0000	-30.61
DE	1.0000 0.6005 1.0000 0 0.2140 0.0000 0.1783 0 0 0.5154 0 1.0000 0.9226 1.0000 0.4431 0.1164 0.2496 0 0.2154 0 0 0.5457 0.7483 0.7388	-34.41
ODE	1.0000 1.0000 0 0.1385 0 0 0.1271 0 0.1580 0.3454 1.0000 0.6367 1.0000 0.9255 0.3543 0.3872 0.1691 0.1933 0 0 0 0.2146 0.7910 0.8686	-38.55

Table 3: Excitation amplitude distribution of 24-element HA using three different optimization techniques

Algorithms	Placement of Elements	Amplitude Distributions						Max. SLL (dB)
PSO	Vertices (A_n)		1	0	0	1	0	0	-27.09
	1st position (B_n)	0.6620	0	0.6761	0.8339	0.8094	0.5046	
	2nd position (C_n)	0.2765	0	0.7325	0.4888	0	0.8614	
	3rd position (D_n)	0	0.3170	0.8608	0.6822	0	1.0000	
HS	Vertices (A_n)	1.0000	0.5811	0	1.0000	0	0.3902	-30.01
	1st position (B_n)	1.0000	0	0.9833	0.9251	0	0.2441	
	2nd position (C_n)	0.2207	0	1.0000	0.9194	0.0035	0.1366	
	3rd position (D_n)	0.0338	0.0026	0.7611	0.5180	0	0.6598	
DE	Vertices (A_n)	1.0000	0.4345	0	1.0000	0	0.0002	-32.67
	1st position (B_n)	1.0000	0	0	0.5435	0.0085	0.3597	
	2nd position (C_n)	0.2094	0.0718	1.0000	1.0000	0	0	
	3rd position (D_n)	1.0000	0	0.7703	0.2914	0.3017	1.0000	
ODE	Vertices (A_n)	1.0000	0.1425	0	1.0000	0	0	-35.00
	1st position (B_n)	1.0000	0	0.4000	1.0000	0	0.2357	
	2nd position (C_n)	0.1017	0.2270	1.0000	0.2146	0.2820	0.8275	
	3rd position (D_n)	0.4004	0.0142	0.6726	0.4989	0	0.6108	

Table 4: Excitation amplitude distribution of 24-element EA using three different optimization techniques for various eccentricities

Eccentricity	Algorithms	Amplitude Distributions	Max. SLL (dB)
	PSO	1.0000 0.9594 0.6003 1.0000 0.4613 0.0039 0.3006 0 0 0 0.7405 1.0000 1.0000 0.6549 1.0000 0 0.0000 0 0 0.2649 0.0852 0.5648 0 1.0000	-27.24
0.2	HS	1.0000 0.8396 1.0000 0.1793 0.0255 0.1666 0.0902 0 0.3046 0.5513 0.2263 0.9866 1.0000 0.6980 0.4884 0.4947 0 0 0 0.2471 0.1430 0.1167 0.6210 0.9908	-30.01
	DE	1.0000 0.6269 0.4678 0.4919 0.1234 0.1005 0.0764 0 0 0 0.5070 1.0000 1.0000 0.8321 0.6037 0.3306 0.0595 0 0.1816 0 0.2235 0.3296 0.6330 1.0000	-36.87
	ODE	1.0000 0.7615 0.1217 0 0 0 0.1513 0 0.2165 0.5649 1.0000 1.0000 1.0000 0.9218 1.0000 0.4867 0.1296 0.0780 0.0601 0 0 0 0 0.7373	-40.79
	PSO	1.0000 0.9997 1.0000 0.4158 0.2818 0 0.1337 0 0 0 0 0.5945 1.0000 1.0000 1.0000 0 0.3524 0.0400 0.3626 0.0879 0 1.0000 0.4307 0.9599	-28.83
0.4	HS	1.0000 1.0000 0 0 0.2443 0.0000 0 0 0 0.3575 0.8697 0.5576 1.0000 1.0000 1.0000 0 0 0 0.4252 0 0.3479 1.0000 0.4241 1.0000	-29.88
	DE	1.0000 0.9958 0.9155 0 0 0.0001 0 0.1896 0.2084 0.6724 0.2593 0.7864 1.0000 0.6065 0 0.5220 0 0 0 0.1996 0 0 1.0000 0.9945	-32.52
	ODE	1.0000 0.5842 0 0.5141 0 0.0975 0.0689 0 0.1592 0.0015 1.0000 1.0000 0.8415 0.5841 0 0.2362 0 0.1652 0 0 0.1390 0.2827 1.0000 1.0000	-37.35
	PSO	1.0000 1.0000 1.0000 0.8836 0 0 0.5940 0 0.0243 0 0 0.9582 1.0000 1.0000 1.0000 1.0000 0 0.5579 0 0 0.4713 0.0144 0.6135 1.0000	-24.23
0.6	HS	1.0000 0.9204 0.1960 0.1872 0 0.6382 0 0.0013 0 0.5610 1.0000 1.0000 1.0000 0.8407 0.3550 0 0 0 0.0306 0.5432 0.0597 1.0000 0.9999 1.0000	-26.91
	DE	1.0000 0.9523 0.7445 0.0142 0.1597 0 0 0.2656 0 0.5499 0.3988 0.7088 0.9991 0.9143 1.0000 1.0000 0 0 0 0.5863 0 0 0.1828 1.0000	-29.92
	ODE	1.0000 0.8457 1.0000 0.0008 0 0.0010 0.2668 0 0.3078 0.7505 0.3061 1.0000 0.9968 1.0000 0.4971 0.0578 0 0.3101 0 0 0 0.5414 0.4716 0.6650	-33.82

Table 5: Performances of 60-elements CCA, CHA and CEA using four optimization techniques

Array Configuration		PSO		HS		DE		ODE	
		SLL (dB)	3-dB BW (degree)	SLL (dB)	3-dB BW (degree)	SLL (dB)	3-dB BW (degree)	SLL (dB)	3-dB BW (degree)
CCA		-25.01	10.6	-25.27	10.8	-30.00	12.2	-33.82	11.8
CHA		-24.39	11.6	-25.43	12.0	-26.60	12.2	-28.27	12.4
CEA	e=0.2	-26.05	11.0	-27.76	11.0	-29.94	11.6	-35.02	12.2
	e=0.4	-26.12	11.6	-28.39	12.0	-30.04	12.0	-31.66	12.0
	e=0.6	-22.85	12.8	-24.91	13.0	-27.66	13.4	-30.37	13.6

Figures 5 (a) and 5 (b) depict the normalized power patterns for CCA and CHA, respectively, using PSO, HS, DE and ODE. Figures 5 (c), 5 (d) and 5 (e) represent the normalized power patterns of CEA with three different values of eccentricity, respectively. From Table 5, it can be seen that ODE produces the best results as compared with other three recently developed algorithms for the design of concentric ring arrays in terms of SLL reduction.

Convergence profiles for all algorithms are also recorded for synthesis of various arrays. The population size and the maximum number of iteration cycles are 100 and 150, respectively.
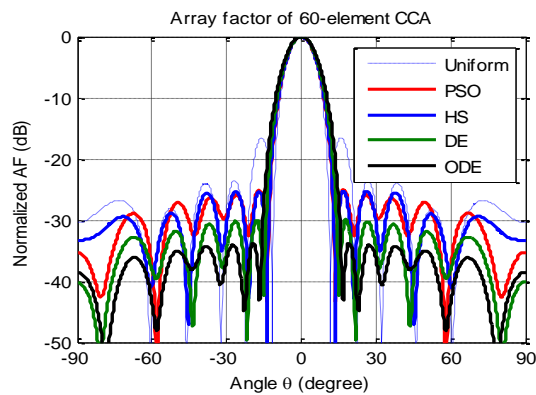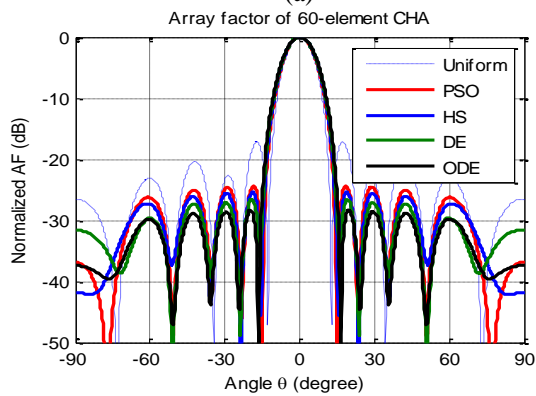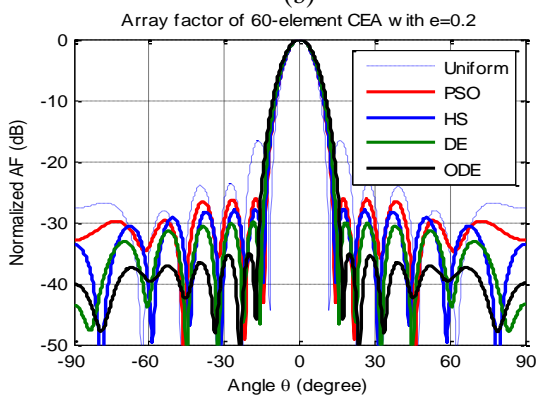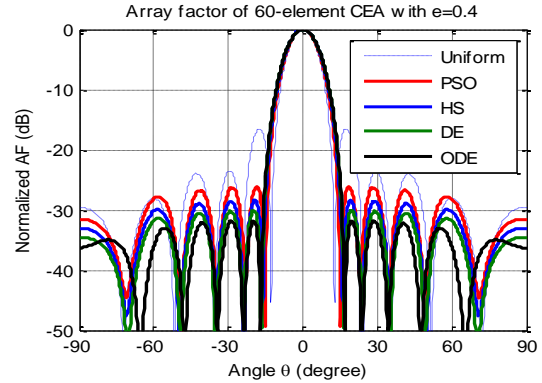
(d)
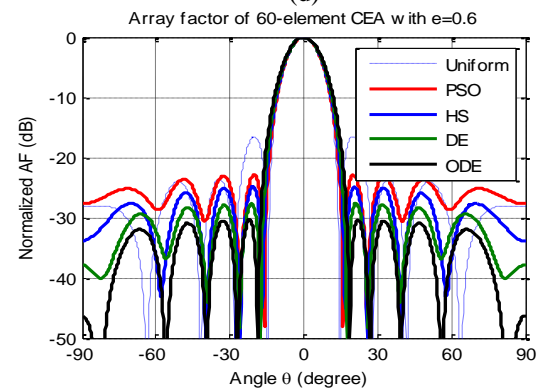
(e)

Fig. 5. Array patterns of: (a) CCA, (b) CHA, (c) CEA with e=0.2, (d) CEA with e=0.4, and (e) CEA with e=0.6.

(a)

(b)

(c)

V. CONCLUSION

ODE proves its better searching ability compared with PSO, HS and DE for the design of various planar arrays in antenna engineering optimization problem. ODE shows its superiority in terms of the best converged solution and convergence speed and efficient SLL reduction. The FNBWs/HPBWs of the synthesized array patterns with fixed inter-element spacing using these algorithms are very close for arrays of same shape and size. From the corresponding tables and figures given in above discussions, it can be observed that ODE produces an array patterns with the reduction of approximately 5 dB in SLL value in compared with PSO, HS and DE in almost all the cases. The other array parameters like directivity or 3-dB beam width of the synthesized array patterns are very close to the arrays of same shape and size. Designing arrays for a low SLL and highly directive pattern, there is no such available direct traditional relation between the SLL and the directivity but it maintains a trade-off relationship. Different array geometries are investigated here rather than the traditional liner or circular array but the combination of them which may explore a new research area in antenna engineering. Consideration of real elements would necessitate a

supplementary calculation of coupling effects. Therefore, the judgment of the algorithm would be based on the various structural parameters and resultant patterns.

REFERENCES

[1] S. Ibrahem, "Pattern synthesis of circular array," *Computers & Electrical Engineering*, vol. 19, no. 3, pp. 251-254, 1993.

[2] A. S. Zare and S. Baghaiee, "Application of ant colony optimization algorithm to pattern synthesis of uniform circular antenna array," *ACES Journal*, vol. 30, no. 8, Aug. 2015.

[3] M. Chryssomallis, "Smart antennas," *IEEE Antennas and Propagation Magazine*, vol. 42, no. 3, pp. 129-136, June 2000.

[4] P. Ioannides and C. A. Balanis, "Uniform circular arrays for smart antennas," *IEEE Antennas and Propagation Magazine*, vol. 47, no. 4, pp. 192-206, Aug. 2005.

[5] F. Gozasht, G. R. Dadashzadeh, and S. Nikmehr, "A comprehensive performance study of circular and hexagonal array geometries in the LMS algorithm for smart antenna applications," *PIER*, vol. 68, pp. 281-296, 2007.

[6] K. R. Mahmoud, M. El-Adway, S. M. M. Ibrahem, R. Basnel, R. Mahmoud, and S. H. Zainud-Deen, "A comparison between circular and hexagonal array geometries for smart antenna systems using particle swarm algorithm," *PIER*, vol. 72, pp. 75-90, 2007.

[7] L. C. Kretly, A. S. Cerqueira Jr., and A. A. S. Tavora, "A hexagonal adaptive antenna array concept for wireless communication applications," *The 13th IEEE International Symposium on Personal, Indoor and Mobile Radio Communications*, vol. 1, pp. 247-249, Sept. 15-18, 2002.

[8] A. A. Lotfi, M. Ghiamy, M. N. Moghaddasi, and R. A. Sadeghzadeh, "An investigation of hybrid elliptical antenna arrays," *IET Microw. Antennas Proag.*, vol. 2, no. 1, pp. 28-34, Jan. 2008.

[9] O. Gassab and A. Azrar, "Novel mathematical formulation of the antenna array factor for side lobe level reduction," *ACES Journal*, vol. 31, no. 12, Dec. 2016.

[10] M. L. M. Lakshmi, K. Rajkamal, S. V. A. V. Prasad, Md. Z. U. Rahman, "Amplitude only linear array synthesis with desired nulls using evolutionary computation technique," *ACES Journal*, vol. 31, no. 11, Nov. 2016.

[11] J. Robinson and Y. Rahmat-Samii, "Particle swarm optimization in electromagnetics," *IEEE Transactions on Antennas and Propagation*, vol. 52, no. 2, pp. 397-407, 2004.

[12] Z. W. Geem, J. H. Kim, and G. V. Loganathan, "A new heuristic optimization algorithm: Harmony search," *Simulation*, vol. 76, no. 2, pp. 60-68, 2001.

[13] C. Lin, A. Qing, and Q. Feng, "Synthesis of unequally spaced antenna arrays by using differential evolution," *IEEE Transaction on Antenna and Propagation*, vol. 58, no. 8, pp. 2553-2561, 2010.

[14] D. W. Boeringer and D. H. Werner, "Particle swarm optimization versus genetic algorithms for phased array synthesis," *IEEE Transactions on Antennas and Propagation*, vol. 52, no. 3, pp. 771-779, Mar. 2004.

[15] M. Azharuddin and P. K. Jana, "Particle swarm optimization for maximizing lifetime of wireless sensor networks," *Computers & Electrical Engineering*, vol. 51, pp. 26-42, Apr. 2016.

[16] M. K. Smail, H. R. E. H. Bouchekara, L. Pichon, H. Boudjefdjouf, and R. Mehasni, "Diagnosis of wiring networks using particle swarm optimization and genetic algorithms," *Computers & Electrical Engineering*, vol. 40, no. 7, Oct. 2014,

[17] H. R. Tizhoosh, "Opposition-based learning: A new scheme for machine intelligence," I*n Proc. Int. Conf. on Computational Intelligence for Modelling Control and Automation*, vol. 1, pp. 695-701, 2005.

[18] H. R. Tizhoosh, "Reinforcement learning based on actions and opposite actions," *In Proc. ICGST Int. Conf. Artif. Intell. Mach. Learn. Egypt*, pp. 94-98, 2005.

[19] H. R. Tizhoosh, "Opposition-based reinforcement learning," *Journal of Advanced Computational Intelligence and Intelligent Informatics*, vol. 10, pp. 578-585, 2006.

[20] S. Rahnamayan, H. R. Tizhoosh, and M. M. A. Salama, "Opposition-based differential evolution," *IEEE Trans. on Evolutionary Computation*, vol. 12, no. 1, pp. 64-79, 2008.

Rajesh Bera passed B.Tech. degree in Electronics and Communication Engineering, from Birbhum Institute of Engineering & Technology, West Bengal, India in 2010. He received the M.Tech. degree from KIIT, Bhubaneswar, India in 2012.

Presently, he is attached with NIT Durgapur, West Bengal, India, as Institute Ph.D. Research Scholar in the Department of ECE. His research interest includes Array Antenna design, Array parameter optimization and beam-pattern synthesis using Evolutionary Computing Techniques.

Durbadal Mandal passed B.E. degree in ECE, from Regional Engineering College, Durgapur, West Bengal, India in the year 1996. He received the M.Tech. and Ph.D. degrees from NIT Durgapur, West Bengal, India in the year 2008 and 2011 respectively.

Presently, he is attached with NIT Durgapur, West Bengal, India, as Assistant Professor in the Department of ECE. His research interest includes Array Antenna design; filter Optimization via Evolutionary Computing Techniques.

Rajib Kar passed B.E. degree in ECE, from Regional Engineering College, Durgapur, West Bengal, India in 2001. He received the M.Tech. and Ph.D. degrees from NIT Durgapur, West Bengal, India in 2008 and 2011, respectively.

Presently, he is attached with National Institute of Technology, Durgapur, West Bengal, India, as Assistant Professor in the Department of Electronics and Communication Engineering. His research interest includes VLSI, signal Processing.

Sakti Prasad Ghoshal passed B.Sc. and B.Tech. degrees in 1973 and 1977, respectively, from Calcutta University, West Bengal, India. He received M.Tech. degree from I.I.T (Kharagpur) in 1979. He received Ph.D. degree from Jadavpur University, Kolkata, West Bengal, India in 1992.

His research interest areas are: Application of Evolutionary Computing Techniques to Electrical Power systems, Digital Signal Processing, Array antenna optimization and VLSI.

On the Theoretical Analysis of Radiation Pattern and Gain of Printed Monopole Antennas

Somen Bhattacharjee [1], Rakhesh S. Kshetrimayum [2], and Ratnajit Bhattacharjee [2]

[1] Department of Electronics and Communication Engineering
Techno India University, Kolkata, 700091, India
b.somen@iitg.ernet.in

[2] Department of Electronics and Electrical Engineering
Indian Institute of Technology, Guwahati, 781039, India
krs@iitg.ernet.in, ratnajit@iitg.ernet.in

Abstract ─ This paper reports a theoretical approach to analyze radiation pattern and gain of Printed Monopole Antennas (PMA). Theoretical analysis of PMAs is performed by modeling PMA as an asymmetrical dipole antenna. The effect of patch and ground plane is considered separately then combined. The far field expressions for rectangular and circular PMAs are derived and verified with available experimental results from published work and High Frequency Structure Simulator (HFSS) simulated results. The analytical, simulated and available measured results are in close agreement. The theoretical gain for rectangular and circular monopole antennas are also computed and compared with HFSS simulation results.

Index Terms ─ Asymmetrical dipole antenna, gain, Printed Monopole Antennas (PMA), radiation pattern.

I. INTRODUCTION

Printed monopole antennas (PMA) are prominent candidate for broadband and ultra-wide band applications, having features of large impedance bandwidth and omni-directional radiation patterns. Some of the simulation and experimental works on PMAs are available in the literature [1]-[5]. However, theoretical analysis of radiation characteristics of PMAs is not adequately dealt in the literature. Microstrip line fed printed monopole antenna can be considered as an asymmetrically driven dipole antenna, in which the patch and the ground plane form two arms of the dipole [6]. The spectral domain field components of an infinitesimal current source on an ungrounded dielectric layer can be found in [7], but it doesn't account radiation pattern and gain calculation. However in [7], numerical approach is adapted to calculate input impedance and reflection coefficient for rectangular and F shaped PMA. But the present literature

is focused on developing analytical approach to calculate radiation pattern and gain of rectangular and circular PMA taking into account the current distribution on the patch as well the effect of the ground plane below the feed line. To the best of the knowledge of the authors, theoretical treatment of PMA along with closed form expressions for the far field radiation patterns of rectangular and circular PMAs has not been reported in literature. The theoretical results of radiation patterns for rectangular and circular PMAs fed by 50Ω microstrip line are compared with available experimental data given in [3] and [4], and simulation results obtained using HFSS. In addition to this, the calculated theoretical gain is also verified by HFSS simulation results.

II. THEORY

A. Radiated field of an HED lying on an ungrounded substrate

The radiated fields of a PMA can be formulated using Green's function of an HED lying on an ungrounded substrate and from the knowledge of current distribution on the patch as well as the ground plane below the feed line. So, an HED lying on a lossless and ungrounded dielectric layer is considered first. To derive spectral domain electric and magnetic field Green's function, an HED is assumed to be lying on a lossless dielectric layer located at (x_0, y_0) shown in Fig. 1. The x-directed current is defined as $J_x = \hat{x}\delta(x-x_0)(y-y_0)$ and the effect of J_x is considered by applying boundary conditions.

The transverse components of the electric field $\tilde{E}_x$ and $\tilde{E}_y$ at $(x = h)$ are given by [7]:

$$\tilde{E}_x = \frac{j}{\omega\epsilon_0 k_\rho^2}\left[\frac{k_x^2 u_2}{D_{TM}} + \frac{k_0^2 k_y^2}{D_{TE}}\right]\tilde{J}_x, \qquad (1)$$

$$\tilde{E}_y = \frac{j}{\omega \epsilon_0 k_\rho^2} \left[\frac{k_y k_x u_2}{D_{TM}} - \frac{k_0^2 k_y k_x}{D_{TE}} \right] \tilde{J}_x , \qquad (2)$$

where

$$D_{TM} = 1 + \frac{u_2 \epsilon_r \left(u_1 + u_0 \epsilon_r tanh(u_1 h) \right)}{u_1 \left(u_0 \epsilon_r + u_1 tanh(u_1 h) \right)} ,$$

$$D_{TE} = u_2 + \frac{\left(u_0 + u_1 tanh(u_1 h) \right)}{\left(1 + \frac{u_0}{u_1} tanh(u_1 h) \right)} ,$$

$$u_2^2 = -k_z^2 = k_\rho^2 - k_0^2 , \; u_1^2 = -k_z^2 = k_\rho^2 - \epsilon_r k_0^2 ,$$

$$u_0^2 = -k_z^2 = k_\rho^2 - k_0^2 \;\; , k_\rho^2 = k_x^2 + k_y^2 .$$

The far field radiation pattern of an HED on an ungrounded dielectric layer in region 2 $(z > h)$ can be written as [8]:

$$E_\theta = \frac{e^{-jk_0 r}}{2\pi r} \left[cos(\phi) \tilde{E}_x + sin(\phi) \tilde{E}_y \right], \qquad (3)$$

$$E_\phi = \frac{e^{-jk_0 r}}{2\pi r} \left[-sin(\phi) cos(\theta) \tilde{E}_x + cos(\phi) cos(\theta) \tilde{E}_y \right]. \quad (4)$$

Now, substituting Equations (1), (2) in Equations (3) and (4), $k_0 sin(\theta) cos(\phi)$, $k_0 sin(\theta) sin(\phi)$, $k_0 cos(\theta)$ in place of k_x, k_y and k_z we get the final far field expressions. The far field radiation pattern of an HED on an ungrounded dielectric layer is expressed as:

$$E_\theta = \alpha_1 \frac{n(\theta) cos(\theta) \{ \epsilon_r cos(\theta) + jn(\theta) tan(\beta_1 h) \}}{2\epsilon_r n(\theta) cos(\theta) + j tan(\beta_1 h) \{ n^2(\theta) + \epsilon_r^2 cos^2(\theta) \}} , \tag{5}$$

$$E_\phi = \alpha_2 \frac{\{ n(\theta) sec(\theta) + j tan(\beta_1 h) \}}{2n(\theta) sec(\theta) + j tan(\beta_1 h) \{ n^2(\theta) sec^2(\theta) + 1 \}} , \tag{6}$$

where

$$\alpha_1 = -cos(\phi) \left(\frac{j\omega\mu_0}{4\pi r} \right) e^{-jk_0 r} , \; \alpha_2 = sin(\phi) \left(\frac{j\omega\mu_0}{4\pi r} \right) e^{-jk_0 r} ,$$

$$\beta_1 = k_0 n(\theta), \; n(\theta) = \sqrt{\epsilon_r - sin^2(\theta)} .$$

The theoretical gain (G) of an HED on an ungrounded dielectric layer in a given direction (θ, ϕ) can be expressed as [9]:

$$G = \frac{4 \left(sin^2 \phi \, | E_\theta |^2 + cos^2 \phi \, | E_\phi |^2 \right)}{\int_0^{\frac{\pi}{2}} (sin\theta) \left[| E_\theta |^2 + | E_\phi |^2 \right] d\theta} . \qquad (7)$$

It may be noted that the above Green's function for far field depend on both substrate thickness and dielectric constant (ϵ_r). Thus, the variation of thickness and dielectric material and their effects on the field as well as in the gain can be theoretically observed.
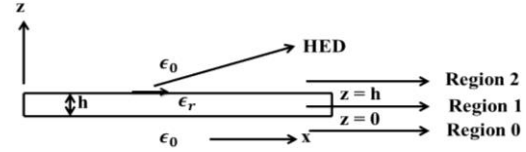
Fig. 1. Geometry of an HED along x-axis on the interface of dielectric and free space.

B. Radiated fields of PMA

The above expressions in Equations (5) and (6) give far fields of a HED on a dielectric substrate. The current supported by the feed in printed monopole antenna shown in Fig. 2 can be expressed in terms of incident traveling wave $(e^{-jk_0(x+f_g)})$ and reflected wave $(\Gamma e^{jk_0(x+f_g)})$ due to impedance discontinuity at the junction of feed and the patch. Note that $x + f_g$ is the total length of the feed including feed gap (f_g) and Γ is the current reflection coefficient. Thus, the net current given to PMA through the feed line can be given by [10]:

$$J(x, y) = \hat{a}_x I_0 (e^{-jk_0(x+f_g)} + \Gamma e^{jk_0(x+f_g)}) . \qquad (8)$$

Hence,

$$\tilde{J}(k_x, k_y) = \int_{-L/2}^{L/2} \int_{-W/2}^{W/2} J(x, y) e^{-j(k_x x + k_y y)} dxdy . \qquad (9)$$

So, after replacing k_x and k_y by $k_0 sin(\theta) cos(\phi)$, $k_0 sin(\theta) sin(\phi)$ and for $\Gamma = -1$, Equation (9) can be written as:

$$\tilde{J}(\theta, \phi) = 4 sinc(0.5 k_0 W sin(\theta) sin(\phi)) [\sigma_1 - \sigma_2], \quad (10)$$

where

$$\sigma_1 = 2sin(0.5 k_0 L sin(\theta) cos(\phi)) cos(0.5 k_0 L) \{ k_0 cos(f_g k_0) + jk_0 sin(\theta) cos(\phi) sin(f_g k_0) \} ,$$

$$\sigma_2 = 2cos(0.5 k_0 L sin(\theta) cos(\phi)) sin(0.5 k_0 L) \{ k_0 sin(\theta) cos(\phi) cos(f_g k_0) + jk_0 sin(f_g k_0) \} .$$
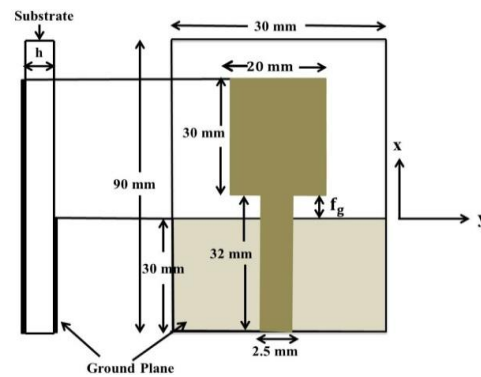
Fig. 2. Geometry of rectangular printed monopole antenna on dielectric substrate $(\epsilon_r = 4.3, tan\delta = 0.02)$ of thickness h=1.52 mm in [3].

It may be noted that current distribution in Equation (10) includes a quadrature term. In case of printed monopole antennas, the ground plane also contributes

to the radiation field. The ground plane acts as an asymmetric image of the monopole to form an asymmetrically driven dipole antenna. The current distribution in the ground plane can be given as:

$$\tilde{J}_g(\theta,\phi) = 4\sin c\left(0.5 k_0 W_g \sin(\theta)\sin(\phi)\right)\left[\sigma_{11} - \sigma_{12}\right], \quad (11)$$

where

$$\sigma_{11} = 2 k_0 \sin\left(0.5 k_0 L_g \sin(\theta)\cos(\phi)\right)\cos\left(0.5 k_0 L_g\right),$$

$$\sigma_{12} = 2 k_0 \cos\left(0.5 k_0 L_g \sin(\theta)\cos(\phi)\right)\sin\left(0.5 k_0 L_g\right)\sin(\theta)\cos(\phi).$$

L_g, W_g represent the length and width of the ground plane of PMA. Thus, the overall radiation pattern for the rectangular printed monopole antenna, including the effect of the partial ground plane as shown in Fig. 2 can be written as:

$$E_{\theta pr} = \left(\frac{j\omega\mu_0}{4\pi r}\right)e^{-jk_0 r}(\tilde{J}(\theta,\phi)+\tilde{J}_g(\theta,\phi))E_\theta, \quad (12)$$

$$E_{\phi pr} = \left(\frac{j\omega\mu_0}{4\pi r}\right)e^{-jk_0 r}(\tilde{J}(\theta,\phi)+\tilde{J}_g(\theta,\phi))E_\phi. \quad (13)$$

The gain for the case of a rectangular printed monopole antenna can be calculated using Equation (7). The closed form expressions for the far field radiation patterns of circular printed monopole antenna shown in Fig. 3 can be written as:

$$E_{\theta pc} = \left(\frac{e^{-jk_0 r}}{r}\right)(\tilde{J}(\theta,\phi)+\tilde{J}_g(\theta,\phi))E_\theta, \quad (14)$$

$$E_{\phi pc} = \left(\frac{e^{-jk_0 r}}{r}\right)(\tilde{J}(\theta,\phi)+\tilde{J}_g(\theta,\phi))E_\phi. \quad (15)$$

For circular PMA, $\tilde{J}(\theta,\phi)$ can be given as:

$$\tilde{J}(\theta,\phi) = \int_0^{2\pi}\int_0^a J\left(a\cos(\theta),a\sin(\theta)\right)e^{-j\left(k_x a\cos(\theta)+k_y a\sin(\theta)\right)}a\,da\,d\theta,$$

where $k_x = k_0\sin(\theta)\cos(\phi)$, $k_y = k_0\sin(\theta)\sin(\phi)$ and a is the radius of the circle. Similar to rectangular PMA, the gain of circular printed monopole antenna can be found using Equation (7).
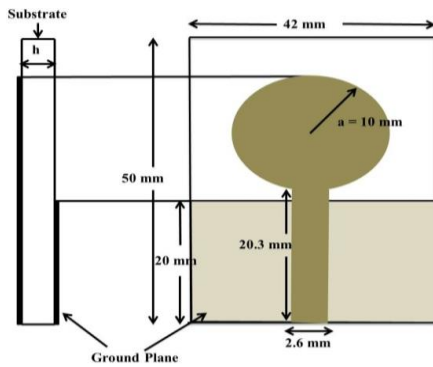
Fig. 3. Geometry of circular printed monopole antenna on dielectric substrate ($\epsilon_r = 4.7, tan\delta = 0.02$) of thickness h=1.5 mm in [4].

III. RESULTS

This section presents the results computed using the analytical expressions derived for the rectangular PMA and circular PMA and compares the same with the measured results available in literature as well with the results obtained through HFSS simulations. The radiation patterns of rectangular printed monopole antenna are shown in Fig. 4 and Fig. 5, whereas the gain plot is shown in Fig. 6. The gain plot shows that the gain is decreasing in the given frequency band. In other words, it can be concluded that the antenna is more directive for lower frequencies in comparison to higher frequencies.

The radiation patterns of circular printed monopole antenna are shown in Fig. 7 and Fig. 8, whereas the gain plot is shown in Fig. 9. From Fig. 9 it can be observed that gain is almost constant for the given band.

(a)

(b)
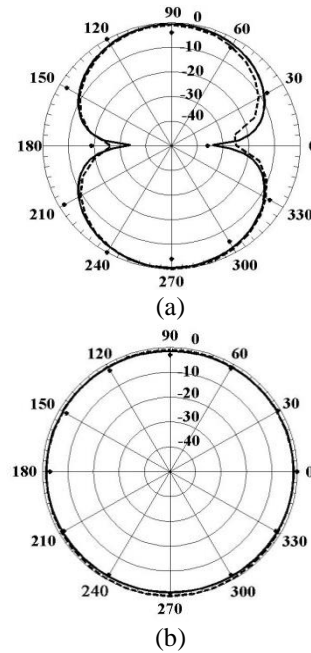
Fig. 4. Radiation patterns: (a) E-plane and (b) H-plane of the rectangular printed monopole antenna shown in Fig. 2 at 2.45 GHz (theory (—), simulation using HFSS (– –), and measured (.) [3]).

(a)

(b)
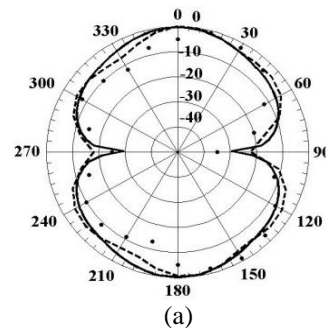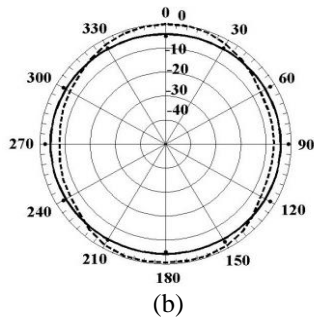
Fig. 5. Radiation patterns: (a) E-plane and (b) H-plane of the rectangular printed monopole antenna shown in Fig. 2 at 5.2 GHz (theory (—), simulation using HFSS (– –), and measured (.) [3]).
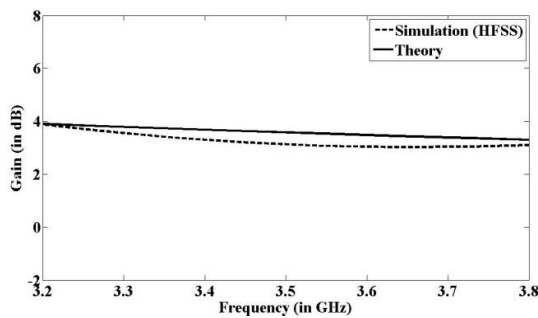
Fig. 6. Gain of rectangular printed monopole antenna on dielectric substrate ($\epsilon_r = 4.3, tan\delta = 0.02$) of thickness h=1.52 mm.

(a)

(b)
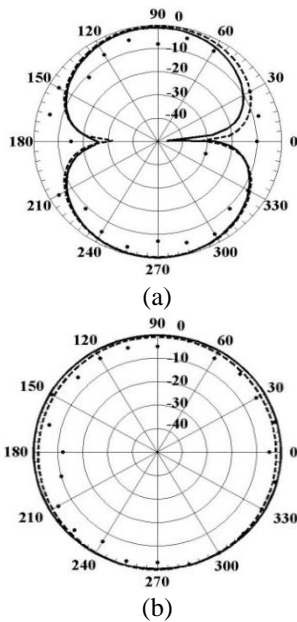
Fig. 7. Radiation patterns: (a) E-plane and (b) H-plane of the circular printed monopole antenna shown in Fig. 3 at 3 GHz (theory (—), simulation using HFSS (– –), and measured (.) [4]).

(a)

(b)
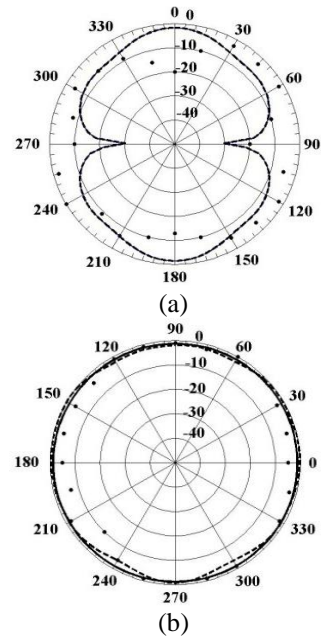
Fig. 8. Radiation patterns: (a) E-plane and (b) H-plane of the circular printed monopole antenna shown in Fig. 3 at 6.5 GHz (theory (—), simulation using HFSS (– –), and measured (.) [4]).
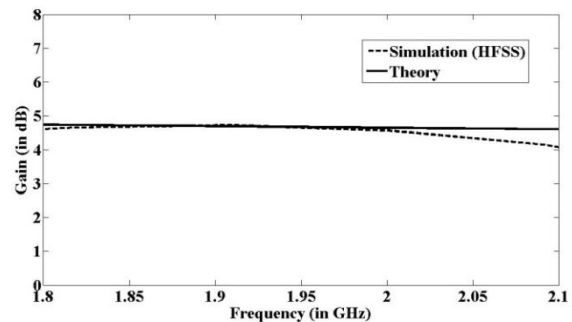
Fig. 9. Gain of circular printed monopole antenna on dielectric substrate ($\epsilon_r = 4.7, tan\delta = 0.02$) of thickness h=1.5 mm.

IV. CONCLUSION

In this paper, the transverse field components in spectral domain are derived for a horizontal electric dipole on a lossless dielectric layer, which is not backed by a conducting ground plane, are used to calculate the radiation patterns for rectangular and circular printed monopole antenna. Since the ground plane also affects the radiation characteristics of PMAs, taking the ground plane as an asymmetric image of the monopole the overall far field components of PMA are derived. However, the modeling has some limitations because the concept can be implemented for regular shape of the patch and the ground plane only. But the theoretical results in the present cases for the radiation pattern are in

good agreement with HFSS and available experimental results. Further, the theoretical gains of both PMAs are also verified using HFSS simulations.

REFERENCES

[1] M. Srifi, S. Podilchak, M. Essaaidi, and Y. Antar, "Compact disc monopole antennas for current and future ultrawideband (UWB) applications," *IEEE Trans. Antennas Propagation*, vol. 59, no. 12, pp. 4470-80, Dec. 2011.

[2] J. R. Panda and R. S. Kshetrimayum, "An F shaped printed monopole antenna for dual-band RFID and WLAN applications," *Microwave and Optical Technology Letters*, vol. 53, pp. 1478-81, July 2011.

[3] M. John, J. Evans, M. Ammann, and J. Modro, "Reduction of ground plane dependent effects on microstrip line fed printed rectangular monopoles," *IET Microwave Antennas Propagation*, vol. 2, no. 1, pp. 42-47, Feb. 2008.

[4] J. Liang, C. Chiau, X. Chen, and C. Parini, "Study of a printed circular disc monopole antenna for UWB system," *IEEE Trans. Antennas Propagation*, vol. 53, no. 11, pp. 3500-04, Nov. 2005.

[5] A. Panahi, X. Bao, G. Ruvio, and M. Ammann, "A printed triangular monopole with wideband circular polarization," *IEEE Trans. Antennas Propagation*, vol. 63, no. 1, pp. 415-18, Jan. 2015.

[6] H. J. Visser, *Approximate Antenna Analysis for CAD*. John Wiley & Sons Ltd, 2009.

[7] S. Bhattacharjee, R. S. Kshetrimayum, and R. Bhattacharjee, "Derivation of potential Green functions for ungrounded dielectric slab and its application in full wave analysis of PMAs," *Journal of Electromagnetic Waves and Applications*, vol. 29, iss. 16, pp. 2242-2256, 2015.

[8] D. G. Fang, *Antenna Theory and Microstrip Antenna*. CRC Press, 2010.

[9] D. Jackson and N. Alexopoulos, "Gain enhancement methods for printed circuit antennas," *IEEE Trans. Antennas Propagation*, vol. 33, no. 9, pp. 976-87, Sep. 1985.

[10] A. K. Bhattacharyya, "Long rectangular patch antenna with a single feed," *IEEE Trans. Antennas Propagation*, vol. 38, no. 7, pp. 987-93, July 1990.

Somen Bhattacharjee received his B.Tech., M.Tech. degrees in Electronics and Communication Engineering from Asansol Engineering College and NIT Durgapur, in 2006 and 2010 respectively. He received Ph.D. degree from the Department of Electronics and Electrical Engineering, IIT Guwahati, India in 2016. Presently, he is an Assistant Professor in Techno India University, Kolkata. His research interests are in the areas of antennas, microwave and electromagnetic theory.

Rakhesh Singh Kshetrimayum is a Professor in the Department of EEE, IIT Guwahati. He received the Ph.D. degree from the School of EEE, NTU Singapore in 2005. Prior to joining IIT Guwahati, he did Postdoctoral research from the Department of EE, Pennsylvania State University USA (2005) and the Department of ECE, IISc Bangalore (2004-2005). He has chaired several IEEE international conferences including NCC 2016, Guwahati (TPC Chair), DSP 2015, Singapore (Session Chair), AEMC 2015, Guwahati (TPC Chair) and WOCN 2011, Paris (TPC Chair), NCC 2011, Bangalore (Session Chair), CMC 2010, Shenzhen (Publication Chair) and NetCom 2009, Chennai (Program Chair). He is an Editorial Board Member of International Journal of RF and Microwave Computer-Aided Engineering (Wiley), Area Editor of AEU International Journal of Electronics and Communications (Elsevier), Associate Editor of IET Journal of Engineering and Editor-in-Chief of International Journal of Ultra Wideband Communications and Systems (Inderscience). Kshetrimayum is the recipient of IETE M. Rathore Memorial Award (2015), Dept. of Science & Technology India (SERC) Fast Track Scheme for Young Scientists (2007-2010) and NTU Research Scholarship from 2001-2004. His current areas of research interests are in microwave/millimeter wave antennas/circuits, UWB communications & MIMO wireless communications. He is a Life Fellow of the IETE, Optical Society of India, Antennas Test & Measurement Society of India, a Senior Member of IEEE, USA, Life Member of Applied Computational Electromagnetics Society, USA and Member of European Microwave Association. He has published a textbook and several research papers in the areas of his research interests.

Ratnajit Bhattacharjee received his B.E. in Electronics and Telecommunication Engineering (First Class Hons.) from Gauhati University, M.Tech. from IIT Kharagpur and Ph.D. (Engineering) from Jadavpur University, Kolkata. Presently, he is a Professor in the Department of Electronics and Electrical Engineering, IIT Guwahati. Prior to joining IIT Guwahati in 2002, he was a Faculty Member in REC (NIT) Silchar. His research interest includes Wireless communication, Wireless networks, Microstrip antennas, Microwave Engineering and Electro-

magnetics. Seven students have completed their Ph.D. under his supervision and at present several students are working under his supervision. He has co-authored about one hundred and twenty research papers in journals, international and national conferences. He has served as General Chair for 5th Edition of Applied Electromagnetic Conference, AEMC 2015 and 22nd National Conference on Communications, NCC 2016. He has also served as TPC member for several conferences. He has developed a web course on Electromagnetic Theory under the NPTEL project of Ministry of Human Resource Development (MHRD). He is also actively involved with the ongoing mission project of MHRD on virtual laboratories. He was a Co-investigator for a contracted research from NICT Japan in the area of Next-Generation Wireless Networks and PI for a project from ISRO in the area of development of matched feed for offset reflector antennas. Currently, he is Chief Coordinator for DeitY supported project for setting up of an E&ICT academy at IIT Guwahati. He is a Member of IEEE and Life Member of Indian Society of Technical Education.